Chair of Structural and Functional Ceramics

Doctoral Thesis

Processing of ceramic materials with tailored microstructures deploying tape casting and stereolithographic 3D-printing

Dipl.-Ing. Anna-Katharina Hofer, BSc

June 2023

MONTANUNIVERSITÄT LEOBEN
www.unileoben.ac.at

AFFIDAVIT

I declare on oath that I wrote this thesis independently, did not use other than the specified sources and aids, and did not otherwise use any unauthorized aids.

I declare that I have read, understood, and complied with the guidelines of the senate of the Montanuniversität Leoben for "Good Scientific Practice".

Furthermore, I declare that the electronic and printed version of the submitted thesis are identical, both, formally and with regard to content.

Date 26.06.2023

Signature Author
Anna-Katharina Hofer

Expressions of gratitude

Coming back to academia and committing to obtain a PhD was not an easy decision for me. Now, after more than three years, being in the stage of finishing, I may say that my choice was the right one.

Many people supported me along this way, who I want to express my thanks to.

The credit should be given to Prof. Raùl Bermejo, my supervisor, who made this all possible. His trust, patience, and his given freedom to explore and follow my own thoughts challenged me but let me grow. I want to thank all my colleagues, from the chair of structural and functional ceramics, who were always willing to help and pass on their knowledge. Fruitful discussions, joint participations at conferences and activities after work, have made colleagues to friends, especially among us PhD students. Great thanks I want address to my office mate Irina Kraleva, my student assistants Andreas Vratanar, Tobias Prötsch and Marlies Wratschko for helping me with the experimental work.

Besides the support from the chair, I could benefit from the experience and knowledge of Dr. Gary L. Messing and Dr. Elizabeth L. Kupp from PennState University. Grateful thanks to them for their advise, explanations and pointing out directions I have often initially not been paying attention to.

Dr. Andraž Kocjan, from the Jožef Stefan Institute, was a visiting researcher at our chair, which resulted in collaboration between the two departments. For me, Andraž became a person of trust, who I also want to express my grateful thanks to.

I feel lucky to have close friends I can always count on. I thank them for their friendships, evenings of cooking, playing, joining me on outdoor adventures and for lifting me up on ‘cloudy’ days.

The greatest thanks though I want to express to my family, Mama Elisabeth, Papa Stefan and my sisters Sophia and Nuria as well as my boyfriend Tobias. Knowing to have them behind my back and on my side, and that they always love me no matter what, gives me strength and motivation to reach all the goals I seek for. Also, thanks to my niece Sarah and her newborn brother Samuel, who fulfill me with joy and make me aware of the little beautiful things in life.

Last, I would like to dedicate this work to my Opa Herbert. He was a fighter and, especially now in the stage of finishing, he kept pushing me and told me that I can do this.

Abstract

Ceramics are often the choice when materials from other classes reach their limits. Their outstanding properties as e.g. low density, wear resistance, biocompatibility, thermal and/or electrical resistance/conductivity are in the first place determined by the ionic and partially covalent bonding. Besides, the polycrystalline grain structure may have a significant effect on structural as well as functional properties. As versatile the properties and application of ceramics, as different the polycrystalline microstructures may be: large/small grains; anisotropic/isotropic crystallographic orientation of grains; high/low porosity; monolithic/composite. Regarding structural properties for example, small grain sizes in a defect free microstructure may be beneficial for improving the mechanical strength, whereas large as well as oriented grains may enhance the fracture resistance.

Whether certain microstructural properties develop depends on the materials diffusivity throughout the sintering process. Ceramic powder size and shape, powder preparation, shaping method, green density, impurities, present sintering additives, dopants and sintering parameters are all exemplary factors which can have an impact on the diffusivity of matter.

In this thesis different shaping methods as well as conventional and non-conventional sintering technologies were investigated to tailor microstructural and consequently mechanical as well as optical properties of alumina ceramics. Tape casting and a stereolithographic 3D-printing technology were used to texture alumina microstructures according to the method of templated grain growth. Monolithic textured alumina ceramics as well as the effect of a second phase were investigated regarding damage tolerance. The sintering of templated samples within a spark plasma sintering furnace with applied pressure was explored in order to obtain highly textured, fully densified and translucent alumina microstructures.

For simple shapes several non-conventional sintering technologies, often combined with applied pressures, are available to optimize microstructural properties. Ceramic components of high complexity, as fabricated with additive manufacturing, are mainly limited to conventional sintering. Here, a pressure-less spark plasma sintering set-up with a heating rate of $\sim$ 450 °C/min was used to tailor the microstructure of stereolithographic 3D-printed alumina ceramics regarding (i) submicron grain sizes and (ii) texture. The obtained results of the rapid sintered samples have demonstrated that this non-conventional sintering technology could open the path to tailor microstructural and mechanical properties of highly complex shaped ceramics with reduced sintering times (minutes) and energy consumption.

Kurzfassung

Keramiken kommen oft zum Einsatz, wenn Materialien anderer Klassen an ihre Grenzen gelangen. Eigenschaften wie geringe Dichte, Abriebbeständigkeit, Biokompatibilität, sowie die Fähigkeit thermisch und/oder elektrisch isolierend beziehungsweise leitend zu sein, werden vor allem durch die ionische und teils kovalente Bindung der Atome bestimmt. Zusätzlich trägt der Aufbau des polykristallinen Gefüges signifikant zu den Struktur- und Funktionseigenschaften von Keramiken bei. So verschieden die Eigenschaften und Einsatzgebiete von Keramiken sein können, so verschieden kann auch ein keramisches Gefüge erscheinen (große/kleine Körner; anisotrope/isotrope kristallographische Orientierung der Körner; hohe/niedrige Porosität; ein-/mehrphasig). Bezogen auf Struktureigenschaften, wird für hohe Festigkeiten ein Gefüge mit feinen Korngrößen bevorzugt, wohingegen grobe und kristallographisch orientierte Körner für eine erhöhte Schadenstoleranz erwünscht sind.

Die Ausbildung genannter Gefügeeigenschaften, wie Korngröße und Porosität, hängt von der Diffusivität der Atome während des Sinterprozesses ab. Die Diffusivität kann durch mehrere Faktoren beeinflusst werden, wie zum Beispiel die Partikelgröße und die Aufbereitung des keramischen Pulvers, die Formgebung, die Gründichte, Verunreinigungen, Sinteradditive, Dotierungselemente sowie die Sinterparameter.

In dieser Arbeit wurden zwei verschiedene Formgebungsverfahren, sowie konventionelle und nicht-konventionelle Sintertechnologien verwendet. Der Einfluss dieser auf die Gefügeeigenschaften von Alumina Keramiken und folglich auf mechanische sowie optische Eigenschaften wurde untersucht. Tape Casting und stereolithographischer 3D-Druck wurden verwendet um texturiertes Alumina nach dem Prinzip von ‘Templated Grain Growth‘ herzustellen. Untersucht wurde das Bruchverhalten sowohl von monolithischen, als auch von zweiphasigen texturierten Alumina Keramiken. Weiters wurden Proben in einem Spark Plasma Sintering (SPS) Ofen unter Druck gesintert, um die Möglichkeit von texturierten, dichten und transluzenten Alumina Keramiken zu untersuchen.

SPS und auch andere nicht-konventionelle Sintertechnologien verwenden oftmals Druck um Gefügeeigenschaften von Keramiken zu optimieren. Durch die Aufbringung des Drucks sind diese Technologien stark limitiert auf einfache Geometrien. Komplexe Bauteile, hergestellt mittels additiver Fertigung, werden bis heute hauptsächlich konventionell gesintert. Ziel war es einen drucklosen SPS Aufbau zu verwenden um das Gefüge von 3D-gedruckten Alumina Keramiken einzustellen. Mit Heizraten von ~ 450 °C/min sollten Korngrößen unter 1 µm, aber auch ein texturiertes Gefüge erreicht werden. Die Ergebnisse zeigen, dass der untersuchte

Aufbau in Zukunft eine Möglichkeit bieten könnte, um bei reduzierter Prozessdauer (im Bereich von Minuten), als auch geringerem Energieverbrauch die Gefügeeigenschaften und folglich auch die mechanischen Eigenschaften von komplexen Keramiken zu optimieren.

Content

Abbreviations and acronyms

2θ	diffraction angle [°]
3YSZ	3 mol% yttria stabilized zirconia
Al_2O_3	aluminum oxide/ alumina
B3B	Ball-on-Three-Ball strength test
CeTZP	ceria partially stabilized tetragonal zirconia
CS	conventional sintering
CTE	coefficient of thermal expansion [/K]
DLP	digital light processing
EA	equiaxed alumina
EA_{SA}	equiaxed alumina with sintering additives
EA_6h	equiaxed alumina with a sintering time of 6 hours
EA+Ti_2AlC	equiaxed alumina with Ti_2AlC as second phase
f-value	volume fraction of oriented material ($0 \leq f \leq 1$) [-]
FWHM	Full-Width-of-Half-Maximum [°]
H	hardness [GPa]
HV	hardness after Vickers [GPa]
K_{Ic}	fracture toughness [MPa $m^{1/2}$]
LCM	lithography-based ceramic manufacturing
LF	Lotgering factor [-]
LP	liquid phase
m	Weibull modulus [-]
MASC	magnetically-assisted slip casting
NLA	nacre-like-alumina
PL-SPS	pressure-less spark plasma sintering
ρ_{rel}	relative density [%]
RS	rapid sintering
r-value	parameter of grain orientation ($0 \leq r \leq 1$) [-]
SEM	scanning electron microscope
SEVNB	Single-Edge-V-Notched-Beam method
σ_0	characteristic strength [MPa]
SPS	spark plasma sintering
SLA	stereolithography

T	temperature [°C]
t	time [s]
TA	textured alumina
TA+xZrO_2	textured alumina with x vol% non-stabilized zirconia
TA+x3YSZ	textured alumina with x vol% 3 mol% yttria stabilized zirconia
TA_2h	textured alumina with a sintering time of 2 hours
TA_6h	textured alumina with a sintering time of 6 hours
TA-SS	textured alumina sintered without sintering additives – solid state sintering
TA-LP	textured alumina sintered with sintering additives – liquid phase sintering
TC	tape casting
TGG	templated grain growth
VPP	vat photopolymerization
XRD	X-ray diffractometry
YSZ	yttria stabilized tetragonal zirconia
ZrO_2	non-stabilized zirconium dioxide/ zirconia
ZTA	zirconia toughened alumina (with yttria-stabilized zirconia, YSZ)

1 Introduction and motivation

Ceramic materials are used in a wide field of applications, where it may be distinguished between structural and functional ceramics. Regarding structural applications properties such as wear resistance, chemical inertness, thermal stability, stiffness or biocompatibility are of interest.[1,2] In the case of functional applications the aim is to exploit for instance thermal and/or electrical conductive/isolating, piezoelectric and/or optical properties. These materials properties are mainly determined by the atomic bonding. Besides, the polycrystalline (micro)structure may also have a great impact. A ceramic microstructure, consisting of multiple grains, can show high/low porosity or large/small grains with anisotropic/isotropic crystallographic orientation. The development of microstructural properties is directly associated with powder properties, the processing route and sintering conditions during the fabrication of a ceramic component.[3,4] Starting with powder preparation, the initial size, shape and specific surface area of powder particles, dopants (impurities) as well as the rheological behavior of the suspension are key to determine the final ceramic microstructures. During shaping, methods such as i.e. slip casting, tape casting or nowadays additive manufacturing often use a binder system for processability as well as for better dispersibility and packing of powder particles. The binder content can range up to 50 vol% and controls the green density of a ceramic component after binder removal. In general a relative green density of ~ 60 % is desired to achieve full densification during sintering. In solid state sintering, the heating of powder compacts to elevated temperatures causes diffusion, with the aim to reduce the surface free energy of the system. The activation energy for matter exchange differs for each material and shows a dependency on particle size. To enhance the diffusion of matter for certain materials liquid phase or viscous sintering may be pursued.

Further, sintering technology and sintering protocol can play an important role in the densification of ceramic parts. Different technologies have been investigated in the last decades, which may be classified in conventional and non-conventional sintering. Conventional sintering uses slow heating rates of ≤ 10 °C/min, where oxide ceramics are typically sintered in air and non-oxides in reducing atmospheres. Non-conventional sintering processes use high pressures (order of 100 MPa) or electric field-assisted rapid heating (100 - 10000 °C/min) to enhance densification and tailor grain size and porosity in ceramic microstructures.[5–7]

Multiple factors along with the different processing steps control the development of a ceramic microstructure and consequently its effect on structural and functional properties. Focusing on structural properties, where mechanical strength, fracture toughness, Young's modulus as well

as hardness are strongly affected by grain size, shape, crystallographic orientation and porosity. Whereas reduced grain sizes are desired to increase strength; for increased fracture toughness large grain sizes are beneficial. Physical properties typically show a strong dependency on density, where the Young's modulus and hardness decrease with increasing porosity. In the case of functional properties, for instance if transparent ceramics are sought, almost 0 % porosity is required for optimized optical properties.[8–16]

The effect of variations in microstructural properties, such as different grain sizes, crystallographic orientation and composites, on structural and functional properties have been extensively investigated on the example of aluminium oxide (alumina, Al_2O_3).[17–23] Alumina is one of the most used ceramics worldwide due to its outstanding properties such as high hardness, thermal shock resistance, electrical isolation, and chemical inertness, and relative competitive price as raw material. Typical applications of alumina are e.g. refractories, thread guides in textile industries, implants, cutting tools, substrates or as polishing and abrasive medium.[22,24] The average particle size of powders used for technical alumina ceramics is typically in the range of 0.3 – 0.5 µm. Alumina shows a high sensitivity regarding exaggerated grain growth, which results in rather large grain sizes (typically 3 – 5 µm,) but high relative densities (> 99 %) for standard sintering conditions (5 °C/min heating rate, 1600 °C maximum sintering temperature and 2 hours sintering time). Standard alumina ceramics show hardness values in the range of 15 – 19 GPa, mechanical strengths of 350 – 650 MPa, fracture toughness of 3.5 – 4 MPa $m^{1/2}$ and high opacity.[22,23,25]

The aim of improving the strength, fracture toughness and the optical properties of alumina ceramics has led to the investigation of different approaches to tailor its microstructural properties regarding grain size and shape, crystallographic orientation and porosity. Three of these approaches, which have been considered for investigations in this thesis, may briefly be discussed here: (i) Texturing of alumina microstructures, (ii) Composite alumina materials and (iii) Rapid sintering of alumina ceramics.

The crystal structures of numerous ceramic materials are asymmetric, which results in anisotropic properties in a single crystal. For example, the hardness of the (0001) plane of an alumina single crystal was determined to be ~ 23 GPa in comparison to ~ 19 GPa in a polycrystalline microstructure.[26] In textured polycrystalline microstructures the aim is to exploit these anisotropic properties by crystallographically orienting the grains. Further the morphology of the grains may be modified towards a tabular shape following the inspiration of the unique 'brick-and-mortar' structure found in nacre, figure 1. This structure is formed by ~ 99 % calcium carbonate (CaO_3) platelets, which are connected by a biopolymer

phase.[18,27,28] The inorganic platelets provide high stiffness, whereas the organic phase contributes as tough and compliant component. This composition and the hierarchical structure of platelets results in a simultaneously tough and stiff material.

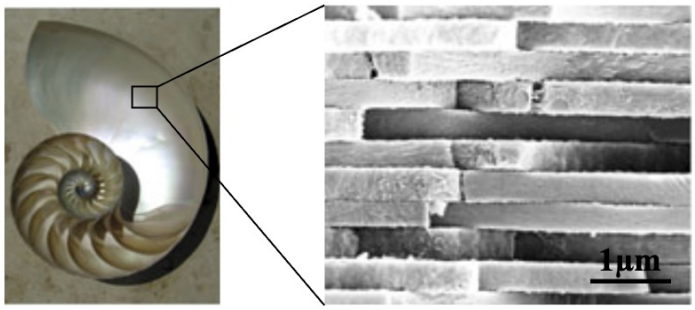

Figure 1: Example of the unique brick-and-mortar structure found in nacre.
Adapted under the terms of license CC-BY 4.0 [27]

Different research groups have used the approach of textured microstructures to improve the performance of functional ceramics (magnetic, ferroelectric, thermoelectric, piezoelectric, superconducting applications), but also the fractural behavior of structural ceramics such as alumina.

Textured alumina microstructures have been fabricated as (I) nacre-like-alumina (NLA) or after the method of templated grain growth (TGG). In the case of NLA, high loads (up to 98 vol%) of high aspect ratio alumina templates are used and growth is impeded through pressure-assisted sintering.[18,27,29] Weak interfaces between the platelets are formed, where different 'mortar' materials have been used, e.g. polymers but also metals to tailor structural and functional properties of NLA.

Regarding templated grain growth, the development of texture is based on coalescence during sintering where a rather small content of large high aspect ratio templates (e.g. 5 vol%) grows at the expense of surrounding smaller-sized equiaxed particles. The strong curvature of small particles leads to a higher tendency of atomic diffusion compared to the templates. Exaggerated grain growth is desired to achieve a tabular shaped grain structure with rather strong interfaces.[9,30,31] In both NLA and textured alumina microstructures through TGG, it has been reported that the toughness of alumina ceramics can significantly be improved by ≥ 40 %, associated with crack deflections provoked through the hierarchical structure and crystallographic orientation of tabular shaped grains.

As mentioned, alumina shows a high tendency to develop exaggerated grain growth. Dopants such as e.g. magnesium oxide or zirconium dioxide (zirconia, ZrO_2) are used to impede grain growth and reduce the grain size to especially improve the mechanical strength. Zirconia is

typically stabilized in its tetragonal phase at room temperature by the addition of ~ 3 mol % yttrium oxide (yttria-stabilized tetragonal zirconia, YSZ), which enables phase transformation toughening from the tetragonal to the monoclinic phase when stress is applied. Phase transformation toughening in dependency on grain size in monolithic YSZ materials results in fracture toughness values of K_{Ic} = 4 - 10 MPa $m^{1/2}$ with a lower hardness (H) than alumina (H ~ 12 GPa).[22,32–35] To reduce the grain size in alumina microstructures and to exploit the higher damage tolerance of YSZ, composites of zirconia toughened alumina (ZTA) have been developed.[36] A typical composition is ZTA with a content of 17 vol% YSZ. The high content of alumina in the ZTA composite obtains high hardness values (H ~ 17 GPa), whereas YSZ contributes to improved fracture toughness for alumina materials (K_{Ic} ~ 6 MPa $m^{1/2}$).[21,25,34,37,38]

The reduction of grain size in pure alumina ceramics, without using dopants, may be achieved by using non-conventional sintering technologies. Technologies such as spark plasma sintering (SPS) use high heating rates (≥ 100 °C/min) and applied pressures (≤ 100 MPa) to impede grain growth and enhance densification. The rapid heating is achieved through the Joule heating of a graphite die with the application of direct pulsed current. In the case of conductive materials, direct heating of the sample may occur through the current flow. Nowadays, multiple structural and functional materials of different material classes are densified using SPS.[39–42] In the case of alumina ceramics it has been shown that by using spark plasma sintering with a heating rate of 100 °C/min, a pressure of ~ 100 MPa and a sintering time of 5 minutes, dense microstructures (~ 98 %) with grain sizes around 500 nm at reduced sintering temperatures of 1200 °C can be obtained.[43] The reduction of grain size in alumina ceramics may contribute to enhanced mechanical strength, but also to tailor optical properties of alumina. Alumina is used as transparent ceramic in armor and jewelry industry. Transparency in polycrystalline materials can be obtained by achieving either (a) grain sizes smaller than the wavelength of light or by (b) enlarged grain sizes with crystallographic orientation to reduce birefringence through reduced numbers of grain boundaries. In both cases almost 100 % relative density is required.[15,20,44–48] The application of SPS on alumina powder compacts with a heating rate of 100 °C/min, a maximum sintering temperature of 1150 °C and a two-step pressure application of 35 MPa and 80 MPa with a sintering time of 60 minutes has led to a porosity of 0.14 % and a transmittance of 19.8 %.[49]

Microstructural properties have been shown to have a crucial effect on consequent materials properties and are influenced by various parameters throughout the fabrication process. In this thesis, the described approaches of texturing alumina microstructures, composite alumina

materials and microstructure control through spark plasma sintering have been taken into consideration to tailor the microstructural properties in tape cast and stereolithographic 3D-printed alumina ceramics. Textured microstructures fabricated after the method of templated grain growth, where templates were aligned with the tape casting process, have been combined with non-stabilized and 3 mol% yttria stabilized zirconia to investigate the effect of a second phase on the texture degree and fracture behavior. With tape casting, ceramic tapes of maximum thicknesses of ~ 3 mm can be fabricated, and geometries are limited to rather simple shapes. Therefore, the fundamentals learned from tape casting of texturing ceramics were aimed to be applied onto a stereolithographic 3D-printing process, to fabricate complex shaped textured alumina components with enhanced properties. An additional aspect of this thesis was to investigate the approach of achieving translucent alumina ceramics through enlarged grains with crystallographic orientation. Here texturing through the printing process as well as the non-conventional sintering technology of spark plasma sintering were combined. Long sintering times and applied pressure were used with the goal to achieve templated grain growth and reduce porosity for translucent textured alumina ceramics. Non-conventional sintering technologies are of great interest, enabling the optimization of microstructural properties regarding grain size and porosity. Applied pressure in many cases limits these technologies to simple geometries such as discs or plates. Nowadays, with the rising market of additive manufacturing, a pressure-less rapid sintering technology for components with high complexity may be desired. By using a pressure-less spark plasma sintering set up (PL-SPS), additive manufactured equiaxed and textured alumina samples were rapidly sintered at heating rates of ~ 450 °C/min with short sintering times (≤ 16 minutes). On the one side the aim was to impede grain growth to achieve submicron equiaxed grain structures to improve the strength in additive manufactured alumina samples. On the other side additive manufactured textured alumina microstructures were desired to be obtained using rapid sintering under the assumption that templated grain growth (TGG) may also take place, contrary to the typically needed prolonged sintering times of several hours (≥ 2 hours) to enhance the texture degree.

A pressure-less rapid sintering technology was used to explore the ability to tailor microstructural properties of additive manufactured complex shaped components and consequently structural and functional properties. Additionally, high heating rates and the process setting itself may reduce time and consumed energy compared to conventional sintering.

The following chapters provide detailed descriptions about the used processing routes (tape casting and vat photopolymerization), the principles of sintering, especially regarding templated grain growth as well as the physics of conventional and non-conventional sintering technologies (SPS and PL-SPS) which have been used in this thesis. Finally, an extended summary of the key publications of this thesis is given.

2 Processing and sintering of ceramic materials

Humankind has discovered and used ceramic materials already more than 20 000 years ago. Clay, a mixture of soil and water, was formed to pots or vessels, dried in air and burnt in covered holes in the ground. Along the centuries, the main principles of ceramic processing are still the same, but a development has occurred regarding the variety of applied ceramic materials and evolved shaping and sintering technologies. Slip casting, injection molding, tape casting and nowadays also additive manufacturing are examples of shaping technologies for different ceramic materials and applications. The densification of ceramic particles may be performed in conventional or non-conventional sintering furnaces, depending on the used material and desired phase composition as well as microstructural properties. In this thesis tape casting and a stereolithographic additive manufacturing technology have been used to shape ceramic powders. The sintering of fabricated ceramic samples was performed using a conventional sintering furnace, and in some cases with a non-conventional pressure-less rapid sintering technology.

2.1 Processing routes

2.1.1 Tape Casting

Tape casting is a process where ceramic tapes with thicknesses in the range of 1 µm to 3 mm can be fabricated. This technique has evolved in the early 1940s to produce capacitors.[50] Nowadays it is also used for the preparation of e.g. substrates for integrated circuits, layered piezo-electric components or membranes of solid oxide fuel cells.[51–53]

For the fabrication of ceramic tapes, low viscosity suspensions are prepared according to "colloidal processing".[54] Typically, the suspension consists of (a) ceramic powder particles, (b) a solvent, (c) a dispersant and (d) a binder with its plasticizers. Suspensions may be differentiated according to the used solvent system, either water- ("aqueous") or non-water-based ("non-aqueous"). In both cases, aqueous or non-aqueous, the solvent is used to support the dispersion of the ceramic powder particles and dissolve components of the polymeric binder. Aqueous systems have widely been used at the beginning of tape casting and are advantageous regarding economy and environment. Higher vapour pressures of organic solvents and consequently rather rapid and controllable evaporation in comparison to water has caused the replacement of aqueous systems by non-aqueous ones. Examples for solvents in non-aqueous systems are ethanol, methanol, toluene, methyl ethyl ketone (MEK) and xylene.

Powder particles of small grain sizes (< 1 µm) tend to agglomerate due to occurring van der Waals attractive forces at short distances between the particles. Therefore, for the separation and homogeneous distribution of the ceramic powder particles, dispersants are added to the system. Whether the suspension is based on water or organic solvents, poly- or monomeric chains are used to separate the particles by either electrostatic or steric repulsion mechanisms, or a combination of both (electro-steric repulsion).[50,54] Menhaden fish oil, phosphoric acid ester or polyethylene glycol (PEG) are examples for dispersants used for the preparation of tape casting suspensions.

Solvent and dispersant are crucial for preparation of a homogeneous and low viscosity suspension. In this thesis, the viscosity of used suspensions was $\eta \sim 300$ mPa·s. However, the function of the binder has its importance in the dried state of the tape, i.e. after casting and evaporation of the solvent. The polymeric matrix embeds the ceramic particles and provides a certain flexibility to the tape, enabling the separation from the carrier tape and ease of shaping such as cutting or stacking. To guarantee its plastic behaviour at room temperature, the binder is modified by the addition of different plasticizers. Plasticizers may contribute through different mechanisms and may be differentiated as plasticizers of type 1 and 2.[50] Type 1 can affect the polymer-chains of the binder chemically, causing a softening and splitting of the chains, which results in an increase of mobility and a reduction of the glass-transition temperature. Type 2 plasticizers are lubricants which enhance the movability of the polymer-chains. Examples of binders and plasticizers are polyvinyl butyral (PVB), polyvinyl alcohol (PVA), polymethylmethacrylate (PMMA) and benzyl butyl phthalat, dioctyl phthalat, dibutyl sebacate, menhaden fish oil or polyalkylene glycol (PAG), respectively.

The mixing of the different components of a tape casting suspension is typically done through ball milling in several steps. First, the ceramic powder is ball milled together with the solvent and the dispersant. In a second step, the binder with its plasticizers is added. After removing the milling balls (screening), the suspension is deaired on a magnetic stirrer prior tape casting.

Figure 2 shows a schematic of a tape casting set-up which was used in this thesis (CAM-L, Keko Equipment Ltd., Žužemberk, Slovenia). For the fabrication of a ceramic tape a low viscosity suspension is applied (fig. 2 (2)) onto a moving carrier tape (Mylar®) (fig. 2 (1)). The thickness of the tape is adjusted through the doctor blade, determining the gap height (fig. 2 (3)). During casting the tape is pulled along a heated and ventilated section for drying, where the solvent content is evaporated (fig. 2 (4)).

For bulk or multi-layer applications the dried tapes are stacked and first uniaxially warm pressed to connect the layers, followed by isostatic pressing. The thermal post processing for binder

removal can vary depending on the binder system and composition, and is typically done up to a maximum temperature of 600 °C. Sintering is then performed at higher temperatures (> 1500 °C) as needed to densify the ceramic.

Details about the preparation steps and compositions of the suspensions of the materials which have been used in this thesis, as well as the heating protocols for binder removal and sintering are found in chapter *3.1.1.*, *publication A* and in the appendix *'Tape casting: compositions'*.[50]

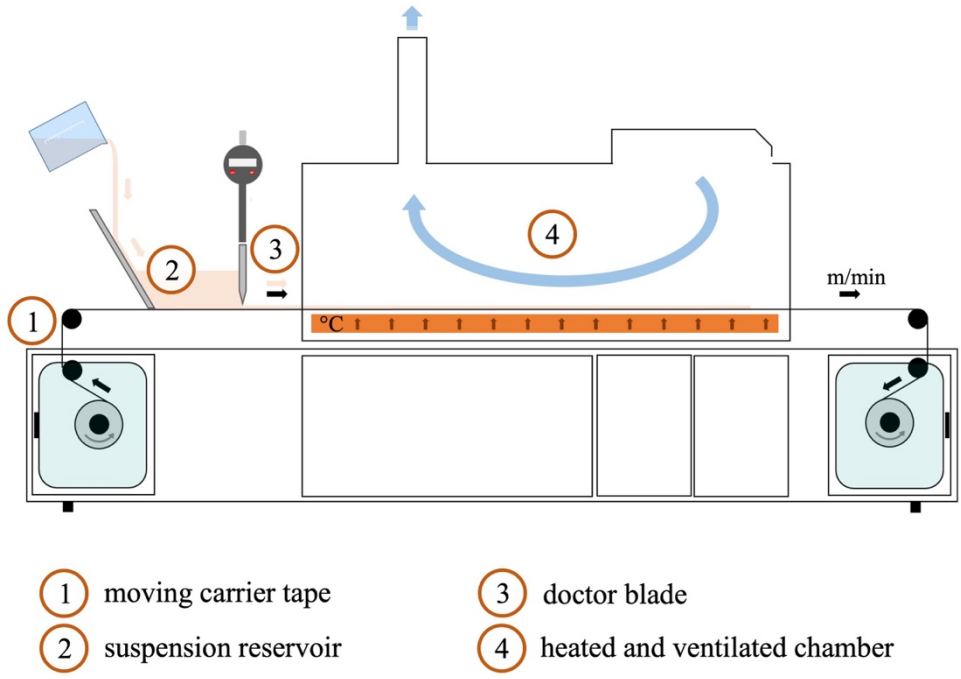

Figure 2: Schematic of the used tape caster to fabricate ceramic tapes

2.1.2 Stereolithographic 3D-printing

Additive manufacturing of ceramic materials is a rapidly growing market.[55,56] Rapid prototyping, the ability to fabricate parts with high complexity and accuracy as well as the lack of machining after processing are of great interest and have led to the development of multiple additive manufacturing technologies for ceramics. Many of these technologies are based on the principles of metal or polymer 3D-printing and can be divided in three main groups regarding the feedstock of the ceramic powder: (a) suspensions, (b) powder-beds or (c) bulk-solids. Stereolithography/ vat photopolymerization (SLA/VPP), digital light processing (DLP) and inkjet printing (IJP) are examples of technologies using suspensions for shaping ceramic powder particles. Powder-bed based technologies are for example binder jetting (BJ), selective laser sintering (SLS) or selective laser melting (SLM). Examples for technologies based on the feedstock of bulk-solids are laminated object manufacturing (LOM) and fused deposition

modelling (FDM).[57] The different technologies have their benefits and drawbacks according to accuracy, sample size and geometry as well as processing time. Regarding highly complex shapes and high resolution (~ 100 µm), technologies based on stereolithography are nowadays most promising to fabricate ceramics which are not realizable with conventional shaping methods. For the investigations in this thesis the so-called lithography-based ceramic manufacturing technology (LCM) was used, which is based on the principles of DLP, which is an extension of stereolithography (SLA), see figure 3a.[58–62] SLA uses a focused light source, i.e. a laser, causing a punctual solidification of a viscous suspension. By following a certain grid, the desired geometry is scanned and samples are built layer-wise. In the case of DLP, the light beam is deflected onto a setting of multiple squared flexible mirrors, where one mirror represents one pixel. Through the adjustment of the flexible mirrors and light reflection, multiple pixels and consequently a connected area can be depicted in one step. For these technologies, SLA and DLP, photopolymerization is used to solidify photo-sensitive polymeric suspensions filled with ceramic powder particles.[63] Figure 3b shows the development of a polymeric network due to photopolymerization induced by the exposure to light (hv). Following equations describe the chemical reactions occurring during photopolymerization:

$$R - R \xrightarrow{hv} 2R^{\bullet}$$ formation of radicals ($R^{\bullet}$) due to light absorption (1)

$$R^{\bullet} + M \rightarrow RM^{\bullet}$$ reaction with unsaturated monomer/oligomer (M) (2)

$$RM^{\bullet} + M \rightarrow RM_n^{\bullet}$$ polymerization with other monomers/oligomer (3)

$$RM_n^{\bullet} + RM_m^{\bullet} \rightarrow RM_nM_mR$$ termination of radical polymerization (4)

n and m are running indices

The polymerization of monomers/oligomers is initiated by radicals ($R^{\bullet}$, equ. (1)), which exist due to the splitting of an initiator, which is induced through the energy of light of a certain wavelength (hv). Further, the radicals provoke the separation of typically unsaturated bonds of monomers/oligomers (M) resulting in a radicalisation of the monomer/oligomer. Thus, leading to the polymerization with other monomers and the formation of a polymeric network (equ. (2) and (3)). The polymerization is terminated by the combination of two radical polymer chains (equ. (4)).[64–66]

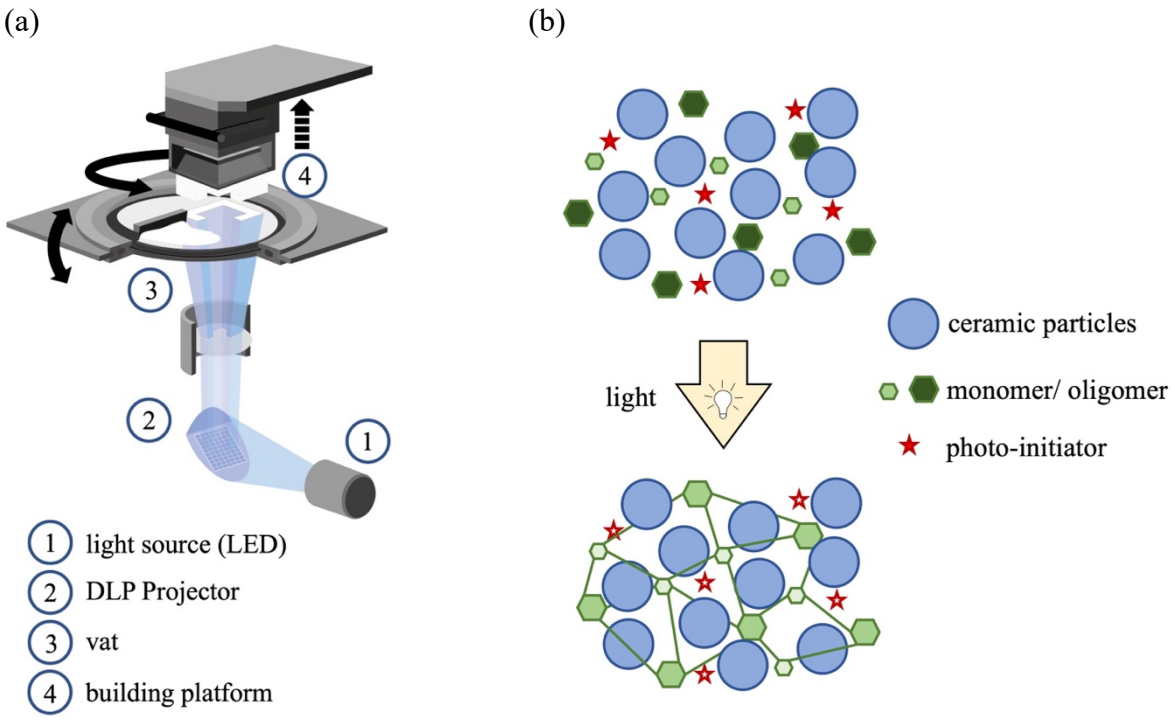

Figure 3: (a) Schematic of the LCM technology. **(b)** Development of a polymeric network through photopolymerization embedding ceramic particles.

The lithography-based ceramic manufacturing technology uses digital light processing to depict desired geometries by photopolymerization of light-sensitive suspensions, containing ceramic particles. The suspensions are compositions of a photocurable binder system and the ceramic powder, with a solids content of typically ≥ 40 vol%, to achieve a desired green density of ~ 60 %.[58,62,67] The photocurable binder system enables the printing and shaping, but has to be removed through a thermal post processing step to obtain a pure ceramic component. For the studies in this thesis commercially available suspensions were used from Lithoz GmbH (Vienna, Austria). These suspensions show a viscosity of $\eta \sim 20$ Pa·s. Figure 3a shows a schematic of the bottom-up set up of the LCM technology. In this study a CeraFab7500 (Lithoz GmbH, Vienna, Austria) was used with a LED as light source (fig. 3a (1)) which has its spectrum in the "blue"-light range, with a maximum at a wavelength of ~ 460 nm. The beam is reflected by the DLP grid of flexible squared mirrors (fig. 3a (2)), with one pixel having the dimensions of 40 x 40 µm, onto the bottom of the transparent vat (fig. 3a (3)). The vat is filled with a photo-sensitive ceramic suspension and through the adjustment of the building platform along the z-axis (fig. 3a (4)) layers are printed typically with a thickness of ~ 25 µm. The exposed area solidifies due to photopolymerization and attaches onto the platform. In a next step, the platform and/or the printed layer is separated from the vat bottom and through vat rotation a new layer of suspension is distributed. By repetition of the different steps, a composite

of a polymeric network, which keeps the ceramic particles separated, is printed layer by layer. The removal of the polymeric network requires a time-consuming thermal post processing, which can take up to one week. A complex debinding program is used with plateaus at different temperatures with long dwell times to gently decompose and burn-out the formed network to remove the different polymeric components. The debinding protocol for used alumina suspensions is found in the appendix *'Stereolithographic 3D-printing: Thermal post processing – binder removal'*. The result after debinding is an open-porous, fragile structure of ceramic powder particles, which is further sintered at elevated temperatures to full densification.[67]

2.2 Sintering mechanisms and technologies

In comparison to metals or polymers, ceramic materials have generally high melting points, above 2000 °C. Processes to reach these temperatures are of high expense and some ceramics, as Si_3N_4, tend to rather evaporate at their melting point instead of forming a melt. Therefore, to fabricate a densified ceramic part, powder particles are sintered, typically at temperatures of 2/3 of their melting point. Diffusion processes lead to atomistic movement and fusion of compacted particles. The global driving force, causing particles to exchange or combine matter, is the reduction of their total interfacial free energy, given as follows [4,36]:

$$\Delta(\gamma \cdot A) = \Delta\gamma \cdot A + \gamma \cdot \Delta A \tag{5}$$

where γ is the specific surface energy and A the total surface area. The change of the interfacial energy ($\Delta\gamma \cdot A$) leads to densification between the powder particles, whereas the change of interfacial area ($\gamma \cdot \Delta A$) causes grain coarsening, see figure 4a. Both terms contribute to the reduction of total interfacial free energy ($\Delta(\gamma \cdot A)$). The sinterability of powder particles and the activation of the mentioned phenomena, as densification and grain coarsening, are affected by different variables, which may be classified in (i) material and (ii) process related variables. According to the former, e.g. powder shape, size, size distribution, agglomeration or impurities control the sintering phenomena and the resulting microstructural properties. The particle size of ceramic powders is typically in the range of 0.1 to 100 µm. The size or more specific the curvature of powder particles determines the local driving force of sintering, described by the LaPlace equation [4,36]:

$$\Delta P = \gamma \cdot \frac{2}{r} \tag{6}$$

where P is the pressure, γ the surface energy and r the particles' radius and/or curvature. Considering this equation, particles with small radius exhibit high pressures, causing a lower stability, and consequently a higher sinterability compared to large powder particles. A certain distribution of size can be beneficial regarding better packing of particles. Agglomerates are generally not desired, because they may lead to enclosed porosity and/or act as impurities, leading to exaggerated and inhomogeneous grain growth.

Regarding process variables, sintering temperature, sintering times, pressure, atmosphere as well as the heating and cooling rates contribute to the densification and coarsening of ceramic materials. Process parameters such as temperature or pressure, significantly affect the diffusivity of atoms. The energy input, which is required to enhance diffusion, varies for each material, being dependent on the crystal structure and the strength of atomic bonding. As a result, the densification of materials (e.g. Si_3N_4, SiC) with strong ionic or covalent bonds, exhibiting a low diffusion constant, may not be possible through solid state sintering. Additives are used to form a liquid phase during sintering (liquid phase sintering), to enhance diffusivity and enable densification. In both cases matter transport occurs, following different paths from/to the centre or the surface of a powder particle. The occurring diffusion mechanisms are divided in (i) densifying and (ii) non-densifying. Figure 4b illustrates the densifying (1 - 3) as well as non-densifying mechanisms (4 - 6):

(1) grain boundary diffusion
(2) lattice diffusion (from the grain boundary)
(3) plastic flow
(4) surface diffusion
(5) lattice diffusion (from the surface)
(6) evaporation-condensation.

The different diffusion mechanisms are associated with different activation energies, with surface diffusion having the lowest energy, followed by grain boundary, plastic-flow and volume diffusion. Especially in the initial stage of sintering densifying diffusion mechanisms are desired, which contribute to neck formation, the exchange of matter and the joining of particles. Densification and coarsening during sintering determine the microstructural properties of a ceramic component. The grain size, shape, phase distribution or porosity can strongly be influenced by the sintering process and control the structural and functional properties of the final ceramic part.[2,4,36,68]

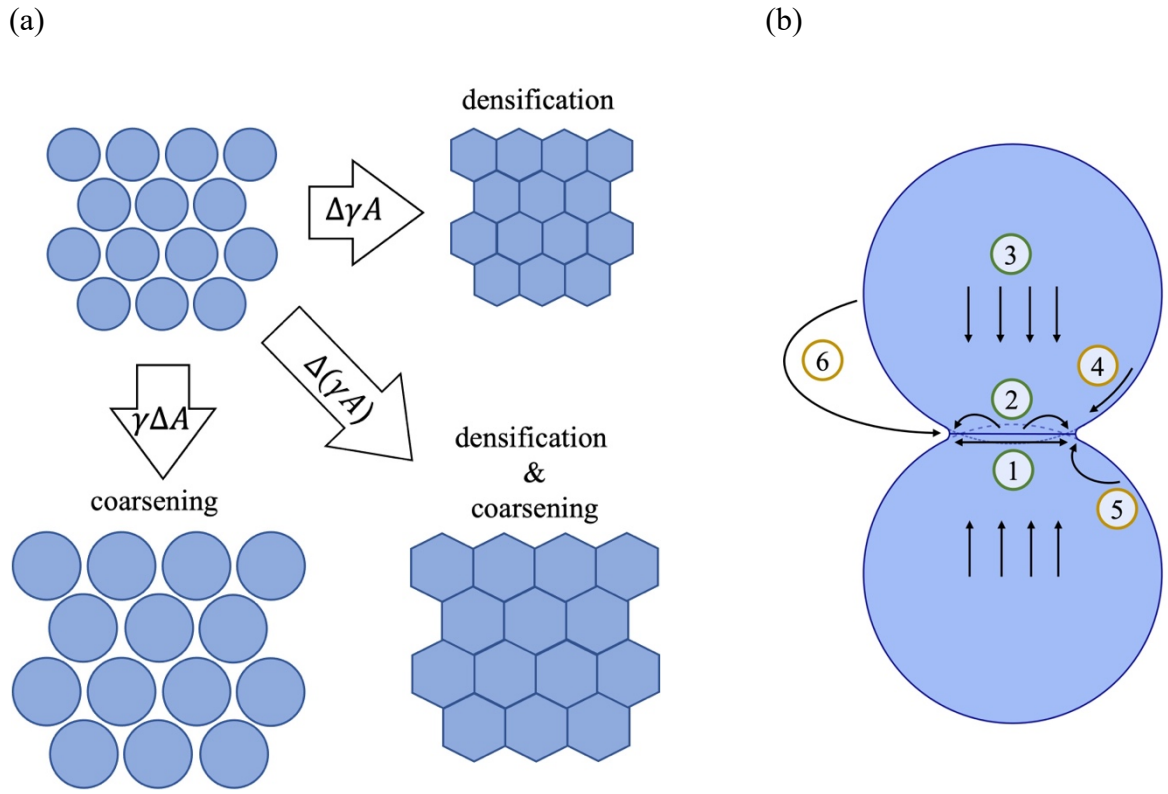

Figure 4: (a) Driving forces of sintering – reduction of surface energy (γ) and area (A). **(b)** Schematic illustrating densifying (1-3) and non-densifying (4-6) diffusion mechanisms.

2.2.1 Coarsening and Templated Grain Growth

Coarsening or grain growth can take place both in a 'normal' or 'abnormal' manner. In both cases the driving force is the reduction of the interfacial energy of grain boundaries, where curved shapes cause pressure differences at the different sides of a grain boundary. Grain growth is strongly dependent on the grain boundary mobility of a system which is affected by e.g. impurities, sintering additives, sintering temperature, or the grain boundary orientation. The 'normal' change in grain size shows a squared dependence on time and is described with following equation [4,36]:

$$\bar{G}_t^2 - \bar{G}_{t_0}^2 = \frac{4 \cdot D_b^{\perp} \cdot \gamma_b \cdot V_m}{\beta \cdot R \cdot T \cdot \omega} \cdot t \qquad (7)$$

where $D_b^{\perp}$ is the atom diffusion coefficient along the grain boundary, γ_b the grain boundary energy, V_m the atom volume, β a proportionality constant, R the gas constant, T the sintering temperature, ω the grain boundary thickness and t the sintering time.[4] Normal grain growth may lead to homogeneous microstructures with narrow and monomodal grain size distributions. In the case of 'abnormal' growth, also called exaggerated grain growth or coalescence, certain grains grow at a higher rate than others. The grain size of relatively large grains increases at the expense of surrounding smaller matrix grains/particles.

One special case of abnormal grain growth is Templated Grain Growth (TGG). TGG is one of the established methods to achieve textured microstructures. High aspect ratio templates are combined with submicron-sized ceramic powders. The content of templates may be in the range between 1 – 25 vol%.[17,69,70] To achieve tailored orientation of tabular grains in [0001] direction (for alumina crystals) after sintering, templates have to be aligned already in the green state. Several techniques have evolved for templates alignment as tape casting (TC), ice-templating or magnetically-assisted slip casting (MASC) and recently also additive manufacturing.[18,27,29,71] The processes used in this thesis to align high aspect ratio templates were (i) tape casting and (ii) lithography-based ceramic manufacturing (LCM).[72] In both cases ceramic powders and templates were dispersed in a suspension, which is distributed through a stable doctor blade and a moving carrier, as described in chapter *2.1.1.* and *2.2.2.* A gap between the blade and the carrier defines the applied thickness of the suspension. The movement of the carrier causes shearing of the suspension in the gap, forcing the templates to align parallel to the direction of distribution. Embedded in the submicron sized matrix, TGG of the aligned templates is provoked during sintering. Small particles experience high pressure due to the large curvature (equ. (6)), resulting in a high tendency of atoms to diffuse.[4] Diffusing matter precipitates onto the larger induced templates with lower surface energies, causing them to grow (Ostwald ripening), see figure 5a. To enhance abnormal growth and densification, sintering additives are often used to form a liquid phase (LP).[4,36,69] Increasing contents of LP have shown to lead to faster densification due to improved grain rearrangement, where homogeneous penetration of the grain boundaries is required.[31,70,73] According to Suvaci et al. templated grain growth can be divided into three stages: (i) densification, (ii) matrix grain growth and (iii) template growth.[73] In the first stage, matrix densification occurs without significant template growth. It was observed that a relative density > 90 % is required for TGG, where grain connectivity is present, and porosity has been reduced.[73,74] Matrix growth is controlled by diffusion through the liquid phase. After Lay's treatment, matrix coarsening can be described with following equation [75–77]:

$$r_t^3 - r_0^3 = 1.05 \cdot K_m \cdot t \tag{8}$$

where r_t and r_0 are the average matrix grain radii at time t and *zero*. K_m is a growth constant at a certain temperature given as follows [77]:

$$K_m = \frac{D \cdot S_0 \cdot M \cdot \sigma_m}{R \cdot T \rho \cdot c} \tag{9}$$

where D is the diffusion constant, S_0 the solubility at equilibrium (i.e. isotropic), M the molecular weight, R the gas constant, T the temperature, ρ the density of the material and c is a constant describing the thickness ($\delta = c \cdot r$) of the liquid phase layer related to the grain radius. c is the ratio between the volume of liquid phase (V_L) and the volume of solids content (V_S) [77]:

$$c = \frac{2 \cdot V_L}{V_S} \tag{10}$$

A high content of liquid phase results in a thicker liquid phase layer, which decreases matrix growth kinetics and consequently reduces growth of the matrix and templates.[4,75,76]
Further, increasing templates loading reduces growth kinetics due to the decrease in supersaturation in the liquid layer. The dissolution of matrix material is reduced resulting in limited saturation as well as decreased matrix and templates growth.
To describe growth of anisotropic templates, Seabaugh et al. investigated the growth of an alumina single crystal in a polycrystalline matrix during liquid phase sintering.[77] Figure 5b displays the anisotropic crystal structure of α-alumina (corundum), and its characteristic planes of $\{0001\}, \{01\bar{1}2\}$ and $\{11\bar{2}0\}$, indicated in blue, green and red, respectively. α-alumina has a rhombohedral lattice built of oxygen ions (anions), which form a hexagonal close packed array, where two thirds of the octahedral sites are filled with aluminum ions (cations). Considering the experiments with an α-alumina single crystal it was shown that growth along the $\{01\bar{1}2\}$ and $\{11\bar{2}0\}$ control the morphological development of the microstructure, which is correlated to the higher surface energies compared to the basal plane. The close atomic packing of the $\{0001\}$ plane results in a low surface energy and a thermodynamically stable state. The growth rates of the different planes can be ranked as $\{0001\} \ll \{01\bar{1}2\} < \{11\bar{2}0\}$. The driving force for the growth of the single crystal is controlled by the supersaturation of matter in the liquid phase layer and is described after the Gibbs-Thomson equation [78]:

$$S_m \approx S_0 \cdot \left(1 + \frac{2 \cdot \sigma_m \cdot M}{\rho \cdot R \cdot T \cdot r}\right) \tag{11}$$

where S_m describes the supersaturated state and S_0 the solubility at equilibrium. Higher solubilities of the non-basal planes lead to preferred growth of the anisotropic single crystal in radial direction. The growth rate of a single crystal at static supersaturation, respecting varying solubilities regarding different lattice planes was given by Henning et al. [79]:

$$\frac{dL}{dt} = \frac{D \cdot S_0}{\delta \cdot \rho} + \left((1 - k_{hkl}) + \frac{2 \cdot \sigma_m \cdot M}{\rho \cdot R \cdot T \cdot r}\right) \tag{12}$$

where L is the scale of the single crystal and k_{hkl} is a constant, relating the solubility of a certain crystal plane (S_{hkl}) to the equilibrium solubility (S_0): $S_{hkl} = k_{hkl} \cdot S_0$.

The coarsening of matrix grains and the growth of a single crystal in radial direction occur parallel. The equations used for describing single crystal growth in a polycrystalline matrix with present liquid phase may also be applicable for templated grain growth. Seabaugh et al. combined and integrated the equations from Lay and Hennings et al. (equ. (7) and equ. (11)) to describe matrix and templates growth with progressive time and change of grain size [77]:

$$R_t - R_0 = 5.8 \cdot K_m^{1/3} \cdot t^{1/3} + 1.4 \cdot K_m^{2/3} \left[\frac{\rho \cdot R \cdot T}{M \cdot \sigma_m} \cdot (1 - k_t) - \frac{k_t \cdot \alpha}{R_0}\right] \cdot t^{2/3} \quad (13)$$

where R_t and R_0 are the template radii at time t and *zero*, k_t and α are constants relating the templates solubility (S_t) and the surface energy (σ_t) of a certain plane to the equilibrium values (S_0 and σ_0), respectively: $S_t = k_t \cdot S_0$ and $\sigma_t = \alpha \cdot \sigma_0$. Due to impingement, radial growth of templates decreases with increasing grain size. Radial growth is followed by thickening of the tabular grains, meaning that enlargement in [0001] direction may occur. Growth of planar smooth basal planes is not controlled by diffusion but by the mechanism of 2D-nucleation. The growth rate of 2D-nucleation exponentially relates inversely to the supersaturation along the basal plane (S_B) [77]:

$$\frac{dL}{dt} = C_1 \cdot (S_B)^n \cdot \exp\left(\frac{-C_2}{T^2 \cdot S_B}\right) \quad (14)$$

with $S_B = \frac{2\sigma M}{\rho r}$ and C_1 and C_2 being constants including material and physical constants. In the case of poly-nucleation (2D) the exponent n equals 5/6.[73,77,80] At elevated temperatures and thin interfacial layers supersaturation is achieved faster. Decreasing liquid phase contents result in the formation of discontinuous and irregular interfaces, enhancing 2D-nucleation and templates thickening in [0001] direction.

The combination of the described three stages of templated grain growth during sintering contributes to the development of textured microstructures.

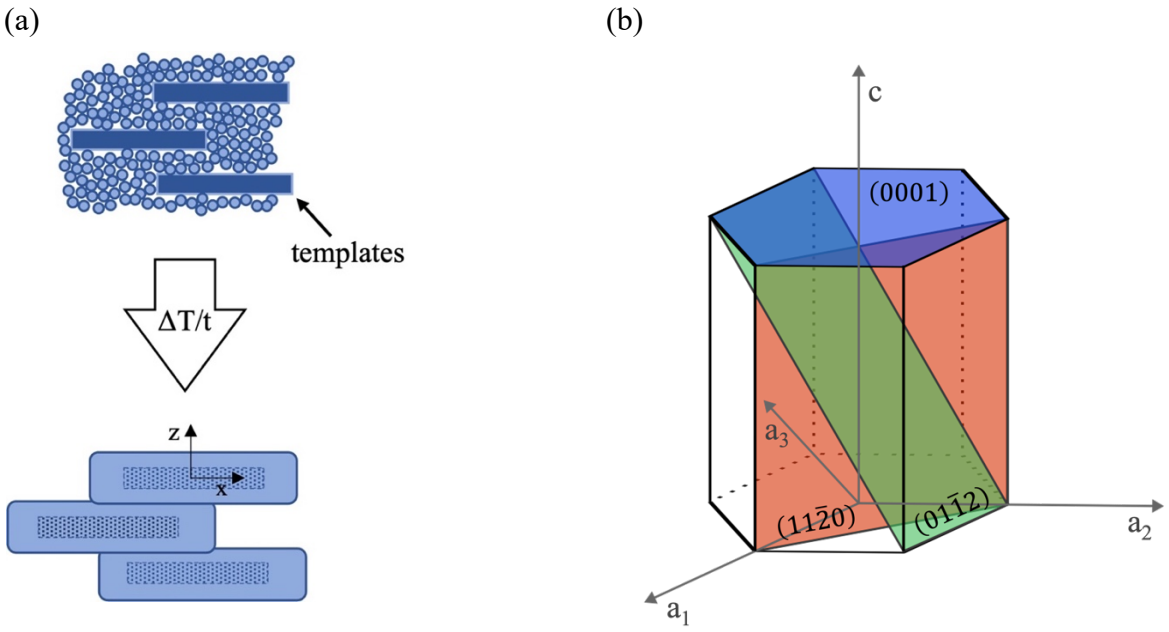

Figure 5: (a) Schematic of method of templated grain growth. **(b)** Hexagonal lattice structure with indicated planes.

2.2.2 Conventional sintering

Conventional sintering may be the simplest process to densify ceramic materials, both oxide ceramics and non-oxides (e.g. nitrides) using a reducing atmosphere for the latter. Typical heating rates are ≤ 10 °C/min, limited by the used heating elements. In early stages of sintering, diffusion mechanisms such as surface diffusion with low activation energies are favoured.[36] At elevated temperatures densifying diffusion mechanisms are activated, resulting in long sintering times and high sintering temperatures. In conventional sintering the heat may be transferred through (i) conduction, (ii) convection and (iii) radiation.[81–84] The driving force for conduction and convection is a temperature gradient from high- to low-temperature regions. Conduction is described as the heat transport along one or more solid bodies, which are in contact with each other. Through conductive heat the motion of bond atoms is stimulated. Following equation shows the direct proportionality of heat through conduction (q_{cd}) to temperature [81,82]:

$$q_{cd} = \frac{\overline{k_{av}} \cdot A}{l} \cdot (T_1 - T_2) \tag{15}$$

where k_{av} is the thermal conductivity of the conducted material at the average temperature of T_1 and T_2, A the conducted area and l the length of the conductor. T_1 and T_2 are the different temperatures of the two sides of a body or between two adjacent bodies.

Convection occurs in gas or liquid media and describes the heat transport through the motion of molecules. The transferred heat (q_{hv}) is directly dependent to the gradient of temperature [81,82]:

$$q_{cv} = \overline{h_c} \cdot A \cdot (T_1 - T_2) \quad (16)$$

where h_c is a coefficient describing the average convection along an area A.
Radiation is based on the emission of energy in form of electromagnetic waves from a heated body. Heating elements can be seen as a grey body, where the emitted energy (q_r) over all wavelengths and in all directions can be described after the law of Stefan-Boltzmann [81–84]:

$$q_r = \sigma \cdot \varepsilon \cdot A \cdot T^4 \quad (17)$$

where σ is the Stefan-Boltzmann constant having a value of 5.67 x 10^{-8} W/m^{2}K^4, ε describes the emissivity of a grey surface with an area A of the radiation source. For a black body $\varepsilon = 1$. The generated heat (q_r) shows a proportionality to temperature to the fourth power, which implies that radiation is the dominating heat transfer especially at elevated temperatures. In comparison, the heat transfer mechanisms of conduction and convection show a direct dependency on temperature and have an impact in the low temperature range.[81–85]

2.2.3 Non-conventional sintering

Structural and functional properties of ceramics strongly depend on their microstructural features, as density, homogeneity or grain size and shape. Sintering in ceramic manufacturing has a strong impact on tailoring those characteristics. For the optimization of microstructural properties and with the attempt to reduce processing time and temperature, alternative sintering technologies to conventional sintering, have been developed and investigated.[86] Non-conventional sintering technologies may be divided in (i) pressure-assisted, (ii) water- or solvent-assisted and (ii) field-assisted sintering.[7,42,87] The former includes hot pressing (HP) and hot isostatic pressing (HIP), where either uniaxial or isostatic pressure is applied.[2] Water- or solvent-assisted sintering such as the cold sintering process (CSP) uses a chemical transient liquid phase and high pressures to densify ceramics at low temperatures (< 300 °C).[88–91] Examples for field-assisted sintering technologies are micro- and millimeter wave sintering (MWS), ultra(-fast) high temperature sintering (UHTS), flash sintering (FS) and spark plasma sintering or field-assisted sintering (SPS or FAST).[19,87,92–97] These technologies have succeeded in applying very high heating rates which can range from 100 °C/min to even 10 000 °C/min. Using high heating rates, the aim is to avoid especially the non-densifying

diffusion mechanism of surface diffusion, which has the lowest activation energy. Surface diffusion may cause the reshaping of pores resulting in larger radii and a reduction of driving force for pore removal. Increased heating rates may enable densifying diffusion mechanisms with higher activation energies at an earlier stage and reduce the time spent in the energy range for surface diffusion. This may lead to the maintenance of high driving forces and more rapid densification in the early stage of sintering. Additionally, grain growth may be reduced since full densification has already been achieved in the short time.[5,98–100] In the case of SPS, additional pressure is applied to enhance densification, limiting grain growth and enable the reduction of sintering temperature. External pressures improve particle rearrangement and increase the driving force and kinetics of densification. Compared to pressure-less sintering, the densification mechanism of plastic deformation and creep can be activated additional to lattice and grain boundary diffusion. This also counts for the processes of HP and HIP.[4]

Among the mentioned field-assisted sintering technologies, SPS might be the most established one and has shown to result in optimized microstructures towards pore-free and submicron grain sizes for various materials. For spark plasma sintering, a cylindrical die, typically of graphite, is filled with a powder or a powder compact. Pressures up to ~ 100 MPa can be applied; limitation here is the yield strength of graphite. The heating of the contacted graphite die is achieved through 'Joule heating' by pulsed electric direct current (DC). Joule heat (Q) generated through the resistance of a material (R) during conduction with a certain current (I) after a certain time (t), follows Joule's first law [81]:

$$Q = I^2 \cdot R \cdot t \tag{18}$$

Figure 6a shows a typical SPS set-up, where heating rates of ~ 100 °C/min can be achieved through Joule heating. The occurring heat transfers are mainly conduction and radiation. Convection may not occur due to applied vacuum. With SPS, optimized microstructural properties towards full densification and small grain sizes may be attained due to high heating rates and applied pressure. However, the applied pressure limits this technology to rather simple shapes of ceramic applications. Regarding complex shapes, especially nowadays with the developing field of additive manufactured ceramics, sintering technologies with high heating rates but without pressure might be of great interest to tailor microstructural properties. Besides MWS and UHTS the technology named as 'radiation-assisted sintering' (RAS), 'sintering with intense thermal radiation' (SITR) or 'pressure-less SPS' (PL-SPS) has been investigated, which could be used for sintering components of high complexity. However, research using this technology to tailor ceramic microstructures is scarce and has only shown first results for zirconia, alumina and lead-free piezoelectric ceramics.[85,101–104] In PL-SPS a modified

graphite die is used within a SPS furnace, as shown in figure 6b. A hollow cylinder is enclosed by two full cylinders at the top and bottom. As in SPS these full cylinders are contacted, and the graphite die is heated through Joule heating. Due to the rather thin walls (~ 5 mm) of the mid hollow cylinder, in comparison to classical SPS, heating rates can be increased up ~ 500 °C/min. The sintering is performed in vacuum at a pressure of about 10 Pa. A shaped sample can be placed within the hollow cylinder on a graphite wool to avoid direct contact to the graphite die (isolation). Thus, the main heat transfer is radiation. Due to the high heating rates, elevated temperatures are achieved more rapid and emitted energy from the graphite crucible follows the temperature to the fourth power (equation (16)).

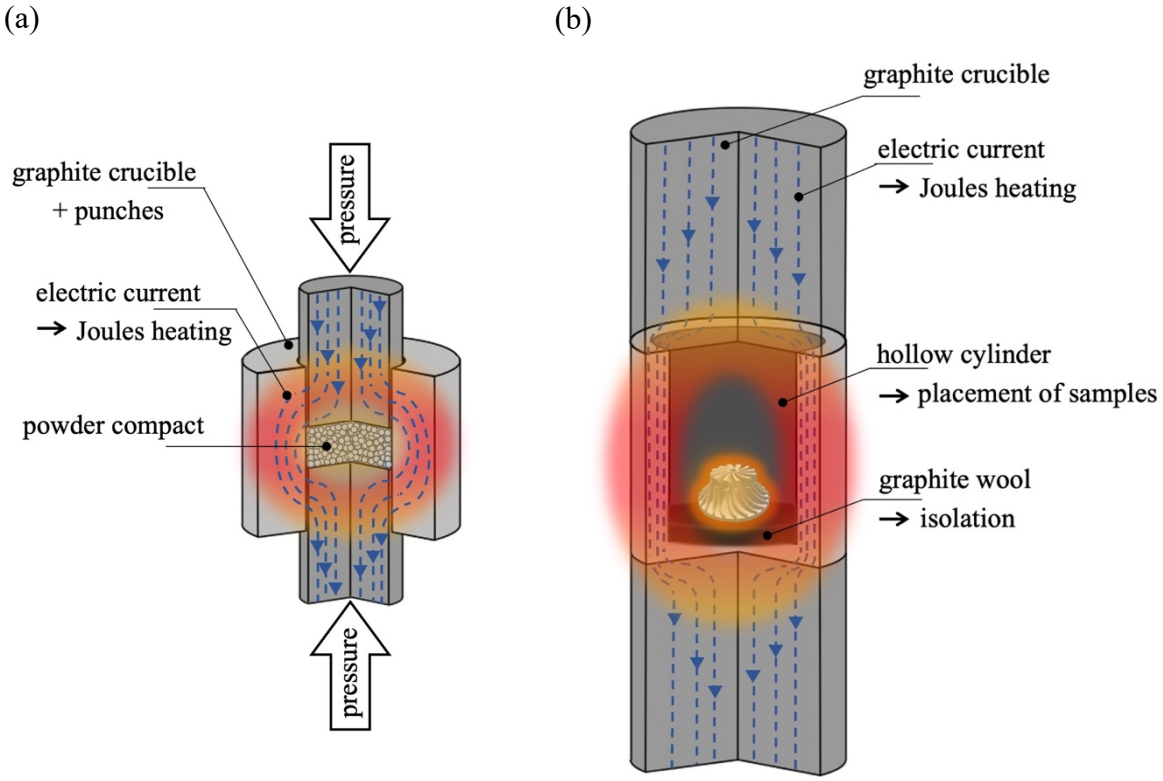

Figure 6: Schematic of graphite crucibles used for **(a)** conventional spark plasma sintering (SPS) and **(b)** pressure-less spark plasma sintering (PL-SPS).

3 Experimental work

The ceramic samples investigated in this thesis have been fabricated using tape casting and stereolithographic 3D-printing. Sintering was performed conventionally and non-conventionally. The samples were further characterized according to microstructural, physical, mechanical and optical properties. Following, a detailed description about the different fabrication steps and applied characterization and testing methods is given.

3.1 Fabrication of investigated materials

The fabrication of materials for tape casting and 3D-printing started with the preparation of suspensions. Colloidal suspensions were prepared by dispersing ceramic powder particles in a viscous binder system. In the case of tape casting, suspensions were prepared in-house, whereby for stereolithographic 3D-printing commercially available photosensitive suspensions (Lithoz GmbH, Vienna, Austria) were used and modified for textured microstructures.

3.1.1 Tape Casting procedure

The tape casting process (hereafter referred to as TC) was used to fabricate equiaxed as well as textured microstructures, utilizing a Keko Equipment (CAM-L, Keko Equipment Ltd., Žužemberk, Slovenia). TC may be divided in different sections: (i) suspension preparation, (ii) tape casting, (iii) sample preparation and (iv) thermal post processing. Along these sections multiple parameters affect the quality of the tape and the final sintered body. In all sections preliminary experiments were performed to achieve samples with high relative density and in the case of textured alumina, a high degree of texture.

(i) Suspension preparation

In a first step, powder particles were dispersed in solvents using a dispersant to enable homogenous dispersibility. In a second step, the binder system was added and mixed. In this work suspension preparation was performed on a ball mill, where the ceramic powder particles were dispersed in a composition of non-aqueous solvents, a steric dispersant and a binder system, see table 1. The effect of the rotation speed of the ball mill and the duration of milling on the dispersibility of the ceramic particles during the first ball milling step was investigated (see Bachelor thesis from Tobias Prötsch for more details).[105] Two rotation speeds of 30 rpm and 137 rpm from different ball mill assemblies as well as different durations of 3, 6, 12, 24, 48 and 96 hours were compared. For this investigation an alumina suspension was prepared according to the composition listed in table 1. As a measure for dispersibility the viscosity of the suspension as well as the particle distribution were determined. The viscosity measurement

was performed in a rotational viscometer (ViscoQC 300, Anton Paar, Graz, Austria) using a constant shear rate of $\gamma = 250$ rpm for one minute in a 75 ml beaker. The particle size distribution, determining the ability of dispersing agglomerates, was measured in a particle size analyser (Granulometer Particle Size Analyzer CILAS 1064 L, CILAS, Orléans, France) based on laser diffraction, where the slurry was distributed in a pipe system filled with water. Figure 7 shows the viscosity measurements for the different ball mill rotation speeds and durations. Best dispersibility was found for the rotation speed of 30 rpm and a milling duration of 24 hours, where the lowest viscosity and smallest particle size with monomodal distribution was reached.

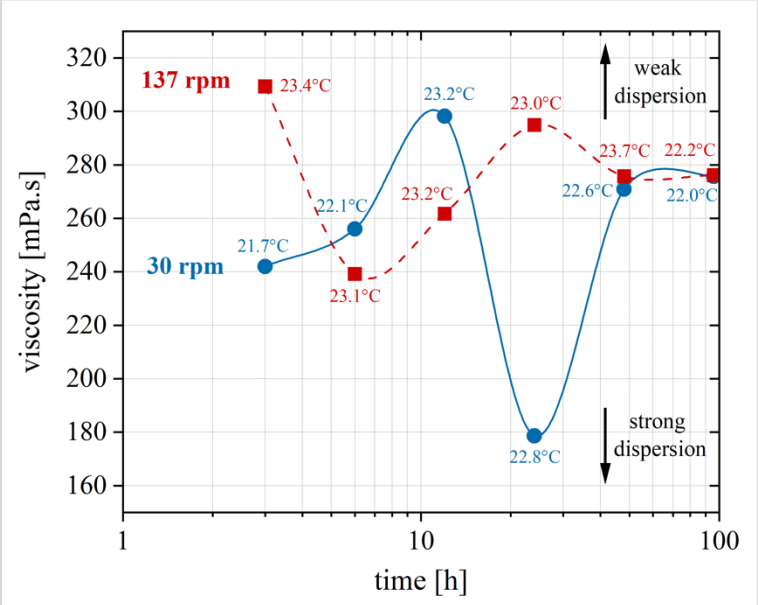

Figure 7: Viscosity measurements of tape casting suspensions after the first ball milling step at different rotation speeds and ball milling times.

According to these measurements, the first ball milling step, in order to mix the ceramic powder particles (α-Al_2O_3 (99.99 % ultrafine), TM-DAR, Taimei Chemicals Co. Ltd., Nagano, Japan) with the solvents (Ethanol 99 % (Sigma-Aldrich GmbH, Darmstadt, Germany) + Xylene (Avantor Performance Materials Poland S.A., Gliwice, Poland)) and the dispersant (Menhaden fish oil, Sigma-Aldrich GmbH, Vienna, Austria), was performed for 24 hours at 30 rpm. In a second step, the binder system, consisting of the binder itself and its plasticizers, was added (Polyvinyl Butyral + Butylbenzyl Phthalate + Dibutyl Sebacate, Sigma-Aldrich GmbH, Steinheim, Germany) and the suspension ball milled for another 24 hours. Following, the suspension was sieved into a beaker, which was covered with a Parafilm©, leaving a small gap to enable evaporation. The suspension was further deaired on a magnetic stirrer for 24 hours prior tape casting.

Textured microstructures: In the case of textured microstructures, which were fabricated for *publication A*, additionally sintering additives for liquid phase sintering as well as high aspect ratio templates were added, see table 1. The sintering additives of CaO, in form of $Ca(NO_3)_2{\cdot}4H_2O$ (ThermoFischer GmbH, Kandel, Germany), and SiO_2, in form of $C_8H_{20}O_4Si$ (ThermoFischer GmbH, Kandel, Germany), were added in a 1:1 ratio during the first ball milling step. A content of 0.10 wt% of CaO and SiO_2, related to the total solids content (powder + templates) was selected. During the first ball milling step only 80 % of the solvent content was added. A ratio of 5 vol% of high aspect ratio templates (with respect to the solids content) was added after the second ball milling step (after 48 hours). The templates with a thickness of ~ 10 µm and a diameter of ~ 5-16 µm (Rona Flair© White Sapphire, EMD Performance Materials Corp., Darmstadt, Germany) were first dispersed in the remaining solvent content of 20 % and 2 drops of additional dispersant through ultrasonication. In a last step this formulation was added to the suspension and ball milled for approximately 30 min.

Table 1 shows exemplary suspension compositions for achieving equiaxed alumina and templated alumina tapes of high green density and optimized tape handability.

Table 1: Exemplary compositions of tape casting suspensions for equiaxed and textured alumina microstructures.

		equiaxed alumina	textured alumina
		vol%	
Solids	Al_2O_3	18.41	18.17
	Templates		0.91
Sintering additives	$Ca(NO_3)_2{\cdot}4H_2O$		0.08
	$C_8H_{20}O_4Si$		0.15
Solvents / Dispersant	Menhaden fish oil	2.51	2.43
	Xylene	33.72	33.28
	Ethanol 99 %	36.70	36.21
Binder / Plasticizer	Polyvinyl Butyral	4.18	5.08
	Butylbenzyl Phthalate	1.87	2.27
	Dibutyl Sebacate	1.34	1.44

(ii) Casting of the tapes

The aim was to achieve strong alignment of the templates parallel to the casting direction for highly textured ceramics. The alignment of the templates is controlled by occurring shear forces in the gap between the doctor blade and moving carrier tape. The viscosity η of the slurry, gap height h as well as the casting speed v are parameters which effect the alignment of templates. The parameters that resulted in a texture degree of 85 % were $\eta \approx 300$ Pa·s, $h = 250$ µm and $v = 0.8$ m/min. These suspension and casting conditions were benchmarks for all further castings of different materials.

(iii) Sample preparation

To achieve bulk samples from cast tapes, single layers were cut and stacked, uniaxially and further isostatically pressed. Uniaxial pressing was performed with a warm press set-up in a universal testing machine (Messphysik MIDI 10-5/6x11, Messphysik Materials Testing GmbH, fürstenfeld, Austria). The pressure of ~ 6.5 MPa was applied for 15 minutes at a temperature of ~ 75 °C. For isostatic pressing (ILS-46, Keko Equipment Ltd., Žužemberk, Slovenia) the samples were vacuum sealed. The isostatic pressing was performed at 20 MPa for 30 minutes at 75 °C. In this thesis plates with dimensions in the green state of 55 x 55 x 5 mm were cut, stacked and pressed, which resulted in sintered dimensions of ~ 45 x 45 x 3 mm (see *publication A* for more details).

(iv) Thermal post processing

The thermal post processing of tape cast samples was performed in two steps: (i) debinding and (ii) sintering. The binder removal of the used binder composition was performed in a convection furnace (Thermoconcept, KU15/65, Bremen, Germany) with a heating rate of 0.3 °C/min to a maximum temperature of 600 °C. A cooling rate of 0.8 °C/min was used to 400 °C, followed by a cooling rate of 3 °C/min to room temperature. The sintering of alumina ceramics was performed in a conventional sintering furnace (Thermoconcept, HTL10/17, Bremen, Germany) to a maximum temperature of 1550 °C for 2 hours sintering time, with a heating and cooling rate of 5 °C/min, respectively.

The described processing protocol and preliminary experiments resulted in homogenous equiaxed microstructures of different materials with relative densities ~ 99 % and highly textured microstructures (*Lotgering factor* ~ 0.85). Different monolithic materials (Al_2O_3, ZTA, ZMA, Cr_2AlC, CeTZP) as well as laminate designs were realized with tape casting and investigated according to different research topics in the frame of this thesis (*publication A*) as well as in the works of J. Schlacher and R. Papšík.[106–108] Additional formulations for the

different materials of study are attached in the appendix *'Tape casting: compositions'*.[17,30,31,50,71,109,110]

3.1.2 Stereolithographic 3D-printing procedure

Stereolithographic 3D-printing was used to fabricate samples for several investigations of *publication B, C, D* and *E,* where sintering was performed in conventional as well as non-conventional furnaces.[72,111] For stereolithographic 3D-printing the lithography-based ceramic manufacturing (LCM) technology (CF7500, Lithoz GmbH, Vienna, Austria) was used. Alumina samples with equiaxed as well as textured microstructures were additive manufactured. For equiaxed alumina, a commercially available photosensitive suspension (LithaLox HP500, Lithoz GmbH, Vienna, Austria) was used. Regarding textured alumina this suspension was modified by the addition of sintering additives as well as high aspect ratio templates. The same sintering additives of CaO and SiO_2 as described for tape casting (chapter *3.1.1.*) were used. A content of 0.25 wt% related to the total solid content was added to the suspension. The mixing was performed on a heated magnetic stirrer for approximately 5 hours at a heat of ~ 50 °C. The high aspect ratio alumina templates were added with 6 wt% additional dispersant, related to the amount of added templates. The ratio of alumina templates, related to the content of ceramic powder, was either 2.5°vol% (see details in *Publications C and E*) or 5 vol% (see details in *Publication B*). Templates were distributed for approximately 1 hour at the heated magnetic stirrer.[72]

For equiaxed and templated alumina, the same printing parameters were used. The slurry height was set to 100 µm and a layer thickness of 25 µm was used to build the samples layer by layer applying an exposure energy of 120 mJ/cm^2. The non-polymerized suspension was removed using an airbrush and a solvent (LithaSol20, Lithoz GmbH, Vienna, Austria). The binder-removal was performed in a convection furnace (Thermoconcept, KU15/65, Bremen, Germany) after a protocol recommended by the suspension supplier, which is found in the appendix '*Stereolithographic 3D-printing: Thermal post processing – binder removal*'.

Regarding *publication B*, here a conventional sintering furnace (Thermoconcept, HTL10/17, Bremen, Germany) was used to densify textured and equiaxed alumina microstructures. Heating was performed with a rate of 5 °C/min at a maximum temperature of 1600 °C and different sintering times of 2 or 6 hours.

Non-conventional sintering routes were applied in the investigations of *publication C, D* and *E*. For *publication C* samples were sintered with a standard spark plasma sintering (SPS, HP D

10-SD, FCT Systeme, Germany) set-up with applied pressure. Here, first a rapid heating with a rate of 100 °C/min was used to reach a temperature of 1200 °C for all samples. At this temperature a pressure of 80 MPa was applied onto the sample, followed by varying sintering parameters as maximum temperature (1400 °C to 1800 °C), heating rates from 1200 °C to maximum temperature (25 °C/min vs. 5 °C/min) and sintering times (1 to 5 hours). The detailed sintering protocols are found in *publication C*.

In the case of *publication D* and *E* a pressure-less spark plasma sintering (PL-SPS, FUJI SPS Dr. Sinter Lab 322Lx, Dr. SINTER, SPS Syntex inc., Japan) set-up was used. For PL-SPS sintering rates of ~ 450 °C/min were used for heating to different maximum temperatures between 1300 °C and 1600 °C for different sintering times in the range of 2 to 64 minutes. More details about sintering parameters are found in the particular *publications* of *D* and *E*.

3.2 Microstructural, physical, mechanical and optical characterization

The microstructural properties regarding grain size, shape, orientation, phase distribution and porosity were evaluated in samples fabricated either with tape casting or 3D-printing, sintered by using different protocols. Hardness, mechanical strength and fracture toughness were determined to investigate the effect of both grain size and texture. Furthermore, selected textured samples were also investigated in terms of optical properties, where the transmittance was evaluated.

3.2.1 Microstructural analysis

The microstructural properties were characterized using images taken with two different scanning electron microscopes (SEM, JEOL JCM-6000Plus Neoscope™, JEOL Ltd., Tokyo, Japan and Tescan Clara, Tescan Orsay Holding, Brno, Czech Republic), a transmission electron microscope (TEM, ARM 200 CF, JEOL Ltd., Tokyo, Japan) as well as X-ray diffractometry (XRD, Brucker AXS D8 Advance DaVinci, Bruker, Billerica, USA).

The relative density of solid materials can be measured with various methods, as for example: (i) geometrical measurement, (ii) Archimedes principle, (iii) mercury porosimetry or (iv) image analysis. Depending on the present porosity, if open or closed, certain methods are applicable and/or valid. According to the Archimedes principle after the standards of EN 623-2 different approaches are used to evaluate the relative density (ρ_{rel}) of solid samples with either closed or open porosity:

Closed porosity:

$$\rho_{rel} = \frac{m_{air}}{m_{air} - m_{liquid}} \cdot \rho_{liquid} \quad (22)$$

where m_{air} is the mass of the sample measured in air, m_{liquid} the mass of the sample suspended in liquid and ρ_{liquid} the theoretical density of the used liquid, adapted to the temperature. This method was applied for samples having a relative density of ≥ 96 %.

Open porosity:

Regarding solids with open porosity, the samples are penetrated with liquid after the measurement in air and are weighted first in liquid and following in air in the saturated state. For the measurements of open porosity in this study, samples were soaked in distilled water for 24 hours prior measuring the mass in liquid and in air after saturation:

$$\rho_{rel} = \frac{m_{air}}{m_{air,saturated} - m_{liquid,saturated}} \cdot \rho_{liquid} \quad (23)$$

where $m_{liquid,saturated}$ is the mass of the sample penetrated measured in liquid and $m_{air,saturated}$ measured in air. In both cases, distilled water was used as liquid medium.[112]

For samples with relative densities ≤ 90 %, mercury porosity was used due to better penetration of mercury compared to water (Pascal 140 & 440, Thermo Fischer Scientific, USA). Infill pressures of 10 kPa to 400 MPa were applied with standard values for surface tension and contact angle for mercury of 0.485 mN/m and 130 °, respectively.

Grain size was measured using the linear intercept method, determining the size in vertical and horizontal direction. In the case of textured microstructures, where the grains show a tabular shape, it was distinguished between diameter (horizontal measurements) and thickness (vertical measurements).

The phase compositions and texture were evaluated through X-ray diffractometry (XRD). XRD uses the diffraction of X-rays in a crystalline material, giving characteristic peaks for certain crystal planes. It is based on the Bragg's law [113]:

$$2 \cdot d \cdot \sin(\theta_B) = n \cdot \lambda \quad (19)$$

where *d* is the lattice constant, θ_B the Bragg angle, *n* the diffraction order and λ the wavelength of the X-rays.

In this thesis XRD was used to evaluate the texture degree in textured alumina samples (*publication A*, *B*, *C* and *E*) and to determine the phase transformation in zirconia phases (*publication A*).[72,106] An estimation of the quality of texture can be given with the Lotgering

factor (*LF*), where the characteristic peaks in the XRD pattern of equiaxed and textured microstructures are compared and rationalized[9,114]:

$$LF = \frac{P_{(00l)} - P_0}{1 - P_0} \tag{20}$$

$$\text{where } P_{(00l)} = \frac{\sum I_{(00l)}}{\sum I_{(hkl)}} \text{ for textured} \tag{21}$$

$$\text{and } P_0 = \frac{\sum I_{0(00l)}}{\sum I_{0(hkl)}} \text{ for equiaxed} \tag{22}$$

microstructures, determining the ratio of intensities of peaks describing the characteristic peaks in [0001] direction ($I_{(00l)}$ and $I_{0(00l)}$), and in all directions ($I_{(hkl)}$ and $I_{0(hkl)}$), respectively. A $LF = 1$ describes a fully textured microstructure. In the case of α-alumina the peaks indicating textured and oriented grains in [0001] direction represent the (0006) and (000 12) planes at a 2θ angle of 41.7 ° and 90.7 °, respectively.

For a more quantitative evaluation of the texture degree, a rocking curve was detected at the 2θ angle of the (000 12) peak at 90.7 °. The rocking curve was fit with the March-Dollase equation. The fitting parameters *f* and *r* give a more detailed information about the quality of texture [115–117].

$$F(f, r, \theta) = f \cdot \left(r^2 \cdot \cos^2\theta + \frac{\sin^2\theta}{r}\right)^{-\frac{3}{2}} + (1 - f) \tag{23}$$

where f ($0 \leq f \leq 1$) describes the volume fraction of oriented material, r ($0 \leq r \leq 1$) the parameter of grain orientation and θ is the tilt angle of the sample, being the angle between the texture axis and the scattering vector. High *f*-values and low *r*-values, as well as a narrow Full-Width-of-Half-Maximum (*FWHM*) of the fitted rocking curve, describe highly textured and strongly oriented grain structures.

Phase analysis of transformable zirconia phases was evaluated on XRD patterns through Rietveld refinement using the software TOPAS (Bruker AXS, Version 6, Bruker, Billerica, USA), which uses position and shape of the characteristic peaks for phase identification and quantification.

3.2.2 Evaluation of mechanical properties

The hardness of the investigated ceramic samples was evaluated using a Vickers indenter after the standards of EN 843-4. Loads of 1 / 5 kg were applied with a Zwick Indenter machine (Zwick 3212B GmbH&Co, 7900 Ulm, Germany) on a polished surface with 1 µm mirror finish (see *publication A and C*). The diagonals of the Vickers were measured using a light microscope and the Vickers hardness evaluated using following equation:

$$HV = \frac{1}{g} \cdot \frac{F \cdot \sin\left(\frac{136°}{2}\right)}{d^2} \approx 0.1891 \cdot \frac{F}{d^2} \quad (24)$$

where g is the gravity wit 9.81 m/s^2, F is the applied load, $\sin\left(\frac{136°}{2}\right)$ is the pyramidal angle of the Vickers indenter and d is the arithmetic average of the two diagonal distances.[118]

The evaluation of the toughness, K_{Ic}, in brittle materials requires the introduction of a crack or cack-like defect. Among the different techniques to evaluate the fracture resistance, the Single-Edge V-notch beam (SEVNB) method was selected for this thesis. A V-shaped notch is induced as an artificial crack by using a shifting razor blade with diamond paste (see figure 8).[119,120] Notched samples are tested under four point bending.

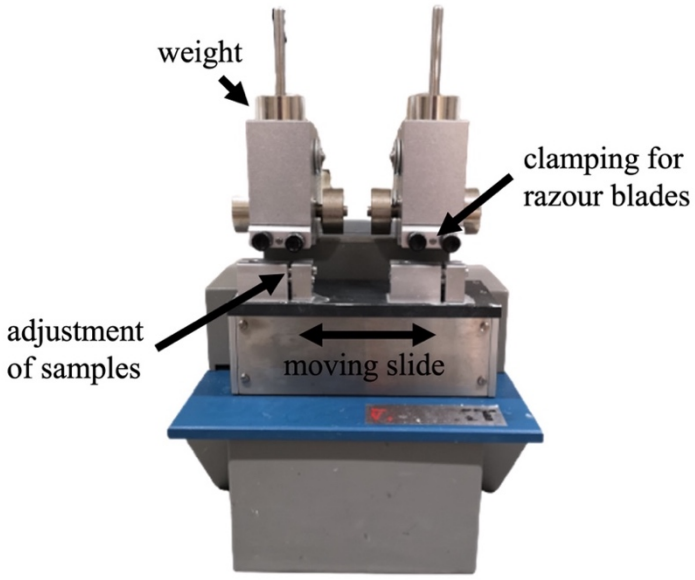

Figure 8: Assembly used for notching samples for SEVNB testing.

According to the standards of ISO 23146 the depth of the notch should be in the range of 20 - 30 % of the height of the sample and the radius should be smaller or similar to the grain size of the material. Following equations are used to determine the fracture toughness (K_{Ic}) along the I-mode of prismatic bars:

$$K_{Ic} = \frac{F}{b \cdot \sqrt{h}} \cdot \frac{L-l}{h} \cdot \frac{3 \cdot \sqrt{\frac{a}{h}}}{2 \cdot \left(1-\frac{a}{h}\right)^{1.5}} \cdot Y \tag{25}$$

where F is the maximum applied load, b and h the thickness and height of the sample respectively, L and l the bottom and top span of the testing assembly, a the notch length and Y the non-dimensional geometrical factor, which is calculated for bar-shaped samples as follows:

$$Y = 1.9887 - 1.326 \cdot \frac{a}{h} - \frac{\left(3.49-0.68 \cdot \frac{a}{h}+1.35 \cdot \left(\frac{a}{h}\right)^2\right) \cdot \frac{a}{h} \cdot \left(1-\frac{a}{h}\right)}{\left(1+\frac{a}{h}\right)^2} \tag{26}$$

The mechanical strength was evaluated under biaxial bending, in order to avoid possible edge defects related to sample preparation. Biaxial strength measurements use a centred biaxial stress field applied on disc-shaped or rectangular samples, avoiding the loading of free edges. Standardized methods to apply a biaxial stress field and evaluate the biaxial strength are Ring-On-Ring (ROR) or Punch-On-Three-Balls (PO3B).[121,122] Besides them, the Ball-on-Three-Ball (B3B) method has shown to result in high accurate measurements.[123,124] The arrangement of the balls is shown in figure 9, where 3 balls are at the tensile surface and one at the compression. The stress of failure (σ) can be calculated using following equation:

$$\sigma = \frac{F}{h^2} \cdot f \tag{27}$$

where F is the maximum applied load, h the height of the tested sample and f is a non-dimensional factor considering the dimensions of the set-up (e.g. ball diameter) and the sample geometry as well as the Poisson's ratio of the tested material. The factor f cannot be calculated analytically and has to be determined through finite element calculations.[123,125,126]

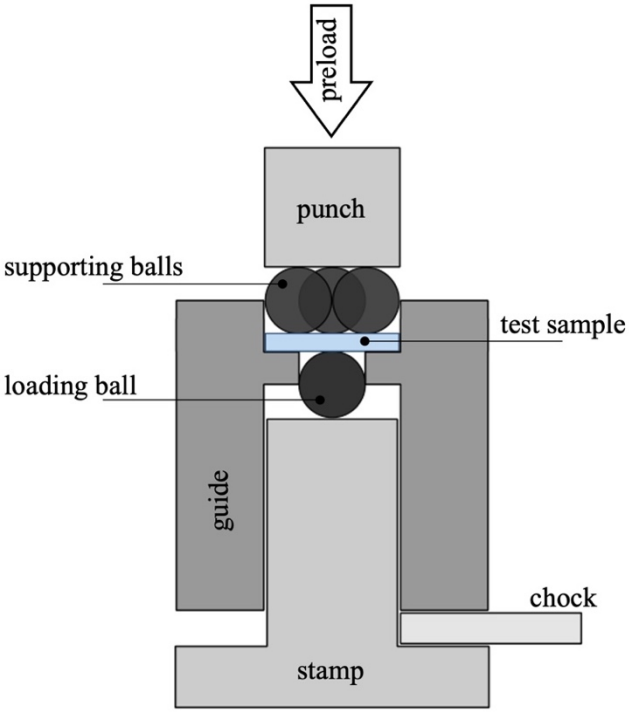

Figure 9: Ball-on-three-ball testing assembly.

The statistical evaluation of investigated brittle materials was done after the statistics of Weibull.[127–130] The probability of failure *P*, the Weibull modulus *m* as well as the characteristic strength σ_0 (σ at 63 % failure rate) were determined with following equations:

$$P(\sigma, V) = 1 - e^{-\left(\frac{V_{eff}}{V_0}\cdot\frac{\sigma}{\sigma_0}\right)^m} \tag{28}$$

where $P(\sigma, V)$ is the probability of failure as a function of the stress of failure σ and the effective volume V_{eff} of the specimen. The characteristic strength σ_0 is reached when $V_{eff} = V_0$, where V_0 describes the reference volume. The Weibull modulus *m* determines the scattering of measured stress values and can be evaluated using the Maximum-Likelihood method:

$$\frac{\sum_{i=}^{N}[\ln(\sigma_{B,i})\cdot\sigma_{B,i}^m]}{\sum_{i=}^{N}\sigma_{B,i}^m} - \frac{1}{N}\sum_{i=}^{N}\ln(\sigma_{B,i}) - \frac{1}{m} = 0 \tag{29}$$

where *N* is the number of tested samples, $\sigma_{B,i}$ is the bending strength of a particular sample with the running index *i*. The characteristic strength σ_0 can be evaluated with following equation:

$$\sigma_0 = \left[\frac{1}{N}\left(\sum_{i=1}^{N}\sigma_{B,i}^m\right)\right]^{\frac{1}{m}} \tag{30}$$

3.2.3 Optical properties

Microstructural features may have an important effect onto the optical properties of a material, whether it is transparent, translucent or opaque. In this thesis textured alumina samples were sintered using SPS to reduce the porosity and achieve a translucent ceramic (see more details in *Publication C*). The absolute translucency was determined by measuring the in-line transmittance of 0.8 mm thick samples, with a spectrophotometer (UV-2450, Shimadzu, Japan) and a mask with a hole of 5 mm with wavelengths from 200 to 800 nm.

4 Extended summary of publications

In the following chapter, an extended summary of the key investigations published during this thesis is given. A short motivation of the particular investigation is followed by a description of the methods employed as well as the main results and conclusion. In some cases, several publications are combined in order to draw more general conclusions. Details on the procedures can be found in the corresponding publications as well as in the appendix section.

4.1 Texturing through tape casting and the effect of a second phase in textured alumina

Graphical abstract

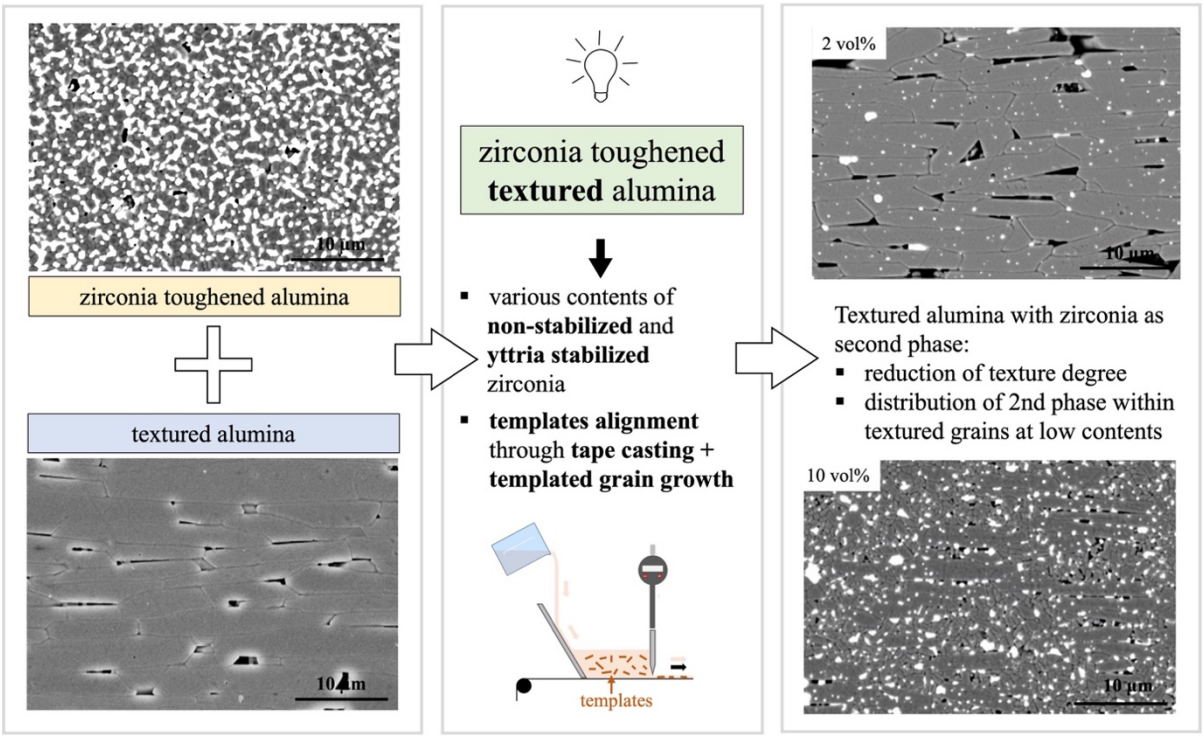

 [106]

Equiaxed composites of zirconia toughened alumina (ZTA) combine the phase transformation toughening from zirconia and high hardness values of alumina to obtain a tough and wear resistant material.[21,25,34,37,38] The morphological arrangement of tabular grains in textured monolithic microstructures may lead to phenomena as crack deflection, bifurcation or arrest, enhancing the fracture behaviour and damage tolerance of ceramics.[9,17,18,27,29,31,69,70] In this work, it was hypothesized that texturing the microstructure of alumina in a composite material, such as ZTA, may lead to an increase in fracture resistance. The effect of zirconia as second phase in tape cast textured alumina on the development of texture, hardness as well as the fracture behaviour was investigated.

Composites of textured alumina with different contents (0, 1, 2, 5 and 10 vol%) of non-stabilized (ZrO_2) and 3 mol% yttria stabilized zirconia (3YSZ) were fabricated via the tape casting process. To enhance templated grain growth a content of 0.10 wt% sintering additives of CaO and SiO_2 were added to form a liquid phase during sintering. For comparison, equiaxed alumina samples were fabricated without and with the addition of the same content of sintering additives as for the TA samples (EA and EA_{SA}). Microstructures were analysed according to their relative densities, grain aspect ratio and the degree of texture by determining the Lotgering factor (LF) and the rocking curve for all materials. The Vickers hardness was evaluated with a load of 5 kg on the polished side surface, corresponding to the prismatic planes of the alumina lattice. The fracture toughness was measured according to the Single-Edge V-notch beam method on prismatic bars and a crosshead displacement speed of 0.5 mm/min. The effect of phase transformation toughening through zirconia was investigated by detecting XRD patterns prior fracture and on the fracture surface. Through Rietveld refinement it was possible to calculate the transformed content of zirconia from the tetragonal to the monoclinic phase and its contribution to toughening.

Figure 10a displays representative microstructures for the composite materials of textured alumina with ZrO_2 (TA+ZrO_2) of contents 0, 2 and 10 vol%. Microstructures of TA with 3YSZ show a similar appearance. It was noticed that for contents $<$ 10 vol%, the zirconia phase is located rather intragranular. In correlation with the microstructural images, the degree of texture, described by the LF, is reduced with increasing zirconia content, see figure 10b. The highest LF-value was determined for monolithic TA with $\sim$ 0.8. For a content of 10 vol% a rather equiaxed composite microstructure was observed in both TA+ZrO_2 and TA+3YSZ compositions.

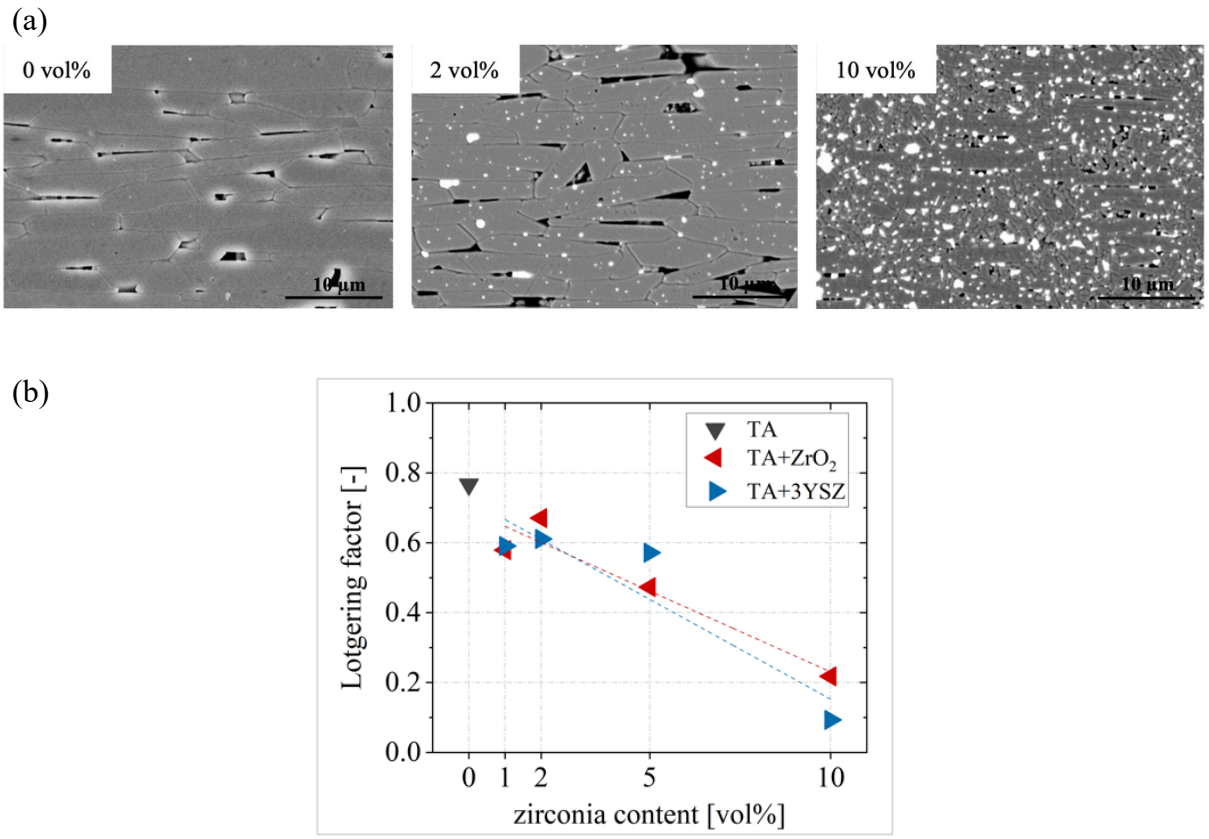

Figure 10: (a) SEM images of representative samples of TA + 0, 2 and 10 vol% ZrO_2. **(b)** Diagram showing the Lotgering factor for monolithic TA and TA+ZrO_2 and TA+3YSZ of different contents. Reused under the terms of license CC-BY 4.0 [106]

Considering the fracture behaviour of monolithic materials, highly textured alumina showed the highest toughness value of $K_{Ic} > 5$ MPa $m^{1/2}$ in comparison to both equiaxed alumina samples of EA and EA_{SA} ($K_{Ic} \sim 3.5$ MPa $m^{1/2}$). Figure 11a shows the measured fracture toughness for monolithic equiaxed and textured alumina as well as for the various compositions of TA+ZrO_2 and TA+3YSZ. The fracture toughness values measured for TA+ZrO_2 and TA+3YSZ revealed a different behaviour with increasing zirconia content. In TA+ZrO_2, K_{Ic} decreased until 5 vol% followed by an increase for 10 vol%. The values for TA+3YSZ are comparable to EA and EA_{SA} samples for all contents. In both cases the decrease of texture degree with increasing content as well as the intragranular distribution of the zirconia phase, for contents ≤ 5 vol%, may have led to the weakening of the textured alumina grains. For TA+ZrO_2 the content of phase transforming zirconia increases with increasing content as seen in figure 11b, explaining the increase at 10 vol% ZrO_2.[131–134] The overstabilization of the tetragonal phase by 3 mol% yttria in 3YSZ has hindered transformation and consequently favoured fracture of the alumina matrix, resulting in K_{Ic} – values comparable to EA.[135]

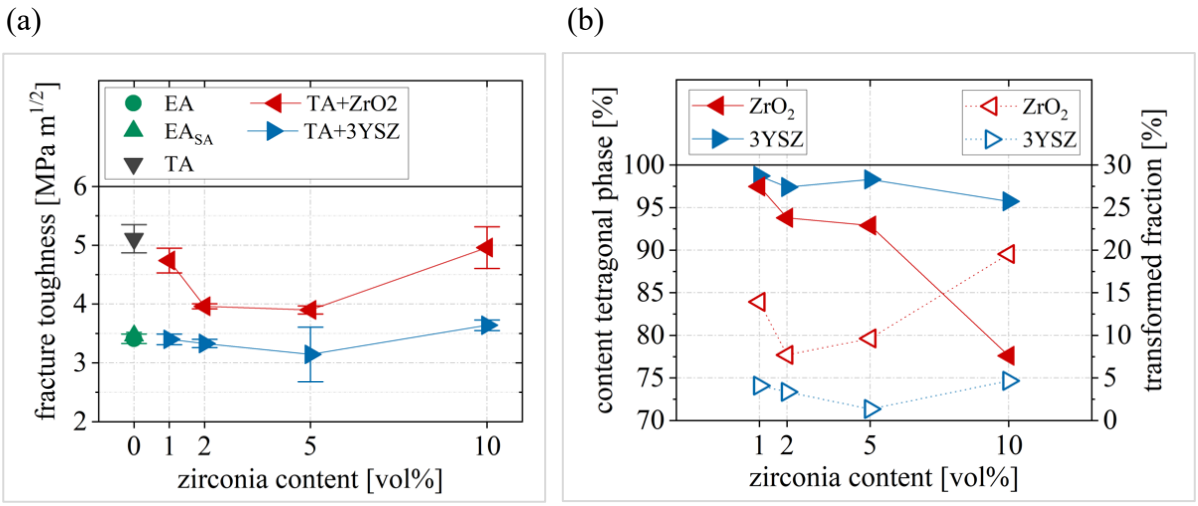

Figure 11: (a) Diagram showing the fracture toughness for monolithic equiaxed and textured alumina samples as well as for TA+ZrO_2 and TA+3YSZ samples of different contents. **(b)** Diagram displaying the content of tetragonal phase in TA+ZrO_2 and TA+3YSZ prior fracture (left axis) and the transformed fraction to the monoclinic phase after fracture (right axis). Reused under the terms of license CC-BY 4.0 [106]

In conclusion, the combined approach of texturing the microstructure in a composite material was explored by fabricating textured alumina microstructures with different contents of non-stabilized (ZrO_2) and 3 mol% yttria-stabilized zirconia (3YSZ) using the tape casting process. It was shown that with increasing zirconia content the texture degree is reduced and that samples with ZrO_2 and 3YSZ develop strongly different fracture behaviour. A counterbalance effect of hardness, texture degree and zirconia content was also found.

4.2 Effect of texturing on mechanical and optical properties in 3D-printed alumina-based ceramics

Graphical abstract

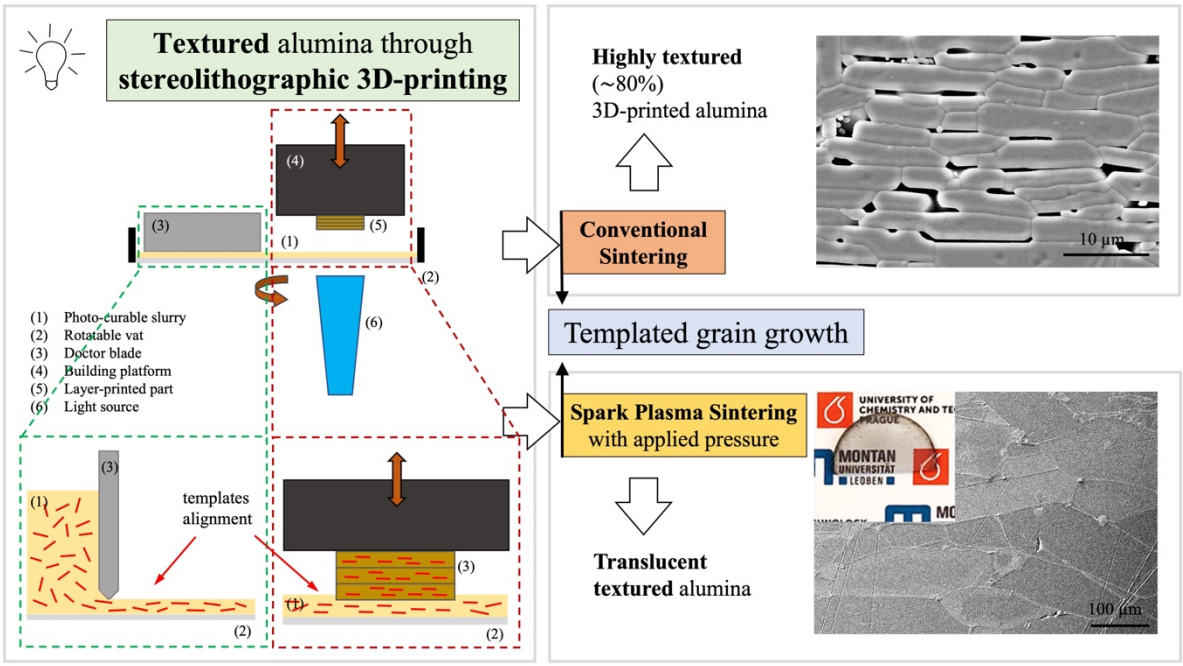

Adapted under the terms of license CC-BY 4.0 [72]

Textured microstructures in ceramics have shown to improve their mechanical response.[27,31] Due to the morphology and the crystallographic orientation of the grains, crack propagation can be affected by deflection, bifurcation or even arrest when load is applied, leading to enhanced damage tolerance. The method of templated grain growth (TGG) has been established to induce texture in different ceramic systems. During sintering, high aspect ratio templates grow at the expense of surrounding comparably small powder particles. For a high degree of orientation after sintering, templates have to be aligned in the green state. The methods for templates alignment are rather limited to simple geometries with low complexity.[17,18,29,71] Little work has been reported on achieving textured microstructures in additive manufactured ceramics.[136] Le Ferrand et al. has given the idea of combining textured microstructures of high toughness with fully dense equiaxed microstructures of high strength for e.g., dental applications.[29] Here, for texturing complex 3D-parts, different processing technologies, as those used so far for templates alignment, would be required.

In this work the additive manufacturing technology of lithography-based ceramic manufacturing (LCM) was used to align templates in the green state.[59] 5 vol% high aspect ratio templates as well as 0.25 wt% of sintering additives (CaO and SiO_2) on the content of solids loading, were added to a commercially available high purity photosensitive alumina

suspension. For comparison, equiaxed alumina samples were fabricated. Disc-shaped samples were 3D-printed and debinded to a maximum temperature of 430 °C. During sintering, templated grain growth (TGG) was achieved, where the effect of different sintering times (2 and 6 hours) at a maximum sintering temperature (1600 °C) was investigated. The degree of texture was evaluated determining the Lotgering factor (*LF*) and the fitting parameters after the March-Dollase equation (*r*, *f*, *FWHM*) of a measured rocking curve at $2\theta = 90.7\,°$ for the (000 12) plane.

Figure 12a shows the microstructural images of the textured microstructures for sintering times of a) 2 h and b) 6 h, where for both the relative densities were ~ 93 %, respectively. The high porosity in textured samples can be attributed to the anisotropic grain growth. The preferential growth of the templates in x- and y- direction leads to mutual impingement and the lack of the ability to close pores.[31] For comparison, equiaxed alumina samples had relative densities above 99 %. Table 2 lists the determined *LF*-, *r*- and *f*-values as well as the *FWHM* of the measured rocking curve for both sintering times.

Table 2: Data describing the degree and quality of texture for 3D-printed textured alumina samples sintered at different sintering times of 2 and 6 hours.

	LF [-]	*r* [-]	*f* [-]	*FWHM* [°]
TA_2h	0.79	0.17	0.64	6.5
TA_6h	0.83	0.17	0.64	6.3

For comparison, the lowest *r*-value and *FWHM* reported in literature were 0.13 and 4.6 °, respectively. Due to the microstructural properties, the sintering parameters with a sintering time of 6 hours were selected for further mechanical testing. The biaxial strength was evaluated using the Ball-on-Three-Ball (B3B) strength test. Strength was measured on 30 samples with textured and equiaxed microstructures, which were sintered at the same conditions. Figure 12b shows the failure stress distribution of the tested textured (TA_6h, blue circular symbols) and equiaxed alumina samples (EA_6h, red squared symbols). Weibull statistics were used to determine the characteristic strength (σ_0) at a probability of failure of 63.21 % and the Weibull modulus (*m*). For textured alumina, sintered for 6 hours $\sigma_0 = 640$ [620-661] MPa and $m = 11$ [8-13], and for equiaxed alumina $\sigma_0 = 570$ [549-592] MPa and $m = 9$ [7-11], respectively; where the values in brackets are the 90 % confidence intervals.

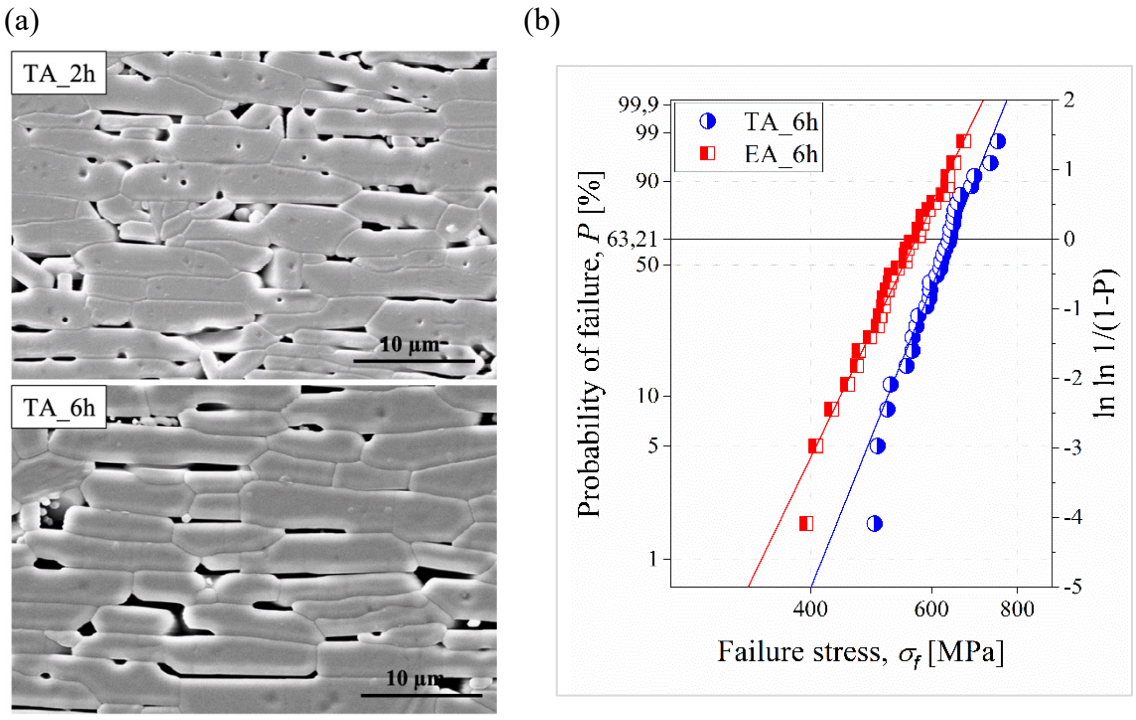

Figure 12: (a) SEM images of 3D-printed textured alumina samples sintered at 2 h and 6 h. **(b)** Weibull statistics for tested textured and reference equiaxed alumina samples sintered with the same conditions for 6 h. Reuse under the terms of license CC-BY 4.0 [72]

The slightly higher strength measured for textured alumina may be a result of the morphology and crystallographic properties of the oriented grains. Further the homogeneity of the microstructure, where pores (porosity of ~ 7 %) are homogeneously distributed in-between the large tabular grains, may have a beneficial effect on the mechanical response. Fractography has shown that in the case of textured alumina, defects induced through the printing process, as entrapped bubbles, have caused failure. In comparison for equiaxed alumina, clusters of abnormally grown grains have been indicated to be the main origins of failure.[72]

Besides the achieved mechanical properties, the ability of using templated grain growth to further tailor functional properties of alumina regarding transparency, was investigated. To obtain high transparency in ceramic materials nearly 100 % relative density has to be achieved. There are two approaches which may be followed to enhance transparency: (i) reducing the grain size below the wavelength of light or (ii) reducing sources of scattering and birefringence by decreasing the number of grain boundaries and by crystallographic orientation of grains. [15,20,44–48]

In this work the idea was to use TGG to achieve translucent alumina ceramics following the second approach. Textured microstructures with tabular shaped and crystallographically oriented grains were fabricated by using LCM 3D-printing for templates alignment and achieving exact disc dimensions for sintering in a spark plasma sintering (SPS) furnace. SPS

with high applied pressures was used to reduce porosity and consequently scattering sources, to obtain translucent alumina ceramics.

According to preliminary studies and the work of Seabaugh et al. the reduction of templates content has shown that the aspect ratio of textured grains can be improved and the porosity reduced.[17] On this regard the used content of templates was 2.5 vol% compared to 5 vol% in the previous study.

Templates and sintering additives (0.25 wt% related to the solids content) were dispersed in the commercially available photosensitive alumina suspension on a magnetic stirrer. Disc shaped samples with a diameter of 20 mm and a thickness of 4 mm were 3D-printed with the LCM technology, debinded to 430 °C and pre-sintered to 1100 °C for 1 h for better handling and stiffness for following spark plasma sintering with applied pressure. SPS was performed by applying a pressure of 80 MPa, comparing the effect of different sintering temperatures (1400 – 1800 °C), sintering times (1 – 5 hours) and heating rates (5 / 25 °C/min). The sintered samples were characterized according to their degree of texture (Lotgering factor), relative density, hardness and transmittance.

Figure 13 shows the microstructure of a translucent sample, which had the best results regarding transmittance (54.6 %). Here the sintering conditions of 1700 °C maximum sintering temperature, 5 °C/min heating rate and 3 hours of sintering time were used. This sample also showed the highest degree of texture (Lotgering factor of 0.67) and the lowest hardness value of 18 GPa, compared to other samples, sintered with different conditions.

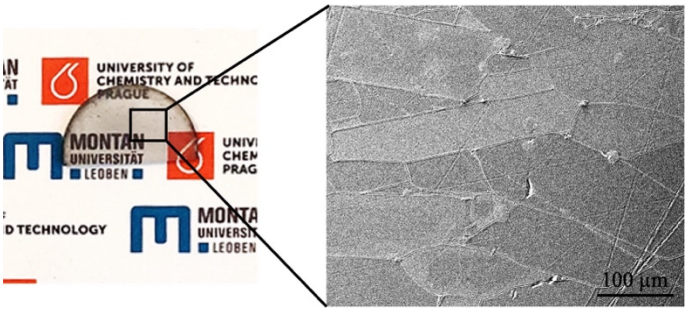

Figure 13: Selected textured alumina sample and its microstructure with high translucency.

In conclusion, the additive manufacturing technology of lithography-based ceramic manufacturing could be used to align high aspect ratio templates throughout the printing process. Applying conventional sintering TGG has led to highly textured alumina microstructures which exhibited higher strength values as for equiaxed alumina (*publication B*). Using a non-conventional sintering technology of spark plasma sintering and applying

additional pressure, has led to a reduction of porosity in textured microstructures and the ability to use TGG to achieve highly translucent alumina ceramics (*publication C*).

4.3 Tailoring of microstructures of additive manufactured samples through rapid sintering

Graphical abstract

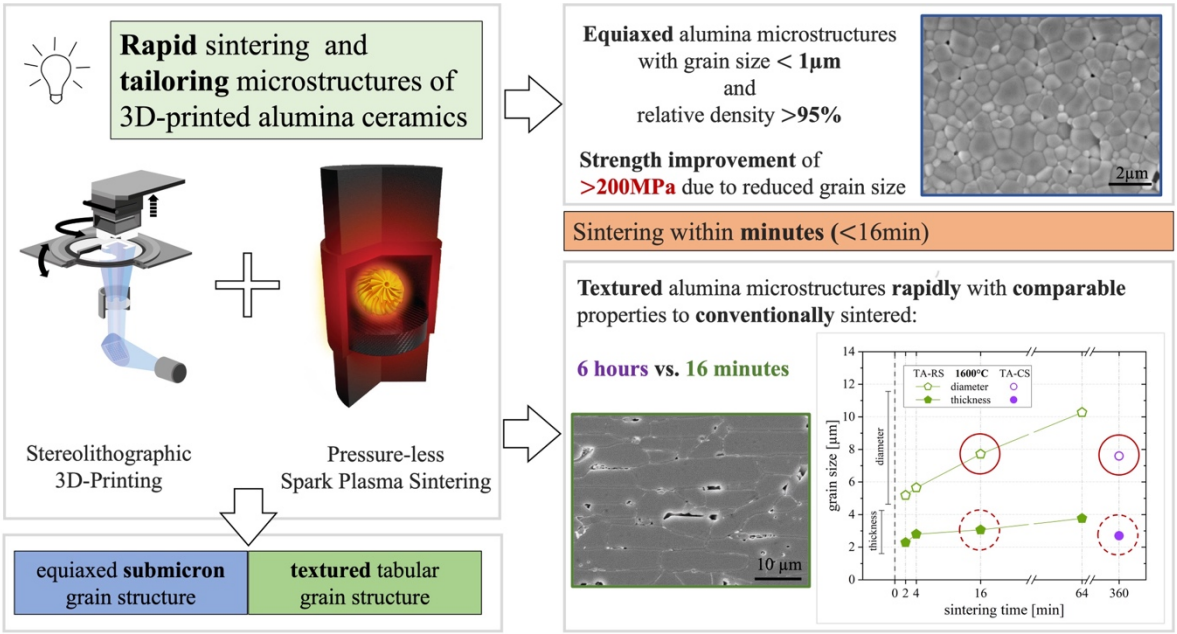

Adapted under the terms of license CC-BY-NC [111]

Nowadays, additive manufacturing attracts attention in various fields of applications for different material classes due to fast prototyping and the ability of fabricating highly complex shaped components without the need of post-machining. In the field of ceramics, also multiple additive manufacturing technologies are developed, most of them adapted from existing polymer and metal 3D-printing technologies.[55] Multiple technologies for additive manufacturing ceramics use polymers filled with ceramic powder particles to shape a green sample. For pure ceramic components these polymers are removed, and the remaining open porous structure is further sintered to a densified body. So far, sintering has been performed following mainly standard sintering protocols in conventional sintering furnaces. Limited research has been done on applying a non-conventional sintering process onto complex shaped 3D-printed ceramics.

In this work, the aim was to apply a rapid sintering technology (pressure-less spark plasma sintering, PL-SPS) to tailor the microstructures of additive manufactured alumina ceramics and consequently the mechanical properties.[85,101,102,104] Typical grain sizes in equiaxed

microstructures of alumina are ~ 3-5 µm using conventional sintering. In this work, we hypothesized that rapid sintering protocols may impede grain growth during sintering and lead to alumina microstructures with an average grain size below 1 µm, and consequently increase the strength. Furthermore, the possibility of texturing alumina using PL-SPS was also explored. In the latter study, templated samples with (0.25wt%, TA-LP) sintering additives for liquid phase sintering and without (TA-SS, solid state sintering) were compared. Prior sintering equiaxed and templated samples with 2.5 vol% high aspect ratio templates (see 3.1.2. and 4.2.) were printed with the LCM technology and debinded to 430 °C, following a recommended thermal post-processing protocol. Samples of both materials were sintered in the set-up of pressure-less spark plasma sintering, as described in 2.2.3 and 3.1.2. Regarding equiaxed alumina, different sintering temperatures, ranging from 1300 °C to 1600 °C, as well as sintering times from 2 – 8 minutes at a constant heating rate of ~ 450 °C/min, were investigated. With regard to textured alumina, the effect of different sintering temperatures (1300 – 1600 °C) and sintering times (2 – 64 minutes) at a heating rate of ~ 450 °C/min, was investigated. Both materials were characterized according to their microstructural properties as grain size and porosity and fracture toughness using SEVNB. In the case of equiaxed alumina additionally biaxial strength, using the B3B method, was determined.

Figure 14a shows an exemplary additive manufactured complex shaped alumina sample along the different processing steps of after (i) printing, (ii) debinding and (iii) rapid sintering. It was observed that for lower sintering temperatures of 1300 °C and 1400 °C independent of dwell time no satisfying densification occurred. Two parameter conditions, RS1: 1600 °C and 2 minutes, as well as RS2: 1500 °C and 8 minutes, fulfilled the desired properties of submicron grain size $< 1\mu m$ and a relative density > 95 %. Figure 14b displays the microstructure, obtained with the sintering conditions of a sintering temperature of 1600 °C and a sintering time of 2 minutes. The measurements for biaxial strength of the sintering conditions RS1 and RS2 showed that the characteristic strength could be significantly improved by more than 200 MPa, in comparison to conventionally sintered alumina samples (CS, sintering temperature = 1600 °C and sintering time 360 minutes). The characteristic strength (σ_0) and the Weibull modulus (m) for RS1 were σ_0 = 808 [743 – 881] MPa and m = 6 [4 – 8], for RS2 σ_0 = 867 [808 – 932] MPa and m = 7 [5 – 9] and for CS σ_0 = 570 [549 – 592] MPa and m = 9 [7 – 11], respectively, where the numbers in brackets indicate the confidence interval of 90 %. Figure 14c shows the distribution of stress to failure values for the rapid sintering conditions of RS1: 1600 °C and 2 minutes as well as for conventional sintering conditions of CS: 1600 °C and 360 minutes.[111]

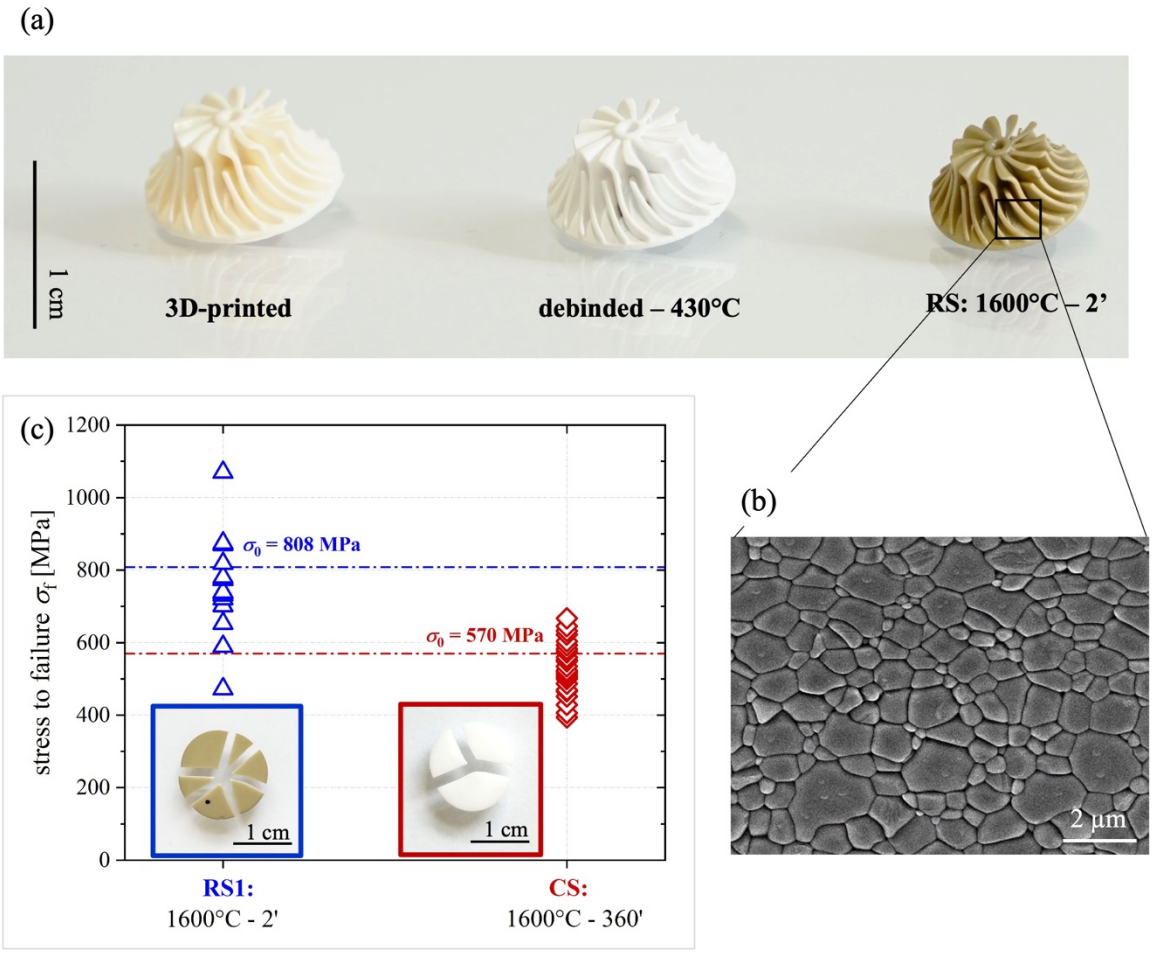

Figure 14: (a) Exemplary 3D-printed sample along the different processing steps. **(b)** SEM image of microstructure rapidly sintered at a sintering temperature of 1600 °C and a sintering time of 2 minutes. **(c)** Stress to failure distributions for the RS1 and CS sintering conditions. Adapted under the terms of license CC-BY-NC [111]

Whereas for equiaxed alumina high heating rates were aimed to impede grain growth, resulting in submicron grain sizes, enhanced grain growth was desired to generate textured microstructures. Typically abnormal grain growth is described as a function of annealing time.[4] In this study it was observed that especially for elevated temperatures (1600 °C) only 2 minutes were sufficient to promote TGG resulting in textured microstructures for samples with and without additional sintering additives. In literature it is reported that a relative density of ≥ 90 % is needed to get TGG, which is reached more rapid using the high heating rates of ~ 450 °C/min during pressure-less spark plasma sintering than in the case of conventional sintering.[73] Figure 15 shows the development of texture with prolonging dwell times at a sintering temperature of 1600 °C for liquid phase and solid state sintered samples (TA-LP and TA-SS). Comparing the microstructural properties as grain diameter and thickness to results

found in literature, where conventional sintering was used, similar results could be obtained with the PL-SPS set-up, although with sintering times of only few minutes.[70,72,76,107,137]

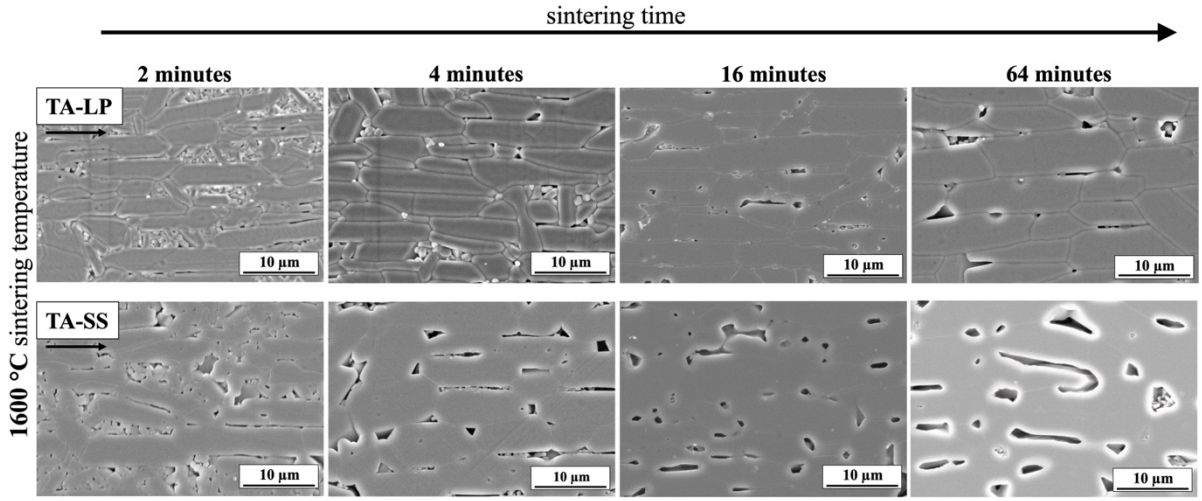

Figure 15: Development of textured alumina microstructures at 1600 °C with prolonging dwell times for samples with liquid phase sintering (TA-LP) and solid state sintering (TA-SS)

In the work of *publication D* and *E* it could be shown that the pressure-less spark plasma sintering set-up could be used to rapidly sinter complex shaped ceramics and tailor their microstructural properties. Equiaxed alumina microstructures were densified within minutes resulting in submicron grain sizes, which caused a significant strength improvement for 3D-printed alumina ceramics. Furthermore, templated grain growth, which is typically addressed as a time dependent process, could be obtained rapidly, leading to textured microstructures with comparable microstructural properties as for conventionally sintered samples, but within a few minutes instead of hours.

5 Conclusion

During this thesis it was possible to explore the capabilities of processing routes such as tape casting and stereolithographic 3D-printing to fabricate homogeneous, fully densified equiaxed and highly textured ceramic microstructures. The combination of different processing routes and sintering protocols enabled tailoring the microstructure and consequently the mechanical and optical properties of alumina-based ceramics. The main conclusions of this thesis may be summarized as follows.

Combining the approaches of texturing and ceramic composites, such as zirconia toughened alumina (ZTA), textured alumina samples containing different contents of (i) non-stabilized (ZrO_2) and (ii) 3 mol% yttria stabilized zirconia (3YSZ) were fabricated using the tape casting process. It could be shown that the degree of texture strongly decreases with increasing second phase content. Further, with increasing ZrO_2 and 3YSZ contents a rather equiaxed composite microstructure was developed, causing higher relative densities and hardness values. In textured alumina samples containing non-stabilized zirconia, phase transformation occurred, resulting in higher fracture toughness values compared to samples containing 3 mol% yttria stabilized zirconia.

The fundamentals learned from tape casting to texture alumina microstructures were aimed to be applied onto the stereolithographic 3D-printing process of lithography-based ceramic manufacturing (LCM). Similarities could be drawn between the two processing routes according to shear forces occurring during suspension distribution causing templates alignment. High aspect ratio templates were aligned using LCM. Longer sintering times improved the degree of texture. The biaxial strength measured for textured alumina was even higher than for equiaxed alumina microstructures sintered with the same sintering conditions, opening the path to improve the mechanical response of 3D-printed alumina ceramics. In addition, non-conventional sintering routes, such as spark plasma sintering (SPS) with applied pressure were used onto 3D-printed templated alumina samples with the aim to achieve textured translucent alumina ceramics. Templated grain growth at elevated temperatures (1700 °C) and applied pressures (80 MPa) during SPS resulted in translucent alumina ceramics with a transmittance of ~ 55 %.

In a further investigation, the use of an adapted pressure-less spark plasma sintering set-up showed great potential in tailoring the microstructure of alumina ceramics through rapid sintering of 3D-printed parts. Additive manufactured equiaxed alumina with reduced grain sizes below 1 µm could be fabricated with a sintering time of 2 minutes at 1600 °C, which resulted

in a strength improvement of > 200 MPa compared to conventionally sintered alumina ceramics. Furthermore, templated grain growth could also be achieved during rapid sintering (i.e. 16 min), leading to comparable microstructural properties as those of alumina ceramics textured through conventional sintering protocols (6 h). The potential of this technique applied to 3D-printed ceramics is yet to be explored.

Overall, textured microstructures could be successfully fabricated deploying different processing routes (tape casting and stereolithographic 3D-printing) supported by non-conventional (rapid) sintering technologies, resulting in highly textured, tough or translucent alumina ceramics. The use of a pressure-less spark plasma sintering set-up on alumina ceramics resulted in impressive microstructural properties and may open the path for the ability to reduce sintering time and energy for complex shaped ceramics fabricated with stereolithographic 3D-printing techniques.

6 Outlook and future work

First investigations have mainly been performed on bulk alumina. Future work will focus on applying these technologies on other ceramic materials and designs. The fabrication of thin layers (< 20 µm) through tape casting opens the possibility to fabricate laminate structures. The combination of multiple materials with mismatching thermo-physical properties have shown to induce residual tensile or compressive stresses in the layers. Investigations of R. Bermejo, R. Papšik and J. Schlacher on materials based on alumina, demonstrated how laminated designs and consequently residual stresses can be used to enhance the mechanical behaviour of ceramics.[107–110,138–143] Key factors which determine the residual stresses may be (a) the magnitude of mismatching thermo-physical properties of the two or more combined materials, (b) the volume ratio and (c) the layer thickness. Further there are two approaches of the order of stacking the layers of different materials (A and B): (i) A-B-A or (ii) B-A-B, in the simplest form. Considering material A having a lower coefficient of thermal expansion (CTE) compared to material B. In the former A-B-A order the lower CTE of A would cause compressive residual stresses in the A layer and tensile in the B layer. Compressive stresses can result in a strength improvement. On the other hand, in the B-A-B design tensile residual stresses are induced in the outer B layer and compressive in the inner A layer. The tensile stresses in the outer B layer favour the formation and propagation of cracks but the second A layer under compression enables the arrest or deflection of a crack. Thus, this B-A-B approach can be used to enhance the damage tolerance in ceramic materials.

This B-A-B laminate structure is currently being used to investigate the fracture behaviour of designs combining (I) a CeTZP-Al_2O_3(8%)-$SrAl_2O_3$(8%) composite (Longlife) with zirconia (50 vol%) toughened alumina (ZTA50) and (II) a MAX phase (Cr_2AlC) with alumina (Al_2O_3). CeTZP-Al_2O_3(8%)-$SrAl_2O_3$(8%), so-called ‘Longlife’, which is aimed to be used for biomedical applications, is a 11 mol% ceria doped zirconia combined with 8 vol% Al_2O_3 and $SrAl_2O_3$ to avoid strong grain growth. In CeTZP materials it is observed that locally transformation bands are formed when load is applied, where the tetragonal phase is transformed to monoclinic resulting in an improved toughness.[144–148] The monolithic Longlife material (CTE (900 °C) = $11.05 \cdot 10^{-6}$ /K) is to be fabricated using the tape casting process and to combine it in a layered B-A-B architecture. For the laminate design ZTA50 has been selected as A-material (CTE (900 °C) = $9.57 \cdot 10^{-6}$ /K). Figure 16 shows the transformation bands formed at a load of ~ 400 MPa for (a) the monolithic Longlife material and (b) the B-A-B laminate where Longlife is combined with ZTA50. The development of transformation bands

is observed to be significantly different. In the monolithic sample only a few defined bands are formed, see fig. 16a. In comparison, fig. 16b., the laminate shows rather fine but a high number of bands, which might be a result of the induced residual tensile stresses in the outer Longlife layer. Further analysis and discussion on the tested samples will be performed, but is out of the scope of this thesis.

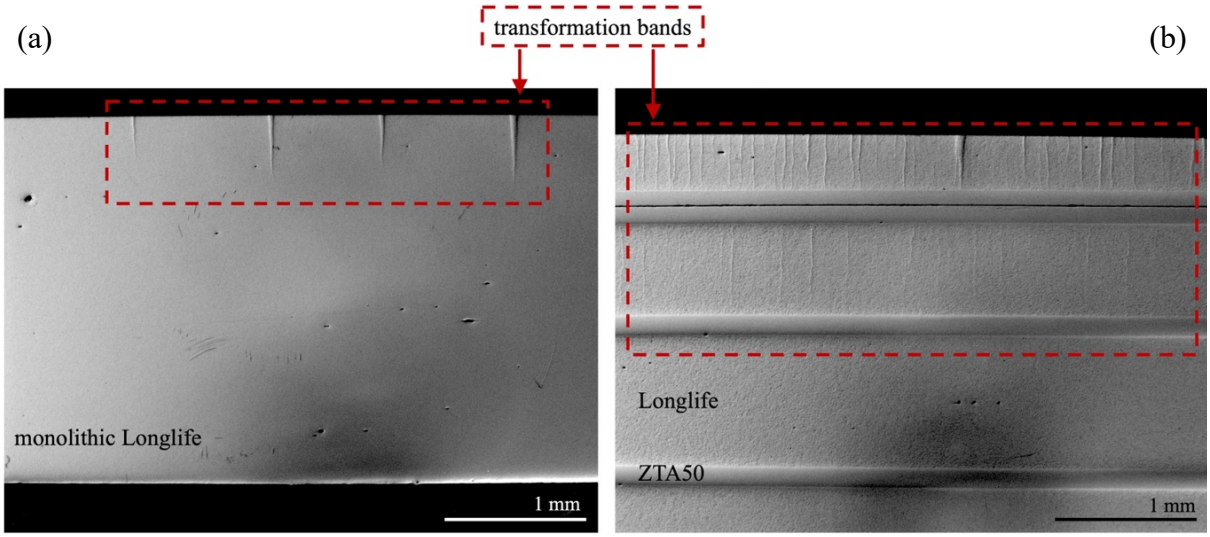

Figure 16: Transformation bands formed in **(a)** a monolithic Longlife material and **(b)** a Longlife + ZTA50 laminate at a load of ~ 400 MPa

MAX phases, which represent a material class combining the properties of metals and ceramics, are a composition of a transition metal (= 'M'), an element from the A-group (= 'A') and carbon or nitrogen (= 'X'). MAX phases have gained interest due to their properties of lightweight, stiffness, thermal conductivity, oxidation resistance at elevated temperatures as well as good machinability, thermal shock resistance and damage tolerance.[149–154] Here, the MAX phase of Cr_2AlC (B) is used to combine it with Al_2O_3 layers (A) after the B-A-B approach. Cr_2AlC shows a larger CTE (CTE (600 °C) = $10.98 \cdot 10^{-6}$ /K) compared to Al_2O_3 (CTE (600 °C) = $7.60 \cdot 10^{-6}$ /K), resulting in tensile residual stresses in the outer Cr_2AlC layers and compressive in the inner Al_2O_3 layers. Figure 17 displays the selected design considering the magnitude of thermo-physical properties, which was fabricated using tape casting and sintered with SPS. Further investigations will be performed to assess its fracture behaviour.

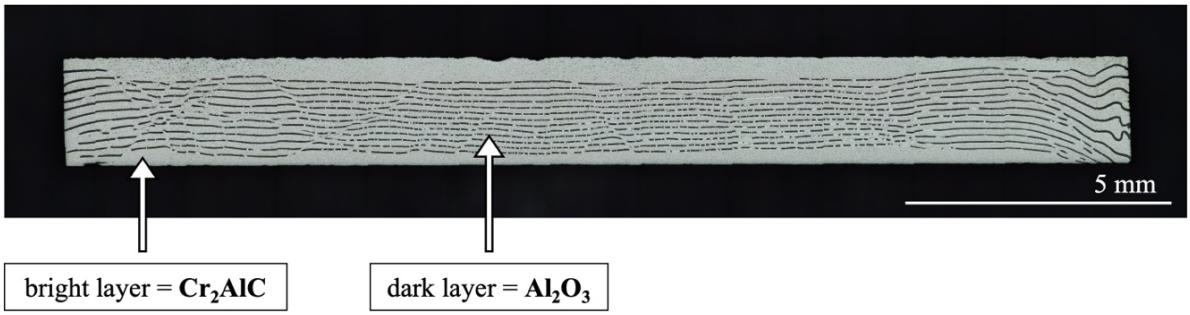

Figure 17: Laminate structure of Cr_2AlC MAX phase and Al_2O_3 layers

Apart from tape casting, another aim was to fabricate composites of alumina and a selected MAX phase (Ti_2AlC) using stereolithographic 3D-printing. Functional properties as thermal and electrical conductivity as well as a comparably high toughness of the Ti_2AlC MAX phase (K_{Ic} ~ 6.5 MPa $m^{1/2}$) is desired to be combined with the high hardness and thermal stability of alumina ceramics. Figure 18 shows exemplary samples of alumina composites containing 0, 10, 20 and 30 vol% of Ti_2AlC, where the limitation was the ability to photo-polymerize suspensions with the dark, metallic and rather coarse MAX powder. The 3D-printed samples were sintered using the pressure-less spark plasma sintering set-up. Investigations according to physical, mechanical and electrical properties will be performed.

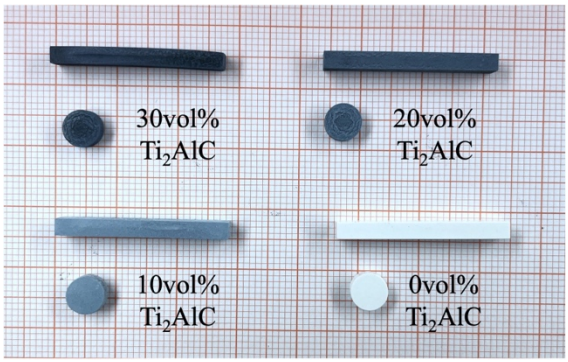

Figure 18: Green samples of EA+Ti_2AlC composites containing 0, 10, 20 and 30vol%.

7 List of publications

7.1 Contributions as first author

Publication A:

Effect of second phase addition of zirconia on the mechanical response of textured alumina ceramics

A.-K. Hofer, I. Kraleva, T. Prötsch, A. Vratanar, M. Wratschko, R. Bermejo

in Journal of the European Ceramic Society 43 (2023) 2935-2942.

doi: https://doi.org/10.1016/j.jeurceramsoc.2022.08058

The effect of second phase addition of zirconia on the mechanical response of textured alumina was analysed. Highly textured monolithic tape-casted alumina was obtained through templated grain growth. Compositions containing 1, 2, 5 and 10 vol% of (i) non-stabilised and (ii) 3 mol% yttria-stabilised zirconia, respectively, were investigated. XRD analyses revealed that the texture degree decreased with increasing second phase content. Microstructural analysis showed zirconia grains inside the textured alumina grains for contents ≤ 5 vol%, affecting the mode of fracture. Fracture toughness of textured alumina significantly decreased with the addition of a second phase. In the case of non-stabilised zirconia, the constraint of the alumina matrix and the small grain size led to a lower fracture toughness in comparison to monolithic textured alumina (K_{Ic} = 5.1 MPa $m^{1/2}$). The fracture toughness of textured alumina with 3 mol% yttria-stabilised zirconia was comparable to equiaxed alumina, independent of the content ratio (K_{Ic} = 3.5 MPa $m^{1/2}$)

Publication B:

Additive manufacturing of highly textured alumina ceramics

A.-K. Hofer, I. Kraleva, R. Bermejo

in Open Ceramics 5 (2021) 100085.

doi: https://doi.org/10.1016/j.oceram.2021.100085

In this work we demonstrate the feasibility of fabricating textured alumina employing a lithography-based ceramic manufacturing process. The combination of vat rotation and platform immersion contributes to the alignment of alumina templates during printing. Templated Grain Growth during sintering provides a high degree of texture (Lotgering Factor ~ 0.80) with relatively low porosity (approx. 7%). A comparable characteristic biaxial strength of 640 MPa and 570 MPa was measured for textured and equiaxed alumina samples,

opening the path for 3D printing textured ceramics of complex architectures for structural and functional applications.

Publication C:

Highly textured 3D-printed translucent alumina

V. Nečina, A.-K. Hofer, R. Bermejo, W. Pabst

(Submitted for publication)

Templated grain growth is a promising method for the fabrication of transparent alumina ceramics and a possible way to circumvent light scattering due to birefringence. In the present paper the effect of temperature, heating rate and dwell time on grain size, orientation, hardness and in-line transmittance is investigated on 3D-printed textured alumina. The samples were prepared by lithography-based ceramic manufacturing (LCM) of suspensions with fine-grained alumina, seeded by high aspect ratio templates and sintered by spark plasma sintering (SPS). A fully developed textured microstructure was achieved at 1600 °C for 1 h, whereas sufficient in-line transmittance of 54.6 % at 550 nm was achieved at 1700 °C for 3 h, albeit at the cost of considerable grain growth and loss of microstructural texturing.

Publication D:

High-strength lithography-based additive manufacturing of ceramic components with rapid sintering

A.-K. Hofer, A. Kocjan, R. Bermejo

in Additive Manufacturing 59 (2022) 103141.

doi: https://doi.org/10.1016/j.addma.2022.103141

Additive manufacturing technology enables the fabrication of technical ceramics and multi-materials with un-precedented geometrical accuracy and complexity, opening the path to new functionalities for engineering applications. A crucial step to consolidate 3D-printed ceramic parts is “sintering”, a time and energy (temperature) intensive densification process. Here we present a strategy for rapid sintering (~ 300–450 °C/min) of lithography-based additively manufactured alumina ceramics enabling consolidation of ceramic components of complex shapes within minutes. Highly dense, fine-grained microstructures were achieved by controlling densification and limiting grain growth through rapid radiation heat transfer. The high mechanical strength and toughness measured in additively manufactured alumina (~ 810 MPa and ~ 4.3 MPa $m^{1/2}$) sintered at 1600 °C within 2 min was superior to that of

conventionally sintered reference parts. This study opens the path for rapid sintering of complex shaped ceramic architectures of high density with tailored microstructure and properties.

Publication E:

Templated Grain Growth in rapid sintered 3D-printed textured alumina ceramics

A.-K. Hofer, A. Kocjan, R. Bermejo

(Submitted for publication)

Textured microstructures in ceramics have gained interest due to their beneficial effect on structural and functional properties. For instance, morphologically textured grains in alumina-based ceramics provide enhanced damage tolerance. Texturing of alumina ceramics may be achieved through templated grain growth (TGG) occurring during sintering at high temperatures with prolonged dwell times (hours) and may be further enhanced by the presence of a liquid phase. In this study, we demonstrate the feasibility of texturing 3D-printed alumina ceramics within minutes by combining rapid heating (~ 450 °C/min) and short dwell times (< 20 min). The effect of sintering temperature and dwell time is investigated on samples with and without liquid phase. Experimental findings show highest texture degree for samples rapid sintered at 1600 °C for 16 min exhibiting a Lotgering factor of 0.6 - 0.7. This study opens the path for tailoring the microstructure of 3D-printed ceramics, using pressure-less rapid sintering protocols.

Publication F (not included in this thesis):

Effect of binder system on the thermophysical properties of 3D-printed zirconia ceramics

A.-K. Hofer, J. Rabitsch, D. Jutrzenka-Trzebiatowska, C. Hofstetter, I. Gavalda-Velasco, J. Schlacher, M. Schwentenwein, R. Bermejo

in International Journal of Applied Ceramic Technology 19 (2022) 174-180.

doi: https://doi.org/10.1111/ijac.1306

7.2 Contributions as co-author

Additive manufacturing of high-strength alumina through a multi-material approach

J. Schlacher, A.-K. Hofer, S. Geier, I. Kraleva, R. Papšik, M. Schwentenwein, R. Bermejo

in Open Ceramics 5 (2021) 100082.

doi: https://doi.org/10.1016/j.oceram.2021.100082

Contact damage tolerance of alumina-based layered ceramics with tailored microstructures

J. Schlacher, A. Jabr, A.-K. Hofer, R. Bermejo

in Journal of the American Ceramic Society 105 (2022) 4387-4399.

doi: https://doi.org/10.1111/jace.18389

Prediction of edge and tunnelling crack formation in layered ceramics using a stress-energy fracture criterion

R. Papšik, O. Ševeček, A.-K. Hofer, I. Kraleva, J. Kreith, R. Bermejo

in Journal of the European Ceramic Society 43 (2023) 2928-2934.

Doi: https://doi.org/10.1016/j.jeurceramsoc.2022.12.022

Stereolithographic 3D Printing of Ceramics: Challenges and Opportunities for Structural Integrity

T. Lube, M. Staudacher, A.-K. Hofer, J. Schlacher, R. Bermejo

in Advanced Engineering Materials 25 (2023) 2200520.

doi: https://doi.org/10.1002/adem.202200520

High-temperature fracture behaviour of layered alumina ceramics with textured microstructure

J. Schlacher, Z. Chlup, A.-K. Hofer, R. Bermejo

in Journal of the European Ceramic Society 43 (2023) 2917-2927.

doi: https://doi.org/10.1016/j.jeurceramsoc.2022.11.046

Press-compaction-assisted binder jetting of textured ceramics

M. Moghadasi, A. Mahdaviarab, A.-K. Hofer, R. Bermejo, Z. Pei, C. Ma

(Submitted for publication)

Effect of airborne particle abrasion and regeneration firing on the strength of 3D-printed 3Y and 5Y zirconia ceramics

T. Mirt, A. Kocjan, A.-K. Hofer, M. Schwentenwein, A. Iveković, R. Bermejo, P. Jevnikar

(Submitted for publication)

7.3 Contributions to the publications as first author

Publication A:

Manuscript preparation, fabrication of samples, microstructural characterization – SEM, XRD measurements, Rietveld refinement, determination of texture degree, hardness measurements, mechanical testing, evaluation of fracture toughness and hardness

Publication B:

Manuscript preparation, 3D-printing and sintering of samples, microstructural characterization – SEM, XRD measurements, determination of texture degree, mechanical testing, statistical analysis of strength distributions

Publication C:

Parts of Manuscript preparation, 3D-printing of samples, XRD measurements, determination of texture degree, hardness measurements, evaluation of hardness

Publication D:

Manuscript preparation. 3D-printing and sintering of samples (PL-SPS), microstructural characterization – SEM, mechanical testing, statistical analysis of strength distributions, evaluation of fracture toughness

Publication E:

Manuscript preparation, 3D-printing and sintering of samples (PL-SPS), microstructural characterization – SEM, XRD measurements, determination of texture degree

8 Funding acknowledgements

The funding for this research, provided by the European Research Council (ERC) excellent science grand “CERATEXT” through the Horizon 2020 program under contract 817615, is gratefully acknowledged.

9 References

[1] W.D. Kingery, H.K. Bowen, D.R. Uhlmann, Introduction to ceramics, Wiley, New York, 1976.

[2] C.B. Carter, M.G. Norton, Ceramic Materials: Science and Engineering, Springer, New York, 2013.

[3] M.F. Ashby, D.R.H. Jones, Engineering Materials: An Introduction to Microstructures and Processing, Elsevier Butterworth-Heinemann, Oxford, 1998.

[4] S.-J.L. Kang, Sintering: Densification, Grain Growth and Microstructure, Elsevier Butterworth-Heinemann, Oxford, 2005.

[5] R.H.R. Castro, Sintering: Mechanisms of Convention, Nanodensification and Field Assisted Processes, Springer, New York.

[6] R.K. Bordia, S.-J.L. Kang, E.A. Olevsky, Current understanding and future research directions at the onset of the next century of sintering science and technology, Journal of the American Ceramic Society (2017) 2314–2352.

[7] A. Indurkar, R. Choudhary, K. Rubenis, J. Locs, Advances in Sintering Techniques for Calcium Phosphates Ceramics, Materials (2021).

[8] Y.V. Milman, S.I. Chugunova, I.V. Goncharova, T. Chudoba, W. Lojkowski, W. Gooch, Temperature dependence of hardness in silicon-carbide ceramics with different porosity, International Jounal of Refractory Metals & Hard Materials (1999) 361–368.

[9] G.L. Messing, St. Poterala, Y. Chang, T. Frueh, E.R. Kupp, B.H. Watson, R.L. Walton, M.J. Brova, A.-K. Hofer, R. Bermejo, R.J. Meyer, Texture-engineered ceramics—Property enhancements through crystallographic tailoring, Journal of Materials Research (2017) 3219–3241.

[10] A.A. Griffith, The Phenomena of Rupture and Flow in Solids, The Royal Society (1921) 163–198.

[11] M. Asmani, C. Kermel, A. Leriche, M. Ourak, Influence of porosity on Young's modulus and Poisson's ratio in alumina ceramics, Journal of the European Ceramic Society (2001) 1081–1086.

[12] H. Jelitto, G.A. Schneider, A geometric model for the fracture toughness of porous materials, Acta Materialia (2018) 443–453.

[13] M. Trunec, Effect of Grain Size on Mechanical Properties of 3Y-TZP-Ceramics, Ceramics-Silikaty (2008) 165–171.

[14] R.W. Rice, S.W. Freiman, J.J. Mecholsky Jr., The Dependence of Strength-Controlling Fracture Energy on the Flaw-Size to Grain-Size Ratio, Journal of the American Ceramic Society (1980) 129–136.

[15] A. Krell, J. Klimke, T. Hutzler, Transparent compact ceramics: Inherent physical issues, Optical Materials (2009) 1144–1150.

[16] A. Krell, P. Blank, Grain Size Dependence of Hardness in Dense Submicrometer Alumina, Journal of the American Ceramic Society (1995) 1118–1120.

[17] M.M. Seabaugh, I.H. Kerscht, G.L. Messing, Texture Development by Templated Grain Growth in Liquid-Phase-Sintered α-Alumina, Journal of the American Ceramic Society (1997) 1181–1188.

[18] S. Deville, E. Saiz, R.K. Nalla, A.P. Tomsia, Freezing as a path to build complex composites, Science (2006) 515–518.

[19] Z. Shen, M. Johnsson, Z. Zhao, M. Nygren, Spark Plasma Sintering of Alumina, Journal of the American Ceramic Society (2002) 1921–1927.

[20] A. Krell, G.M. Baur, C. Dähne, Transparent sintered sub-µm Al_2O_3 with IR transmissivity euqal to sapphire, Proceedings of SPIE (2003) 199–207.
[21] J. Wang, R. Stevens, Zirconia-toughened alumina (ZTA) ceramics, Journal of Materials Science (1989) 3421–3440.
[22] H. Salmang, H. Scholze, Keramik, Springer, Berlin Heidelberg, 2007.
[23] E. Dörre, H. Hübner, Alumina: Processing, Properties, and Applications, Springer, Berlin, 1984.
[24] I.-J. Bae, S. Baik, Abnormal Grain Growth of Alumina, Journal of the American Ceramic Society (1997) 1149–1156.
[25] R. Danzer, T. Lube, R. Morrell, P. Supancic, Handbook of Advanced Ceramics: Materials, Applications, Processing and Properties, Elsevier, Amsterdam, 2013.
[26] I.J. McColm, Ceramic Hardness, Plenum Press, New York, 1990.
[27] F. Bouville, Strong and tough nacre-like aluminas: Process-structure-performance relationships and position within the nacre-inspired composite landscape, Journal of Materials Research (2020) 1076–1094.
[28] M. Suzuki, H. Nagasawa, Mollusk shell structures and their formation mechanism, Canadian Journal of Zoology (2013) 349–366.
[29] H. Le Ferrand, F. Bouville, T.P. Niebel, A.R. Studart, Magnetically assisted slip casting of bioinspired heterogeneous composites, Nature materials (2015) 1172–1179.
[30] M.M. Seabaugh, I.H. Kerscht, G.L. Messing, Texture Development by Templated Grain Growth in Liquid-Phase-Sintered α-Alumina, Journal of the American Ceramic Society (1997) 1181–1188.
[31] R.J. Pavlacka, G.L. Messing, Processing and mechanical response of highly textured Al_2O_3, Journal of the European Ceramic Society (2010) 2917–2925.
[32] R. Garvie, R. Hannink, R. Pascoe, Ceramic steel?, Nature (1975) 703–704.
[33] C. Piconi, G. Maccauro, Zirconia as a ceramic biomaterial, Biomaterials (1999) 1–25.
[34] J. Chevalier, A. Liens, H. Reveron, F. Zhang, P. Reynaud, T. Douillard, L. Preiss, V. Sergo, V. Lughi, M. Swain, N. Courtois, Forty years after the promise of «ceramic steel?»: Zirconia-based composites with a metal-like mechanical behavior, Journal of the American Ceramic Society (2020) 1482–1513.
[35] Y.-W. Chen, J. Moussi, J.L. Drury, J.C. Wataha, Zirconia in biomedical applications, Expert review of medical devices (2016) 945–963.
[36] M.N. Rahaman, Sintering of Ceramics, Taylor & Francis Group, Boca Raton, 2007.
[37] M. Kuntz, R. Krüger, The effect of microstructure and chromia content on the properties of zirconia toughened alumina, Ceramics International (2018) 2011–2020.
[38] G.K. Bansal, A.H. Heuer, On a Martensitic Phase Transformation in Zirconia (ZrO_2) - I. Metallographic Evidence, Acta Metallica (1972) 1281–1289.
[39] R. Orrù, R. Licheri, A.M. Locci, A. Cincotti, G. Cao, Consolidation/synthesis of materials by electric current activated/assisted sintering, Materials Science and Engineering: R: Reports (2009) 127–287.
[40] O. Guillon, J. Gonzalez-Julian, B. Dargatz, T. Kessel, G. Schierning, J. Räthel, M. Herrmann, Field-Assisted Sintering Technology/ Spark Plasma Sintering: Mechanisms, Materials, and Technology Developments, Advanced Engineering Materials (2014) 830–849.
[41] U. Anselmi-Tamburini, Encyclopedia of Materials: Technical Ceramics and Glasses: Spark Plasma Sintering, Elsevier, Oxford, 2021.

[42] S. Grasso, Y. Sakka, G. Maizza, Electric current activated/assisted sintering (ECAS): a review of patents 1906–2008, Science and Technology of Advanced Materials (2009) 1–24.
[43] J.G. Santanach, A. Weibel, C. Estournès, Q. Yang, Ch. Laurent, A. Peigney, Spark plasma sintering of alumina: Study of parameters, formal sintering analysis and hypotheses on the mechanism(s) involved in densification and grain growth, Acta Materialia (2011) 1400–1408.
[44] A. Krell, P. Blank, H. Ma, T. Hutzler, M.P.B. van Bruggen, R. Apetz, Transparent Sintered Corundum with High Hardness and Strength, Journal of the American Ceramic Society (2003) 12–18.
[45] A. Krell, T. Hutzler, J. Klimke, Transmission physics and consequences for materials selection, manufacturing and applications, Journal of the European Ceramic Society (2009) 207–221.
[46] T. Ashikaga, B.-N. Kim, H. Kiyono, T.S. Suzuki, Effect of crystallographic orientation on transparency of alumina prepared using magnetic alignment and SPS, Journal of the European Ceramic Society (2018) 2735–2741.
[47] H. Chen, J. Zhao, S. Shimai, X. Mao, J. Zhang, G. Zhou, S. Wang, N. Gu, K. Zheng, High transmittance and grain-orientated alumina ceramics fabricated by adding fine template particles, Journal of Advanced Ceramics (2022) 582–588.
[48] H. Chen, S. Shimai, J. Zhao, X. Mao, J. Zhang, G. Zhou, S. Wang, Highly oriented α-Al_2O_3 transparent ceramics shaped by shear force, Journal of the European Ceramic Society (2021) 3838–3843.
[49] S. Grasso, C. Hu, G. Maizza, B.-N. Kim, Y. Sakka, Effects of Pressure Application Method on Transparency of Spark Plasma Sintered Alumina, Journal of the American Ceramic Society (2011) 1405–1409.
[50] R.E. Mistler, E.R. Twiname, Tape Casting: Theory and Practice, The American Ceramic Society, Westerville, 2000.
[51] H. Moon, S.D. Kim, E.W. Park, S.H. Hyun, H.S. Kim, Characteristics of SOFC single cells with anode active layer via tape casting and co-firing, International Journal of Hydrogen Energy (2008) 2826–2833.
[52] J.-h. Myung, J.H. Ko, H.-G. Park, M. Hwan, S.-H. Hyun, Fabrication and characterization of planar-type SOFC unit cells using the tape-casting/lamination/co-firing method, International Journal of Hydrogen Energy (2012) 498–504.
[53] J.-h. Myung, H.J. Ko, Ch.H. Im, J. Moon, S.-H. Hyun, Development of solid oxide fuel cells (SOFCs) by tape-casting and single-step co-firing of monolithic laminates, International Journal of Hydrogen Energy (2014) 2313–2319.
[54] D. McKinney, W. Sigmund, Colloidal Processing Fundamentals, in: Handbook of Advanced Ceramics, Elsevier, Oxford, 2013.
[55] Z. Chen, Z. Li, J. Li, C. Liu, C. Lao, Y. Fu, C. Liu, Y. Li, P. Wang, Y. He, 3D printing of ceramics: A review, Journal of the European Ceramic Society (2019) 661–687.
[56] J.-Ch. Wang, H. Dommati, Sh.-J. Hsieh, Review of additive manufacturing methods for high-performance ceramic materials, The International Journal of Advanced Manufacturing Technology (2019) 2627–2647.
[57] F42 Committee, Terminology for Additive Manufacturing Technologies, West Conshohocken, PA, ASTM International, 10.1520/F2792-12A.
[58] G. Mitteramskogler, R. Gmeiner, R. Felzmann, S. Gruber, C. Hofstetter, J. Stampfl, J. Ebert, W. Wachter, J. Laubersheimer, Light curing strategies for lithography-based additive manufacturing of customized ceramics, Additive Manufacturing (2014) 110–118.

[59] M. Schwentenwein, P. Schneider, J. Homa, Lithography-based Ceramic Manufacturing: A Novel Technique for Additive Manufacturing of High-Performance Ceramics, Advances in Science and Technology (2014) 60–64.
[60] A.D. Lantada, A. de Blas Romero, M. Schwentenwein, C. Jellinek, J. Homa, Lithography-based ceramic manufacture (LCM) of auxetic structures: present capabilities and challenges, Smart Materials and Structures (2016) 1–10.
[61] J. Homa, M. Schwentenwein, A Novel Additive Manufacturing Technology for High-Performance Ceramics, Ceramic Engineering and Science Proceedings (2014) 33–40.
[62] J.W. Halloran, Ceramic Stereolithography: Additive Manufacturing for Ceramics by Photopolymerization, Annual Review of Materials Research (2016) 19–40.
[63] R. Phillips, Photopolymerization, Journal of Photochemistry (1984) 79–82.
[64] J.K. C.E. Hoyle, J.F. Kinstle, Radiation Curing of Polymeric Materials, American Chemical Society, Washington DC, 1990.
[65] A. Ravve, Light-Associated Reactions of Synthetic Polymers, Springer, New York, 2006.
[66] J.V. Crivello, E. Reichmanis, Photopolymer Materials and Processes for Advanced Technologies, Chemistry of Materials (2014) 533–548.
[67] M. Schwentenwein, J. Homa, Additive Manufacturing of Dense Alumina Ceramics, International Journal of Applied Ceramic Technology (2015) 1–7.
[68] R.L. Coble, Initial Sintering of Alumina and Hematite, Journal of the American Ceramic Society (1958) 55–62.
[69] M.M. Seabaugh, G.L. Messing, M.D. Vaudin, Texture Development and Microstructure Evolution in Liquid-Phase-Sintered α-Alumina Ceramics Prepared by Templated Grain Growth, Journal of the American Ceramic Society (2000) 3109–3116.
[70] Y. Chang, St. Poterala, D. Yener, G.L. Messing, Fabrication of Highly Textured Fine-Grained α-Alumina by Templated Grain Growth of Nanoscale Precursors, Journal of the American Ceramic Society (2013) 1390–1397.
[71] R.L. Walton, M.D. Vaudin, A.-K. Hofer, E.R. Kupp, R.J. Meyer, G.L. Messing, Tailoring particle alignment and grain orientation during tape casting and templated grain growth, Journal of the American Ceramic Society (2019) 2405–2414.
[72] A.-K. Hofer, I. Kraleva, R. Bermejo, Additive manufacturing of highly textured alumina ceramics, Open Ceramics (2021) 100085.
[73] E. Suvaci, G.L. Messing, Critical Factors in the Templated Grain Growth of Textured Reaction-Bonded Alumina, Journal of the American Ceramic Society (2000) 2041–2048.
[74] J.E. Burke, Role of Grain Boundaries in Sintering, Journal of the American Ceramic Society (1957) 80–85.
[75] K.W. Lay, Grain Growth in UO_2-Al_2O_3 in the Presence of a Liquid Phase, Journal of the American Ceramic Society (1968) 373–376.
[76] E. Suvaci, K.-S. Oh, G.L. Messing, Kinetics of Template Growth in Alumina during the Process of Templated Graing Growth (TGG), Acta Materialia (2001) 2075–2081.
[77] M.M. Seabaugh, E. Suvaci, B. Brahmaroutu, G.L. Messing, Modeling Anisotropic Single Crystal Growth Kinetics in Liquid Phase Sintered α-Al_2O_3, Interface Science (2000) 257–267.
[78] P.C. Hiemenz, R. Rajagopalan, Principles of Colloid and Surface Chemistry, 3rd ed., Marcel Dekker, New York, 1997.
[79] D.F.K. Hennings, R. Jannsen, P.J.L. Reynen, Control of Liquid-Phase-Enhanced Discontinuous Grain Growth in Barium Titanate, Journal of the American Ceramic Society (1987) 23–27.

[80] D. Kashchiev, Two-dimensional nucleation in crystal growth: thermodynamically consistent desription of the nucleation work, Journal of Crystal Growth (2004) 685–702.
[81] F. Kreith, R.M. Manglik, M.S. Bohn, Principles of Heat Transfer, 7th ed., Cengage Learning, Stamford, 2011.
[82] J.R. Welty, C.E. Wicks, R.E. Wilson, G.L. Rorrer, Fundamentals of Momentum, Heat and Mass Transfer, 5th ed., John Wiley & Sons, Inc., New York, 2008.
[83] M.F. Modest, Radiative Heat Transfer, 3rd ed., Elsevier, Oxford, 2013.
[84] J.R. Howell, M.P. Menguc, R. Siegel, Thermal Radiation Heat Transfer, 6th ed., Taylor & Francis Group, Boca Raton, 2016.
[85] D. Li, Rapid sintering of ceramics by intense thermal radiation. Dissertation, Stockholm, 2016.
[86] G.L. Messing, A.J. Stevenson, Toward Pore-Free Ceramics, Science (2008) 381–383.
[87] M. Biesuz, S. Grasso, V.M. Sglavo, What's new in ceramics sintering? A short report on the latest trends and future prospects, Current Opinion in Solid State and Materials Science (2020) 1–23.
[88] J. Guo, R. Floyd, S. Lowum, J.-P. Maria, Th. Herisson de Beauvoir, J.-H. Seo, C.A. Randall, Cold Sintering: Progress, Challenges, and Future Opportunities, Annual Review of Materials Research (2019) 275–295.
[89] S. Dursun, K. Tsuji, S.H. Bang, A. Ndayishimiye, C.A. Randall, A Route towards Fabrication of Functional Ceramic/Polymer Nanocomposite Devices Using the Cold Sintering Process, ACS Applied Electronic Materials (2020) 1917–1924.
[90] A. Jabr, H.N. Jones, A.P. Argüelles, S. Trolier-McKinstry, C.A. Randall, R. Bermejo, Scaling up the cold sintering process of ceramics, Journal of the European Ceramic Society (2023) 5319–5329.
[91] A. Jabr, J. Fanghanel, Zh. Fan, R. Bermejo, C.A. Randall, The effect of liquid phase chemistry on the densification and strength of cold sintered ZnO, Journal of the European Ceramic Society (2023) 1531–1541.
[92] R. Chaim, M. Levin, A. Shlayer, C. Estournes, Sintering and densification of nanocrystalline ceramic oxide powders: a review, Advances in Applied Ceramics (2008) 159–169.
[93] M. Kermani, J. Dong, M. Biesuz, Y. Linx, H. Deng, V.M. Sglavo, M.J. Reece, Ch. Hu, S. Grasso, Ultrafast high-temperature sintering (UHS) of fine grained α-Al_2O_3, Journal of the European Ceramic Society (2021) 6626–6633.
[94] I.-W. Chen, X.-H. Wang, Sintering dense nanocrystalline ceramics without final-stage grain growth, Nature (2000) 168–171.
[95] M. Cologna, B. Rashkova, R. Raj, Flash Sintering of Nanograin Zirconia in <5s at 850°C, Journal of the American Ceramic Society (2010) 3556–3559.
[96] Ch. Wang, W. Ping, Q. Bai, H. Cui, R. Hensleigh, R. Wang, A.H. Brozena Zh. Xu, J. Dai, Y. Pei, Ch. Zheng, G. Pastel, J. Gao, X. Wang, H. Wang, J.-Ch. Zhao, B. Yang, X.R. Zheng, J. Luo, Y. Mo, B. Dunn, L. Hu, A general method to synthesize and sinter bulk ceramics in seconds, Science (2020) 521–526.
[97] D. Agrawal, Sintering of Advanced Materials: Microwave sintering of ceramics, composites and metal powders, Woodhead Publishing, Swaston, 2010.
[98] E.A. Olevsky, L. Froyen, Ludo, Impact of Thermal Diffusion on Densification During SPS, Journal of the American Ceramic Society (2009) 122-132.
[99] E.A. Olevsky, S. Kandukuri, L. Froyen, Consolidation enhancement in spark-plasma sintering: Impact of high heating rates, Journal of Applied Physics (2007) 1–11.

[100] M.P. Harmer, E.W. Roberts, R.J. Brook, Rapid Sintering of Pure and Doped α-Al_2O_3, Journal of the British Ceramic Society (1979) 22–25.
[101] A. Kocjan, M. Logar, Zh. Shen, The agglomeration, coalescence and sliding of nanoparticles, leading to the rapid sintering of zirconia nanoceramics, Scientific reports (2017) 1–8.
[102] D. Kuscer, A. Kocjan, M. Majcen, A. Meden, K. Radan, J. Kovač, B. Malič, Evolution of phase composition and microstructure of sodium potassium niobate –based ceramic during pressure-less spark plasma sintering and post-annealing, Ceramics International (2019) 10429–10437.
[103] W.L. Bradbury, E.A. Olevsky, Production of SiC–C composites by free-pressureless spark plasma sintering (FPSPS), Scripta Materialia (2010) 77–80.
[104] D. Salamon, Zh. Shen, Pressure-less spark plasma sintering of alumina, Materials Science and Engineering: A (2008) 105–107.
[105] T. Prötsch, Untersuchung der Einflussgröße "Kugelmühle" auf die Dispergierung bzw. Partikelgrößenverteilung in keramischen Schlickern für den Tape Casting-Prozess. Bachelor thesis, Leoben.
[106] A.-K. Hofer, I. Kraleva, T. Prötsch, A. Vratanar, M. Wratschko, R. Bermejo, Effect of second phase addition of zirconia on the mechanical response of textured alumina ceramics, Journal of the European Ceramic Society (2023) 2935–2942.
[107] J. Schlacher, Z. Chlup, A.-K. Hofer, R. Bermejo, High-temperature fracture behaviour of layered alumina ceramics with textured microstructure, Journal of the European Ceramic Society (2023) 2917–2927.
[108] R. Papšík, O. Ševeček, A.-K. Hofer, I. Kraleva, J. Kreith, R. Bermejo, Prediction of edge and tunnelling crack formation in layered ceramics using a stress-energy fracture criterion, Journal of the European Ceramic Society (2023) 2928–2934.
[109] Y. Chang, R. Bermejo, G.L. Messing, Improved Fracture Behavior of Alumina Microstructural Composites with Highly Textured Compressive Layers, Journal of the American Ceramic Society (2014) 3643–3651.
[110] A.-K. Hofer, R. Walton, O. Ševeček, G.L. Messing, R. Bermejo, Design of damage tolerant and crack-free layered ceramics with textured microstructure, Journal of the European Ceramic Society (2020) 427–435.
[111] A.-K. Hofer, A. Kocjan, R. Bermejo, High-strength lithography-based additive manufacturing of ceramic components with rapid sintering, Additive Manufacturing (2022) 1–8.
[112] EN 623-2, Advanced technical ceramics - Monolithic ceramics - General and textural properties - Part 2: Determination of density and porosity, 1994.
[113] L. Spiess, G. Teichert, R. Schwarzer, H. Behnken, Ch. Genzel, Moderne Röntgenbeugung, Springer Fachmedien Wiesbaden, Wiesbaden, 2019.
[114] F.K. Lotgering, Topotactical Reactions with ferrimagnetic Oxides having hexagonal Crystal Structures, Journal of Inorganic Nuclear Chemistry (1959) 113–123.
[115] M.D. Vaudin, M.W. Rupich, M. Jowett, G.N. Riley Jr., A method for crystallographic texture investigations using standard x-ray equipment, Journal of Materials Research (1998) 2910–2919.
[116] W.A. Dollase, Correction of Intensities for Preferred Orientation in Powder Diffractometry: Application of the March Model, Journal of Applied Crystallography (1986) 267–272.

[117] M.M. Seabaugh, M.D. Vaudin, J.P. Cline, G.L. Messing, Comparison of Texture Analysis Techniques for Highly Oriented α-Al_2O_3, Journal of the American Ceramic Society (2000) 2049–2054.
[118] ENV 843-4, Advanced technical ceramics - Monolithic ceramics - Mechanical properties at room temperature - Part 4: Vickers, Knoop and Rockwell superficial hardness tests, 1994.
[119] ISO/FDIS 23146, Fine ceramics (advanced ceramics, advanced technical ceramics) - Test methods for fracture toughness of monolithic ceramics - Single-edge V-notch beam (SEVNB) method, 2008.
[120] C.V. Rocha, C.A. Da Costa, Effect of Notch-Root Radius on the Fracture Toughness of Composite Si_3N_4 Ceramics, Journal of Materials Engineering and Performance (2006) 591–595.
[121] ISO 6872, Dentistry - ceramic materials, 2015.
[122] ISO 17167, Fine ceramics (advanced ceramics, advanced technical ceramics) - Mechanical properties of monolithic ceramics at room temperature - Determination of flexural strength by the ring-on-ring test, 2018.
[123] M. Staudacher, T. Lube, P. Supancic, The Ball-on-Three-Balls strength test for discs and plates: Extending and simplifying stress evaluation, Journal of the European Ceramic Society (2023) 648–660.
[124] M. Staudacher, T. Lube, J. Schlacher, P. Supancic, Comparison of biaxial strength measured with the Ball-on-Three-Balls- and the Ring-on-Ring-test, Open Ceramics (2021) 1–10.
[125] A. Börger, P. Supancic, R. Danzer, The ball on three balls test for strength testing of brittle discs: stress distribution in the disc, Journal of the European Ceramic Society (2002) 1425–1436.
[126] A. Börger, P. Supancic, R. Danzer, The ball on three balls test for strength testing of brittle discs: Part II: analysis of possible errors in the strength determination, Journal of the European Ceramic Society (2004) 2917–2928.
[127] EN 843-5, Advanced technical ceramics - Monolithic ceramics - Mechanical tests at room temperature - Part 5: Statistical analysis, 1997.
[128] W. Weibull, A statistical distribution function of wide applicability, Journal of Applied Mechanics (1951) 293–297.
[129] R. Danzer, A General Strength Distribution Function for Brittle Materials, Journal of the European Ceramic Society (1992) 461–472.
[130] R. Danzer, T. Lube, P. Supancic, R. Damani, Fracture of Ceramics, Advanced Engineering Materials (2008) 275–298.
[131] N. Yildirim, R. Kern, Mechanical properties and ageing resistance of slip cast and pressurelessly sintered ZTA - the influence of composition and heat treatment conditions, Science of Sintering (2019) 243–256.
[132] F.F. Lange, Transformation Toughening, Journal of Materials Science (1982) 247–254.
[133] V. Naglieri, P. Palmero, L. Montanaro, J. Chevalier, Elaboration of Alumina-Zirconia Composites: Role of the Zirconia Content on the Microstructure and Mechanical Properties, Materials (Basel, Switzerland) (2013) 2090–2102.
[134] A.H. Heuer, N. Claussen, W.M. Kriven, M. Rühle, Stability of Tetragonal ZrO_2 Particles in Ceramic Matrices, Journal of the American Ceramic Society (1982) 642–650.

[135] M.A. Gafur, Md. S.R. Sarker, Md. Z. Alam, M.R. Qadir, Effect of 3 mol% Yttria Stabilized Zirconia Addition on Structural and Mechanical Properties of Alumina-Zirconia Composites, Materials Sciences and Applications (2017) 584–602.
[136] R.L. Walton, M.J. Brova, B.H. Watson, E.R. Kupp, M.A. Fanton, R.J. Meyer, G.L. Messing, Direct writing of textured ceramics using anisotropic nozzles, Journal of the European Ceramic Society (2023) 648-600.
[137] R.P. Behera, M.J.-H. Reavley, Z. Du, C.L. Gan, H. Le Ferrand, Ultrafast high-temperature sintering of dense and textured alumina, Journal of the European Ceramic Society (2022) 7122–7133.
[138] R. Bermejo, A.J. Sánchez-Herencia, L. Llanes, C. Baudín, High-temperature mechanical behaviour of flaw tolerant alumina–zirconia multilayered ceramics, Acta Materialia (2007) 4891–4901.
[139] R. Bermejo, Y. Torres, A.J. Sánchez-Herencia, C. Baudín, M. Anglada, L. Llanes, Residual stresses, strength and toughness of laminates with different layer thickness ratios, Acta Materialia (2006) 4745–4757.
[140] L. Sestakova, R. Bermejo, Z. Chlup, R. Danzer, Strategies for fracture toughness, strength and reliability optimisation of ceramic-ceramic laminates, International Journal of Materials Research (2011) 613–626.
[141] W.J. Clegg, K. Kendall, N. McN. Alford, T.W. Button, J.D. Birchall, A simple way to make tough ceramics, Nature (1990) 455–457.
[142] Y. Chang, R. Bermejo, O. Ševeček, G.L. Messing, Design of alumina-zirconia composites with spatially tailored strength and toughness, Journal of the European Ceramic Society (2015) 631–640.
[143] J. Schlacher, A. Jabr, A.-K. Hofer, R. Bermejo, Contact damage tolerance of alumina-based layered ceramics with tailored microstructures, Journal of the American Ceramic Society (2022) 4387–4399.
[144] A. Liens, H. Reveron, Th. Douillard, N. Blanchard, V. Lughi, V. Sergo, R. Laquai, B.R. Müller, G. Bruno, W. Schomer, T. Fürderer, E. Adolfsson, N. Courtois, M. Swain, J. Chevalier, Phase transformation induces plasticity with negligible damage in ceria-stabilized zirconia-based ceramics, Acta Materialia (2020) 261–273.
[145] A. Liens, M. Swain, H. Reveron, J. Cavoret, Ph. Sainsot, N. Courtois, D. Fabrègue, J. Chevalier, Development of transformation bands in ceria-stabilized-zirconia based composites during bending at room temperature, Journal of the European Ceramic Society (2021) 691–705.
[146] I. Touaiher, M. Saâdaoui, J. Chevalier, L. Preiss, H. Reveron, Fracture behavior of Ce-TZP/alumina/aluminate composites with different amounts of transformation toughening. Influence of the testing methods, Journal of the European Ceramic Society (2018) 1778–1789.
[147] M. Hayakawa, Y. Inoue, M. Oka, H. Nakagawa, Martensitic Transformation and Mechanical Properties of (Y, Ce)-Tetragonal Zirconia Polycrystals, Materials Transactions (1995) 729–734.
[148] R. Benzaid, J. Chevalier, M. Saâdaoui, G. Fantozzi, M. Nawa, L.A. Diaz, R. Torrecillas, Fracture toughness, strength and slow crack growth in a ceria stabilized zirconia-alumina nanocomposite for medical applications, Biomaterials (2008) 3636–3641.
[149] J. Gonzalez-Julian, I. Kraleva, M. Belmonte, F. Jung, Th. Gries, R. Bermejo, Multifunctional performance of Ti_2AlC MAX phase/2D braided alumina fiber laminates, Journal of the American Ceramic Society (2022) 120–130.

[150] S. Badie, D. Sebold, R. Vaßen, O. Guillon, J. Gonzalez-Julian, Mechanism for breakaway oxidation of the Ti_2AlC MAX phase, Acta Materialia (2021) 1–10.
[151] M.W. Barsoum (Ed.), MAX Phases: Properties of machinable ternary carbides and nitrides, Wiley-VCH Verlag GmbH, Weinheim, 2013.
[152] T. Go, R. Vaßen, O. Guillon, J. Gonzalez-Julian, Processing and oxidation response of Cr_2AlC MAX-phase composites containing ceramic fibers, Open Ceramics (2021) 1–13.
[153] J. Gonzalez-Julian, Processing of MAX phases: From synthesis to applications, Journal of the American Ceramic Society (2021) 659–690.
[154] J. Gonzalez-Julian, G. Mauer, D. Sebold, D.E. Mack, R. Vassen, Cr_2AlC MAX phase as bond coat for thermal barrier coatings: Processing, testing under thermal gradient loading, and future challenges, Journal of the American Ceramic Society (2020) 2362–2375.

Appendix

Publication A

Effect of second phase addition of zirconia on the mechanical response of textured alumina ceramics

Anna-Katharina Hofer, Irina Kraleva, Tobias Prötsch, Andreas Vratanar, Marlies Wratschko, Raúl Bermejo

Department of Materials Science, Montanuniversitaet Leoben, Franz Josef-Strasse 18, A-8700 Leoben, Austria

Journal of the European Ceramic Society 43 (2023) 2935-2942.

doi: https://doi.org/10.1016/j.jeurceramsoc.2022.08058

Journal of the European Ceramic Society 43 (2023) 2935–2942

Contents lists available at ScienceDirect

Journal of the European Ceramic Society

journal homepage: www.elsevier.com/locate/jeurceramsoc

Effect of second phase addition of zirconia on the mechanical response of textured alumina ceramics

Anna-Katharina Hofer *, Irina Kraleva, Tobias Prötsch, Andreas Vratanar, Marlies Wratschko, Raul Bermejo

Department of Materials Science, Montanuniversität Leoben, 8700 Leoben, Austria

ARTICLE INFO

Keywords:
Texture
Textured alumina-zirconia composites
Tape casting
Templated grain growth

ABSTRACT

The effect of second phase addition of zirconia on the mechanical response of textured alumina was analysed. Highly textured monolithic tape-casted alumina was obtained through templated grain growth. Compositions containing 1, 2, 5 and 10 vol% of (i) non-stabilised and (ii) 3 mol% yttria-stabilised zirconia, respectively, were investigated. XRD analyses revealed that the texture degree decreased with increasing second phase content. Microstructural analysis showed zirconia grains inside the textured alumina grains for contents $\leq$ 5 vol%, affecting the mode of fracture. Fracture toughness of textured alumina significantly decreased with the addition of a second phase. In the case of non-stabilised zirconia, the constraint of the alumina matrix and the small grain size led to a lower fracture toughness in comparison to monolithic textured alumina (K_{Ic} = 5.1 MPa $m^{1/2}$). The fracture toughness of textured alumina with 3 mol% yttria-stabilised zirconia was comparable to equiaxed alumina, independent of the content ratio (K_{Ic} = 3.5 MPa $m^{1/2}$).

1. Introduction

Ceramic materials are used for various applications, as in dentistry, for cutting tools or in electronic devices owed to their outstanding properties such as chemical and thermal stability, high wear resistance as well as insulating or conductive properties. A strong limitation of ceramics is the brittle fracture behaviour, resulting in a low damage tolerance. Microstructural defects introduced during processing or from post-machining may lead to catastrophic failure. In this regard, various approaches have been investigated to improve the damage tolerance of ceramics. Considering aluminium oxide (alumina, Al_2O_3), which is widely used in ceramic industries due to its high hardness (~ 19 GPa) and wear resistance, it shows a rather low fracture toughness K_{Ic} ~ 3.5 – 4 MPa $m^{1/2}$ [1,2]. To enhance the fracture behaviour of alumina, composites with the addition of yttriumoxide-stabilised tetragonal zirconia (YSZ), typically in a content of 17 vol%, are fabricated [2,3]. The fracture toughness of zirconia toughened alumina (ZTA), with 17 vol% of YSZ is reported to be ~ 6 MPa $m^{1/2}$ and a hardness of ~ 17 GPa [3–5]. This increase can be explained through the toughening phase transformation of YSZ. The toughening of YSZ occurs at the tip of a propagating crack, where stresses cause the lattice to transform martensitic from tetragonal to monoclinic phase, with an associated volume increase. The resulting compressive stresses around the crack tip hinders crack propagation [5–7]. The transformability of YSZ depends on different factors such as (i) the concentration of yttrium oxide (yttria, Y_2O_3), (ii) grain size of the zirconia phase and/or (iii) the location of the second phase (intergranular or intragranular) [8–10]. The former correlates with the content of zirconia [11]. In the case of ZTA containing 17 vol% there is a narrow concentration of 1.1–1.2% yttria, to obtain a stability of the tetragonal phase at room temperature and promote phase transformability during mechanical loading [8]. Further, phase transformation of YSZ only occurs beyond a certain threshold grain size of the zirconia phase, which is reported to be ~ 0.4 μm [8,10]. The discussed requirements for transformability of YSZ are valid for intergranular zirconia. In the case of intragranular grains phase transformation is impeded due to the constraint of the alumina matrix [10].

Another approach to toughen alumina is tailoring the microstructure, based on the outstanding mechanical behaviour of the "brick-and-mortar" structure found in nacre [12,13]. In this case, inorganic high aspect ratio platelets are stacked on top of each other in a very controlled order and orientation, and are surrounded by an organic matrix. This composite structure enables nacre to withstand high forces without fracturing. The so-called nacre-like aluminas (NLAs) have been fabricated with high contents (95–100 vol%) of high aspect ratio alumina

* Corresponding author.
E-mail address: anna-katharina.hofer@unileoben.ac.at (A.-K. Hofer).

https://doi.org/10.1016/j.jeurceramsoc.2022.08.058
Received 27 June 2022; Received in revised form 28 August 2022; Accepted 30 August 2022
Available online 5 September 2022

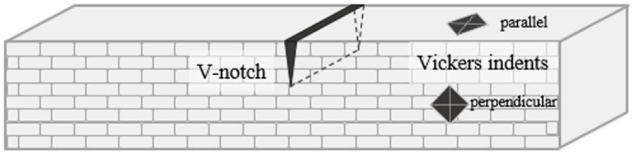

Fig. 1. Testing orientation for measurements of Vickers hardness and fracture toughness.

Table 1
Average grain size (d_{50}) and volume of second phase.

	d_{50} grain size		Phase analysis	
2nd phase content	ZrO_2 [μm]	3YSZ [μm]	ZrO_2 [vol%]	3YSZ [vol%]
1 vol%	0.18	0.17	1.05 ± 0.12	1.07 ± 0.14
2 vol%	0.17	0.17	1.83 ± 0.24	2.04 ± 0.17
5 vol%	0.20	0.19	5.31 ± 0.33	5.23 ± 0 50
10 vol%	0.23	0.18	10.34 ± 0.30	10.43 ± 0.98

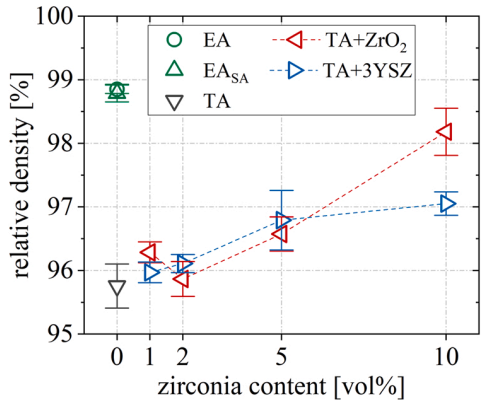

Fig. 2. Relative density vs. second phase content of monolithic reference materials (EA, EA_{SA}) and TA) and the composite materials of textured alumina with (i) non-stabilised ZrO_2 (TA+ZrO_2) or (ii) 3 mol% yttria-stabilised ZrO_2 (TA+3YSZ).

templates, using processes such as ice-templating or magnetically-assisted-slip-casting for alignment [14,15]. These materials have been typically sintered using spark plasma sintering (SPS) to impede the growth of the platelets. Systems using a glassy phase (SiO_2 +CaO) or aluminium borate as matrix have been investigated for high temperature applications, reaching K_{Ic}-values of ~ 5.1 MPa $m^{1/2}$ and ~ 7.4 MPa $m^{1/2}$, respectively [15].

Templated grain growth (TGG) is another method to texture ceramic microstructures [16,17]. In contrast to NLAs, here grain growth is achieved during conventional sintering. A much lower high aspect ratio templates content (2–10 vol%) compared to NLAs, is mixed with submicron-sized ceramic powder to induce Oswald ripening during the sintering step [18,19]. For textured alumina ceramics tape-casting is an established processing route to align the platelets for a tailored orientation of the sintered grain structure. Fracture toughness of TGG alumina materials of ~ 4.4 MPa $m^{1/2}$ has been previously reported for 5 vol% alumina templates [19,20]. Recently, textured alumina has been also obtained on 3D printed parts using stereolithographic technique [21].

The question arises on how the incorporation of zirconia (as second phase) can affect the degree and quality of texture of the microstructure and the related mechanical properties.

2. Experimental procedure

2.1. Sample fabrication

Tape casting was employed for the fabrication of the samples, where ceramic tapes with thicknesses between 10 and 1000 μm can be processed by pouring a viscous suspension onto a moving carrier tape. The viscosity of the suspension, the speed of the carrier tape as well as the height of the doctor blade determine the thickness of the tape. The shear forces generated in the gap between doctor blade and moving carrier tape is particularly important to align the high aspect ratio templates parallel to the moving direction [22]. During the sintering process, the aligned templates preferentially grow, due to dissolution and precipitation of submicron-sized ceramic powders onto the templates, producing textured microstructures. Monolithic textured alumina (TA) as well as TA composites with various contents of non-stabilised zirconia (ZrO_2) and 3 mol% yttria-stabilised zirconia (3YSZ) were prepared. The volume percent of added zirconia in the composite samples was 1, 2, 5 and 10 vol%, respectively. Sintering additives (CaO and SiO_2) were used in order to promote liquid phase formation during sintering to enhance templated grain growth (TGG). For comparison and to investigate the effect of the liquid phase, monolithic equiaxed alumina samples without (EA) and with sintering additives (EA_{SA}) were processed.

2.2. Suspension and sample preparation

For the preparation of the suspension to fabricate textured alumina ceramic tapes, α-alumina powder (99.99% ultrafine α-Al_2O_3, TM-DAR, Taimei Chemicals Co. Ltd., Nagano, Japan) and various contents of non-stabilised or 3 mol% yttria-stabilised zirconia (ZrO_2 (TZ-0Y) or 3YSZ (TZ-3Y), Tosoh, Tokyo, Japan) were weighted and mixed with the solvents xylene and ethanol, which were in a 1:1 ratio (Xylene, Avantor Performance Materials Poland S.A., Gliwice, Poland) (Ethanol 99%, Sigma-Aldrich, Darmstadt, Germany). Menhaden fish oil was employed as dispersant (Sigma-Aldrich GmbH, Vienna, Austria). Additionally, for the enhancement of templated grain growth, 0.10 wt% of SiO_2 and CaO (with respect to the ceramic powder content) were added as sintering additives for liquid phase sintering. SiO_2 and CaO were added in a 1:1 ratio, SiO_2 in form of $C_8H_{20}O_4Si$ (ThermoFischer GmbH, Kandel, Germany) and CaO in form of $Ca(NO_3)_2 \bullet 4H_2O$ (ThermoFischer GmbH, Kandel, Germany). After 24 h of ball milling, the binder system consisting of Polyvinylbutyral (Sigma-Aldrich GmbH, Steinheim, Germany), Butylbenzyl Phthalate (Sigma-Aldrich GmbH, Steinheim, Germany) and Dibutyl sebacate (Sigma-Aldrich, Steinheim, Germany) was added and ball milled for another 24 h. Prior to sieving, 5 vol% of high aspect ratio α-alumina platelets (Rona Flair© White Sapphire, EMD Performance Materials Corp., Darmstadt, Germany) were added to the suspension. The platelets had a thickness of ~ 0.10 μm and a diameter of ~ 5–16 μm. Before tape-casting, the sieved suspension was stirred and degassed for another 24 h with the addition of cyclohexanone as homogeniser (ThermoFischer GmbH, Kandel, Germany). The tape casting was performed on a Tape Caster (CAM-L, Keko Equipment Ltd., Žužemberk, Slovenia), setting a gap height of 250 μm for the doctor blade and a constant casting speed of 0.3 m/min.

The dried tape (thickness ~ 60 μm) was cut into 55 × 55 mm layers, further stacked to a total thickness of ~ 5 mm, uniaxially (~ 6 MPa, 75 °C, 15 min) (Messphysik MIDI 10–5/6x11, Messphysik Materials Testing GmbH, Fürstenfeld, Austria) and isostatically pressed (~ 20 MPa, 75 °C, 30 min) (ILS-46, Keko Equipment Ltd., Žužemberk, Slovenia).

For the removal of the binder system, a thermal treatment with a constant heating rate of 0.3 °C/min at a maximum temperature of 600 °C for 2 h was performed. The samples were sintered at 1550 °C and a dwell time of 2 h, with heating and cooling rates of 5 °C/min. The sintered plates, with dimensions of approximately 45 × 45 × 3 mm

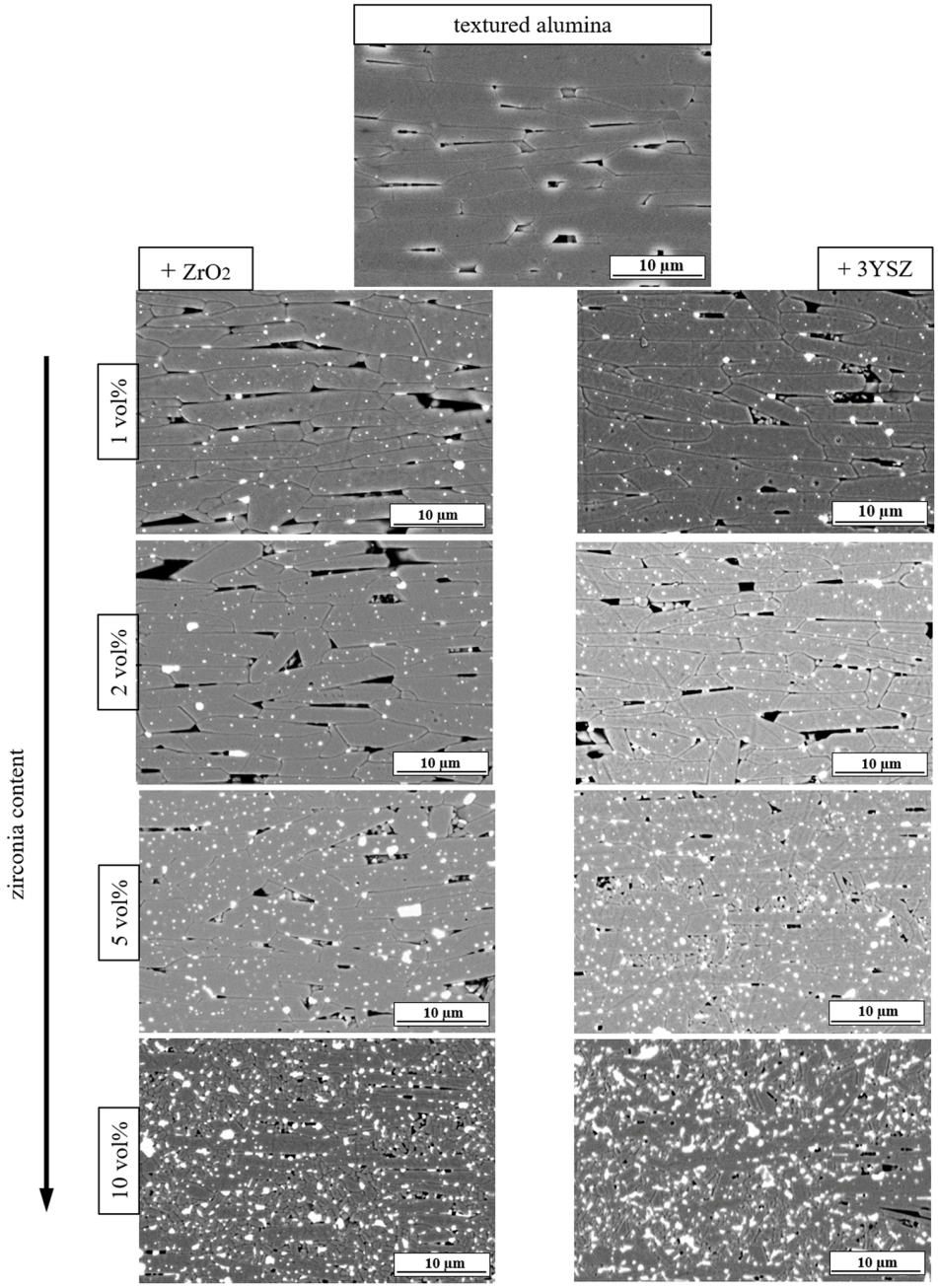

Fig. 3. SEM images showing microstructures of monolithic TA and TA composites with non-stabilised (+ZrO_2) *(left)* and 3 mol% yttria-stabilised zirconia (+3YSZ) *(right)* as second phase.

were cut into ~ 45 × 4 × 3 mm prismatic bars for further analysis and mechanical testing.

Equiaxed alumina (EA) samples were processed in the same fashion, but without the addition of templates. For equiaxed alumina samples with sintering additives (EA_{SA}), the same content of 0.10 wt% was used as in the textured alumina samples.

2.3. Microstructural characterisation

To evaluate the quality of texture and the effect of the second phase, microstructural images were taken on the polished side surface, parallel to the prismatic planes of the hexagonal lattice in the polycrystalline α-alumina material, using a scanning electron microscope (SEM, JEOL JCM-6000Pluse Neoscope™, JEOL Ltd., Tokyo, Japan).

For a quantitative determination of the texture degree an X-ray diffractometer (XRD, Brucker AXS D8 Advance, Bruker, Billerica, USA) was used to measure the XRD-patterns of equiaxed alumina as reference material and all textured samples with various contents of ZrO_2 and 3YSZ. For the XRD measurement a step size of 0.2° and a scan speed of 1.2 s/step have been used.

A rocking curve analysis was performed at the significant (00 12) peak at $2\theta = 90.7°$.

Using the intensities of all characteristic peaks for alumina from the XRD-patterns from equiaxed and textured alumina samples, the Lotgering factor (*LF*) was determined as [23]:

$$LF = \frac{P_{(00l)} - P_0}{1 - P_0} \quad (1)$$

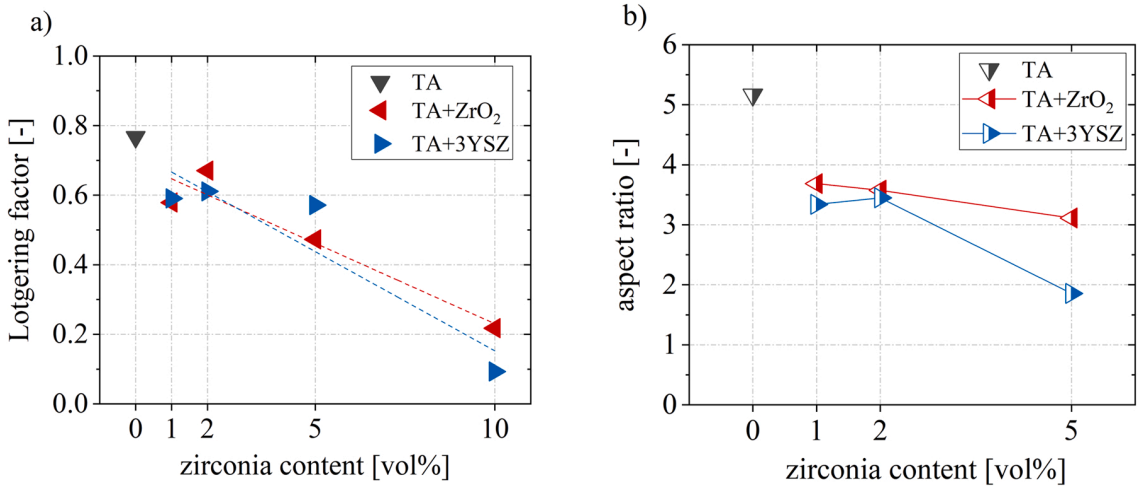

Fig. 4. Characteristic values to describe the degree and quality of texture in monolithic TA and TA composites. a) Lotgering factor and b) aspect ratio versus second phase contents.

Table 2
Characteristic values describing the degree and quality of texture.

2nd phase content	LF [-]		r [-]		f [-]		FWHM [°]	
	ZrO_2	3YSZ	ZrO_2	3YSZ	ZrO_2	3YSZ	ZrO_2	3YSZ
0 vol%	0.77		0.15		0.85		5.3	
1 vol%	0.58	0.59	0.22	0.23	0.87	0.94	9.3	9.8
2 vol%	0.67	0.61	0.20	0.21	0.84	0.82	7.8	8.7
5 vol%	0.47	0.57	0.24	0.16	0.70	0.46	10.1	5.4
10 vol%	0.22	0.09	0.18	0.25	0.16	0.16	6.5	10.9

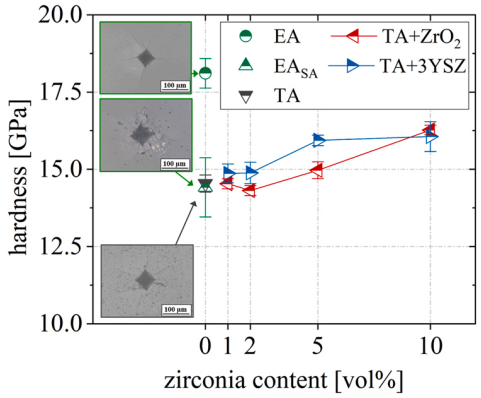

Fig. 5. Vickers hardness versus second phase content for monolithic reference materials (EA, EA+SA and TA) and TA composites with either ZrO_2 or 3YSZ as second phase. Close-up images show Vickers imprints of EA *(top)*, EA_{SA} *(middle)* and TA tested perpendicular to the basal plane of the alumina lattice *(bottom)*.

where $P_{(00l)}$ is the ratio of intensities for textured materials and P_0 for the equiaxed reference material. $P_{(00\,l)}$ and P_0 can be determined with the following equations:

$$P_{(00l)} = \frac{\sum I_{(00l)}}{\sum I_{(hkl)}} \text{ for textured} \quad (2)$$

$$P_0 = \frac{\sum I_{0(00l)}}{\sum I_{0(hkl)}} \text{ for equiaxed} \quad (3)$$

where $I_{(00\,l)}$ and $I_{0(00\,l)}$ are the intensities of the peaks representing the characteristic (0001) peaks for textured alumina; $I_{(hkl)}$ and $I_{0(hkl)}$ are the intensities of all characteristic peaks for alumina detected in the XRD patterns. The Lotgering factor describes the degree of orientation, where a $LF = 1$ defines a perfectly textured microstructure.

More detailed information about the quality of texture can be given through the measurement of the rocking curve at the dominant (00 12) peak of the equiaxed and textured material. The data of the rocking curve (absolute intensity values) measured for textured alumina samples was normalised by the equiaxed alumina data [24]. The resulting curve was then fit with the following March-Dollase equation [25,26]:

$$F(f,r,\theta) = f\left(r^2\cos^2\theta + \frac{\sin^2\theta}{r}\right)^{-\frac{3}{2}} + (1-f) \quad (4)$$

where $f\,(0 \le f \le 1)$ is the volume fraction of oriented material, $r\,(0 \le r \le 1)$ the orientation parameter of the grains and θ the specimen tilt angle (angle between the texture axis and the scattering vector). A small r-value indicates a narrow distribution of oriented platelets normal to the sample surface. For a perfectly textured system, r would be 0 and $f = 1$. Additionally, to the fitting parameters, the full-width of half maximum (*FWHM*) of the fitted curve provides information about the texture. A narrow *FWHM* implies highly oriented grains. [13,17,18].

For phase analysis, X-ray diffractometry patterns (Brucker AXS D8 Advance, Bruker, Billerica, USA) were taken on non-polished and fractured surfaces. Determination whether zirconia is in the tetragonal or monoclinic phase was done applying Rietveld refinement with the software TOPAS (Bruker AXS, Version 6, Bruker, Billerica, USA).

2.4. Determination of physical and mechanical properties

The bulk relative densities of the textured alumina samples with different contents (0–10 vol%) of non-stabilised or stabilised zirconia as second phase were measured after the Archimedes principle for porous materials [27]. In the case of composite materials, the rule of mixture was used with the theoretical densities of the monolithic materials, i.e. $\rho_{th}(Al_2O_3) = 3.986\ g/cm^3$, $\rho_{th}(ZrO_2) = 5.830\ g/cm^3$ and $\rho_{th}(3YSZ) = 6.050\ g/cm^3$, respectively.

Hardness was determined using a Vickers indenter with an applied load of 5 kg [28]. Ten indents per sample were made on two polished surfaces, respectively: (i) at the side surface, parallel to the prismatic planes and (ii) at the upper surface, parallel to the basal planes of the alumina lattice (Fig. 1). Polishing to 1 µm surface finish was performed on a Struers polishing machine (Tegramin-30, Struers GmbH, Willich, Germany).

The fracture toughness, K_{Ic}, was measured after the Single-edge V-

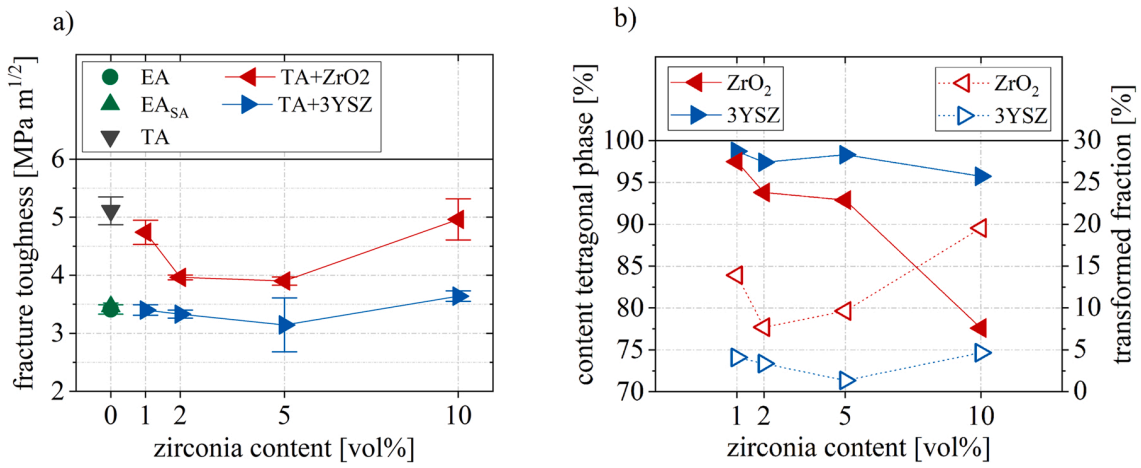

Fig. 6. a) K_{Ic}-values for monolithic reference materials (EA, EA$_{SA}$ and TA) and TA composites with various contents of ZrO_2 or 3YSZ as second phase. b) Evaluation of tetragonal zirconia after processing and the fraction of transformed tetragonal phase after fracture.

notch beam method (SEVNB), notching the textured alumina and composite samples parallel to the basal planes of the alumina grains (Fig. 1) [29]. The notch radius was in the order of the grain size of the microstructure to avoid overestimation of the K_{Ic}. The bending tests were performed on five notched samples of each material, using a universal testing machine (Zwick Z010, Zwick GmbH&Co, Ulm, Germany) and the data were evaluated with the software TestXpertII.

3. Results and discussion

3.1. Microstructural characterisation

The grain size and measured phase contents of the fabricated textured alumina (TA) composites are listed in Table 1. Fig. 2 shows the relative density values for the compositions of TA with different contents of non-stabilised zirconia (ZrO_2) and 3 mol% yttria-stabilised zirconia (3YSZ), as well as the values for the monolithic equiaxed (EA and EA$_{SA}$) and textured alumina (TA) materials, taken as reference. The relative density of TA (< 96%) is lower than that of EA (> 99%), which can be attributed to the anisotropic grain growth impeding pore closure. This effect has been observed in other alumina-based textured materials [19,20,30]. With increasing addition of zirconia as second phase, templated grain growth (TGG) is hindered. As a consequence, the development of texture is reduced, resulting in (normal) grain growth. In these cases, relative density increases, associated with pore closure favoured by the resulting equiaxed microstructure. At contents of 10 vol% second phase, TA+ZrO_2 shows significantly higher relative density than TA+3YSZ. This difference might be related to the larger average grain size for non-stabilised ZrO_2, with a value of d_{50} ~ 0.23 μm, in comparison to 3YSZ with d_{50} ~ 0.18 μm, as listed in Table 1. The growth of non-stabilised ZrO_2 grains might have led to a reduction of porosity.

Fig. 3 shows the microstructures corresponding to the different composite samples. TA composites with second phase contents ≤ 5 vol% (either as TA+ZrO_2 or TA+3YSZ) reveal similar microstructures. The zirconia phase is rather distributed inside the grains. This can be explained by the effect of liquid phase sintering. The sintering additives employed (CaO and SiO_2) enhance diffusion processes and grain boundary mobility, favouring the distribution of the second phase inside the grains [10,19,31,32]. For samples with a content of > 10 vol%, grain growth is impeded by the zirconia phase, which results in a rather equiaxed composite microstructure with homogeneously distributed intergranular ZrO_2 or 3YSZ grains. Zirconia limits TGG, resulting in a strong reduction of the texture degree with increasing second phase content.

Fig. 4a and b show the Lotgering factors (*LF*) and the corresponding aspect ratios for the monolithic TA as well as the composite TA materials, indicating the degree and quality of texture. The *LF* for the monolithic TA was ~ 0.8, corresponding to a relatively high degree of texture. The *LF* value for TA composites drops for 1 and 2 vol% of ZrO_2 or 3YSZ to ~ 0.6. For 5 vol% zirconia content the *LF* slightly decreases, and for 10 vol% a significant reduction to ~ 0.2 was measured. Values for *LF*, for the fitting parameters *r* and *f*, as well as the full-width of half-maximum (*FWHM*) from the measured rocking curves, are given in Table 2. The *r*-value for both TA+ZrO_2 and TA+3YSZ is 0.2, which implies a high preferential orientation of the textured grains parallel to the z-axis. The fraction of highly oriented grains is given with the *f*-value, which decreases with increasing second phase content in the textured alumina composite samples. Highly textured microstructures develop for TA composites with zirconia contents ≤ 5 vol%. Here, the aspect ratio (AR) of the textured grains (i.e. length to thickness) was measured to determine the effect of second phase on the TGG process (Fig. 4b). Monolithic TA shows the highest AR-value of ~ 5. For both composites (TA+ZrO_2 and TA+3YSZ) with 1 vol% and 2 vol% of second phase the aspect ratio strongly decreases to ~ 3.5. However, for composites with 5 vol% a significant difference in the AR can be observed, between non-stabilised and 3 mol% yttria-stabilised zirconia samples. The lower AR-value for TA+3YSZ correlates with the microstructural images (Fig. 3). A larger amount of small zirconia grains is found between the elongated textured alumina grains. In contrast, the microstructural image of TA+ZrO_2 shows a more textured microstructure, with zirconia being located both within the grains and along the grain boundaries. In light of these observations, the second phase within the textured grains seems to have a lower impact on the reduction of the elongation of textured grains, explaining the higher AR-value for the TA composite up to 5 vol% ZrO_2. For higher contents (i.e. 10 vol%) the significant reduction of texture is attributed to the reduction of grain boundary mobility due to the relatively large second phase content. [33].

3.2. Hardness dependence on composition

Fig. 5 illustrates the Vickers hardness (HV) of the textured alumina composites measured in two directions: (i) perpendicular and (i) parallel to the basal planes of the alumina grains, respectively. TA samples show a significantly lower hardness than EA samples. This might be mainly attributed to the higher porosity and larger grain size measured in TA samples. However, the hardness of equiaxed samples fabricated with same additional sintering additives as in TA samples (i.e. EA$_{SA}$) was similar to that of TA samples, while retaining a high relative density of ~ 99%. This important finding reveals the importance of the sintering

additives in tailoring the hardness of alumina based materials. The decrease in hardness can be explained by the larger grain size of the EA_{SA}, with ~ 15 µm, being significantly larger than that for EA with ~ 1.35 µm, as shown in different microstructures [34,35]. Indentation cracks formed around the imprints in TA and EA_{SA} samples are irregular and around the indent, compared to the common cracks formed at the corners of the imprint in EA samples (see close-ups in Fig. 5). Based on these findings, it may be expected that the glass phase formed by the sintering additives can additionally affect the response of the material during indentation (e.g. hardness) as well as the resistance of the material against crack propagation. In this regard EDX measurements were performed, however, due to the low amount of 0.10 wt%, no glass phase could be detected along the grain boundaries nor within the grains.

In the TA composites with ZrO_2 or 3YSZ, it is observed that the content of second phase hardly has an effect on the hardness values. For 1 and 2 vol%, HV is comparable to the hardness value of TA. With increasing second phase content HV increases, which can be explained by the strong dependence of hardness on relative density [36]. Comparing the relative density in Fig. 2 with the hardness in Fig. 5, a strong correlation can be observed. At higher second phase contents (i.e. > 5 vol%), the decrease in grain size and the increasing amount of randomly oriented and spherically shaped grains contribute to higher hardness values. Furthermore, no significant difference was observed between TA composites with non-stabilised or 3 mol% yttria-stabilised zirconia addition.

Taking into account the Vickers imprints made parallel to the basal planes of the alumina lattice, sliding of oriented grains occurs, which contributes to the formation of micro-cracks, propagating along the basal planes of the textured alumina grains [37]. However, quantification of the hardness was not feasible due the shape of the imprints.

3.3. Toughness as function of zirconia addition

Fig. 6a shows the evaluated values of fracture toughness (K_{Ic}) for TA composite materials with various contents of zirconia as second phase and for the monolithic reference materials EA, EA_{SA} and TA. The larger toughness was measured for monolithic textured alumina ceramics, with $K_{Ic} = 5.1$ MPa $m^{1/2}$, compared to ~ 3.5 MPa $m^{1/2}$ for both EA and EA_{SA}.

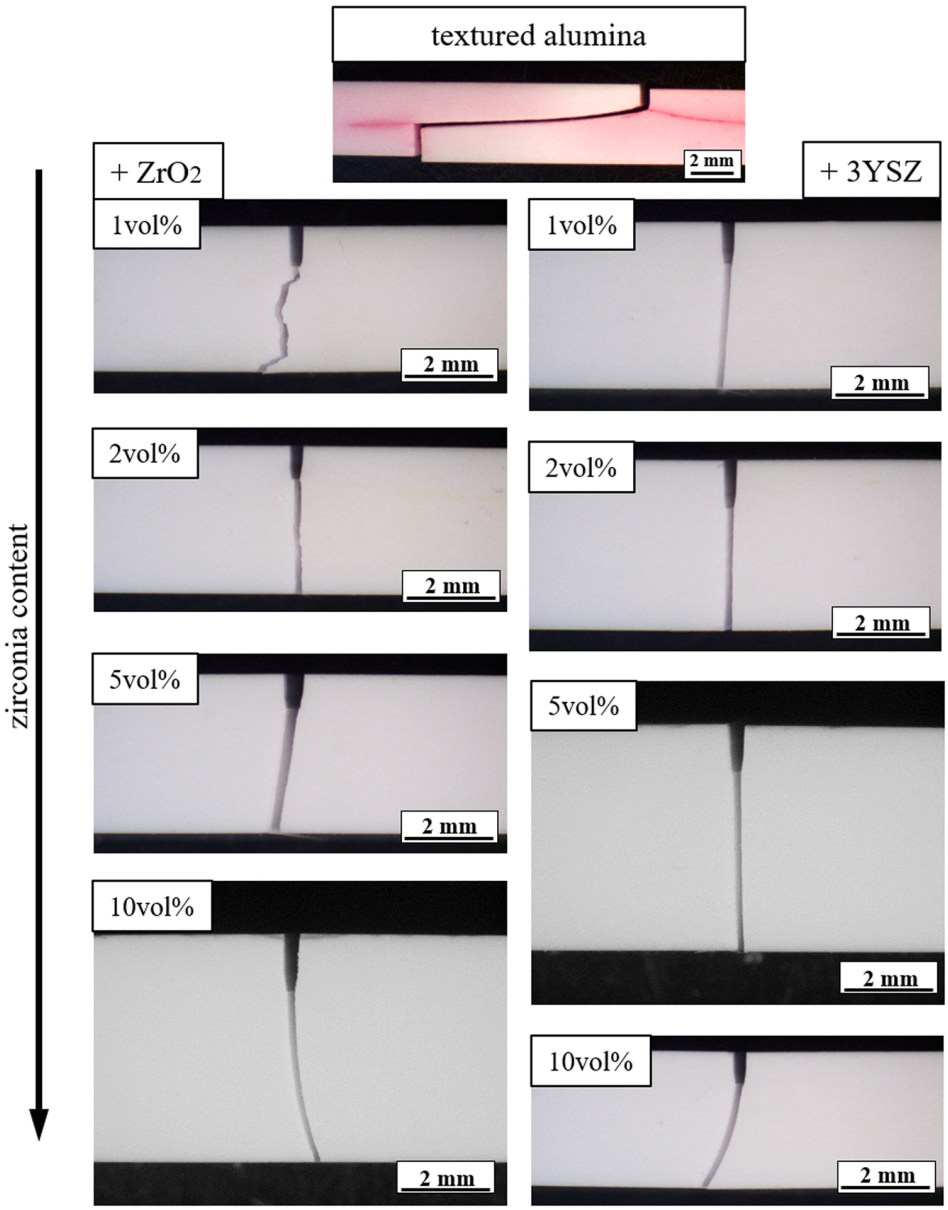

Fig. 7. Images of fracture path after SEVNB testing for TA and TA composites with ZrO_2 and 3YSZ as second phase.

The addition of a second phase to textured alumina significantly decreased the toughness in comparison to the monolithic TA material. In the case of TA with non-stabilised zirconia (TA+ZrO_2) a slightly toughness decrease is observed after 1 vol% ZrO_2 addition, with a significant decrease for 2 and 5 vol%, and a recovery of toughness for a content of 10 vol% ZrO_2 (Fig. 6a). In the case of TA with stabilised zirconia (TA+3YSZ), already for a 1 vol% 3YSZ addition the fracture toughness drops significantly to ~ 3.5 MPa $m^{1/2}$ (similar to the toughness of EA or EA_{SA}), despite the relatively high degree of texture (i.e. LF ~ 0.60). The toughness slightly decreases for samples with 2 and 5 vol% zirconia content, and slightly increases for 10 vol% zirconia.

Fig. 7 shows the corresponding fracture paths of selected specimens for TA monolith as well as TA+ZrO_2 and TA+3YSZ composites. For monolithic TA, a strong effect of the texture can be observed promoting crack deflection, which leads to higher toughness. The fracture path of TA+ZrO_2 with 1 vol% ZrO_2 shows a tortuous crack path, which agrees with the measured toughness (Fig. 6a). However, for higher contents of ZrO_2 (i.e. 2 and 5 vol%) straight fracture occurs, comparable to the fracture behaviour of equiaxed fine grained alumina ceramics. The same brittle behaviour is observed for 10 vol% ZrO_2 addition. The fracture path of TA+3YSZ composites shows no indication of crack deflection for all zirconia additions (from 1 to 10 vol%).

The different behaviour of the zirconia composites may be explained by the zirconia phase present before and after the fracture process as well as the distribution of the zirconia grains in the alumina matrix. Fig. 6b shows the content of tetragonal phase after processing (full symbols) and the fraction of tetragonal phase transformed after fracture (empty symbols). TA+3YSZ samples between 1 and 10 vol% zirconia retained more than 95% of tetragonal phase after sintering. In the case of TA+ZrO_2, the content was decreasing with the zirconia content, reaching a minimum of ~ 75% for 10 vol% zirconia. This decrease is attributed to the higher transformability of intergranular zirconia grains, where the amount increases with increasing ZrO_2 content. Relative densities < 97% may also lead to enhanced transformability for ZrO_2 contents of 2 and 5 vol% [11]. Regarding TA+ZrO_2 with 10 vol% ZrO_2 approx. 25% of the zirconia phase has transformed to monoclinic during cooling from sintering, which may lead to microcracking and a stress free microstructure, contributing to the toughness value [4,38]. The fraction of transformed tetragonal zirconia to monoclinic zirconia during fracture ranges between ~ 15% for 1 vol% ZrO_2, ~ 10% for 2 vol % and 5 vol% ZrO_2, and ~ 20% for 10 vol% ZrO_2. This profile correlates well with the toughness profile in Fig. 6a for the TA+ZrO_2 composites. The limited phase transformation from tetragonal to monoclinic during the fracture process is attributed to the constraint of the alumina matrix (specially for compositions below 5 vol% zirconia), where the majority of the ZrO_2 phase is intragranular, as well as the small size of the ZrO_2 particles (~0.2 μm) [8–10]. In the case of TA+3YSZ the transformation fraction during fracture remains below 5% for all compositions, which is associated with the "overstabilization" of the tetragonal phase with 3 mol% yttria, thus impeding phase transformation during fracture (blue empty symbols in Fig. 6b) [39].

The similar K_{Ic} values (~ 3.5 MPa $m^{1/2}$) for TA+3YSZ samples with contents of 1, 2 and 5 vol% refute stress-induced microcrack toughening due to mismatching coefficients of thermal expansion of alumina (CTE ~ 8×10^{-6} K^{-1}) and 3 mol% yttria-stabilised zirconia (CTE ~ 9×10^{-6} K^{-1}) [40,41]. Only for samples with 10 vol% 3YSZ, where the 3YSZ is no longer trapped within the alumina grains, a slight increase of the K_{Ic}-value can be observed. This might be a result of the increased transformed tetragonal phase and possible toughening through stress-induced microcracking [40].

4. Conclusion

Textured alumina composites (TA) with different contents of non-stabilised (ZrO_2) and 3 mol% yttria-stabilised zirconia (3YSZ) were fabricated using the tape-casting process to study the effect of a second phase on the texture evolution of the microstructure and the related mechanical properties. The measured hardness values showed a dependency on relative density, where hardness increased with increasing relative density for both composite materials. The degree of texture decreased with increasing second phase zirconia content for both TA+ZrO_2 and TA+3YSZ composites, which was attributed to the reduction of grain boundary mobility during template grain growth. The higher fracture toughness in TA+ZrO_2 composites was related to the higher fraction of transformed tetragonal zirconia during the fracture process compared to TA+3YSZ. The significantly lower fracture toughness of TA+3YSZ (K_{Ic} ~ 3.5 MPa $m^{1/2}$) compared to TA monolith (K_{Ic} ~ 5.1 MPa $m^{1/2}$) was attributed to overstabilization in 3YSZ, which limits phase transformation toughening. It can be concluded that adding zirconia as second phase on textured alumina can be employed to tailor density and hardness, however it may not contribute to enhance fracture toughness.

Declaration of Competing Interest

The authors declare that they have no known competing financial interests or personal relationships that could have appeared to influence the work reported in this paper.

Acknowledgements

Funding for this research was provided by the European Research Council (ERC) excellent science grant "CERATEXT" through the Horizon 2020 program under contract 817615.

References

[1] I.J. McColm. Ceramic Hardness, 1st ed., Plenum Press, New York, 1990.
[2] R. Danzer, T. Lube, R. Morrell, P. Supancic, Handbook of Advanced Ceramics: Materials, Applications, Processing, and Properties, Elsevier Inc. Academic Press, 2013.
[3] M. Kuntz, R. Krüger, The effect of microstructure and chromia content on the properties of zirconia toughened alumina, Ceram. Int. 44 (2018) 2011–2020, https://doi.org/10.1016/j.ceramint.2017.10.146.
[4] J. Wang, R. Stevens, Review: zirconia-toughened alumina (ZTA) ceramics, J. Mater. Sci. 24 (1989) 3421–3440.
[5] G.K. Bansal, A.H. Heuer, On a martensitic phase transformation in zirconia (ZrO2)-I. Metallographic evidence, Acta Metall. 20 (1972) 1281–1289.
[6] J. Chevalier, A. Liens, H. Reveron, F. Zhang, P. Reynaud, T. Douillard, L. Preiss, V. Sergo, V. Lughi, M. Swain, N. Courtois, Forty years after the promise of "ceramic steel?": zirconia-based composites with a metal-like mechanical behavior, J. Am. Ceram. Soc. 103 (2020) 1482–1513, https://doi.org/10.1111/jace.16903.
[7] F. Kern, H. Reveron, J. Chevalier, R. Gadow, Mechanical behaviour of extremely tough TZP bioceramics, J. Mech. Behav. Biomed. Mater. 90 (2019) 395–403, https://doi.org/10.1016/j.jmbbm.2018.11.001.
[8] N. Yildirim, F. Kern, Mechanical properties and ageing resistance of slip cast and pressurelessly sintered ZTA - the influence of composition and heat treatment conditions, Sci. Sinter. 51 (2019) 243–256, https://doi.org/10.2298/SOS1903243Y.
[9] V. Naglieri, P. Palmero, L. Montanaro, J. Chevalier, Elaboration of alumina-zirconia composites: role of the zirconia content on the microstructure and mechanical properties, Materials 6 (2013) 2090–2102, https://doi.org/10.3390/ma6052090.
[10] A.H. Heuer, N. Claussen, W.M. Kriven, M. Rühle, Stability of tetragonal ZrO2 particles in ceramic matrices, J. Am. Ceram. Soc. 65 (1982) 642–650.
[11] F.F. Lange, Transformation toughening - Part 4 Fabrication, fracture toughness and strength of Al2O3-ZrO2 composites, J. Mater. Sci. 17 (1982) 247–254.
[12] M. Suzuki, H. Nagasawa, Mollusk shell structures and their formation mechanism, Can. J. Zool. 91 (2013) 349–366, https://doi.org/10.1139/cjz-2012-0333.
[13] G.L. Messing, S. Poterala, Y. Chang, T. Frueh, E.R. Kupp, B.H. Watson III, R. L. Walton, M.J. Brova, A.-K. Hofer, R. Bermejo, R.J. Meyer Jr, Texture-engineered ceramics - property enhancements through crystallographic tailoring, J. Mater. Res. 32 (2017) 3219–3241.
[14] S. Deville, E. Saiz, R.K. Nalla, A.P. Tomsia, Freezing as a path to build complex composites, Science 311 (2006) 515–518.
[15] F. Bouville, Strong and tough nacre-like aluminas: process-structure-performance relationships and position within the nacre-inspired composite landscape, J. Mater. Res. 35 (2020) 1076–1094.
[16] M.M. Seabaugh, I.H. Kerscht, G.L. Messing, Texture development by templated grain growth in liquid-phase-sintered α-alumina, J. Am. Ceram. Soc. 80 (1997) 1181–1188.

[17] M.M. Seabaugh, G.L. Messing, M.D. Vaudin, Texture development and mircostructure evolution in liquid-phase-sintered alumina ceramics prepared by templated grain growth, J. Am. Ceram. Soc. 83 (2000) 3109–3116.
[18] Y. Chang, S. Poterala, D. Yener, G.L. Messing, Fabrication of highly textured fine-grained alumina by templated grain growth of nanoscale precursors, J. Am. Ceram. Soc. 96 (2013) 1390–1397.
[19] R.J. Pavlacka, G.L. Messing, Processing and mechanical response of highly textured Al2O3, J. Eur. Ceram. Soc. 30 (2010) 2917–2925, https://doi.org/10.1016/j.jeurceramsoc.2010.02.009.
[20] A.-K. Hofer, R. Walton, O. Ševeček, G.L. Messing, R. Bermejo, Design of damage tolerant and crack-free layered ceramics with textured microstructure, J. Eur. Ceram. Soc. 40 (2020) 427–435.
[21] A.-K. Hofer, I. Kraleva, R. Bermejo, Additive manufacturing of highly textured alumina ceramics, Open Ceram. 5 (2021), 100085, https://doi.org/10.1016/j.oceram.2021.100085.
[22] R.L. Walton, M.D. Vaudin, A.-K. Hofer, E.R. Kupp, R.J. Meyer, G.L. Messing, Tailoring particle alignment and grain orientation during tape casting and templated grain growth, J. Am. Ceram. Soc. 102 (2019) 2405–2414, https://doi.org/10.1111/jace.16144.
[23] F.K. Lotgering, Topotactical reactions with ferrimagnetic oxides having hexagonal crystal structures - I, J. Inorg. Nucl. Chem. 9 (1959) 113–123.
[24] M.D. Vaudin, M.W. Rupich, M. Jowett, G.N. Riley, J.F. Binert, A method for crytallographic texture investigations using standard x-ray equipment, J. Mater. Res. 13 (1998) 2910–2919.
[25] W.A. Dollase, Correction of intensities for preferred orientation in powder diffractometry: application of the march model, J. Appl. Crystallogr. 19 (1986) 267–272.
[26] M.M. Seabaugh, M.D. Vaudin, J.P. Cline, G.L. Messing, Comparison of texture analysis techniques for highly oriented α-Al2O3, J. Am. Ceram. Soc. 83 (2000) 2049–2054.
[27] EN 623-2, Advanced Ceramics, Monolithic Ceramics, General and textural properties, Part 2: Determination of density and porosity, 1994.
[28] ENV 843-4, Advanced technical ceramics, Monotlihic ceramics, Mechanical properties at room temperature, Part 4: Vickers, Knoop and Rockwell superficial hardness tests, 1994.
[29] ISO/FDIS 23146, Fine ceramics (advanced ceramics, advanced technical ceramics) - Test methods for fracture toughness of monolithic ceramics - Single-edge V-notch beam (SEVNB) method, 2008.
[30] Y. Chang, S. Poterala, D. Yener, G.L. Messing, Fabrication of highly textured fine-grained α-alumina by templated grain growth of nanoscale precursors, J. Am. Ceram. Soc. 96 (2013) 1390–1397, https://doi.org/10.1111/jace.12286.
[31] J. Chevalier, S. Deville, G. Fantozzi, J.F. Bartolome, C. Pecharroman, J.S. Moya, L. A. Diaz, R. Torrecillas, Nanostructured ceramic oxides with a slow crack growth resistance close to covalent materials, Nano Lett. 5 (2005) 1297–1307.
[32] K. Biotteau-Deheuvels, L. Zych, L. Gremillard, J. Chevalier, Effects of Ca-, Mg- and Si-doping on microstructures of alumina–zirconia composites, J. Eur. Ceram. Soc. 32 (2012) 2711–2721, https://doi.org/10.1016/j.jeurceramsoc.2011.11.011.
[33] D.-K. Kim, W.M. Kriven, Processing and characterization of multiphase ceramic composites part II: triplex composites with a wide sintering temperature range, J. Am. Ceram. Soc. 91 (2008) 793–798, https://doi.org/10.1111/j.1551-2916.2008.02262.x.
[34] A. Krell, P. Blank, Grain size dependence of hardness in dense submicrometer alumina, J. Am. Ceram. Soc. 78 (1995) 1118–1120.
[35] R.W. Rice, C. Cm. Wu, F. Borchelt, Hardness–grain-size relations in ceramics, J. Am. Ceram. Soc. 77 (1994) 2539–2553.
[36] Y.V. Milman, S.I. Chungunova, I.V. Goncharova, T. Chudoba, W. Lojkowski, E. Gooch, Temperature dependance of hardness in silicon-carbide ceramics with different porosity, Int. J. Refract. Met. Hard Mater. 17 (1999) 361–368.
[37] J. Schlacher, A. Jabr, A.-K. Hofer, R. Bermejo, Contact damage tolerance of alumina-based layered ceramics with tailored microstructures, J. Am. Ceram. Soc. 6 (2022) 4387–4399, https://doi.org/10.1111/jace.18389.
[38] G. Gregori, W. Burger, V. Sergo, Piezo-spectroscopic analysis of the resiual stresses in zirconia-toughened alumina ceramics: the influence of the tetragonal-to-monoclinic transformation, Mater. Sci. Eng. A271 (1999) 401–406.
[39] M.A. Gafur, Md.S.R. Sarker, Md.Z. Alam, M.R. Qadir, Effect of 3 mol% yttria stabilized zirconia addition on structural and mechanical properties of alumina-zirconia composites, Mater. Sci. Appl. 8 (2017) 584–602, https://doi.org/10.4236/msa.2017.87041.
[40] R. Langlois, K.J. Konsztowicz, Toughening in zirconia-toughened alumina composites with non-transforming zirconia, J. Mater. Sci. Lett. 11 (1992) 1454–1456.
[41] H. Salmang, H. Scholze, Keramik, Rainer Telle, Springer-Verlag, Berlin Heidelberg, 2007.

Publication B

Additive manufacturing of highly textured alumina ceramics

Anna-Katharina Hofer, Irina Kraleva, Raúl Bermejo

Department of Materials Science, Montanuniversitaet Leoben, Franz Josef-Strasse 18, A-8700 Leoben, Austria

Open Ceramics 5 (2021) 100085.

doi: https://doi.org/10.1016/j.oceram.2021.100085

Open Ceramics 5 (2021) 100085

Contents lists available at ScienceDirect

Open Ceramics

journal homepage: www.editorialmanager.com/oceram

Additive manufacturing of highly textured alumina ceramics

Anna-Katharina Hofer *, Irina Kraleva, Raul Bermejo

Department of Materials Science, Montanuniversität Leoben, Franz Josef Strasse 18, A-8700, Leoben, Austria

ARTICLE INFO

Keywords:
LCM-technology
3D-printing
Textured microstructure
Textured alumina
3D-printed ceramics
Additive manufacturing

ABSTRACT

In this work we demonstrate the feasibility of fabricating textured alumina employing a lithography-based ceramic manufacturing process. The combination of vat rotation and platform immersion contributes to the alignment of alumina templates during printing. Templated Grain Growth during sintering provides a high degree of texture (Lotgering Factor ~ 0.80) with relatively low porosity (approx. 7%). A comparable characteristic biaxial strength of 640 MPa and 570 MPa was measured for textured and equiaxed alumina samples, opening the path for 3D printing textured ceramics of complex architectures for structural and functional applications.

1. Introduction

An approach to enhance the structural and/or functional properties of polycrystalline ceramics is to "texture" the microstructure, with grains showing a preferential orientation [1]. Inspiration have been sought in natural systems such as nacre [2], which resembles a "brick-mortar" architecture, where inorganic elongated particles (templates) are stacked in a layered fashion. Nacre-like alumina has been fabricated through different processing routes, using Templated Grain Growth (TGG) as a strategy to obtain high degree "morphological" and "crystallographic" texture, as a result of controlled grain growth in [0001] direction [3,4]. Due to the tailored orientation, anisotropic properties of the hexagonal crystal structure may be exploited. For instance, α-Al_2O_3 single crystals exhibit higher Vicker's hardness perpendicular to the crystallographic basal plane, compared to polycrystalline alumina, i.e. ~23 GPa versus ~19 GPa [5]. Furthermore, mechanical behaviour can be improved through crack deflection mechanisms, associated with the preferred [0001] orientation of the grains with respect to the applied load [6].

Textured microstructures have been successfully fabricated through various methods: (i) tape casting, (ii) ice templating or (iii) magnetic alignment [1,3,4,6]. For tape casting, texture quality is based on the alignment of the templates already during the casting process [6,7]. A strong limitation of these techniques is that rather simple geometries may be fabricated, e.g. discs, bars or plates. In this regard, additive manufacturing techniques have proved successful in fabricating 3D monolithic structural and functional ceramics with complex geometries. The control of fibre or particle orientation in polymers or ceramic matrix composites has already been investigated and published applying various additive manufacturing techniques [8–12]. However, only few research works focus on texturing ceramics using 3D printing processes [13,14]. In this work, we explore the feasibility of employing the lithography-based ceramic manufacturing (LCM) process to fabricate highly horizontally textured α-alumina ceramics. Density, microstructure, the effect of sintering time on grain growth and mechanical biaxial strength are assessed in textured alumina (TA) and compared to equiaxed alumina (EA) samples.

2. Materials and methods

A commercially available α-alumina slurry (LithaLox HP500, Lithoz GmbH, Vienna, Austria), containing approx. 50 vol% polymeric binder, was employed as reference material. To fabricate the TA samples, the commercial slurry was modified by adding 5 vol% of α-alumina templates (Rona Flair® White Sapphire, EMD Performance Materials Corp., Darmstadt, Germany) with a high aspect ratio (thickness ~0.1 μm, diameter 5–16 μm[1]). In order to enhance TGG during sintering, CaO (i.F. of $Ca(NO_3)_2{*}4H_2O$, ThermoFischer, Kandel, Germany) as well as SiO_2 (i.F. of $C_8H_{20}O_4Si$, ThermoFischer, Karlsruhe, Germany) were added in a 1 : 1 ratio. The added amount of dopants was 0.25 wt% of the total ceramic content. The ratio of templates as well as the content of sintering additives were chosen as recommended in the literature for a high degree of texture in alumina ceramics of the same kind employing the Tape Casting process [15]. The templates as well as the dopants were mixed with the commercial α-alumina slurry (using a magnetic stirrer) for 24 h

* Corresponding author.
E-mail address: anna-katharina.hofer@unileoben.ac.at (A.-K. Hofer).

[1] Values as reported by the supplier company.

https://doi.org/10.1016/j.oceram.2021.100085
Received 30 December 2020; Received in revised form 24 February 2021; Accepted 3 March 2021
Available online 5 March 2021

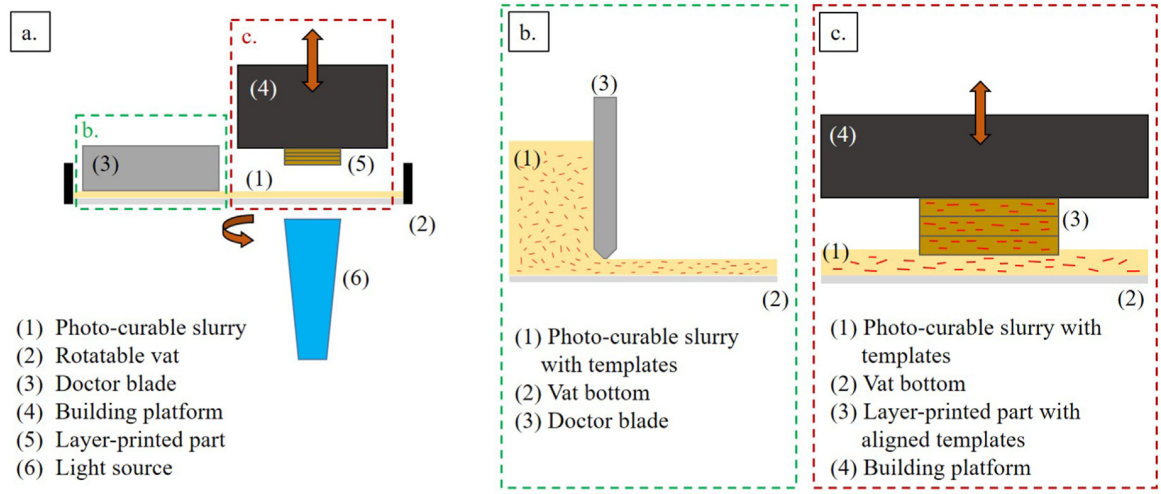

Fig. 1. Schematic of **a)** the LCM-technology, **b)** templates alignment through slurry distribution, **c)** templates alignment in the printed layers.

at 25 °C, with 6 wt% additional dispersant related to the amount of templates.

A 3D printer (model CeraFab 7500, Lithoz GmbH, Vienna, Austria) was employed to fabricate the parts "layer-by-layer" (Fig. 1a). A photo-curable ceramic slurry (1) was filled into a transparent rotatable vat (2) where a new film of slurry is distributed by a blade (3). The slurry height was set to 100 µm, using a rotation speed of 100°/s for slurry distribution. Afterwards, the building platform (4) was immersed into the slurry bed, leaving a gap, of few microns (~25 µm), between vat bottom and building platform (or last printed layer (5)). The corresponding layer was polymerized, with an exposure time of 1.5 s, by the light source (6) from beneath the vat. This process was repeated for each layer until the final height of the part (total number of layers) was reached [16–18].

The alignment of templates (Fig. 1b (1)) was enhanced through the shear stresses generated in the gap between the vat bottom (2) and the doctor blade (3), during rotation of the vat. This approach has been thoroughly investigated and successfully employed with the Tape Casting process [7,19,20]. Additionally, it may be expected that through the immersion of the building platform into the slurry bed the in-plane distribution of templates for each layer might be enhanced (Fig. 1c). In this regard, a preliminary study was carried out to assess the influence of the individual layer thickness on the texture quality. Three samples printed with different layer thicknesses, i.e. (i) 10 µm, (ii) 15 µm and (iii) 25 µm were fabricated and analysed. Since no significant difference in texture between samples could be observed, the thickness for each printed layer was set to 25 µm for further investigation. Cylindrical samples were manufactured with final dimensions in the sintered state of ~10 mm diameter and ~1 mm height.

The 3D-printed samples were thermal treated up to 430 °C to burn-out the polymer. Sintering was done at 1600 °C, with a heating rate of 5 °C/min and two different dwelling times of 2 h and 6 h were used, for both EA and TA samples, to investigate the effect of dwelling time on texture.

The relative density was determined with the Archimedes method, measuring 3 samples of each material, considering a theoretical density of $\rho_{th} = 3.985$ g/cm^3 for α-Al_2O_3 [21]. Grain size distribution was evaluated with the point-counting method on SEM images (JEOL JCM-6000Plus, NeoscopeTM, JEOL Ltd., Tokyo, Japan). For the equiaxed

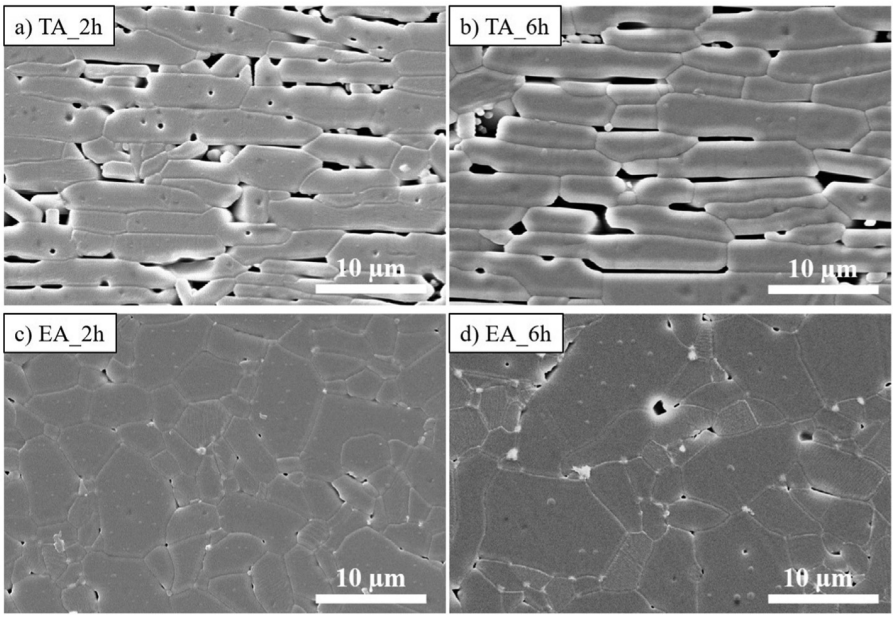

Fig. 2. SEM images of textured alumina (TA) with **a)** 2 h and **b)** 6 h dwell time, and equiaxed alumina (EA) with **c)** 2 h and **d)** 6 h dwell time, taken as reference.

Table 1
Density, microstructural features and XRD parameters in TA and EA samples.

Sample	Relative density [%]	Average grain size d_{50} [μm]		Mean aspect ratio [−]	LF [−]	FWHM [°]
		Horizontal	Vertical			
TA_2h	92.87 ± 0.05	6.4 ± 4.0	2.5 ± 0.9	2.5	0.79	6.5
TA_6h	93.05 ± 0.07	7.6 ± 4.6	2.7 ± 1.0	2.9	0.83	6.3
EA_2h	99.74 ± 0.70	3.6 ± 1.9		–	–	–
EA_6h	99.26 ± 0.04	5.3 ± 2.8		–	–	–

microstructure ~1000 grains were measured in random directions, whereas for the textured microstructure ~500 grains each were measured in both horizontal and vertical directions, respectively.

The degree of texture was determined using (i) the Lotgering Factor (LF) and (ii) the rocking curve (RC) method by XRD. Phase analysis and rocking curve measurements on Al_2O_3 (00.12) reflections were performed using a 5-axis diffractometer (SmartLab, Rigaku, Tokyo, Japan).

LF gives information about the degree of orientation in textured microstructures (LF = 1 corresponds to perfect orientation). The [000l] peaks of the equiaxed and textured Alumina XRD-pattern were compared [1,22]:

$$LF = \frac{P_{(00l)} - P_0}{1 - P_0} \quad (1)$$

where

$$P_{(00l)} = \frac{\sum I_{(00l)}}{\sum I_{(hkl)}} \text{ for textured and}$$

$$P_0 = \frac{\sum I_{0(00l)}}{\sum I_{0(hkl)}} \text{ for equiaxed}$$

RC describes the quality of alignment and fraction of textured grains, and was fit with the March-Dollase equation according to Refs. [1,3,6,7,23]:

$$F(f, r, \theta) = f\left(r^2 cos^2\theta + \frac{sin^2\theta}{r}\right)^{-\frac{3}{2}} + (1 - f) \quad (2)$$

where θ is the angle between the texture axis and the scattering factor, f is the volume fraction of oriented material, and r the degree of orientation of oriented grains. For a perfect grain orientation (i.e. $r = 0$ and $f = 1$), the Full-width-of-half-maximum (FWHM) from the RC should be low.

Bending strength was evaluated for textured and equiaxed alumina samples, sintered for 6 h, using the Ball-on-Three-Ball (B3B) testing method [24,25]. For the case of TA specimens, the load was applied perpendicular to the (0001) basal plane. For statistical significance of the strength data, 30 specimens of each material were tested using a universal testing machine with a 10 kN load cell (Zwick Z010, Zwick GmbH&Co, Ulm, Germany). The testing was performed at ambient conditions (~24 °C and ~27% relative humidity) applying a preload of 20 N and a displacement rate of 1 mm/min until fracture. The measured data were evaluated using Weibull statistics to determine the characteristic strength (σ_0) and the Weibull modulus (m) applying the Maximum-Likelihood-method [26–28]. Fractography was carried out on broken specimens to identify the fracture origin and location of critical flaws in both textured and equiaxed samples. Selected fracture surfaces were sputtered with gold using an Agrar Sputter Coater and investigated using a SEM (JEOL JCM-6000Plus, NeoscopeTM, JEOL Ltd., Tokyo, Japan).

3. Results and discussion

Fig. 2 shows microstructures of the cross-section of a TA and EA sample from the side view, sintered with 2 h (a, c) and 6 h (b, d) dwell time, respectively. A high degree of (morphological) texture is achieved in the TA sample, compared to the equiaxed microstructure in the EA sample. Slightly larger grain size results for both TA and EA samples when sintered with 6 h dwell time. Higher porosity is apparent in TA compared to the rather isolated pores in EA. It is worth highlighting the presence of internal pores (i.e. inside the grains) in the TA microstructure (2 h), compared to the porosity encountered at grain boundaries and "triple points" in the TA microstructure (6 h), as well as in both 2h and 6h EA samples.

The relative density in the TA reached ~93%, compared to the ~99% achieved in the EA sample (Table 1). This finding agrees with the SEM observations in Fig. 2. The higher porosity in TA sample has been encountered in other textured alumina materials fabricated using conventional processing routes (e.g. tape casting), in some cases hindering texture [6,29]. In our case, no significant effect of the sintering time on density was found in either TA or EA samples. The grain size of the TA sample is slightly larger than that of the EA sample as a consequence of the TGG. No significant grain growth associated with longer dwell times was observed in either TA or EA materials (Table 1), the slightly increase being within the standard deviation of the grain size distribution. It is worth pointing out the aspect ratio found in TA samples, where the average grain size in horizontal direction was approx. 3 times larger than in vertical direction. The horizontal length of the measured textured grains ranged within ~2–10 μm and ~3–12 μm for the samples sintered

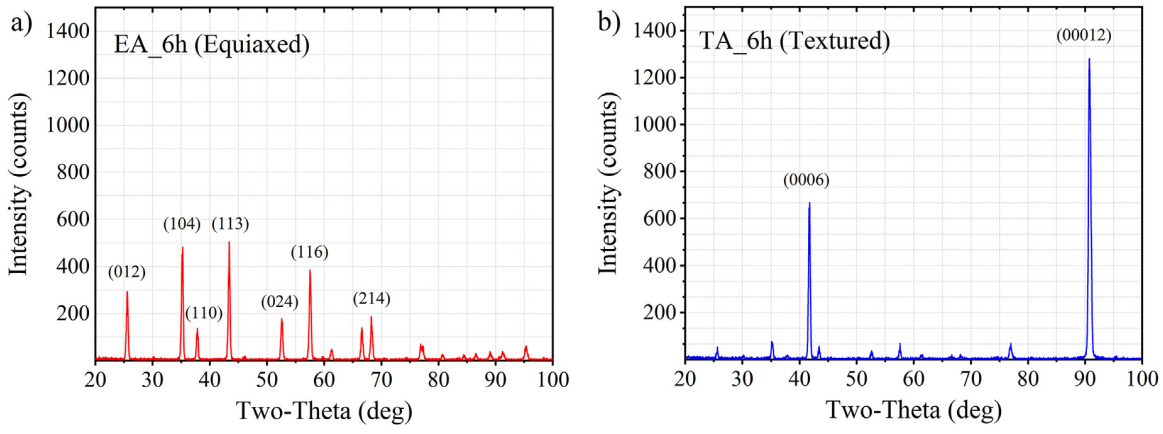

Fig. 3. XRD intensity counts versus 2-Theta angle for **a)** EA and **b)** TA 6 h samples.

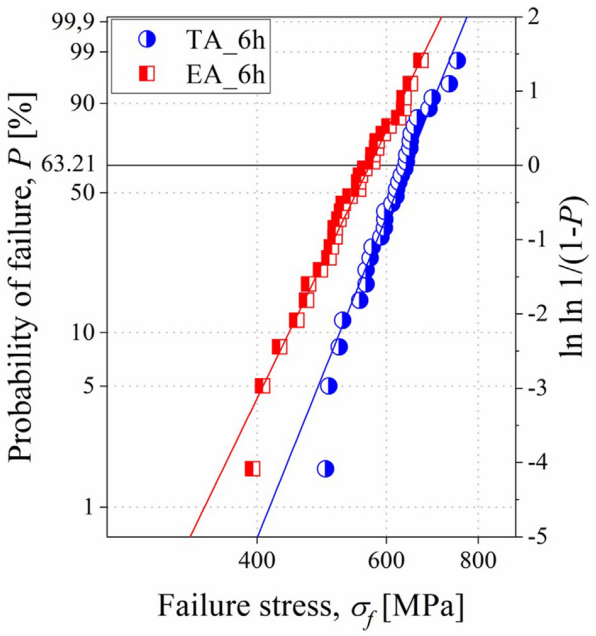

Fig. 4. Probability of failure versus failure stress for textured (TA) and equiaxed alumina (EA) samples sintered for 6 h.

for 2 h and 6 h, respectively. The average template size, measured from SEM images on approx. 250 powder particles, was ~8 ± 3 μm. The determined starting template size indicates no grain growth in horizontal direction, but significant templated grain growth in vertical direction.

Crystallographic texture was quantified comparing the XRD patterns of TA and EA samples (Table 1). Fig. 3 shows two representative patterns corresponding to an equiaxed (Fig. 3a) and a textured microstructure (Fig. 3b), sintered with 6 h dwell time.

For the textured microstructure both (00.6) and (00.12) peaks are clearly dominant, corresponding to the [0001] direction of the grains (vertical direction in Fig. 2). The LF calculated with Eq. (1) for 3D-printed TA sintered for 2 h and 6 h was 0.79 and 0.83, respectively.

To describe the "quality" of orientation of the textured microstructure, the measured rocking curves were evaluated in TA samples according to their FWHM and fitted with Eq. (2). A FWHM of ~6° could be reached for both TA samples. Representative, the *r*-value for TA sintered for 6 h was evaluated to be 0.17 with a covariance between 7.6×10^{-6} – 6.60×10^{-5} and the f-value of 0.64 with a covariance between 6.60×10^{-5} – 6.48×10^{-4}. To our knowledge, the lowest FWHM and *r*-value found in literature so far for textured alumina was 4.6° and 0.13 respectively [6].

Fig. 4 represents the strength distribution of TA and EA samples (sintered for 6 h) in a Weibull diagram. The probability of failure, *P*, is plotted versus the failure stress, σ_f. Both TA and EA samples follow a Weibull distribution. It is worth pointing out the slight bend shape observed in both distributions for lower failure stress values. This effect might be related to a maximum critical defect size in the sample, associated with the printing process (i.e. printing layer thickness). Further interpretation would require testing a larger sample population, which is out of the scope of this paper.

The characteristic strength σ_0 and the Weibull modulus *m* for both samples were evaluated using the Maximum-likelihood method in the framework of the Weibull statistics [26,27], following the EN-843-5 standards [28]. For the TA sample, $\sigma_0 = 640$ [620−661] and $m = 11$ [8−13], whereas for the EA sample $\sigma_0 = 570$ [549−592] and $m = 9$ [7−11]; the numbers in brackets represent the 90% confidence intervals. Interestingly, despite a relatively high porosity of about 7% in the TA sample, a comparable strength to the EA sample (with <1% porosity) was measured.

Fig. 5a and c illustrate fracture surfaces and corresponding fracture origins (b, d) after the B3B test in TA and EA specimens, respectively. By analysing the fracture surfaces of TA, it was observed that major defects leading to failure were pores, induced during the 3D-printing process. In comparison, for EA, mainly abnormally grown clustered grains acted as critical defects. All fracture origins were found at the surface set under tension during the B3B experiments.

The higher strength of TA in comparison to EA may be related to a higher fracture toughness in the former, as observed in other textured

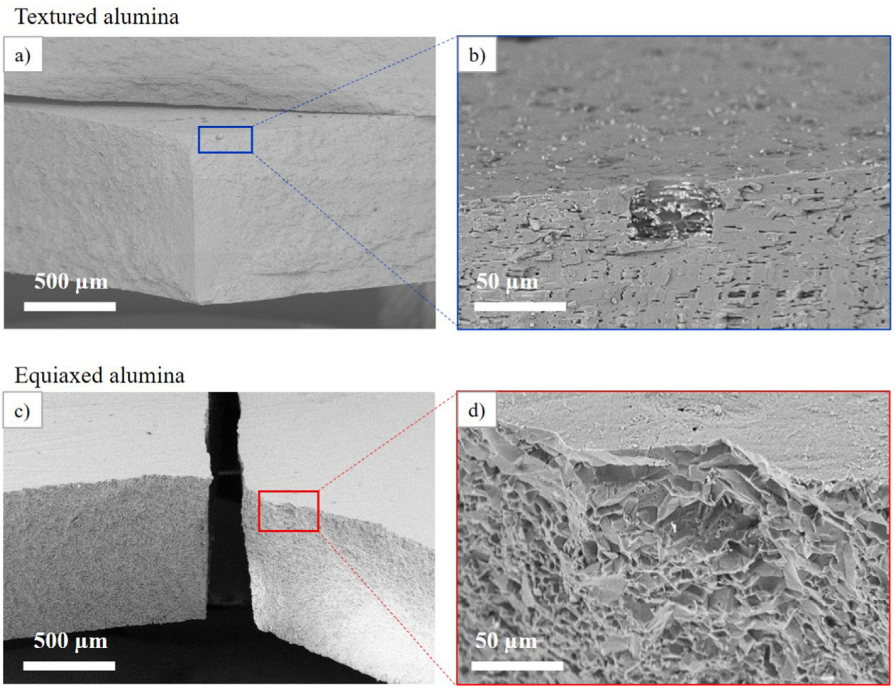

Fig. 5. Fracture surfaces and fracture origins of representative TA **(a,b)** and EA **(c,d)** specimens, respectively.

microstructures [30]. This increase in fracture toughness might be a result of crack deflection, bridging and pull-out mechanisms due to the tailored grain orientation in [0001] direction [1,31].

Future experiments will focus on controlling porosity in textured materials through variation of printing parameters and investigate its influence on mechanical properties.

4. Conclusion

3D-printed highly textured alumina was fabricated combining the LCM technology and templated grain growth during sintering. Relative densities of >93% were reached for textured alumina, compared to 99% on equiaxed reference alumina material. A high LF of ~0.80 and very low FWHM of ~6° indicate the high degree and high quality of texture achieved with 3D-printing. A characteristic strength of 640 MPa was measured for textured alumina, comparable to 570 MPa obtained in equiaxed alumina. This study opens new possibilities in the fabrication of complex 3D ceramic geometries with horizontally aligned textured microstructure, aiming to tailor structural and/or functional properties.

Declaration of competing interest

The authors declare that they have no known competing financial interests or personal relationships that could have appeared to influence the work reported in this paper.

Acknowledgement

Funding for this research was provided by the European Research Council (ERC) excellent science grant “CERATEXT” through the Horizon 2020 program under contract 817615.

References

[1] G.L. Messing, S. Poterala, Y. Chang, T. Frueh, E.R. Kupp, B.H. Watson, R.L. Walton, M.J. Brova, A.-K. Hofer, R. Bermejo, R.J. Meyer, Texture-engineered ceramics—property enhancements through crystallographic tailoring, J. Mater. Res. 32 (2017) 3219–3241, https://doi.org/10.1111/j.1151-2916.1997.tb02961.x.

[2] S. Deville, E. Saiz, R.K. Nalla, A.P. Tomsia, Freezing as a path to build complex composites, Science 311 (2006) 515–518, https://doi.org/10.1126/science.1120937.

[3] Matthew M. Seabaugh, Ingrid H. Kerscht, Gary L. Messing, Texture development by templated grain growth in liquid-phase-sintered α-alumina, J. Am. Ceram. Soc. (1997) 1181–1188.

[4] F. Bouville, Strong and tough nacre-like aluminas: process–structure–performance relationships and position within the nacre-inspired composite landscape, J. Mater. Res. 35 (2020) 1076–1094, https://doi.org/10.1557/jmr.2019.418.

[5] I.J. McColm (Ed.), Ceramic Hardness, first ed., Springer, New York, 1990.

[6] R.J. Pavlacka, G.L. Messing, Processing and mechanical response of highly textured Al2O3, J. Eur. Ceram. Soc. 30 (2010) 2917–2925, https://doi.org/10.1016/j.jeurceramsoc.2010.02.009.

[7] R.L. Walton, M.D. Vaudin, A.-K. Hofer, E. Kupp, R.J. Meyer, G.L. Messing, Tailoring particle alignment and grain orientation during tape casting and templated grain growth, J. Am. Ceram. Soc. (2018), https://doi.org/10.1111/jace.16144.

[8] Z. Lu, J. Cao, Z. Song, D. Li, B. Lu, Research progress of ceramic matrix composite parts based on additive manufacturing technology, Virtual Phys. Prototyp. 14 (2019) 333–348, https://doi.org/10.1080/17452759.2019.1607759.

[9] L.R. Holmes, J.C. Riddick, Research summary of an additive manufacturing technology for the fabrication of 3D composites with tailored internal structure, J. Occup. Med. 66 (2014) 270–274, https://doi.org/10.1007/s11837-013-0828-4.

[10] H. Zhang, Y. Yang, K. Hu, B. Liu, M. Liu, Z. Huang, Stereolithography-based additive manufacturing of lightweight and high-strength Cf/SiC ceramics, Additive Manufacturing 34 (2020) 101199, https://doi.org/10.1016/j.addma.2020.101199.

[11] D.E. Yunus, R. He, W. Shi, O. Kaya, Y. Liu, Short fiber reinforced 3d printed ceramic composite with shear induced alignment, Ceram. Int. 43 (2017) 11766–11772, https://doi.org/10.1016/j.ceramint.2017.06.012.

[12] H. Luo, Y. Tan, F. Zhang, J. Zhang, Y. Tu, K. Cui, Selectively enhanced 3D printing process and performance analysis of continuous carbon fiber composite material, Materials 12 (2019), https://doi.org/10.3390/ma12213529.

[13] E. Feilden, C. Ferraro, Q. Zhang, E. García-Tuñón, E. D'Elia, F. Giuliani, L. Vandeperre, E. Saiz, 3D printing bioinspired ceramic composites, Sci. Rep. 7 (2017) 13759, https://doi.org/10.1038/s41598-017-14236-9.

[14] R.L. Walton, M.J. Brova, B.H. Watson, E.R. Kupp, M.A. Fanton, R.J. Meyer, G.L. Messing, Direct writing of textured ceramics using anisotropic nozzles, J. Eur. Ceram. Soc. 41 (2021) 1945–1953, https://doi.org/10.1016/j.jeurceramsoc.2020.10.021.

[15] Y. Chang, R. Bermejo, G.L. Messing, Improved fracture behavior of alumina microstructural composites with highly textured compressive layers, J. Am. Ceram. Soc. 97 (2014) 3643–3651, https://doi.org/10.1111/jace.13168.

[16] M. Schwentenwein, J. Homa, Additive manufacturing of dense alumina ceramics, Int. J. Appl. Ceram. Technol. 12 (2015) 1–7, https://doi.org/10.1111/ijac.12319.

[17] A. de Blas Romero, M. Pfaffinger, G. Mitteramskogler, M. Schwentenwein, C. Jellinek, J. Homa, A. Díaz Lantada, J. Stampfl, Lithography-based additive manufacture of ceramic biodevices with design-controlled surface topographies, Int. J. Adv. Manuf. Technol. 88 (2017) 1547–1555, https://doi.org/10.1007/s00170-016-8856-1.

[18] A.D. Lantada, A. de Blas Romero, M. Schwentenwein, C. Jellinek, J. Homa, Lithography-based ceramic manufacture (LCM) of auxetic structures: present capabilities and challenges, Smart Mater. Struct. 25 (2016) 54015, https://doi.org/10.1088/0964-1726/25/5/054015.

[19] H.J. Kim, M.J.M. Krane, K.P. Trumble, K.J. Bowman, Analytical fluid flow models for tape casting, 0, J. Am. Ceram. Soc. (2006), https://doi.org/10.1111/j.1551-2916.2006.01163.x, 060623005134007-???.

[20] A. Wonisch, P. Polfer, T. Kraft, A. Dellert, A. Heunisch, A. Roosen, A comprehensive simulation scheme for tape casting: from flow behavior to anisotropy development, J. Am. Ceram. Soc. 94 (2011) 2053–2060, https://doi.org/10.1111/j.1551-2916.2010.04358.x.

[21] EN 623-2, Advanced Technical Ceramics – Monolithic Ceramics – General and Textural Properties – Part 2: Determination of Density and Porosity, 1993.

[22] F.K. Lotgering, Topotactical Reactions with ferrimagnetic Oxides having hexagonal crystal structures - I, J. Inorg. Nucl. Chem. (1959) 113–123.

[23] Y. Chang, S. Poterala, D. Yener, G.L. Messing, Fabrication of highly textured fine-grained α-alumina by templated grain growth of nanoscale precursors, J. Am. Ceram. Soc. 96 (2013) 1390–1397, https://doi.org/10.1111/jace.12286.

[24] A. Börger, P. Supancic, R. Danzer, The ball on three balls test for strength testing of brittle discs: stress distribution in the disc, J. Eur. Ceram. Soc. (2002) 1425–1436.

[25] A. Börger, P. Supancic, R. Danzer, The ball on three balls test for strength testing of brittle discs: Part II: analysis of possible errors in the strength determination, J. Eur. Ceram. Soc. 24 (2004) 2917–2928, https://doi.org/10.1016/j.jeurceramsoc.2003.10.035.

[26] W. Weibull, A Statistical Theory of the Strength of Materials, fifteenthfirst ed., Generalstabens litografiska anstalts förlag, Stockholm, 1939.

[27] W. Weibull, A statistical distribution function of wide applicability, J. Appl. Mech. (1951) 293–297.

[28] EN-843-5, Advanced Technical Ceramics - Monolithic Ceramics - Mechanical Tests at Room Temperature - Part 5: Statistical Analysis, 1997.

[29] M. Zhang, Y. Chang, R. Bermejo, G. Jiang, Y. Sun, J. Wu, B. Yang, W. Cao, Improved fracture behavior and mechanical properties of alumina textured ceramics, Mater. Lett. 221 (2018) 252–255, https://doi.org/10.1016/j.matlet.2018.03.123.

[30] A.-K. Hofer, R. Walton, O. Ševeček, G.L. Messing, R. Bermejo, Design of damage tolerant and crack-free layered ceramics with textured microstructure, J. Eur. Ceram. Soc. 40 (2020) 427–435, https://doi.org/10.1016/j.jeurceramsoc.2019.09.004.

[31] P.W. Hall, J. St Swinnea, D. Kovar, Fracture resistance of highly textured alumina, J. Am. Ceram. Soc. (2001) 1514–1520.

Publication C

Highly textured 3D-printed translucent alumina

Vojtech Nečina[1,†], Anna-Katharina Hofer[2,†], Raúl Bermejo[2], Willi Pabst[1]

[1]Department of Glass and Ceramics, University of Chemistry and Technology, Prague (UCT Prague) Technická 5, 166 28 Prague 6, Czech Republic

[2]Department of Materials Science, Montanuniversitaet Leoben, Franz Josef-Strasse 18, A-8700 Leoben, Austria

[†]Authors contributed equally to this work

(Submitted for publication)

Highly textured 3D-printed translucent alumina

Vojtěch Nečina[1,*,†], Anna-Katharina Hofer[2,†], Raul Bermejo[2], Willi Pabst[1]

[1]*Department of Glass and Ceramics, University of Chemistry and Technology, Prague (UCT Prague) Technická 5, 166 28 Prague 6, Czech Republic*

[2]*Department of Materials Science, Montanuniversität Leoben, Franz Josef-Strasse 18, A-8700, Leoben, Austria*

**Corresponding author's email: necinav@vscht.cz*

†Authors contributed equally to this work

Graphical abstract

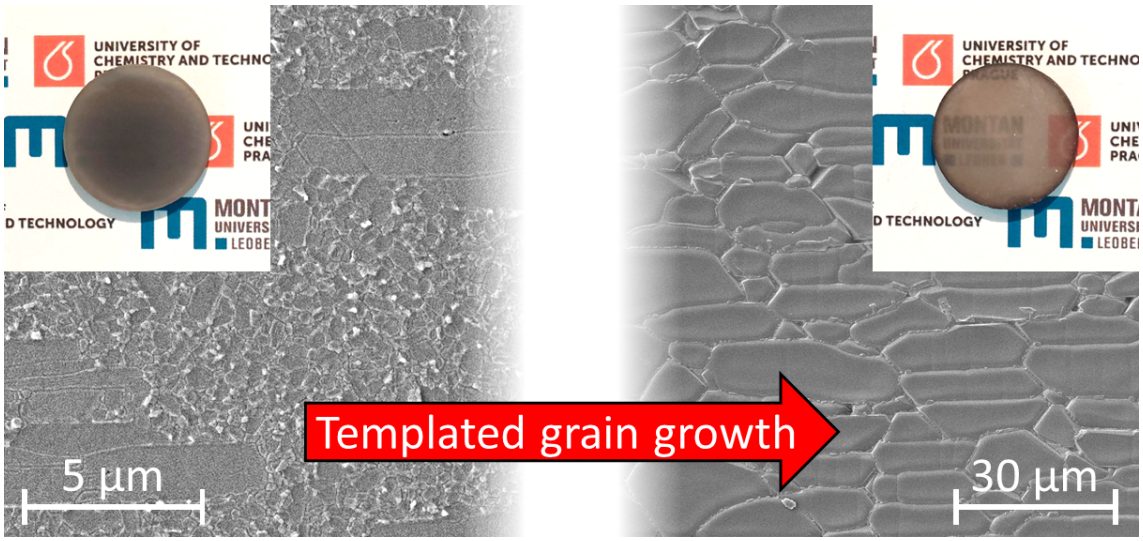

Abstract

Templated grain growth is a promising method for the fabrication of translucent alumina ceramics and a possible way to circumvent light scattering due to birefringence. In the present paper the effect of temperature, heating rate and dwell time on grain size, orientation, hardness and in-line transmittance is investigated on 3D-printed textured alumina. The samples were prepared by lithography-based ceramic manufacturing (LCM) of suspensions with fine-grained alumina, seeded by high aspect ratio templates and sintered by spark plasma sintering (SPS). A fully developed textured microstructure was achieved at 1600 °C for 1 h, whereas sufficient in-line transmittance of 54.6 % at 550 nm was achieved at 1700 °C for 3 h, albeit at the cost of considerable grain growth and loss of microstructural texturing.

Keywords: *transparent alumina, stereolithographic 3D-printing, spark plasma sintering, templated grain growth, textured alumina*

Introduction

Alumina is a material of interest for multiple applications across various fields, one of them being transparent armor, where it is used due to its exceptional hardness, high thermal resistance and excellent transmittance in the VIS and near-IR region[1, 2]. For transparent alumina, the ultimate goal is to bypass the negative effects caused by birefringence, which inevitably leads to the loss of resolution with increasing distance of the observed object (transparency). In polycrystalline materials, grains are typically randomly oriented. Regarding materials based on crystallites with cubic and thus optically isotropic crystal structures, e.g. $MgAl_2O_4$ and $Y_3Al_5O_{12}$, scattering due to birefringence is not an issue. However, in alumina, which shows a non-cubic, i.e. optically anisotropic crystal structure, every single grain boundary – even if clean (impurity-free) – is a potential source of scattering. Although the contribution to scattering by a single grain boundary may be negligible (when the birefringence is small), the multiplication over a polycrystalline bulk may result in opaque appearance of the material[3-5].

To achieve high transmittance in alumina there are two different approaches: (i) Tailoring the microstructure with a grain size smaller than the wavelength of light (< 300 nm)[3, 6-8] or (ii) orientation and exaggerated growth of the individual grains to reduce birefringence[9-15]. Besides, both of these approaches have to fulfill the common requirements for transparent ceramics, i.e., complete densification and phase purity.

In the first approach, the relevant wavelength of light is no longer able to distinguish differently oriented grains. The processing of nanocrystalline ceramics requires precise green body preparation using nano-sized powders, with either subsequent pressure-less sintering followed by hot isostatic pressing (HIP) or using high pressure (~600 MPa) to suppress grain growth considerably as reported by Ratzker *et al.* [16, 17]. It has been shown that both sintering routes resulted in highly transparent bodies[6, 7, 18].

In the second approach, the aim is to control grain orientation in order to reduce the refractive index jumps across the grain boundaries and thus the scattering due to birefringence (in the ideal case, for perfectly aligned grains, no scattering due to birefringence occurs). Increasing the grain size can be an additional factor that may help to improve transmittance by reducing the number of grain boundaries. In particular, grain orientation can be achieved through high-strength magnetic fields or through the flow-induced alignment of high aspect ratio templates in the green state. Established processes are for example magnetically-assisted slip casting (MASC), tape casting and more recently 3D-printing. The alumina templates are introduced and oriented in the matrix of fine particles prior to sintering[9, 12-15]. During sintering templated

grain growth (TGG) occurs, where the templates grow under the expense of the surrounding fine particles, resulting in textured microstructures with oriented grains. In the case of alumina the crystallographic c-axis is oriented parallel to the [001] direction[10, 11, 19-23]. TGG performed in a conventional pressure-less sintering furnace impedes pore closure due to the anisotropic grain growth, resulting in relative densities of ~ 95 % and an opaque appearance.

The aim of this study is to achieve highly transparent textured alumina microstructures through TGG by reducing the porosity with applying pressure onto the sample via spark plasma sintering (SPS). Prior to sintering, the templates are aligned through lithography-based ceramic manufacturing (LCM). The effect of different sintering parameters, such as heating rate, sintering temperature and dwell time, on porosity, texture degree and transmittance are investigated.

Experimental

The alignment of templates in green bodies was achieved through the additive manufacturing technology of lithography-based ceramic manufacturing (LCM), as described in detail elsewhere[24]. To achieve textured microstructures, a commercially available photopolymeric high-purity alumina suspension (LithaLox HP500, Lithoz, Austria) was modified by the addition of 2.5 vol% of high aspect ratio (~0.1 µm in thickness, 5-16 µm in diameter) α-alumina templates (Rona Flair® White Sapphire, EMD Performance Materials Corp., Germany) as well as 0.25 wt% sintering additives (related to the solid content) of CaO (i.F. of $Ca(NO_3)_2 \cdot 4H_2O$, ThermoFischer, Germany) and SiO_2 (i.F. of $C_8H_{20}O_4Si$, ThermoFischer, Germany) in a 1:1 ratio. Disc-shaped samples with 20 mm diameter and 4 mm thickness were 3D-printed with the LCM technology (model CeraFab 8500, Lithoz, Austria). After printing, the samples consisted of a polymeric network embedding ceramic particles. The removal of the polymer was done by thermal post processing with multiple dwell times at different temperatures, with a final maximum temperature of 430 °C, lasting for 102 hours, followed by a pre-sintering step at 1100 °C for 1 hour. After pre-sintering the diameter of the samples was ~19.1 mm with a porosity of ~40 %.

The sintering was performed in a spark plasma sintering furnace (SPS, HP D 10-SD, FCT Systeme, Germany), where the pre-sintered sample was placed into a graphite die with an inner diameter of 20 mm (lined with graphite paper). The sintering started by heating up to 1000 °C at a rate of 100 °C/min and up to 1200 °C at 25 °C/min. Further heating was maintained at 5 °C/min up to the final temperature of 1400–1800 °C where a dwell time of 1 h was applied.

A pressure of 80 MPa was applied at 1200 °C within 5 min. Selected samples followed different regimes and are listed together with former regimes in Table 1.

The measurement of the in-line transmittance was performed directly on the sample with a spectrophotometer (UV-2450, Shimadzu, Japan) in the wavelength range of 0.2–0.8 µm, through a mask with a 5 mm hole. Prior, the samples were mirror-polished to a final thickness of ~1.8 mm. The porosity of the samples was determined by the Archimedes method with water as immersive medium. A scanning electron microscope (SEM, LYRA3, Tescan, Czech Republic) was used to investigate the cross-section, which was polished down to 1 µm and thermally etched at a temperature lower than the maximum sintering temperature by 100 °C.

Due to the anisometric nature of the microstructure, the mean chord length $\bar{L}$ (grain size) was determined in two mutually perpendicular directions. Therefore a ratio is reported as $\bar{L}_X/\bar{L}_Y$, where X is the direction perpendicular (horizontal) and Y parallel (vertical) to the applied pressure, respectively. The mean chord length in both directions was determined using the following equation

$$\bar{L} = \frac{1}{P_L}, \quad (1)$$

where P_L is the number of grain boundary intersections per probe length[25].

In one particular case, the microstructure was composed of a fine-grained matrix with embedded platelets of alumina. Smaller grains were isometric, so the mean chord length was determined only in one direction using equation (1). The microstructure as a whole (duplex microstructure with a bimodal size distribution) was treated as a two-phase system in this case, and the volume fraction ϕ of alumina platelets was determined using the point fraction (according to the Delesse-Rosiwal law). The mean chord length in both directions was determined by using the following equation

$$\bar{L} = \frac{2\phi}{2P_{iL} + P_{eL}}, \quad (2)$$

where P_{iL} is the number of internal (intraphase) grain boundary intersections per probe length and P_{eL} is the number of external (interphase) grain boundary intersections per probe length.

XRD analysis was performed to determine the Lotgering factor (LF), describing the degree of orientation in textured microstructures. X-ray diffractometer patterns (Brucker AXS D8 Advance DaVinci, Bruker, Billerica, USA) of all the SPS-sintered textured alumina samples as

well as one equiaxed alumina sample as reference and comparison were measured. LF was evaluated as follows[20, 26]

$$LF = \frac{P_{(00l)} - P_0}{1 - P_0}, \quad (3)$$

$$P_{(00l)} = \frac{\sum I_{(00l)}}{\sum I_{(hkl)}}, \quad (4)$$

$$P_0 = \frac{\sum I_{0(00l)}}{\sum I_{0(hkl)}}, \quad (5)$$

where $P_{(00l)}$ and P_0 are the intensity ratios for textured and equiaxed materials, respectively. $I_{(00l)}$ and I_0 are the intensities of characteristic (001) peaks, in the case of alumina (006) and (00 12) at 2θ-angles of 41.6 ° and 90.7 °, respectively. $I_{(hkl)}$ and $I_{0(hkl)}$ are the intensities in the XRD-pattern of all characteristic peaks for α-alumina.

Hardness was measured with a Vickers indenter (HV), applying a load of 1 kg[27]. The measurement was performed on the surface perpendicular to the (001) direction, making 10 indents per sample. Prior to testing the surface was mirror-polished down to 1 µm.

Results and discussion

Sintering parameters and measured properties (grain size, in-line transmittance, porosity, Lotgering factor and hardness) of the prepared samples are summarized in Table 1.

Table 1: Sintering parameters, microstructural, physical and optical properties of templated alumina samples.

Sample	T_{max}	Dwell time	Heating rate[a]	Grain size ($\bar{L}_X/\bar{L}_Y$)	In-line transmittance[b]	Porosity	LF	HV
	[°C]	[h]	[°C/min]	[µm]	[%]	[%]	[-]	[GPa]
A	1400	1	5	4.6/1.2[c]	11.6	0.9	0.36	21.0±0.6
B	1500	1	5	7.1/2.6	1.7	1.2	0.62	18.5±0.6
C	1600	1	5	10.4/3.2	2.5	0.7	0.65	19.2±0.6
D	1700	1	5	14.5/6.2	10.1	0.5	0.50	19.4±0.6
E	1800	1	5	155.4/102.6	44.8	0.6	0.63	19.3±0.8
F	1500	1	25	6.9/2.6	0.8	0.7	0.64	19.4±0.6
H	1700	1	25	13.9/5.3	4.5	0.6	0.57	19.7±0.6
G	1600	5	5	11.3/3.9	6.1	0.8	0.62	19.5±0.5
I	1700	3	5	90.3/43.8	54.6	0.5	0.67	18.0±1.0

a – starting from 1200 °C up to final temperature
b – at 550 nm for 0.8 mm thickness
c – grain size of larger grains (platelets)

The development of the textured microstructures with increasing sintering temperature (samples A to E in Table 1) is displayed in Fig. 1. It is observed that at 1400 °C the templates are embedded in a fine-grained (~0.30 µm) matrix, without undergoing TGG. At 1500 °C significant TGG takes place, with a full texture development.

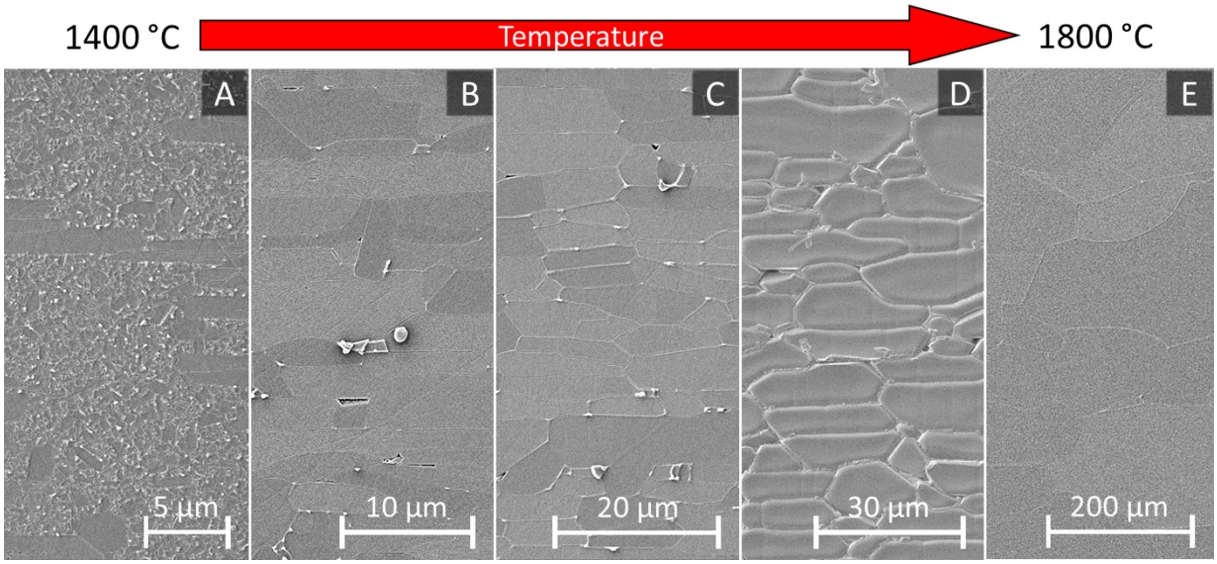

Fig. 1: Microstructure evolution with increasing temperature (samples A–E).

Fig. 2 depicts the development of grain size in horizontal (triangles) and vertical (circles) direction (L_x/L_y) with increasing temperature from 1400 up to 1800 °C. Until a sintering temperature of 1700 °C a steady increase in grain size can be observed, but for sample E, sintered at 1800 °C, abrupt grain growth occurs. This is presumably the result of low-angle grain boundaries for which the grain boundary energy is lower. Nevertheless, the possibility of different mechanism of grain growth, e.g. dislocation glide and climb may not be ruled out[28].

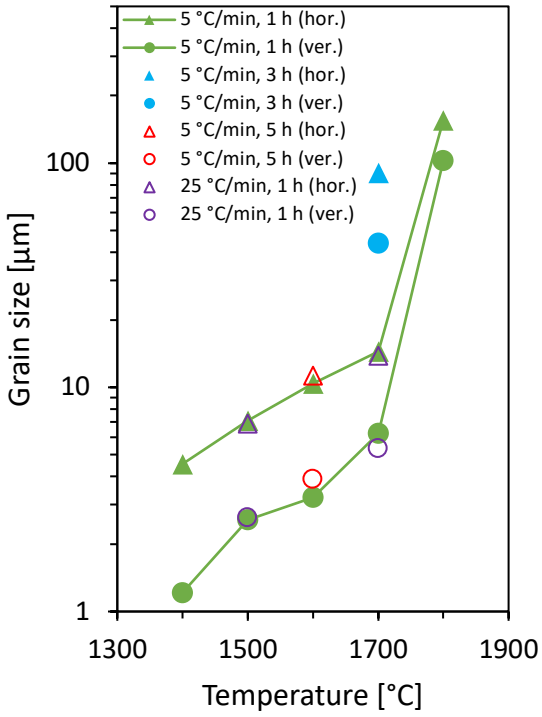

Fig. 2: Grain size (mean chord length) versus sintering temperature for all samples in horizontal (triangles) and vertical (circles) direction.

Note that the mean chord length ratio $\bar{L}_X/\bar{L}_Y$ (i.e., average aspect ratio of grain sections) changes with sintering temperature. TGG preferentially occurs in horizontal direction, causing a tabular grain structure with high aspect ratio until the oriented grain growth is impeded in this direction by neighboring grains. The comparably large grain size in the microstructure of sample E may be responsible for higher transmittance ~45 % at 550 nm at a sample thickness of 0.8 mm (see Table 1) comparing samples A to E, where the same heating rate and dwell time was used with increasing sintering temperatures. Enhanced grain growth leads to a reduction of the number of grain boundaries and consequently to less sources of scattering.

The in-line transmittance of sample E and other samples which exhibit a certain level of transparency is displayed in Fig. 3 in comparison with results reported in the literature (only templated grain growth and magnetic alignment methods are included)[9-13, 15]. The relatively high transmittance of sample A (~11 %) is caused by the fine-grained matrix (~0.3 µm) with fine pores, which are limited sources for light scattering. This is reflected in Fig. 3 by the steeper decrease of the in-line transmittance with decreasing wavelength (sample A), in comparison to e.g., sample D.

The increase of transmittance for sample B to D, sintered at 1500 to 1700 °C, may be attributed to the increase in grain size and the reduction of porosity.

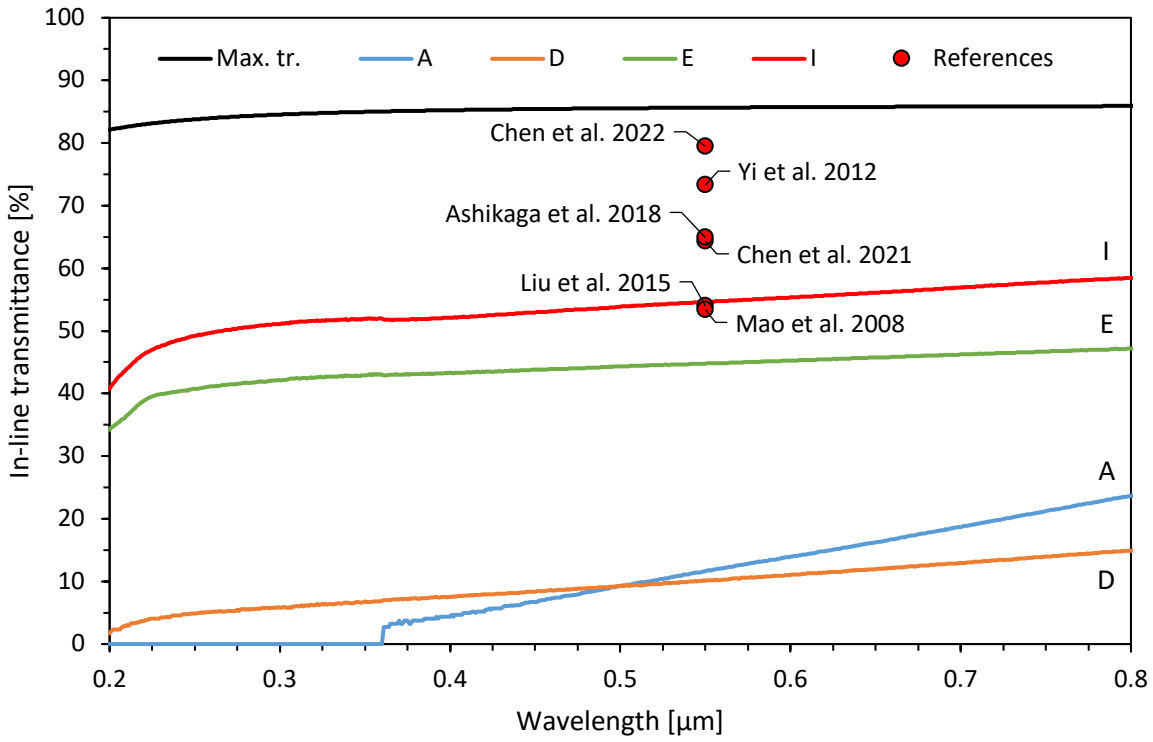

Fig. 3: In-line transmittance of alumina ceramics (samples A, D, E and I) prepared by templated grain growth in the present work and values reported in literature[9-13, 15] (for thickness of 0.8 mm).

Further sintering experiments were performed at a higher heating rate or longer dwell time Fig. 4 displays exemplary microstructural images for the samples sintered at 1700 °C with different heating rates of 5 °C/min (sample D) and 25 °C/min (sample H), where similar textured microstructures can be observed (the suppression of grain growth was insignificant). Further a slight difference in porosity may be observed at the sintering temperature of 1500 °C, where sample F sintered with a higher heating rate (25 °C/min) reached a higher relative density compared to sample B (5 °C/min). The impact of dwell time (from 1h to 5h) was insignificant at 1600 °C (sample G), where the final grain size increased by 9 % and 22 % in horizontal and vertical direction, respectively. The grain growth was more pronounced at 1700 °C (sample I), increasing five and six times in horizontal and vertical direction, respectively, as can be seen in Fig. 2 (blue symbols).

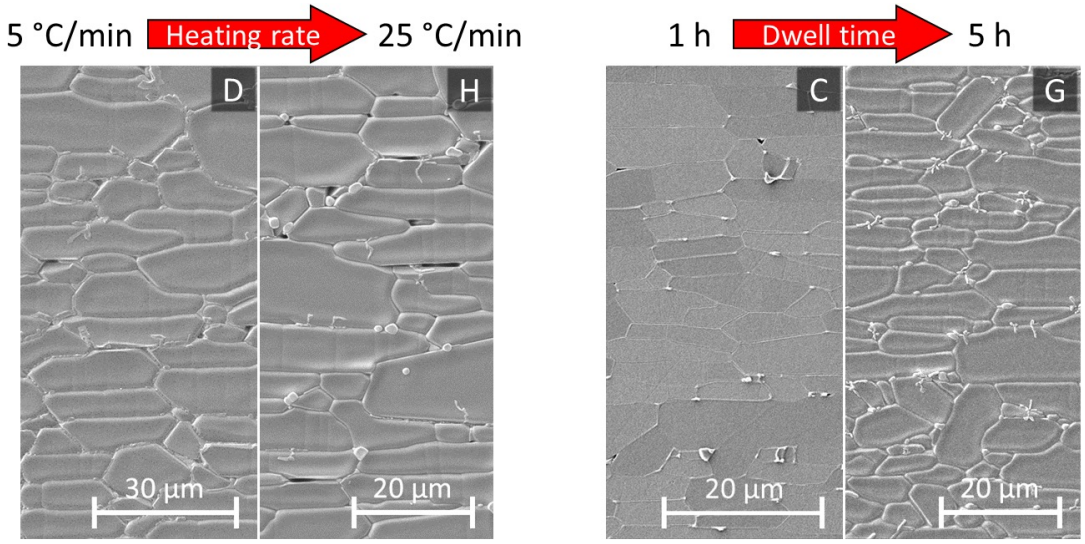

Fig. 4: Microstructure evolution with increasing heating rate (samples D and H) and with increasing dwell time (samples C and G).

The microstructural features of sample I sintered with the conditions of 1700 °C, 5 °C/min and 3 hours dwell time have led to the highest transmittance of ~ 55 % determined in these investigations. The in-line transmittance in Fig. 3 for sample I shows that at a wavelength of 550 nm and a sample thickness of 0.8 mm, similar to results reported by Mao *et al.* and Lui *et al.* could be obtained[12, 13]. Fig. 5 shows the macroscopic appearance of sample D and I.

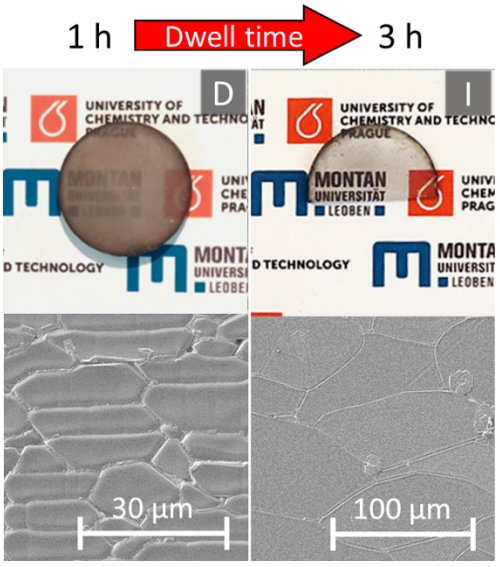

Fig. 5: Microstructure evolution with increasing dwell time for sintering temperatures of 1700 °C: sample D and I with inserted images of their macroscopic appearance

The evaluated Lotgering factors (LF) of most samples was in the range of 0.6 to 0.65, which indicate a reproducible alignment and homogenous growth of templates. Exceptions are sample A and D, where significantly lower LF values were determined. The low LF of 0.36 for

sample A can be explained by the rather equiaxed microstructure. According to sample D misalignment during printing or deformation during the application of pressure in the sintering process might have caused a reduced LF. Due to the comparable LF values throughout the different sintering parameters no clear correlation could be observed between quality of texture and transmittance.

The Vickers hardness of all textured samples was measured to be around 19 GPa. This value is comparable to other values measured on polycrystalline alumina ceramics, which are reported to be ~19 GPa[20, 29]. The slightly higher HV value for sample A (HV = 21.0±0.6 GPa) is attributed to the rather equiaxed and fine-grained microstructure (Knudsen effect)[30].

Recently, Chen *et al.*[11] reported the highest value of in-line transmittance of 78.4 % at 600 nm and for textured alumina with thickness of 1 mm prepared by spontaneous coagulation casting followed by pressureless sintering in vacuum at 1840 °C for 6 h and hot isostatic pressing (HIP) at 1850 °C for 3 h at 200 MPa. Based on their SEM micrographs, one can see that such high temperatures and dwell times resulted in a loss of the textured character of the microstructure, similarly to the result at 1800 °C in this study. Prior to HIP, the in-line transmittance with addition of 5 wt.% platelets reached ~25 % at 550 nm and 1 mm thickness. Only the subsequent HIP was able to improve the transmittance considerably by removal of residual pores. We hypothesize that our results could be improved as well following the same procedure of HIP, perhaps to such an extent that the brick-wall structure may be preserved while achieving complete densification.

Conclusions

Textured ceramics were fabricated up to transparency using the method of templated grain growth (TGG). Templates were aligned using a stereolithographic 3D-printing technology followed by pressure-assisted spark plasma sintering (SPS). Several sintering schedules (i.e., different sintering temperatures, dwell times and heating rates) were used and the resulting materials compared. At a sintering temperature of 1600 °C the textured microstructure was fully developed. A further increase in temperature and/or dwell time progressively reduced the degree of texturing, although, the orientation (Lotgering factor) remained essentially unchanged. Residual porosity was measured in all samples, with the lowest value of 0.49 %. at 1700 °C. Prolonged dwell times promote grain growth and consequently improve the in-line transmittance. Best results were obtained for the sample sintered with a heating rate of 5 °C/min at 1700 °C for 3 hours, where the in-line transmittance was determined to be 54.6 % at 550 nm at a sample thickness of 0.8 mm.

Based on the results of this paper we are convinced that templated grain growth is a promising method to fabricate transparent alumina ceramics. It is expected that subsequent hot isostatic pressing (HIP) would improve the transparency even more. However, in order to improve the transmittance without HIP, considerable process optimization is necessary to control the evolution of the microstructure (grain growth and pore shrinkage) more effectively.

Acknowledgments

A. K. Hofer and R. Bermejo acknowledge that funding for this research was provided by the European Research Council (ERC) excellent science grant "CERATEXT" through the Horizon 2020 program under contract 817615.

V. Nečina and Willi Pabst acknowledge that this work was supported from the grant of Specific university research – grant No A1:FCHT_2022_002.

References

1. Harris DC. Materials for infrared windows and domes: Properties and performance. Bellingham: SPIE-The Intemational Society for Optical Engineering; 1999.
2. Goldstein A, Krell A, Burshtein Z. Transparent Ceramics: Materials, Engineering, and Applications: John Wiley & Sons; 2020. 384 p.
3. Krell A, Hutzler T, Klimke J. Transmission physics and consequences for materials selection, manufacturing, and applications. J Eur Ceram Soc. 2009;29(2):207–21.
4. Pauling L, Hendricks SB. The crystal structures of hematite and corundum. J Am Chem Soc. 1925;47(3):781–90.
5. Thomas ME, Andersson SK, Sova RM, Joseph RI. Frequency and temperature dependence of the refractive index of sapphire. Infrared Phys Technol. 1998;39(4):235–49.
6. Krell A, Blank P, Ma H, Hutzler T, van Bruggen MPB, Apetz R. Transparent sintered corundum with high hardness and strength. J Am Ceram Soc. 2003;86(1):12–8.
7. Krell A, Baur GM, Dahne C, editors. Transparent sintered sub-µm Al_2O_3 with IR transmissivity equal to sapphire. ProcSPIE; 2003.
8. Krell A, Klimke J, Hutzler T. Transparent compact ceramics: Inherent physical issues. Optical Materials. 2009;31(8):1144–50.
9. Ashikaga T, Kim B-N, Kiyono H, Suzuki TS. Effect of crystallographic orientation on transparency of alumina prepared using magnetic alignment and SPS. J Eur Ceram Soc. 2018;38(7):2735–41.

10. Chen H, Shimai S, Zhao J, Mao X, Zhang J, Zhou G, et al. Highly oriented α-Al_2O_3 transparent ceramics shaped by shear force. J Eur Ceram Soc. 2021;41(6):3838–43.

11. Chen H, Zhao J, Shimai S, Mao X, Zhang J, Zhou G, et al. High transmittance and grain-orientated alumina ceramics fabricated by adding fine template particles. J Adv Ceram. 2022;11(4):582–8.

12. Liu P, Yi H, Zhou G, Zhang J, Wang S. HIP and pressureless sintering of transparent alumina shaped by magnetic field assisted slip casting. Opt Mater Express. 2015;5(2):441–6.

13. Mao X, Wang S, Shimai S, Guo J. Transparent polycrystalline alumina ceramics with orientated optical axes. J Am Ceram Soc. 2008;91(10):3431–3.

14. Suzuki TS, Sakka Y, Kitazawa K. Orientation amplification of alumina by colloidal filtration in a strong magnetic field and sintering. Adv Eng Mater. 2001;3(7):490–2.

15. Yi H, Mao X, Zhou G, Chen S, Zou X, Wang S, et al. Crystal plane evolution of grain oriented alumina ceramics with high transparency. Ceram Int. 2012;38(7):5557–61.

16. Ratzker B, Wagner A, Kalabukhov S, Frage N. Improved alumina transparency achieved by high-pressure spark plasma sintering of commercial powder. Ceram Int. 2020;46(13):21794–9.

17. Ratzker B, Wagner A, Sokol M, Kalabukhov S, Dariel MP, Frage N. Optical and mechanical properties of transparent alumina fabricated by high-pressure spark plasma sintering. J Eur Ceram Soc. 2019;39(8):2712–9.

18. Apetz R, van Bruggen MPB. Transparent alumina: A light-scattering model. J Am Ceram Soc. 2003;86(3):480–6.

19. Carisey T, Leviri I, Brandon DG. Microstructure and mechanical properties of textured Al_2O_3. J Eur Ceram Soc. 1995;15(4):283–9.

20. Messing GL, Poterala S, Chang Y, Frueh T, Kupp ER, Watson BH, et al. Texture-engineered ceramics – Property enhancements through crystallographic tailoring. J Mater Res. 2017;32(17):3219–41.

21. Pavlacka RJ, Messing GL. Processing and mechanical response of highly textured Al_2O_3. J Eur Ceram Soc. 2010;30(14):2917–25.

22. Seabaugh MM, Kerscht IH, Messing GL. Texture development by templated grain growth in liquid-phase-sintered α-alumina. J Am Ceram Soc. 1997;80(5):1181–8.

23. Seabaugh MM, Messing GL, Vaudin MD. Texture development and microstructure evolution in liquid-phase-sintered α-alumina ceramics prepared by templated grain growth. J Am Ceram Soc. 2000;83(12):3109–16.

24. Hofer A-K, Kraleva I, Bermejo R. Additive manufacturing of highly textured alumina ceramics. Open Ceram. 2021;5:100085.

25. Pabst W, Gregorová E, Uhlířová T. Microstructure characterization via stereological relations - A shortcut for beginners. Mater Charact. 2015;105:1–12.

26. Lotgering FK. Topotactical reactions with ferrimagnetic oxides having hexagonal crystal structures—I. J Inorg Nucl Chem. 1959;9(2):113–23.

27. SIST. Advanced technical ceramics - Monolithic ceramics - Mechanical properties at room temperature - Part 4: Vickers, Know and Rockwell superficial hardness tests. 1994.

28. Sutton AP, Balluffi RW. Interfaces in crystalline materials. United States: Oxford University Press Inc., New York; 1995. 819 p.

29. McColm IJ. Ceramic Hardness. New York: Springer New York, NY; 1990. 324 p.

30. Knudsen FP. Dependence of mechanical strength of brittle polycrystalline specimens on porosity and grain size. J Am Ceram Soc. 1959;42(8):376–87.

Publication D

High-strength lithography-based additive manufacturing of ceramic components with rapid sintering

Anna-Katharina Hofer[1], Andraž Kocjan[2], Raúl Bermejo[1]

[1]Department of Materials Science, Montanuniversitaet Leoben, Franz Josef-Strasse 18, A-8700 Leoben, Austria

[2]Department for Nanostructured Materials, Jožef Stefan Institute, Jamova 39, Sl-1000 Ljubljana, Slovenia

Additive Manufacturing 59 (2022) 103141.

doi: https://doi.org/10.1016/j.addma.2022.103141

Additive Manufacturing 59 (2022) 103141

Contents lists available at ScienceDirect

Additive Manufacturing

journal homepage: www.elsevier.com/locate/addma

High-strength lithography-based additive manufacturing of ceramic components with rapid sintering

Anna-Katharina Hofer [a,*], Andraž Kocjan [b,*], Raúl Bermejo [a]

[a] Department of Materials Science, Montanuniversitaet Leoben, Franz Josef-Strasse 18, A-8700 Leoben, Austria
[b] Department for Nanostructured Materials, Jožef Stefan Institute, Jamova 39, Sl-1000 Ljubljana, Slovenia

ARTICLE INFO

Keywords:
Ceramics
Sintering
Stereolithography
Microstructure
Mechanical properties

ABSTRACT

Additive manufacturing technology enables the fabrication of technical ceramics and multi-materials with unprecedented geometrical accuracy and complexity, opening the path to new functionalities for engineering applications. A crucial step to consolidate 3D-printed ceramic parts is "sintering", a time and energy (temperature) intensive densification process. Here we present a strategy for rapid sintering (~ 300–450 °C/min) of lithography-based additively manufactured alumina ceramics enabling consolidation of ceramic components of complex shapes within minutes. Highly dense, fine-grained microstructures were achieved by controlling densification and limiting grain growth through rapid radiation heat transfer. The high mechanical strength and toughness measured in additively manufactured alumina (~ 810 MPa and ~ 4.3 MPa $m^{1/2}$) sintered at 1600 °C within 2 min was superior to that of conventionally sintered reference parts. This study opens the path for rapid sintering of complex shaped ceramic architectures of high density with tailored microstructure and properties.

1. Introduction

The advent of additive manufacturing (AM) of ceramics offers unprecedented accuracy, geometrical and functional complexity with the potential of unveiling completely new or significantly improved solutions for cutting-edge automotive, aerospace, environmental and biomedical applications [1,2]. There are many available AM techniques for shaping ceramics that are generally classified based on the type of the feedstock employed, i.e., powder based, solid or liquid based [3–5]. In the powder based techniques, a deposition of a uniform powder bed layer is crucial, which is then directly and selectively fused by using a laser [6] or binder system in the cases of selective laser sintering (SLS) or binder jetting, respectively. Solid based techniques, such as fused filament fabrication (FFF), rely on thermoplastic feedstocks which are solid at room temperature but are melted and extruded at elevated temperatures during the AM process. Liquid based techniques are represented by photopolymerization, jetting and robocasting, where suspensions with a high ceramic powder concentration are prepared and shaped [7,8]. Lithography-based ceramic manufacturing (LCM) is nowadays one of the most prominent AM technologies among the many available. LCM is based on the concept of digital light processing (DLP), where sub-micron ceramic powders are combined with a photosensitive polymer binder to enable printing of complex geometries with finest accuracy and resolution [9].

However, in contrast to AM of metals and polymers, which are final, fully consolidated products, except for SLS, sintering is needed for full densification of ceramics after the process of AM. Sintering is a time and energy demanding step. Until now, the process of densification of the AM ceramic parts has mainly been performed in conventional furnaces, following standard sintering conditions [10]. The sintering process is crucial to provide ceramics with their final microstructure and corresponding structural and functional properties. Specially in the case of advanced structural ceramics, high densities and fine-grained microstructures are sought, aiming to obtain high strength and fracture resistance.

The processing of pore-free, fine-grained (sub-micron-sized) ceramics thus remains challenging especially when employing conventional slow sintering routes [11]. In an attempt to reduce sintering time and temperature, advanced sintering strategies, such as Spark Plasma Sintering (SPS or FAST) [12], flash (FS)[13,14] or cold sintering [15,16], have all attracted attention aiming to promote rapid densification at reduced overall energy consumption [17–19]. For instance, the success in the development of refined microstructures with SPS is associated with the simultaneous application of mechanical pressure and electric

* Corresponding authors.
E-mail addresses: anna-katharina.hofer@unileoben.ac.at (A.-K. Hofer), a.kocjan@ijs.si (A. Kocjan).

https://doi.org/10.1016/j.addma.2022.103141
Received 15 June 2022; Received in revised form 5 July 2022; Accepted 7 September 2022
Available online 9 September 2022

current [10]. The result is ceramics that may be sintered within minutes by markedly increased heating rates (~ 100 °C/min), also ensuring minimal grain growth at significantly lower sintering temperatures [20]. An "ultra-fast" high temperature sintering (UHS) technique was recently introduced, which employs a Joule heated carbon felt strip for reaching temperatures as high as 3000 °C. Various ceramics have been sintered in seconds to near full density through a massive heating flux (>500 W/cm^2) and ultrahigh heating rates [18,21]. Due to the sharp thermal gradients involved and associated structural problems, the UHS technique has been limited to small and very thin specimens. Furthermore, although these techniques may lead to fully dense and fine-grained microstructures, most of them are limited to simple, planar-shaped geometries, partly associated with the required applied mechanical pressure onto the part [10,11,22]. Thus posing a challenge to obtain fine grained and highly dense microstructures through rapid sintering of complex shaped additive manufactured ceramic.

A promising method that may be employed to sinter AM parts is radiation assisted sintering (RAS). The use of RAS allows high heating rates, which favors densifying diffusion mechanisms and limits grain growth. RAS was first conducted as pressure-less SPS attaining high heating rates (~ 500 °C/min) through the Joule heated radiation of a graphite crucible in vacuum [23]. Recent results have shown how RAS can enable sintering of zirconia nanoceramics [24] or sub-micrometer-sized lead-free piezoelectric functional ceramics with improved dielectric properties [25] by only 2-minute exposure to radiation at ~ 1300 °C (~ 350 °C/min). *Quasi* diffusion-less solid-state densification by coalescence and sliding of zirconia particles was revealed as the main sintering mechanism. As a consequence, grain growth is impeded during the initial sintering stages, yielding a nanoscale microstructure. Such process involving particle "agglomeration" and "reorganization" to minimize surface free energy are typical encountered in aqueous colloidal systems [26,27] or in advanced sintering strategies such as SPS or FS, both being triggered by pressure and/or electric current [28–31]. In the alumina system, Salomon et al. reported inhomogeneous microstructures with relatively large grain sizes (~ 6.5 μm) in α-Al_2O_3 samples sintered by RAS [32]. They explained the inhomogeneity with agglomerates and non-uniform particle compaction after uniaxial pressing of green parts. However, exploiting RAS concept for fast consolidation of 3D-printed parts has not been attempted yet.

In this work, we demonstrate the feasibility of sintering of lithography-based additively manufactured alumina ceramics within minutes instead of hours by the radiation-assisted rapid sintering (RAS) technique. A SPS set-up was adapted, where no direct pressure nor current is applied onto the ceramic sample to allow sintering of complex geometries, as for example a turbocharger engine rotor. Moreover, such sintering protocol yielded fine-grained microstructures (~ 1 μm) with densities ~ 99% and the ability of rapid sintering complex 3D printed parts, with an energy input of ~ 1 MJ as compared to ~ 25 MJ for conventional sintering [33]. We investigate the effect of rapid sintering processing conditions, in terms of maximum sintering temperature and time, on the microstructural evolution and properties of 3D printed ceramics. It follows that intense radiation can be used as unique source of thermal transfer mechanism to sinter ceramics within minutes, opening a path to rapid sintering of 3D ceramic components with controlled microstructure and properties.

2. Material and methods

2.1. Additive manufacturing, debinding and sintering of parts

For 3D-printing of samples a CF8500 printer from Lithoz GmbH (Vienna, Austria) was employed, which uses the technology of lithography-based ceramic manufacturing (LCM), Fig. 1a [9]. A commercially available photo-sensitive alumina suspension (LithaLox HP500, Lithoz GmbH, Vienna, Austria) was utilized to fabricate high purity alumina samples of different complexity. The LCM is a bottom-up process using photosensitive suspensions, containing ceramic particles as fillers. In our case high purity α-alumina powder, with a particle size of 150 nm and a surface area of ~ 10 – 15 m^2/g, was selected. The suspension was filled in a transparent vat and distributed through its rotation and a stable doctor blade. The light source, with a certain wavelength, is located beneath the vat. Due to the exposure with light, photopolymerisation is activated and the layer of the desired geometry solidifies, consisting of consolidated α-alumina ceramic particles embedded in a polymer matrix, Fig. 1b. The final part is built up stepwise, layer-by-layer. The layer thickness was selected to be 25 μm, other printing parameters were set after recommendations found in data sheets for the applied suspension. After printing, the samples were cleaned using a solvent to remove non-polymerized suspensions from

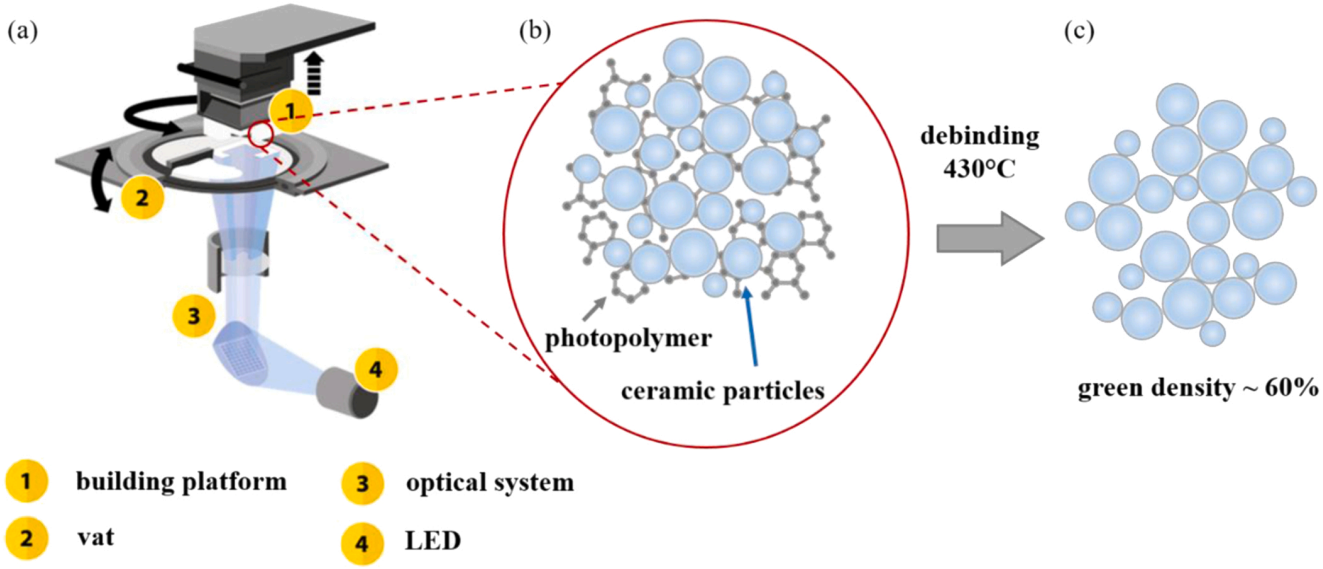

Fig. 1. Ceramic processing applying lithography-based ceramic manufacturing (LCM). (a) LCM technology based on digital light processing (DLP). (b) Photopolymerized network forming the matrix to organize the ceramic particles in a 3D-printed shape. (c) The removal of the polymeric network leads to an open-porous fragile structure [9,34].

the samples and were stored in a drying furnace at 42 °C before debinding. The polymeric network, shaping the 3D-printed part, was removed during a thermal treatment with a maximum temperature at 430 °C, in a convection furnace (Thermoconcept, KU15/65, Bremen, Germany), Fig. 1b-c.

For the conventional sintering a high temperature furnace was used (Thermoconcept HTL 10/17, Bremen, Germany), with a heating rate of 5 °C/min to a sintering temperature of 1600 °C and a dwell time of 6 h, followed by a cooling rate of 5 °C/min.

For the pressure-less sintering a spark plasma sintering furnace (FUJI SPS Dr. Sinter Lab 322Lx, Dr. SINTER, SPS Syntex Inc., Japan) was used, with a modified graphite die set up. A stack of three cylinders with a diameter of ~ 35 mm was built, whereas the middle cylinder was hollow with an inner diameter of ~ 30 mm, resulting in a wall thickness of ~ 5 mm. The samples were placed inside the hollow cylinder on a graphite wool. The graphite crucible was heated through pulsed, direct, electrical current, and the samples were rapid sintered (~ 450 °C/min) due to intense thermal radiation heat transfer at different maximum temperatures (1300 °C, 1400 °C, 1500 °C and 1600 °C) at various dwell times (2 min, 4 min and 8 min). The temperature was measured using an infrared pyrometer, where the measuring point was pointed at a hole (diameter ~ 3 mm) in the hollow cylinder at the location of the sample.

2.2. Microstructure and grain size analyses

For microstructural analysis the samples were polished to a mirror surface finish of 1 μm using a Struers polishing machine (Struers Tegramin-30, Struers Tech, Copenhagen, Denmark) and thermal etched 100 – 200 °C below the sintering temperature. Scanning Electron Microscopy (SEM) images were taken on two different microscopes, depending on the grain size. For microstructures sintered at lower maximum temperatures (1300 °C and 1400 °C) a SEM with higher resolution was used (Tescan Clara, Tescan Orsay Holding, Brno, Czech Republic). The microstructures of maximum sintering temperatures of 1500 °C and 1600 °C were analysed with a table SEM, JEOL JCM-6000Plus Neoscope™ (JEOL Ltd., Tokyo, Japan). The average grain size was determined on ~ 1000 grains using the linear intercept method on SEM images. Transmission electron microscopy (TEM) was performed using a 200 kV Cs probe-corrected scanning transmission electron microscope (ARM 200 CF, Jeol Ltd., Toky, Japan). Here, the samples were prepared by cutting them with an ultrasonic cutter into a cylindrical shape of ~ 3 mm in diameter (Sonicut™ 380 Ultrasonic Cutter, SBT, USA). The TEM specimen was then ground to a thickness of 100 μm and dimpled to 15 μm at the disc center (Dimple grinder, Gatan Inc., Warrendale PA, USA. Further, the specimen was finally ion-milled (PIPS, Precision Ion Polishing System, Gatan Inc., USA) using 3 kV Ar^+-ions at an incidence angle of 8° until perforation.

2.3. Porosity measurement

The porosity of samples sintered at maximum temperatures of 1500 °C and 1600 °C, with a relative density > 90%, was measured after Archimedes principle [35]. For the samples, with relative density < 90% mercury porosimetry (Pascal 140 and Pascal 440, Thermo Fisher Scientific, USA) was used to determine the value of porosity, with infill pressures ranging from 10 kPa up to 400 MPa. The surface tension and the contact angle of the mercury were set to standard values of 0.485 mN/m and 130°, respectively.

2.4. Mechanical testing

The Vickers hardness of the samples sintered at different maximum temperatures and for different dwell times, was measured using a Vickers indenter with a load of 1 kg [36]. The diagonals of the imprint were determined using a light microscope and the corresponding software (BX50 Olympus, Shinjuku, Tokyo, Japan). The fracture toughness (K_{IC}) was evaluated with the Single-edge V-notch beam method (SEVNB) in a 4-point bending set-up (span 40 – 20 mm) [37]. The testing was performed on five prismatic bars (~ 3×4x25 mm) for statistic validity for the selected sintering parameters of RS1: 1500 °C and 8 min and RS2: 1600 °C and 2 min. At ambient conditions (T = 23 °C, RH = 22%) a universal testing machine (Zwick Z010, Zwick GmbH & Co., Ulm, Germany) and the corresponding software (TestXpertII) were used. The samples were placed with the V-notch on the side loaded under tension, a pre-load of 8 N was applied, followed by loading with a displacement rate of 0.5 mm/min until failure. Biaxial strength was evaluated on as-printed disc-shaped specimens (diameter = 10 mm and height = 1 mm), without any post-machining, at ambient conditions (T = 23 °C, RH = 29%) using a Ball-on-Three-Ball set-up (ball diameter = 6.35 mm) in a universal testing machine (Zwick Z010, Zwick GmbH & Co., Ulm, Germany). The applied pre-load was 20 N and the specimens were tested with a displacement rate of 1 mm/min. At least 15 specimens per sample were tested and analysed to ensure statistical significance. The biaxial strength distribution was evaluated according to Weibull statistics to determine the characteristic strength (σ_0) and the Weibull modulus (m) of the samples [38,39]. The used equations to calculate the presented data are explained in the supplementary file.

3. Results and discussion

3.1. Microstructure and properties after rapid sintering

AM of dense ceramic components with high complexity and accuracy is demonstrated on alumina ceramic samples, printed using the LCM printing technology. Fig. 2a shows a ceramic turbocharger engine rotor after 3D-printing. The photosensitive suspensions utilized requires 50 vol% polymer binder to print the alumina parts [9]. After binder removal at ~ 430 °C, a green density of ~ 60% was achieved (Fig. 2b). The 3D-printed and debinded pure alumina components were rapidly sintered by the RAS concept in an adapted SPS sintering set-up (Fig. 2d). The graphite crucible was designed with thin walls to enable very high heating rates of up to 450 °C/min. The resistance on the pulsing DC electric current passing through the graphite crucible walls, when placed in between the SPS rams, caused Joule heating. Thermal radiation was the only heat source employed to densify the ceramic parts (neglecting conduction and convection due to thermal isolation and vacuum, respectively). Fig. 2c shows the ceramic turbocharger engine rotor consolidated at a maximum temperature of 1600 °C with 2-minute-long dwell time (referred to as RS1 sintering conditions). A relative density of ρ_{rel} ~ 97% was achieved. For comparison, a reference 3D-printed sample was conventionally sintered (CS) at 1600 °C with a heating rate of 5 °C/min and a sintering time of 6 h, resulting in a relative density of ρ_{rel} ~ 99%. The sintering cycles for the RS1 and CS and the corresponding microstructures are represented in Fig. 2e-g. Comparing the microstructures of rapid (Fig. 2f.) and conventionally (Fig. 2g.) sintered un-doped alumina parts, a significant difference in grain size was observed. Sub-micron grain size (~ 640 nm) was achieved for the RS1 alumina part, being approximately 10-times smaller than that of CS alumina (~ 5.3 μm) [40]. The RS1 sample had an homogeneous microstructure consisting of fine, equiaxed grains, whereas larger (abnormally grown anisotropic) grains were observed in the CS sample, as commonly found in un-doped alumina [41].

The mechanical properties of the 3D-printed samples were evaluated after sintering. In ceramics, structural properties such as hardness, strength and fracture resistance (toughness) are strongly related to the composition and/or microstructure (e.g. grain size, porosity) of the consolidated part. In particular, the fracture strength,σ_f, is generally inversely proportional to the grain size and is directly dependent on the fracture resistance (toughness) of the material. Using the Griffith criterion for brittle fracture [42], based on linear elastic fracture mechanics, a good estimation for the strength in ceramics follows the relation

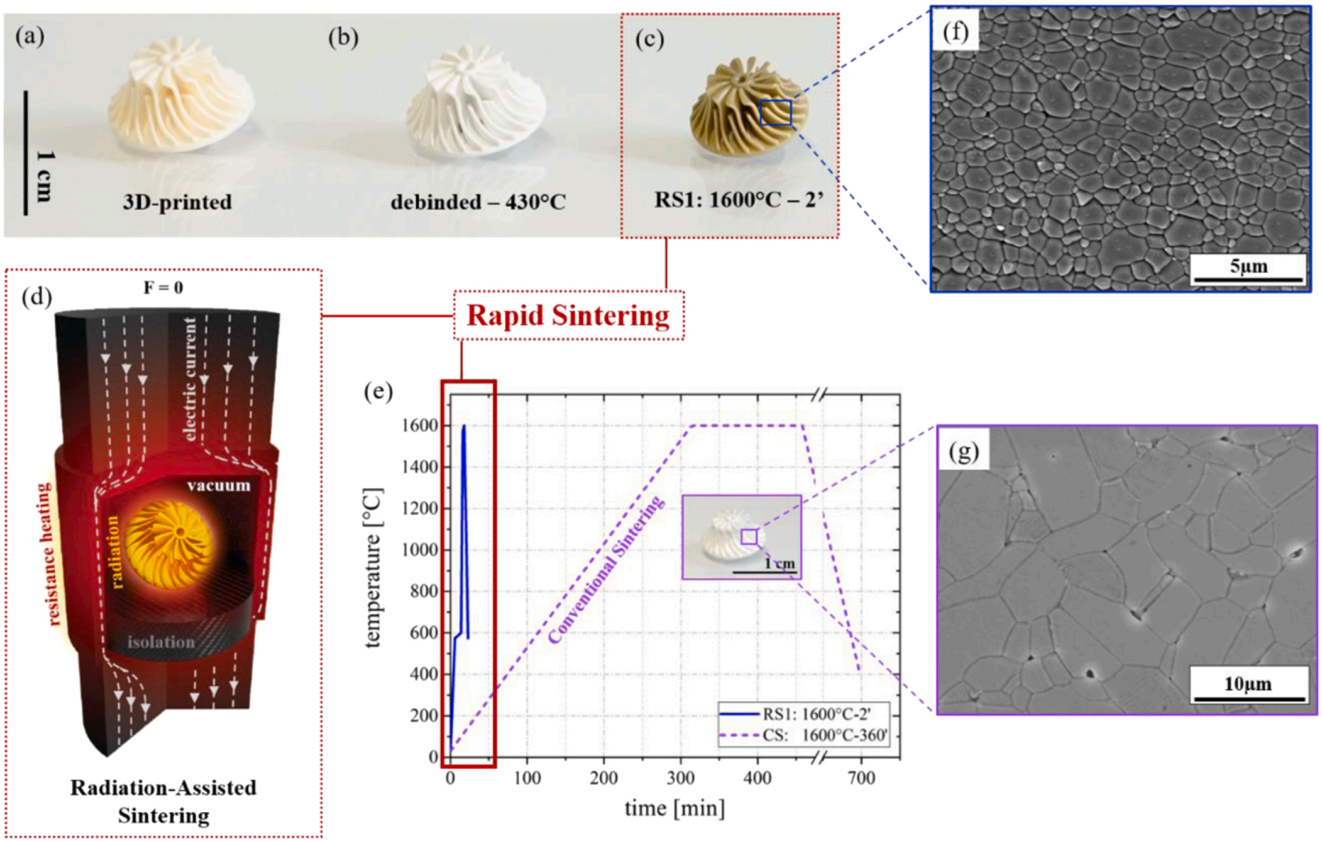

Fig. 2. Radiation-Assisted Sintering (RAS) vs. Conventional Sintering (CS). (a-c) Processing of a turbocharger engine rotor: (a) after LCM 3D-printing, (b) after binder removal at ~ 430 °C and (c) after RAS sintering at 1600 °C with 2 min dwell time (RS1). (d) Set-up of the RAS technique where thermal radiation, induced through Joule heating due to resistance of the electric current, is the only heat transfer used for densifying the ceramic component. (e) Sintering protocol for rapid (RS1) and conventional sintering (CS). (f,g) Resulting microstructures of the(f) rapid (RS1) and (g) the conventional sintering protocol (CS).

$\sigma \approx \frac{K_{Ic}}{\sqrt{\pi \bullet GS}}$, with GS being the average grain size, and K_{Ic} the fracture toughness of the material. In order to quantify the effect of grain size on strength, simple disc- and bar- shaped specimen geometries were 3D-printed and sintered using the same protocols as for the turbocharger. The fracture toughness was measured on bending bars using the standard Single-Edge V-Notched Beam Method (SEVNB) [37]. Toughness values of ~ 4.3 MPa $m^{1/2}$ and ~ 3.8 MPa $m^{1/2}$ were obtained for RS1 and CS samples, respectively. Mechanical strength was determined under biaxial bending using the Ball-on-three-Balls (B3B) testing method [43,44]. Strength data were analysed according to Weibull theory [38], with the Weibull parameters (characteristic strength,σ_0, and Weibull modulus, m) being evaluated following the standards [39]. A higher characteristic strength of σ_0 ~ 810 MPa was measured for the RS1 specimen, as compared to σ_0 ~ 570 MPa for the CS specimen. The significant increase in strength can be directly related to the smaller grain size of the RS1 material.

3.2. Effect of time and temperature on microstructural evolution

The effect of time and temperature on the density and final properties of rapid sintered ceramics was evaluated on 3D-printed disc-shaped alumina parts (d = 10 mm and h = 1 mm) sintered in the adapted pressure-less SPS set-up with a heating rate of ~ 450 °C/min between 1300 °C and 1600 °C at short dwell times in the range of 2–8 min [45]. Relative density was determined and cross-sections of the sintered samples were prepared for the SEM microstructural analysis according to grain size.

Fig. 3 shows representative microstructures after a given maximum temperature and dwell time. Fig. 4 shows grain size distribution versus relative density for all samples. For all dwell times investigated (2, 4 and 8 min) similar microstructures were obtained at sintering temperatures of 1300 °C and 1400 °C (Fig. 3a-f.); this finding holds for sintering at 1500 °C for 2 min or 4 min as well (Fig. 3g-h). Here, sub-micron grains seem to agglomerate into "clusters", leaving regions of remnant porosity. The high heating rates, causing high activation energies, favor densifying lattice and grain boundary diffusion, which may result in rearrangement of adjacent grains to lower the grain boundary energy [46,47]. Further, the amount of atoms at the grain boundaries in relation to atoms in the interior of a grain increases with decreasing grain size. Instead of neck formation, it is likely that crystallographically coherent grain interfaces attach, annihilating the grain boundary [32]. In our case, images taken with a transmission electron microscope (TEM) indicated vanishing of grain boundaries for the sintering parameters of 2 min at 1400 °C (close-up in Fig. 4b). Regarding to the lack of neck formation and the small grain size, the angles between the grains reveal a relatively low dihedral angle, compared to θ ~ 120 °C for alumina ceramics in equilibrium (Fig. 3a-h) [10]. This suggests that surface diffusion hardly took place, which would have led to neck formation and a more "stagnant" densifying microstructure. This leads to the conclusion that enhanced volume diffusion and a low dihedral angle results in rearrangement of grains between 1300 °C and 1400 °C.

The first microstructural differences appeared at 1500 °C, sintered for 8 min (Fig. 3i). For maximum sintering temperatures of 1600 °C a significant change can be clearly seen for all dwell times.

At sintering temperatures of 1500 °C with dwell times of 8 min, and at 1600 °C with 2 min (Fig. 3f-g). The shape of the grains becomes equiaxed and the grain size is about 500 nm, with relative densities above 95% (Fig. 4). The strong curvatures of the grain boundaries

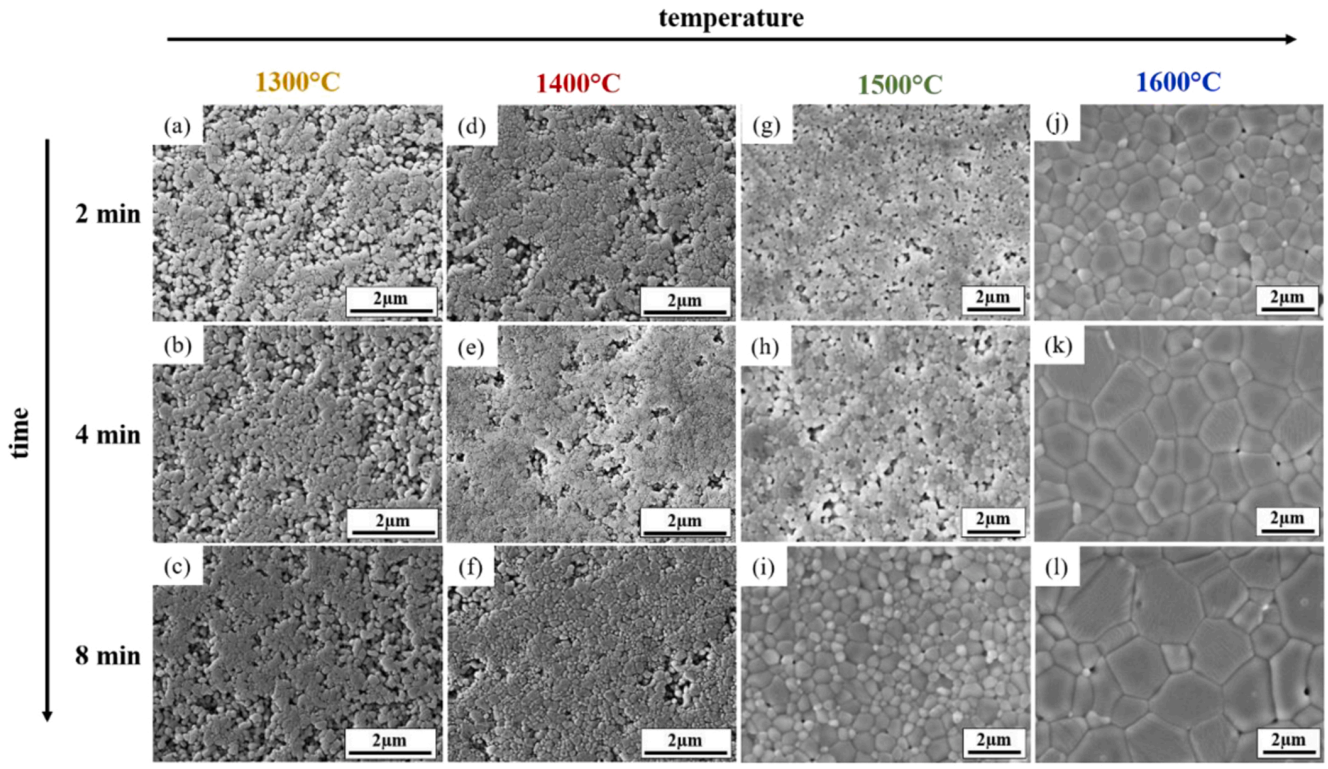

Fig. 3. Development of alumina microstructures as function of maximum sintering temperature and dwell time. (a) 1300 / 2, (b) 1300 / 4, (c) 1300 / 8, (d) 1400 / 2, (e) 1400 / 4, (f) 1400 / 8, (g) 1500 / 2, (h) 1500 / 4, (i) 1500 / 8, (j) 1600 / 2, (k) 1600 / 4, (l) 1600 / 8 (T_{max} / t_{dwell} represent the maximum sintering temperature in [°C] and the dwell time in [minutes]).

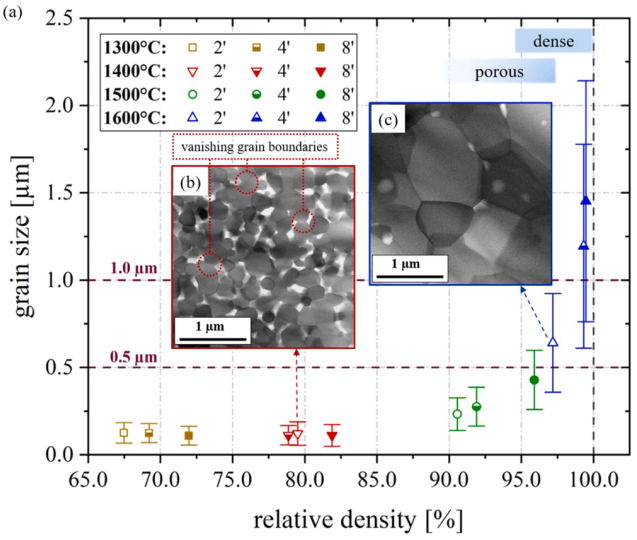

Fig. 4. Development of grain size and relative density according to different maximum sintering temperatures and dwell times. (a) grain size [µm] plotted vs. relative density [%]. (b) TEM image of the microstructure sintered at T_{max} = 1400 °C with t_{dwell} = 2 min (**c**) TEM image of the microstructure sintered at T_{max} = 1600 °C with t_{dwell} = 2 min.

indicate that densification has not yet been fully completed. A TEM image of the microstructure from the 2 min at 1600 °C sintering condition shows nano-sized pores within the grains as well as along the grain boundaries (close-up in Fig. 4c). Due to the elevated temperatures, the mobility of the grain boundaries is enhanced, leading to an enclosure of pores within the grains. The spherical shape of the trapped pores facilitates pore growth. In contrast, pores along the grain boundaries have rather lenticular shapes (energetically unstable), and therefore shall be removed after longer dwell times (see Fig. S1) [10].

At higher temperatures and dwell times (i.e. 1600 °C, 4 min and 8 min) the relative density increased to > 99% (Fig. 4), with an average small grain size of ~ 1.5 µm, as compared to the larger grain size of ~ 5.3 µm after conventional sintering. In Fig. 3j-l the linear shape of the grain boundaries (with a rough estimation of 6 neighboring grains for a number of grains) suggests microstructural stability and explains the full densification obtained. Regarding the evolution of alumina microstructures during rapid sintering, the dependence on temperature and time is consistent with observations in conventional sintering [10].

Microstructural observations agree with the relative density and mean grain size, Fig. 4. At low sintering temperatures of 1300 °C and 1400 °C densification occurs without an evident grain growth process, resulting in a constant mean grain size of approximately 150 nm, measured for both temperatures for all dwell times, being comparable to the starting powder particle size. The relative density increased with longer dwell times from ~ 68% to ~ 82% (Fig. 4). Regarding elevated sintering temperatures of 1500 °C and 1600 °C, the densification is accompanied with grain growth, where relative density and mean grain size increases with longer dwell times. In conclusion, rapidly sintered samples show homogeneous microstructures in terms of grain and pores size distribution. The annihilation of pore regions accompanied with evident grain growth is observed at nearly full densified microstructures (ρ_{rel} > 95%) at elevated temperatures. This can be related to the two orders of magnitude higher heating rates, favouring densifying diffusion mechanisms allowing the realization of significantly finer microstructures.

3.3. *Effect of rapid sintering conditions on the mechanical properties*

To investigate the effect of the different sintering conditions on the

mechanical properties, hardness, mechanical strength and toughness were evaluated on 3D-printed parts. Vickers hardness was determined on polished surfaces with 1 kg indentations. Fig. 5 shows hardness plotted versus sintering time for different sintering temperatures. A strong dependence of hardness on the sintering-temperature-related alumina ceramic microstructure can be observed. Hardness increases with relative density (Fig. 4) [48]. An exception is found for the hardness measured on samples sintered at 1600 °C with different dwell times. Whereas the relative density increases with increasing dwell time, from 2 min to 8 min, the hardness slightly decreases from ~ 23 GPa to ~ 21 GPa. This can be explained considering the grain size of the investigated microstructures. As seen in Fig. 3 and SEM images in Fig. 5(a-c) the grain size from the shortest (2 min) to the longest (8 min) dwell times ranges from ~ 600 nm to ~ 1.5 μm. Here, the effect of grain size prevails over the relatively small difference in densities between the two microstructures (~ 97% versus ~ 99%).

To understand the implications of grain size and density on the mechanical strength and fracture toughness, samples sintered for 2 min at 1600 °C (RS1) and 8 min at 1500 °C (RS2) were tested and compared to a reference CS sample. The individual failure stresses σ_f are illustrated in Fig. 6 for the selected rapid sintering protocols of RS1 and RS2, as well as for conventionally sintered specimen at 1600 °C for 6 h.

The corresponding strength distributions are presented in a Weibull diagram in Fig. S2. For the sintering parameters 8 min at 1500 °C a characteristic strength of $\sigma_0 = 867$ [808–932] MPa with m = 7 [5–9] were measured, where the numbers in brackets represent the 90% confidence interval. Even though the porosity in the RS2 samples was higher (~ 4%) than in the RS1 samples (~ 3%), σ_0 appears to be higher than for the sintering parameters of 2 min at 1600 °C, $\sigma_0 = 808$ [743–881] MPa and $m = 6$ [4–8]. Considering the Griffith criterion, $\sigma \propto \left(\frac{1}{GS}\right)^{\frac{1}{2}}$, this can be attributed to the slightly smaller average grain size of ~ 430 nm for RS2, whereas the average grain size of RS1 was ~ 640 nm [42,49–51]. Since the confidence intervals of σ_0 and m of the different sintering parameters overlap, and thus no statistical difference in the results can be drawn. It has to be also emphasized that each series contained a specimen exceeding the strength of 1000 MPa. Comparing these biaxial σ_0 values of RS samples with conventionally sintered alumina ceramics [52], where, as reported in Hofer et. al [40], $\sigma_0 = 570$ [549–592] MPa and $m = 9$ [7–11], an outstanding strength in 3D printed alumina ceramics can be achieved by the decrease of grain size realised

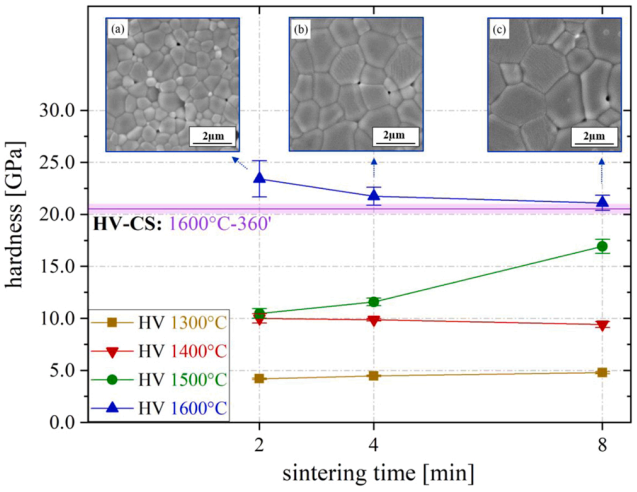

Fig. 5. Hardness of RAS alumina samples. Vickers hardness for samples sintered at different temperatures (1300 °C, 1400 °C, 1500 °C and 1600 °C) and different dwell times (2 min, 4 min and 8 min). Vickers hardness correlates with the relative density except for samples sintered at 1600 °C, (a-c). Increasing grain size decreased hardness values, although relative density increased.

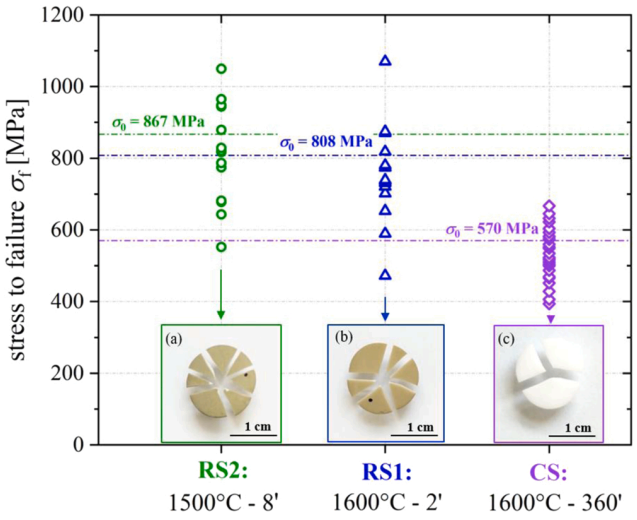

Fig. 6. Strength increase in rapid sintered samples. Distribution of biaxial failure stresses σ_f [MPa] with the corresponding characteristic strength σ_0 [MPa] for the selected RAS protocols of RS1 and RS2, and for the CS protocol taken as a reference. The number of pieces of the fractured samples correlates with the increase in strength (a-c).

by using RAS. A qualitative indication of the higher strength of the RS parts is the larger number of broken pieces after the bending test, as illustrated in Fig. 6(a-c). The fracture toughness was $K_{Ic} = 4.25 \pm 0.37$ MPa $m^{1/2}$ for RS1 and $K_{Ic} = 4.18 \pm 0.37$ MPa $m^{1/2}$ for RS2, is of the same order of magnitude as that measured in CS ($K_{Ic} = 3.83 \pm 0.18$ MPa $m^{1/2}$) alumina.

4. Conclusions

In summary, here we demonstrate the feasibility of using Radiation-Assisted Sintering (RAS) as an efficient method for rapid consolidation of 3D-printed complex-shaped ceramics. When combined with 3D-printing, RAS enables advanced engineering of dense and strong ceramic architectures for cutting-edge applications manufactured from commercial feedstocks. It is shown how 3D-printed alumina components can be densified and sintered, retaining a fine-grained, homogeneous and dense microstructure (grain size < 500 nm), an order of magnitude finer when compared to conventionally sintered alumina ceramic counterparts (grain sizes of ~ 5.3 μm). The decrease in grain size led to a significant increase in strength, following the predictions of Griffith theory of brittle fracture. The present study opens the path to employ RAS to control the microstructure of 3D-printed parts with the potential of not only enhancing their mechanical but also functional properties, which can be applied to material systems such as biomedical, magnetic, optical, catalytic (porous) materials, thin films and electroceramics.

CRediT authorship contribution statement

Bermejo Raúl: Writing – original draft, Validation, Supervision, Conceptualization. **Hofer Anna-Katharina:** Writing – review & editing, Writing – original draft, Visualization, Methodology, Investigation, Conceptualization. **Kocjan Andraž:** Writing – review & editing, Visualization, Validation, Supervision, Methodology, Investigation, Conceptualization.

Declaration of Competing Interest

The authors declare that they have no known competing financial interests or personal relationships that could have appeared to influence

the work reported in this paper.

Data availability

Data will be made available on request.

Acknowledgment

The funding for this research was provided by the European Research Council (ERC) excellent science grant "CERATEXT" through Horizon 2020 program under contract 817615. A.K. acknowledges The Slovenian Research Agency for funding through Research program P2–0087 and Fellowship to visit ERC Grantee (5110–1/2019–50). The company Lithoz GmbH is gratefully acknowledged for providing the materials for 3D-printing. We acknowledge I. Kraleva and G. Hawranek (Department of Materials Science, Montanuniversitaet Leoben, Leoben, Austria) for the support in scanning electron microscopy and microstructural analysis. Sandra Drev (Center for Electron Microscopy and Microanalysis, Jožef Stefan Institute, Ljubljana, Slovenia) is acknowledged for the support regarding the preparation and analysis of samples in transmission electron microscopy. The authors are grateful to Aljaž Iveković for graphic design of Fig. 1d. The company Lithoz GmbH (1060 Vienna, Austria) is acknowledge for providing the suspensions for 3D-printing.

Appendix A. Supporting information

Supplementary data associated with this article can be found in the online version at doi:10.1016/j.addma.2022.103141.

References

[1] Y.-M. Chiang, D.P. Birnie, W.D. Kingery (Eds.), Physical Ceramics: Principles for Ceramic Science and Engineering, John Wiley & Sons, Inc, 1997.
[2] A. Zocca, P. Colombo, C.M. Gomes, J. Günster, Additive manufacturing of ceramics: issues, potentialities, and opportunities, J. Am. Ceram. Soc. 98 (2015) 1983–2001, https://doi.org/10.1111/jace.13700.
[3] J. Deckers, J. Vleugels, J.-P. Kruth, Additive manufacturin of ceramics: a review, KU Lueven (2014), https://doi.org/10.4416/JCST2014-00032.
[4] Z. Chen, Z. Li, J. Li, C. Liu, C. Lao, Y. Fu, C. Liu, Y. Li, P. Wang, Y. He, C. Lao, 3D printing of ceramics: A review, J. Eur. Ceram. Soc. 39 (2019) 661–687, https://doi.org/10.1016/j.jeurceramsoc.2018.11.013.
[5] I. Özden, A. Iveković, A. Kocjan, Additive manufacturing of ceramics from thermoplastic feedstocks, Open Ceram. 6 (2021), 100129, https://doi.org/10.1016/j.oceram.2021.100129.
[6] A. Zocca, P. Colombo, J. Günster, T. Mühler, J.G. Heinrich, Selective laser densification of lithium aluminosilicate glass ceramic tapes, Appl. Surf. Sci. 265 (2013) 610–614, https://doi.org/10.1016/j.apsusc.2012.11.058.
[7] F42 Committee, Terminology for Additive Manufacturing Technologies, ASTM International, West Conshohocken, PA.
[8] N. Travitzky, A. Bonet, B. Dermeik, T. Fey, I. Filbert-Demut, L. Schlier, T. Schlordt, P. Greil, Additive manufacturing of ceramic-based materials, Adv. Eng. Mater. 16 (2014) 729–754, https://doi.org/10.1002/adem.201400097.
[9] J.H.M. Schwentenwein, Additive manufacturing of dense alumina ceramics, Int. J. Appl. Ceram. Technol. 12 (2015) 1–7, https://doi.org/10.1111/ijac.12319.
[10] M.N. Rahaman , Sintering of Ceramics, CRC Press, - libgen.lc, CRC Press, Taylor & Francis Group, 6000 Broken Sound Parkway NW, Suite 300, 2007.
[11] A.S.G.L. Messing, Toward pore-free ceramics, Science 322 (2008) 381–383, https://doi.org/10.1126/science.1162962.
[12] Z. Shen, M. Johnsson, Z. Zhao, M. Nygren, Spark plasma sintering of alumina, J. Am. Ceram. Soc. (2002) 1921–1927.
[13] M. Cologna, B. Rashkova, R. Raj, Flash sintering of nanograin zirconia in <5 s at 850°C, J. Am. Ceram. Soc. 93 (2010) 3556–3559, https://doi.org/10.1111/j.1551-2916.2010.04089.x.
[14] R.I. Todd, E. Zapata-Solvas, R.S. Bonilla, T. Sneddon, P.R. Wilshaw, Electrical characteristics of flash sintering: thermal runaway of Joule heating, J. Eur. Ceram. Soc. 35 (2015) 1865–1877, https://doi.org/10.1016/j.jeurceramsoc.2014.12.022.
[15] J. Guo, H. Guo, A.L. Baker, M.T. Lanagan, E.R. Kupp, G.L. Messing, C.A. Randall, Cold sintering: a paradigm shift for processing and integration of ceramics, Angew. Chem. Int. Ed. Engl. 55 (2016) 11457–11461, https://doi.org/10.1002/anie.201605443.
[16] A.S.F. Bouville, Geologically-inspired strong bulk ceramics made with water at room temperature, Nat. Commun. 8 (2017) 14655, https://doi.org/10.1038/ncomms14655.
[17] M. Biesuz, S. Grasso, V.M. Sglavo, What's new in ceramics sintering? A short report on the latest trends and future prospects, Curr. Opin. Solid State Mater. Sci. 24 (2020), 100868, https://doi.org/10.1016/j.cossms.2020.100868.
[18] C. Wang, W. Ping, Q. Bai, H. Cui, R. Hensleigh, R. Wang, A.H. Brozena, Z. Xu, J. Dai, Y. Pei, C. Zheng, G. Pastel, J. Gao, X. Wang, H. Wang, J.-C. Zhao, B. Yang, X. Zheng, J. Luo, Y. Mo, B. Dunn, L. Hu, A general method to synthesize and sinter bulk ceramics in seconds, Science (2020) 521–526.
[19] X.-H.W.I. Wei Chen, Sintering dense nanocrystalline ceramics without final-stage grain growth, Nature (2000) 168–171.
[20] R. Chaim, M. Levin, A. Shlayer, C. Estournes, Sintering and densification of nanocrystalline ceramic oxide powders: a review, Adv. Appl. Ceram. 107 (2008) 159–169, https://doi.org/10.1179/174367508×297812.
[21] M. Kermani, J. Dong, M. Biesuz, Y. Linx, H. Deng, V.M. Sglavo, M.J. Reece, C. Hu, S. Grasso, Ultrafast high-temperature sintering (UHS) of fine grained α-Al2O3, J. Eur. Ceram. Soc. 41 (2021) 6626–6633, https://doi.org/10.1016/j.jeurceramsoc.2021.05.056.
[22] L.F.E.A. Olevsky, Impact of thermal diffusion on densification during SPS, J. Am. Ceram. Soc. 92 (2009) S122–S132, https://doi.org/10.1111/j.1551-2916.2008.02705.x.
[23] E.O.W.L. Bradbury, Production of SiC–C composites by free-pressureless spark plasma sintering (FPSPS, Scr. Mater. 63 (2010) 77–80, https://doi.org/10.1016/j.scriptamat.2010.03.009.
[24] A. Kocjan, M. Logar, Z. Shen, The agglomeration, coalescence and sliding of nanoparticles, leading to the rapid sintering of zirconia nanoceramics, Sci. Rep. 7 (2017) 2541, https://doi.org/10.1038/s41598-017-02760-7.
[25] D. Kuscer, A. Kocjan, M. Majcen, A. Meden, K. Radan, J. Kovač, B. Malič, Evolution of phase composition and microstructure of sodium potassium niobate –based ceramic during pressure-less spark plasma sintering and post-annealing, Ceram. Int. 45 (2019) 10429–10437, https://doi.org/10.1016/j.ceramint.2019.02.102.
[26] R.L. Penn, G. Oskam, T.J. Strathmann, P.C. Searson, A.T. Stone, D.R. Veblen, Epitaxial assembly in aged colloids, J. Phys. Chem. B 105 (2001) 2177–2182, https://doi.org/10.1021/jp003570u.
[27] R.L. Penn, Kinetics of oriented aggregation, J. Phys. Chem. B ((2004) 12707–12712.
[28] Z. Shen, Y. Xiong, T. Höche, D. Salamon, Z. Fu, L. Belova, Ordered coalescence of nanocrystals: a path to strong macroporous nanoceramics, Nanotechnology 21 (2010), 205602, https://doi.org/10.1088/0957-4484/21/20/205602.
[29] Z.S.J. Hu, Grain growth by multiple ordered coalescence of nanocrystals during spark plasma sintering of SrTiO3 nanopowders, Acta Mater. 60 (2012) 6405–6412, https://doi.org/10.1016/j.actamat.2012.08.027.
[30] R. Chaim, Densification mechanisms in spark plasma sintering of nanocrystalline ceramics, Mater. Sci. Eng.: A 443 (2007) 25–32, https://doi.org/10.1016/j.msea.2006.07.092.
[31] W. Ji, J. Zhang, W. Wang, Z. Fu, R.I. Todd, The microstructural origin of rapid densification in 3YSZ during ultra-fast firing with or without an electric field, J. Eur. Ceram. Soc. 40 (2020) 5829–5836, https://doi.org/10.1016/j.jeurceramsoc.2020.07.027.
[32] Z.S.D. Salamon, Pressure-less spark plasma sintering of alumina, Mater. Sci. Eng.: A 475 (2008) 105–107, https://doi.org/10.1016/j.msea.2007.01.162.
[33] D.S.B. Heidary, M. Lanagan, C.A. Randall, Contrasting energy efficiency in various ceramic sintering processes, J. Eur. Ceram. Soc. 38 (2018) 1018–1029, https://doi.org/10.1016/j.jeurceramsoc.2017.10.015.
[34] M. Schwentenwein, P. Schneider, J. Homa, Lithography-Based Ceramic Manufacturing: A Novel Technique for Additive Manufacturing of High-Performance Ceramics, 13th Int. Ceram. Congr. - Part B, Trans. Tech. Publ. LtdSwitzerland (2014) 60–64.
[35] EN-623–2, Advanced technical ceramics - Monolithic ceramics - General and textural properties - Part 2. Determination of density and porosity, 1994.
[36] EN 843–4, Advanced technical ceramics -Monolithic ceramics - mechanical properties at room temperature - Part 4: Vickers, Knoop and Rockwell superficial hardness tests, 1994.
[37] ISO/FDIS, Fine ceramics (advanced ceramics, advanced technical ceramics) - Test methods for fracture toughness of monolithic ceramics - Single-edge V-notch beam (SEVNB) method, 2008.
[38] W. Weibull, A. Statistical Distribution, Function of wide Applicability, J. Appl. Mech. (1951) 293–297.
[39] EN 843–5, Advanced technical ceramics - Monolithic ceramics - Mechanical tests at room temperature - Part 5: Statistical analysis, 1997.
[40] A.-K. Hofer, I. Kraleva, R. Bermejo, Additive manufacturing of highly textured alumina ceramics, Open Ceram. 5 (2021), 100085, https://doi.org/10.1016/j.oceram.2021.100085.
[41] S.B.I.-J. Bae, Abnormal Grain Growth of Alumina, J. Am. Ceram. Soc. (1997) 1149–1156.
[42] A.A. Griffith, The Phenomena of Rupture and Flow in Solids, R. Soc. (1921) 163–198.
[43] A. Börger, P. Supancic, R. Danzer, The ball on three balls test for strength testing of brittle discs: stress distribution in the disc, J. Eur. Ceram. Soc. (2002) 1425–1436.
[44] A. Börger, P. Supancic, R. Danzer, The ball on three balls test for strength testing of brittle discs: Part II: analysis of possible errors in the strength determination, J. Eur. Ceram. Soc. 24 (2004) 2917–2928, https://doi.org/10.1016/j.jeurceramsoc.2003.10.035.
[45] Z.S.D. Li, Sintering by intense thermal radiation (SITR): A study of temperature distribution by simulation and experiments, J. Eur. Ceram. Soc. 35 (2015) 3303–3309, https://doi.org/10.1016/j.jeurceramsoc.2015.03.021.
[46] A.J. Haslam, S.R. Phillpot, D. Wolf, d. Moldovan, H. Gleiter, Mechanisms of grain growth in nanocrystalline fcc metals by molecular-dynamics simulation, Mater. Sci. Eng.: A (2001) 293–312.

[47] R. Chaim, R. Marder-Jaeckel, J.Z. Shen, Transparent YAG ceramics by surface softening of nanoparticles in spark plasma sintering, Mater. Sci. Eng.: A 429 (2006) 74–78, https://doi.org/10.1016/j.msea.2006.04.072.
[48] Y.V. Milman, S.I. Chugunova, I.V. Goncharova, T. Chudoba, W. Lojkowski, W. Gooch, Temperature dependence of hardness in silicon-carbide ceramics with different porosity, Int. J. Refract. Met. Hard Mater. (1999) 361–368.
[49] W. Duckworth, Discussion of Ryshkewitch, Pap. J. Am. Ceram. Soc. (1953) 68.
[50] J.P. Singh, A.V. Virkar, D.K. Shetty, R.S. Gordon, Strength-grain size relations in polycrystalline ceramics, J. Am. Ceram. Soc. (1979) 179–183.
[51] R.W. Rice, S.W. Freiman, J.J. Mecholsky Jr., The dependence of strength-controlling fracture energy on the flaw-size to grain-size ratio, J. Am. Ceram. Soc. (1980) 129–136.
[52] J. Schlacher, A.-K. Hofer, S. Geier, I. Kraleva, R. Papšík, M. Schwentenwein, R. Bermejo, Additive manufacturing of high-strength alumina through a multi-material approach, Open Ceram. 5 (2021), 100082, https://doi.org/10.1016/j.oceram.2021.100082.

Supplementary Information

High-strength lithography-based additive manufacturing of ceramic components with rapid sintering

Anna-Katharina Hofer[1], Andraž Kocjan[2], Raúl Bermejo[1]

[1]Department of Materials Science, Montanuniversitaet Leoben, Franz Josef-Strasse 18, A-8700 Leoben, Austria

[2]Department for Nanostructured Materials, Jožef Stefan Institute, Jamova 39, Sl-1000 Ljubljana, Slovenia

Pore Elimination

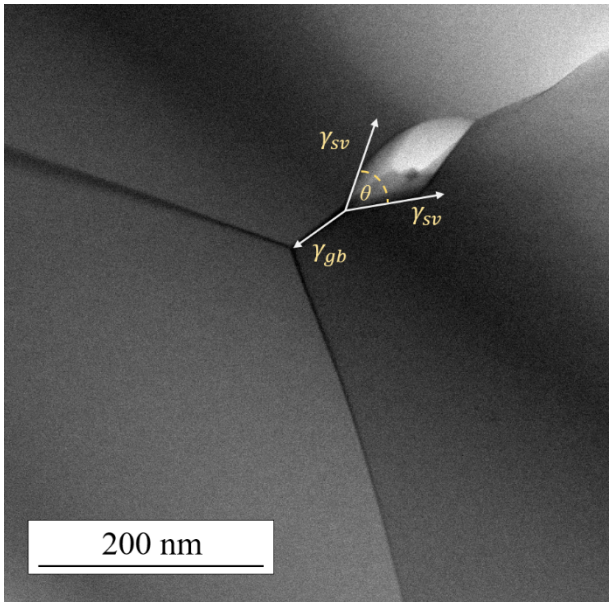

Supplementary figure S1. Elimination of lenticular pore due to low dihedral angles. γ_{sv} represents the surface tension occurring at the solid-vapour interface and γ_{gb} the surface tension at the solid-solid interface. θ describes the dihedral angle.

Equation (1) describes the correlating angle θ [rad] (=dihedral angle) between the surface tension [N/m] of a (i) grain boundary (γ_{gb}) and (ii) solid-vapour interface (γ_{sv}).

$$\cos\left(\frac{\theta}{2}\right) = \frac{\gamma_{gb}}{2\gamma_{sv}} \qquad (1)$$

At a dihedral angle of $\theta \leq 120\,°$ pore shrinkage occurs, leading to an equilibrium state where γ_{gb} equals γ_{sv}.[158]

Determination of the Weibull distribution

To evaluate the stress to failure σ_f for Ball-on-Three-Ball tested samples can be calculated as follows:

$$\sigma_f = f\left(\frac{t}{R}, \frac{R_a}{R}, \nu\right) \cdot \frac{F}{t^2} \quad (2)$$

where f is a dimensionless factor, considering (i) the sample geometry t/R, (ii) the support geometry R_a/R and (iii) the Poisson's ratio ν. Regarding (i) t is the thickness and R the radius of the disc-shaped sample in [m]. For (ii) R_a/R, R_a is the apparent radius of the contact points of the testing balls at the sample in [m]. F describes the maximum load at fracture in [N].

For the evaluation of factor f, $\nu = 0.23$ was used for pure alumina, resulting in a f-value of ~ 1.8.[159,160]

For the Weibull distribution the stress to failure values (σ_f) are plotted versus the probability of failure $F(\sigma)$ in [%] which is determined according to equation (3):

$$F(\sigma) = 1 - exp\left[-\left(\frac{\sigma_f}{\sigma_0}\right)^m\right] \quad (3)$$

where σ_0 is the characteristic strength in [MPa] and m the dimensionless Weibull modulus m [-].

The Weibull modulus m can be evaluated with the Maximum–Likelihood-method, applying following approximation formula:

$$\frac{\sum_{i=}^{N}[\ln(\sigma_{f,i}) \cdot \sigma_{f,i}^m]}{\sum_{i=}^{N} \sigma_{f,i}^m} - \frac{1}{N}\sum_{i=}^{N} \ln\left(\sigma_{f,i}\right) - \frac{1}{m} = 0 \quad (4)$$

Where N is the total number of tested samples, $\sigma_{f,i}$ represents the stress to failure for a particular sample in [MPa] and i is the running index for the number of specimen. The determination of the characteristic strength σ_0 was evaluated as follows:[161,162]

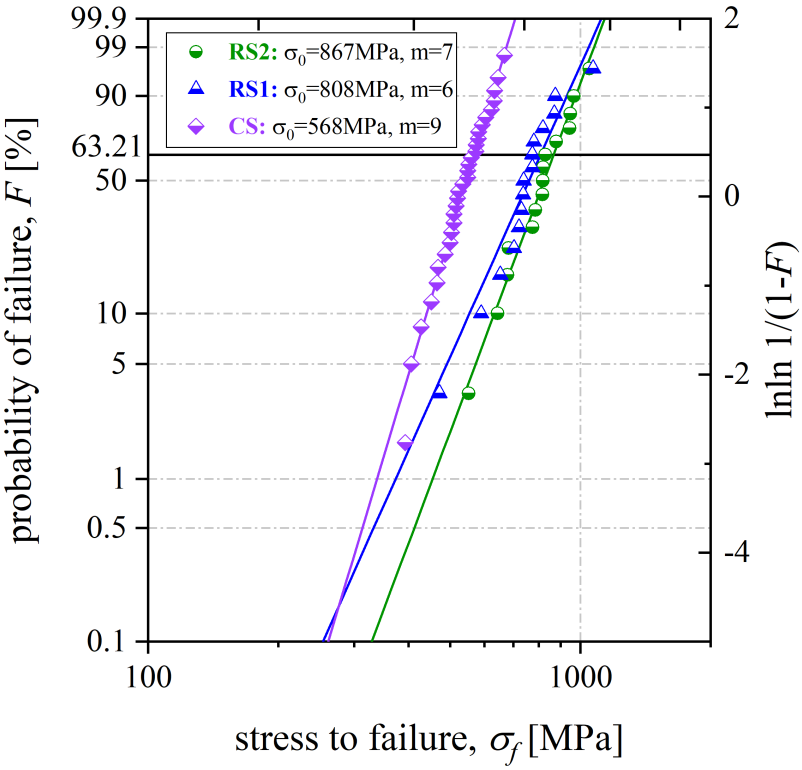

Supplementary figure S2. Weibull distribution for selected sintering parameters. Measured stress to failure stresses σ_f are plotted versus the probability of failure F. The values for rapid sintering parameters RS2: T_{max} = 1500 °C and t_{dwell} = 8 min are indicated in green; RS1: T_{max} = 1600 °C and t_{dwell} = 2 minutes in blue; and the conventionally sintering parameters CS: T_{max} = 1600 °C and t_{dwell} = 6 hours in purple.

$$\sigma_0 = \left[\frac{1}{N}\left(\sum_{i=1}^{N} \sigma_{f,i}^{m}\right)\right]^{1/m} \qquad (5)$$

The values of the stress to failure σ_f are plotted versus the probability of failure, figure S3. The characteristic strength σ_0 describes the applied stress, with a probability of failure of $F \sim 63$ %.

Determination of Vickers hardness

$$HV = 1.8544 \cdot \frac{F}{d^2} \quad (6)$$

Where *HV* is the hardness after Vickers, where a pyramidal diamond indenter was used. *F* is the applied load in [kg]. *d* is the average value of the two diagonals in [mm].[163]

To obtain a hardness value in GPa, following equation was used:

$$HV\ [GPa] = 0.00981 \cdot \frac{2F}{d^2} \quad (7)$$

Determination of fracture toughness after SEVNB

$$K_{Ic,SEVNB} = \frac{F}{B\sqrt{W}} \cdot \frac{S_1 - S_2}{W} \cdot \frac{3\sqrt{\alpha}}{2(1-\alpha)^{1.5}} \cdot Y^* \quad (8)$$

where $K_{Ic,SEVNB}$ is the evaluated fracture toughness according to SEVNB in [MPa], *F* is the applied load in [N], *B* the width of the prismatic test bar in [mm] and *W* the thickness in [mm]. S_1 describes the lower and S_2 the upper span width of the 4-point-bending testing set-up in [mm]. α is the ratio between the thickness (*W* in [mm]) and the average notch length *a* [mm], see equ. (9). Y^* describes the geometrical factor [-], calculated according to equation (10).[164]

$$\alpha = \frac{W}{a} \quad (9)$$

$$Y^* = 1.9887 - 1.326\alpha - \frac{(3.49 - 0.68\alpha + 1.35\alpha^2)\alpha(1-\alpha)}{(1+\alpha)^2} \quad (10)$$

References

[1] M. Schwentenwein, P. Schneider, J. Homa, Lithography-Based Ceramic Manufacturing: A Novel Technique for Additive Manufacturing of High-Performance Ceramics, in: 13th International Ceramics Congress - Part B, Trans Tech Publications LtdSwitzerland, 2014, pp. 60–64.

[2] J.H. M. Schwentenwein, Additive Manufacturing of Dense Alumina Ceramics, Int. J. Appl. Ceram. Technol. 12 (2015) 1–7. https://doi.org/10.1111/ijac.12319.

[3] M.N. Rahaman, Sintering of Ceramics (2007, CRC Press) - libgen.lc, CRC Press, Taylor & Francis Group, 6000 Broken Sound Parkway NW, Suite 300, 2007.

[4] A. Börger, P. Supancic, R. Danzer, The ball on three balls test for strength testing of brittle discs: stress distribution in the disc, Journal of the European Ceramic Society (2002) 1425–1436.

[5] A. Börger, P. Supancic, R. Danzer, The ball on three balls test for strength testing of brittle discs: Part II: analysis of possible errors in the strength determination, Journal of the European Ceramic Society 24 (2004) 2917–2928. https://doi.org/10.1016/j.jeurceramsoc.2003.10.035.

[6] W. Weibull, A Statistical Distribution Function of wide Applicability, Journal of Applied Mechanics (1951) 293–297.

[7] EN 843-5, Advanced technical ceramics - Monolithic ceramics - Mechanical tests at room temperature - Part 5: Statistical analysis, 1997.

[8] EN 843-4, Advanced technical ceramics -Monolithic ceramics - mechanical properties at room temperature - Part 4: Vickers, Knoop and Rockwell superficial hardness tests, 1994.

[9] ISO 23146, Fine ceramics (advanced ceramics, advanced technical ceramics) - Test methods for fracture toughness of monolithic ceramics - Single-edge V-notch beam (SEVNB) method, 2008.

Publication E

Templated Grain Growth in rapid sintered 3D-printed textured alumina ceramics

Anna-Katharina Hofer[1], Andraž Kocjan[2], Raúl Bermejo[1]

[1]Department of Materials Science, Montanuniversitaet Leoben, Franz Josef-Strasse 18, A-8700 Leoben, Austria

[2]Department for Nanostructured Materials, Jožef Stefan Institute, Jamova 39, Sl-1000 Ljubljana, Slovenia

(Submitted for publication)

Templated grain growth in rapid sintered 3D-printed alumina ceramics

Anna-Katharina Hofer[1], Andraž Kocjan[2], Raul Bermejo[1,*]

[1]Department of Materials Science, Montanuniversitaet Leoben, Franz Josef-Strasse 18, A-8700 Leoben, Austria

[2]Department for Nanostructured Materials, Jožef Stefan Institute, Jamova 39, Sl-1000 Ljubljana, Slovenia

[*]Corresponding author: raul.bermejo@unileoben.ac.at

Abstract

Textured microstructures in ceramics have gained interest due to their beneficial effect on structural and functional properties. For instance, morphologically textured grains in alumina-based ceramics can increase their damage tolerance. Texturing of alumina ceramics may be achieved through templated grain growth (TGG) occurring during sintering at high temperatures with prolonged dwell times (hours) and may be further enhanced by the presence of a liquid phase. In this study, we demonstrate the feasibility of texturing 3D-printed alumina ceramics within minutes by combining rapid heating (~ 450 °C/min) and short dwell times (< 20 min). The effect of sintering temperature and dwell time is investigated on samples with and without liquid phase. Experimental findings show highest texture degree for samples rapid sintered at 1600 °C for 16 min, opening the path for tailoring the microstructure of 3D-printed ceramics using pressure-less rapid sintering protocols.

1. Introduction

A number of ceramic materials have anisotropic crystal structures. As a consequence, physical, mechanical as well as thermal or electrical properties may show anisotropic behaviour, regarding the direction of application of mechanical or electrical load, respectively. To exploit the enhanced properties of a certain plane in polycrystalline materials, techniques have been developed for the fabrication of textured microstructures, where grains may grow along a preferential direction during the sintering step.[1,2] One strategy is to promote templated grain growth (TGG), where large aspect ratio particles grow at the expense of finer particles (Ostwald ripening), the grain growth being enhanced by the presence of a liquid phase.[3,4] TGG is usually performed with relatively slow heating rates and prolonged dwell times during sintering.[3,5,6] The result is a textured polycrystalline microstructure, where tabular grains show a preferential crystallographic and morphologic orientation, which resembles the “brick-and-mortar” structure found in mollusc shells.[7]

TGG has been utilized to develop textured microstructures in various ceramics. Among them, alumina ceramics for structural applications have been extensively exploited in order to tailor microstructures with grains aligned in the preferential orientation [001].[8–10] Forming technologies such as tape-casting and, more recently, 3D-printing have been successfully employed to align the platelets in a preferential direction by shear forces during casting and printing, respectively.[3,4,6,10,11] It has been shown that the fracture resistance of alumina can be enhanced through morphologic and crystallographic texture.[9,12–14] An increase in toughness between 15% and 30% has been reported on tape cast textured alumina samples, associated with crack deflection mechanisms during crack propagation.[10,14] Recent work has also demonstrated the potential of textured microstructures to enhance the mechanical strength of 3D-printed ceramic parts.[13] A biaxial characteristic strength of 640 MPa was measured on textured alumina, compared to 570 MPa on equiaxed alumina, despite the lower density of the former, i.e. ~ 93 % versus ~ 99 %, respectively.

Processing of alumina ceramics with a textured microstructure involves the homogeneous incorporation of high aspect ratio templates (e.g. alumina platelets), typically < 10 vol%, into a fine-grained powder matrix. It has been shown that properties such as relative density, degree of texture or grain morphology of textured microstructures developed through TGG may be affected by (i) the loading of high aspect ratio templates, (ii) the content of liquid phase (LP) as well as (iii) the sintering temperature and (iv) dwell time.[3,4,6,9,10,15,16] For instance, increasing template loading to > 10 vol% reduces the relative density and grain size.[1,3,9,15,16] Small LP contents (< 1 wt%), with respect to the solids content, have been reported to enhance densification. However, higher contents have shown either no further improvement or even a decrease in relative density.[4,9,10,15,16] In general, TGG of textured alumina with a relative density larger than 90 % has been reported for sintering temperatures above 1450 °C [4,16–18], with the template growth process showing a strong dependency on the sintering time.[5,6,9,15,17,18]

In an attempt to reduce the sintering temperature and time of ceramic parts, rapid sintering strategies have been explored, which commonly involve applying pressure during the densification process. The combination of high heating rates with applied pressure has led to dense ceramic systems of simple (planar) geometries with significantly reduced grain size.[19–24] One example is the use of a field assisted sintering technology (FAST), or spark plasma sintering (SPS), applying electric current and mechanical pressure to reduce sintering time and thus inhibiting grain growth.[24–26] However, when pressure is involved, the sintering of complex 3D parts is compromised. In this regard, recent work of the authors has demonstrated

the feasibility of rapid sintering highly dense 3D-printed alumina parts, with equiaxed microstructures, using an adapted "pressureless" SPS system.[25,27] Homogeneous microstructures were achieved within minutes using high heating rates (~ 450 °C/min), with the corresponding grain growth starting at sintering temperatures above 1500 °C. A preliminary study showed that changing dwell times from 2 min to 8 min, increased the average grain size from ~0.6 µm to ~1.5 µm and the relative density from 97 % to 99 % at 1600 °C.[27] Recent work by Behera et al. reported the Ultra-fast High Temperature Sintering (UHTS) of textured alumina through templated grain growth, where templates were aligned in the green state by magnetically-assisted slip casting (MASC).[28] It was shown that the grain diameter could increase within very short dwell times, i.e. from 10 s to 20 s.

In this paper we report on the feasibility of texturing 3D printed alumina ceramics through high heating rates (~ 450 °C/min) using a pressureless SPS rapid sintering set-up. The microstructural evolution and the degree of texture of alumina with and without a liquid phase is investigated and compared to conventionally sintered and UHTS samples. The fracture response of rapid sintered textured samples is analysed and compared to conventionally sintered textured alumina.

2. Materials and Methods

3D printed alumina (TA) samples were fabricated using a stereolithography process.[6] Two different suspensions were prepared: (i) alumina with addition of sintering additives for liquid phase sintering (TA-LP) and (ii) alumina without sintering additives, resulting in solid state sintering (TA-SS). For both compositions, 2.5 vol% high aspect ratio (~0.1 µm in thickness, 5-16 µm in diameter) α-alumina templates (Rona Flair® White Sapphire, EMD Performance Materials Corp., Darmstadt, Germany) were added to a commercially available 99.99 % high purity α-alumina suspension (LithaLox HP500, Lithoz GmbH, Vienna, Austria). For TA-LP samples in total 0.25 wt% of CaO (added in the form of $Ca(NO_3)_2 \cdot 4H_2O$, ThermoFischer, Kandel, Germany) and SiO_2 (added in the form of $C_8H_{20}O_4Si$, ThermoFischer, Karlsruhe, Germany) were added in a 1:1 molar ratio. The 2.5 vol% templates and the 0.25 wt% sintering additives relate to the content of alumina powder. Samples with dimensions of 3x4x10 mm were built "layer-by-layer" using a 3D printer (model CeraFab 7500, Lithoz GmbH, Vienna, Austria), based on the lithography-based ceramic manufacturing technology (LCM), see Figure 1a.[29–31] The alignment of the templates in the [00 1] direction was achieved due to the shear forces generated in the gap between the fixed doctor blade and the rotating vat during suspension distribution (close-up in Figure 1a.).[6] After printing, the compound consisted of a

polymeric network with embedded ceramic particles. The polymeric content was burned-out at a maximum temperature of 430 °C prior to sintering. Pressure-less rapid sintering was performed in an adapted spark plasma sintering furnace (FUJI SPS Dr. Sinter Lab 322Lx, Dr. SINTER, SPS Syntex Inc., Japan) with a modified graphite die set up, as described in.[26,27,32] Figure 1b shows the set up consisting of three ~ 35 mm diameter graphite cylinders . The central cylinder was hollow, with a wall of thickness ~ 5 mm. Samples were placed inside the cylinder on graphite wool for isolation, to avoid direct contact to the surrounding graphite die and thus possible thermal gradients in the sample. The set up was contacted electrically both at the top and bottom and heated using pulsed, direct electrical current. Sintering was performed under vacuum with a heating rate of 450 °C/min to different maximum temperatures (i.e. 1300 °C, 1400 °C, 1500 °C, and 1600 °C) and using various dwell times (i.e. 2 min, 4 min, 16 min and 64 min), respectively. At least two specimens per sample, with and without liquid phase, were sintered at the different sintering conditions. For comparison, two additional samples were conventionally sintered in air at a maximum sintering temperature of 1600 °C for 6 h and 12 h dwell times, respectively.

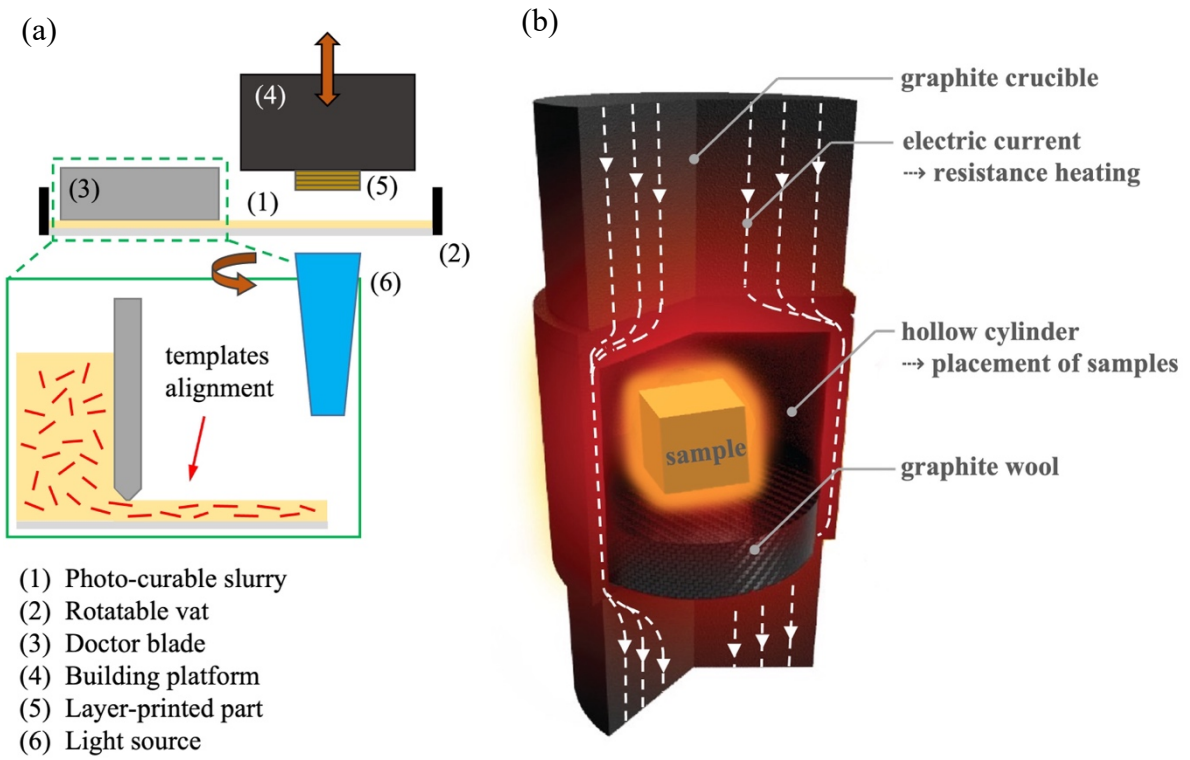

Figure 1: (a) Schematic of the LCM technology with the close-up highlighting the alignment of the templates; **(b)** SPS "pressureless" rapid sintering set-up.

Bulk density was determined using the Archimedes principle.[33] The relative density was calculated assuming a theoretical density of 3.986 g/cm^3 for α-alumina. Microstructural images

were taken with a scanning electron microscope (SEM, JEOL JCM-6000 Plus, NeoscopeTM, JEOL Ltd., Tokyo, Japan). Prior to SEM analysis the side surface of the samples, perpendicular to the z-axis, was polished to 1 µm mirror surface finish (Struers Tegramin-30, Struers GmbH, Willich, Germany). The polished samples were thermally etched for 20 min at 1200 °C or 1400 °C depending on the maximum sintering temperatures of 1300 °C/1400 °C or 1500 °C/1600 °C, correspondingly. The degree of texture was determined using the Lotgering factor (LF), where X-ray diffractometer patterns (Brucker AXS D8 Advance DaVinci, Bruker, Billerica, USA) of a textured and equiaxed microstructure were compared[1].[1,34]

$$LF = \frac{P_{(00l)} - P_0}{1 - P_0} \quad (1)$$

$$\text{with } P_{(00l)} = \frac{\sum I_{(00l)}}{\sum I_{(hkl)}} \quad \text{for textured} \quad (2)$$

$$\text{and } P_0 = \frac{\sum I_{0(00l)}}{\sum I_{0(hkl)}} \quad \text{for equiaxed} \quad (3)$$

where $P_{(00l)}$ and P_0 are the ratios of the intensities for textured and equiaxed materials, respectively. $I_{(00l)}$ and $I_{0(00l)}$ are the intensities of the peaks representing the characteristic (001) peaks, in the case of alumina the (006) and (00 12) at 2θ = 41.6 ° and 2θ = 90.7 °, respectively. Further, $I_{(hkl)}$ and $I_{0(hkl)}$ are the intensities of all characteristic peaks describing the XRD-pattern of α-alumina.

The fracture toughness (K_{Ic}) was determined on five TA-LP samples sintered at 1600 °C and 16 minutes according to the Single-Edge V-Notch Beam method (SEVNB).[35] The notch was introduced parallel to the [000 1] direction of the textured alumina grains. The testing was performed at a displacement rate of 0.5 mm/min and a preload of 7 N with a universal testing machine (Zwick Z010, Zwick GmbH&Co, Ulm, Germany) and data were analysed with the software TestXpertII.

3. Results and discussion

3.1 Density and microstructure

Figure 2 shows the measured relative densities (ρ_{rel}) for the TA-LP and TA-SS samples sintered at different conditions. The relative density increased with increasing sintering temperature. TA-LP samples show substantially higher ρ_{rel} than TA-SS for all sintering temperatures and times, except for 1300 °C, where in both cases the ρ_{rel} remained below 80%. In the case of 1400 °C and 1500 °C the relative density increased with increasing sintering time. However,

[1] A Lotgering factor of $LF = 1$ describes a perfect orientation of grains.

for samples sintered at 1600 °C, the average density measured for 2 and 4 min sintering time was slightly higher than for 16 and 64 min.

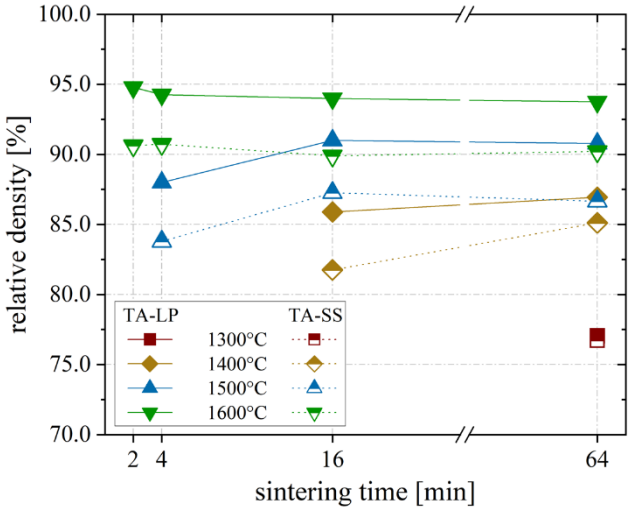

Figure 2: Relative densities of different sintering times for textured alumina sintered with (TA-LP) and without liquid phase (TA-SS) at different temperatures.

Figure 3 shows microstructures corresponding to samples sintered at different maximum temperatures and dwell times. A correlation between relative density (Fig. 2) and microstructural texture (Fig. 3) can be found. It is observed that TGG and consequently a textured microstructure develops when the relative density is ≥ 90 %, as has been reported in literature for alumina ceramics.[16]

Figure 3a. represents the microstructure sintered at 1300 °C for 64 min, where poor densification occurred without significant TGG, whether for TA-SS nor for TA-LP. In the case of TA-LP, the eutectic temperature of the ternary CaO-Al_2O_3-SiO_2 system is reported to be at ~ 1380 °C.[3,9] Consequently at a sintering temperature of 1300 °C no improvement of densification and templated grain growth can be observed in TA-LP due to the lack of the liquid phase formation, resulting in comparable relative densities of ~ 77 % for both TA-LP and TA-SS samples.

At the sintering temperature of 1400 °C relative densities of TA-SS and TA-LP show a significant difference, which is attributed to the formation of the liquid phase during sintering. An increase in grain size of the textured grains can be observed from sintering times of 16 min to 64 min (Fig. 3b.). The microstructures show large high aspect ratio oriented grains embedded in an equiaxed fine grained matrix. However, full texturing was not achieved.

Figure 3c shows microstructures from samples sintered at 1500 °C, for 4, 16 or 64 min, respectively. Whereas a textured microstructure is developed at 16 and 64 min, no texture is

observed at 4 min. The microstructural images in the latter show a “bimodal” grain size distribution, where (individual) high aspect ratio templated grains are embedded in an equiaxed fine grained microstructure, leading to a low relative density for both TA-LP (ρ_{rel} ~ 88 %) and TA-SS (ρ_{rel} ~ 83 %) samples. However, for longer sintering times (i.e. 16 min and 64 min) development of textured microstructures can be observed.

Figure 3d shows the microstructures for TA-LP and TA-SS samples, sintered at 1600 °C at different sintering times (2, 4, 16 and 64 min). It is observed that textured microstructures develop for all sintering times, with the grain size increasing with longer sintering times. For sintering times of 2 and 4 min at 1600 °C, it is observed that smaller equiaxed and randomly oriented grains fill the voids between the textured grains, resulting in a better packing and consequently slightly higher relative density (Fig. 2). Comparing the microstructures of textured alumina with and without liquid phase, the presence of liquid phase enhances diffusion (as in conventional sintering), leading to more densified microstructures, where TA-LP and TA-SS show relative densities of ~ 95 % and ~ 90 %, respectively.

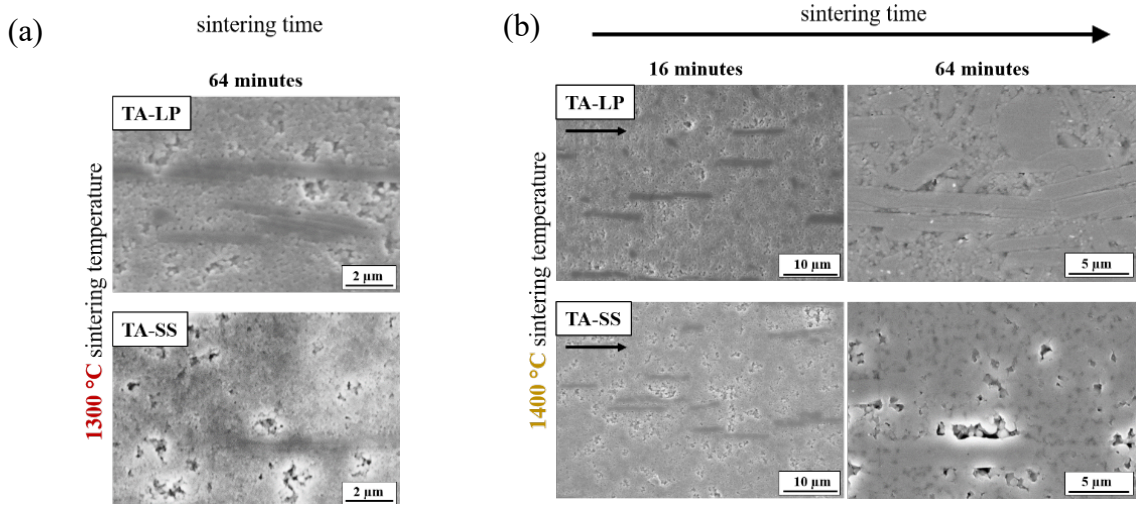

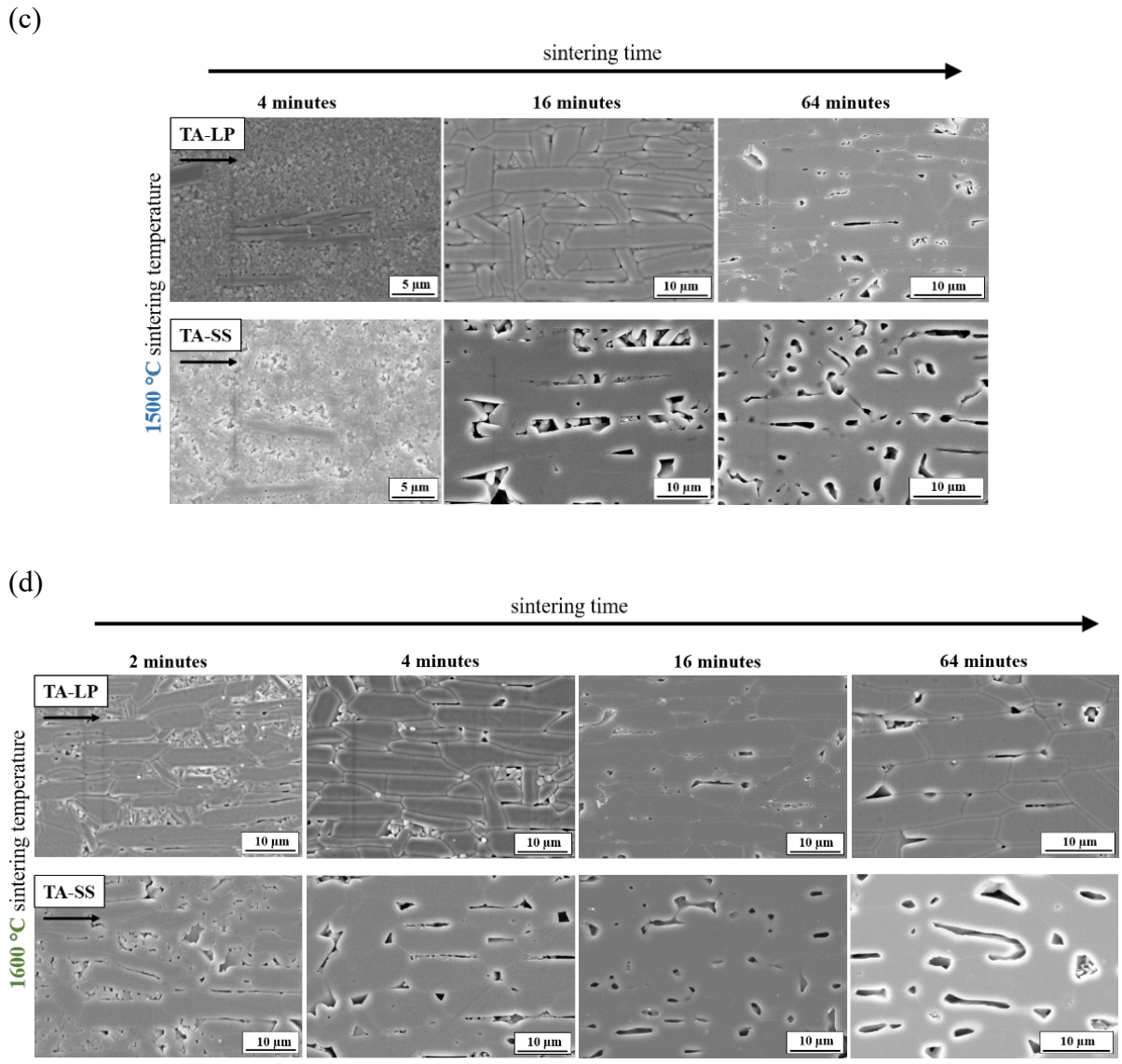

Figure 3: Microstructural images of TA-LP and TA-SS samples, sintered at different sintering temperatures (T) and sintering times (t): **(a)** T = 1300 °C for t = 64 min; **(b)** T = 1400 °C for t = 16 and 64 min; **(c)** T = 1500 °C for t = 4, 16 and 64 min and **(d)** T = 1600 °C for t = 2, 4, 16 and 64 min.

3.2 Texture degree and template aspect ratio

Figure 4 shows the Lotgering factor (LF) of TA-LP and TA-SS samples for the different sintering conditions of maximum temperature and dwell time. For sintering temperatures of 1300 °C, 1400 °C and 1500 °C the determined LF correlate with the observed microstructures (Fig. 3). In microstructures, where TGG hardly occurred (T = 1500 °C and t = 4 min, T = 1400 °C and t = 16 min, and T = 1300 °C and t = 64 min), the LF was below 0.1, indicating no texture development. In the case of 1500 °C only for longer sintering times (16 and 64 min) LF > 0.5 were measured for both TA-LP and TA-SS. LF for samples sintered at 1600 °C (green symbols) increases with increasing sintering time from 2 to 4 min. The lower LF values of ~ 0.32 for TA-LP and ~ 0.44 for TA-SS, for sintering times of 2 min, can be attributed to the

presence of small equiaxed grains in-between the tabular oriented grains (Fig. 3a). For sintering times of 4, 16 and 64 min LF is similar, being LF~ 0.58, ~ 0.62 and ~ 0.64 for TA-LP and ~ 0.64, ~ 0.71 and ~ 0.65 for TA-SS, respectively. Comparing the values for textured alumina samples with and without liquid phase, slightly higher LF values were determined for TA-SS samples. This may be explained by the effect of the liquid phase, enhancing also the growth of fine and randomly oriented agglomerated particles in TA-LP, thus leading to a reduction of the LF.

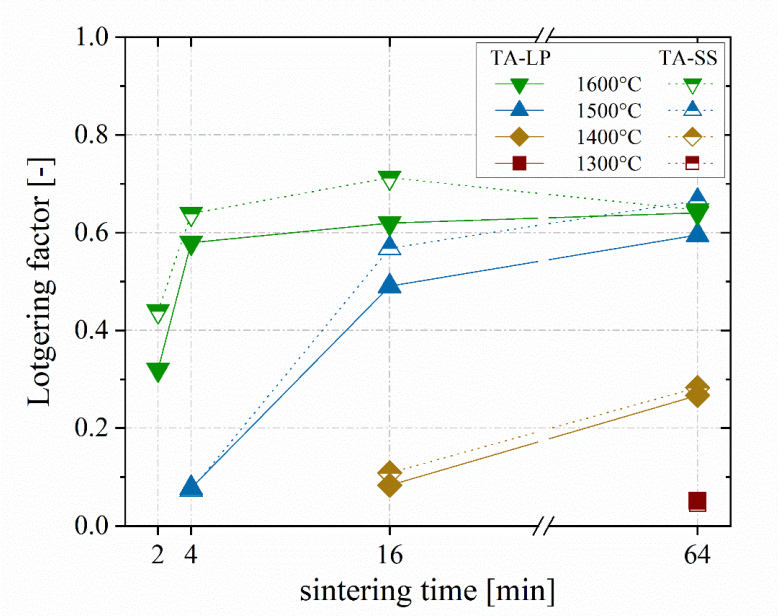

Figure 4: Lotgering factor of TA-LP and TA-SS samples sintered at different maximum temperatures and dwell times.

The morphology of the textured grains was examined in detail in samples sintered at 1600°C, where TGG was clearly visible for all dwell times. Figure 5 shows the aspect ratio of template grains (thickness versus diameter) for different sintering dwell times. The grain diameter for rapid sintered TA-LP and TA-SS show a strong dependency on the sintering time, as observed for textured alumina ceramics during conventionally sintering.[3,4,6,9,36] The increase in grain diameter with dwell times is similar for both TA-LP (light green empty hexagonal symbols) and TA-SS (dark green empty circular symbols) samples. Regarding the thickness, TA-SS grains (dark green full circular symbols) were thicker than TA-LP grains (light green full hexagonal symbols), especially for dwell times longer than 4 min. The smaller grain thickness at 2 min for TA-LP and TA-SS might be attributed to a preliminary state of grain growth, where a bimodal microstructure containing tabular grains and small equiaxed grains is observed (Fig. 3a).

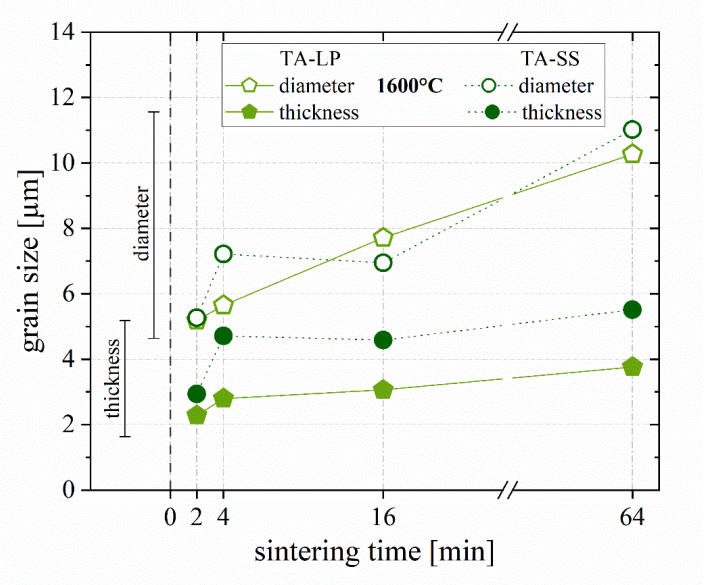

Figure 5: Grain diameter and grain thickness of TA-LP and TA-SS samples as function of sintering time.

It can be concluded that for TA-LP the development of the microstructure is dominated by the growth of templates in *xy*-direction, whereas for TA-SS more significant growth in *z*-direction is observed. A possible explanation may be the smaller diffusion distances associated with lower liquid phase content, as reported in literature for other systems.[10,37] The formation of a liquid phase during sintering causes a separation of the solid particles through a liquid film. As a result, the longer diffusion distances in the case of TA-LP may limit the growth to the planes perpendicular to the (000 1) direction, having higher surface energies.[3] However, during solid state sintering, there is a shorter diffusion path for matter to be transported in between the grains, leading to a rather isotropic growth of both templates and matrix particles.

3.3. Rapid sintering versus conventional sintering

Both grain growth and TGG in ceramics have been associated with prolonged dwell time during the sintering step. In an attempt to enhance the densification rate and limit grain growth high heating rates and reduced sintering (dwell) times have been utilized on alumina ceramics, fabricated using conventional routes (see for instance [19,20,23,24,38,39]). In a previous study, the authors demonstrated the feasibility of pressure-less rapid sintering (~ 450 °C/min) of complex-shaped 3D-printed alumina ceramics, with an average grain size of approximately 500 nm.[27] In the current study, using the same sintering procedure, textured microstructures with exaggerated tabular grains were developed within minutes. In order to compare the textured microstructure of rapid and conventional sintered textured alumina (TA), samples with

the same composition as TA with liquid phase (TA-LP) were sintered in air at a heating rate of 5 °C/min at 1600 °C for 6 and 12 hours, respectively. Figure 6 compares the grain diameter versus relative density for the samples sintered rapidly (TA-LP-RS) and conventionally (TA-LP-CS) at 1600 °C at different dwell times, as well as with data reported in literature.[6,9,15,28,40] We caution the reader that only works reporting comparable data for grain diameter and relative density have been considered for comparison (Table S1 in Supplementary file). All selected references used TGG to achieve textured alumina microstructures, although templates dimensions and content as well as liquid phase content and processing parameters may have been different, as listed in Table S1.

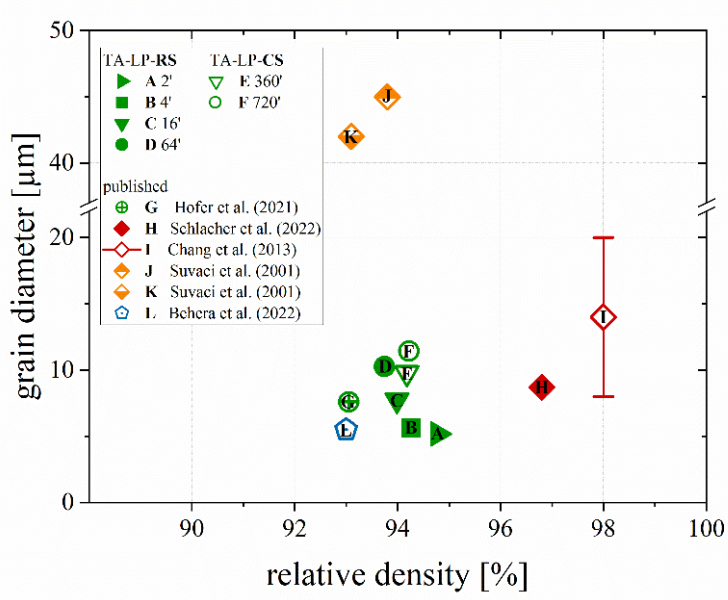

Figure 6: Comparison of textured alumina samples through TGG using rapid or conventional sintering protocols.

First, TA-LP samples of the same composition, both rapid (full green symbols, A-D) and conventional sintered (empty green symbols, E-F) are compared, referred to as TA-LP-RS and TA-LP-CS, respectively. The measured relative density and grain diameter for both TA-LP-CS samples with different sintering times (i.e. 360 min and 720 min) are similar, with sample D (sintering time of 64 min) being almost identical to samples E and F. For shorter sintering times (4 min and 16 min, B and C) the relative density is in the range of that of the TA-LP-CS samples, although a decrease in grain diameter is observed (Fig. 5). In the work of Hofer et al. (G) templates were aligned using the LCM technology and a sintering time of 360 min.[6] The content of liquid phase was the same but a higher volume content of templates (5 vol%) was used. In comparison, TA-LP-RS samples with a sintering time of 16 min (C), having a templates content of 2.5 vol%, developed a similar grain diameter but slightly higher relative densities. The templates content in Schlacher et al. (H) was 5 vol% with a liquid phase content of 0.10 wt

using tape-casting for templates alignment and sintering parameters of 1550 °C for 120 min.[9,40] The tape-cast samples of (H) exhibited a grain diameter comparable to the samples fabricated with LCM, either rapidly or conventionally sintered, but a significantly higher relative density. Chang et al. (I) as well as Suvaci et al. (J, K) also utilized tape-casting for the alignment of templates, but different templates dimensions were selected. For (I) nanoscale precursors (3 x 0.35 µm) were used for TGG; in the case of (J and K) templates with the dimensions of 15-25 x 2 µm were added, whereas in this study templates with dimensions 5-16 x 0.1 µm were employed.[9,36] Both relative density and grain diameter of the tape-cast samples with nanoscale precursors are reported to be respectively higher and larger than on the investigated rapid sintered textured alumina samples. Because of the larger templates used in (J and K), larger grain diameters were achieved with comparable relative densities measured for samples sintered with higher heating rates. Recent work from Behera et al. used an ultrafast high-temperature sintering (UHTS) procedure to achieve textured alumina through TGG.[28] Textured microstructures were obtained at sintering temperatures of ~ 1700 °C with dwell times below 1 min. Templates were aligned through magnetically-assisted slip casting (MASC), where the added magnetic iron oxide nanoparticles (Fe_3O_4, SPION) formed the liquid phase during sintering, instead of CaO-SiO_2, as employed in this investigation and the reported literature. The diameter of the templates is comparable as of the precursors used in our study, although a higher content of 5 vol% templates was used in comparison to 2.5 vol%. With UHTS and the reported sintering parameters, similar grain diameter as for TA-LP-RS with a sintering time of 4 min was achieved. The lower relative density of ~ 93% might be a consequence of the higher template content.[3,9,10]

3.4. Fracture response of rapid sintered textured alumina

The fracture resistance of a rapid sintered textured samples, i.e. TA-LP_1600-16 (sintered at 1600 °C and 16 minutes), was evaluated with the SEVNB method, resulting in a fracture toughness of $K_{Ic} = 3.6 \pm 0.5$ MPa $m^{1/2}$. This value is similar to the fracture toughness of equiaxed alumina, as reported in the literature.[41] However, it is below the fracture toughness of alumina fabricated with tape casting followed by conventional sintering (TA-CS, 5 °C/min, 1550 °C, 2 hours), where a K_{Ic} of 5.1 ± 0.2 MPa $m^{1/2}$ was measured.[42] The lower fracture toughness may be explained by the different aspect ratio of the textured grains (AR) and the Lotgering factor (LF). For TA-LP_1600-16 AR equals 2.5 and LF = 0.62, whereas for TA-CS AR was determined to be 5.2 and LF = 0.77, respectively. Nevertheless, the textured morphology of the template alumina grains affects the crack propagation (Fig. 7), where crack

deflection along the textured grains may be observed. The weaker development of tabular shaped and oriented grains may be a result of templates fracture caused by suspension preparation, the higher viscosity of LCM - compared to tape casting – suspensions, and suspension distribution during the printing process. The smaller size of templates may lead to a weaker alignment in the green state and lower templated grain growth in the preferential x- and y-directions. Further research is needed to optimize the texture degree and mechanical properties of rapid sintered textured alumina.

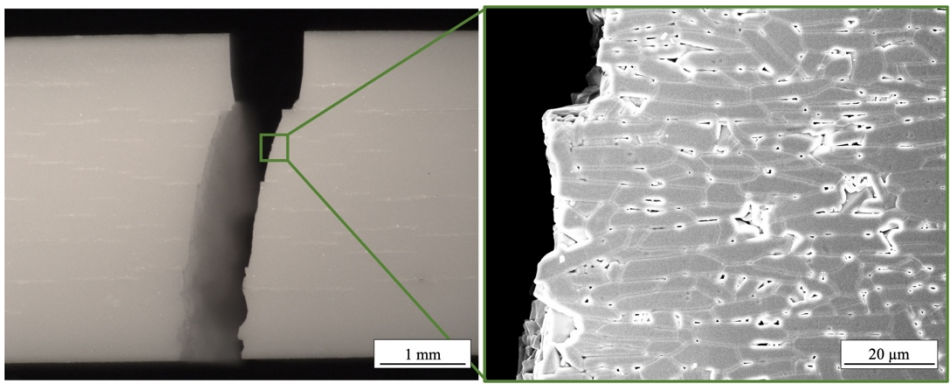

Figure 7: Fracture behaviour of a TA-LP sample rapid sintered at a maximum temperature of 1600 °C and 16 minutes sintering time.

In summary, the crystallographic and morphological texture obtained on 3D-printed alumina using rapid sintering protocols is comparable to textured alumina sintered either with conventional routes or UHTS. In a previous work it was shown that 3D-printed textured alumina ceramics with relative density of ~ 93% exhibited comparable strength values as for equiaxed microstructures, both sintered under conventional routes. The high texture degree and relative density (ca. 94 %) obtained in this work on 3D-printed alumina parts, using rapid sintering protocols, suggests comparable mechanical behaviour, and will be further investigated in future work.

4. Conclusion

Textured alumina microstructures, prepared by aligning templates in a stereolithographic 3D-printing process, were obtained through pressure-less rapid sintering protocols, using ~ 450 °C/min heating rates with few minutes dwell time at temperatures above 1500 °C. The addition of sintering additives to induce liquid phase sintering increased the relative density of the (textured) alumina samples by approximately 5 %, as well as the ratio of diameter to thickness of tabular grains, especially for higher sintering temperatures. The optimal combination of high relative density and texture degree was obtained for samples sintered at

1600 °C with 16 min dwell time, resulting in ρ_{rel} ~ 94% and LF ~ 0.6 for liquid phase sintered samples and in ρ_{rel} ~ 90 % and LF ~ 0.7 for solid state sintered samples. The fracture toughness evaluated on the sample rapid sintered with a liquid phase reached that of equiaxed alumina, but was lower than conventionally sintered textured alumina. The feasibility of texturing alumina ceramics within minutes opens the path for controlling both grain size and grain morphology in 3D printed ceramic parts and may be extended to other ceramic materials and systems, for both structural and functional applications.

Acknowledgements

The funding for this research was provided by the European Research Council (ERC) excellent science grant "CERATEXT" through Horizon 2020 program under contract 817615. The company Lithoz GmbH (1060 Vienna, Austria) is acknowledge for providing the suspensions for 3D-printing.

References

[1] G.L. Messing, S. Poterala, Y. Chang, T. Frueh, E.R. Kupp, B.H. Watson, R.L. Walton, M.J. Brova, A.-K. Hofer, R. Bermejo, R.J. Meyer, Texture-engineered ceramics—Property enhancements through crystallographic tailoring, Journal of Materials Research 32 (2017) 3219–3241. https://doi.org/10.1557/jmr.2017.207.

[2] F. Bouville, Strong and tough nacre-like aluminas: Process–structure–performance relationships and position within the nacre-inspired composite landscape, J. Mater. Res. 35 (2020) 1076–1094. https://doi.org/10.1557/jmr.2019.418.

[3] M.M. Seabaugh, I.H. Kerscht, G.L. Messing, Texture Development by Templated Grain Growth in Liquid-Phase-Sintered α-Alumina, Journal of the American Ceramic Society (1997) 1181–1188.

[4] M.M. Seabaugh, G.L. Messing, M.D. Vaudin, Texture Development and Micrsotructure Evolution in Liquid-Phase-Sintered α-Alumina Ceramics Prepared by Templated Grain Growth, Journal of the American Ceramic Society (2000) 3109–3116.

[5] M.N. Rahaman, Sintering of Ceramics, CRC Press, Taylor&Francis Group, 2007.

[6] A.-K. Hofer, I. Kraleva, R. Bermejo, Additive manufacturing of highly textured alumina ceramics, Open Ceramics 5 (2021) 100085. https://doi.org/10.1016/j.oceram.2021.100085.

[7] S. Deville, E. Saiz, R.K. Nalla, A.P. Tomsia, Freezing as a path to build complex composites, Science 311 (2006) 515–518. https://doi.org/10.1126/science.1120937.

[8] Y. Chang, R. Bermejo, Raul, G.L. Messing, Improved Fracture Behavior of Alumina Microstructural Composites with Highly Textured Compressive Layers, J. Am. Ceram. Soc. 97 (2014) 3643–3651. https://doi.org/10.1111/jace.13168.

[9] Y. Chang, S. Poterala, D. Yener, G.L. Messing, Fabrication of Highly Textured Fine-Grained α-Alumina by Templated Grain Growth of Nanoscale Precursors, J. Am. Ceram. Soc. 96 (2013) 1390–1397. https://doi.org/10.1111/jace.12286.

[10] R.J. Pavlacka, G.L. Messing, Processing and mechanical response of highly textured Al2O3, Journal of the European Ceramic Society 30 (2010) 2917–2925. https://doi.org/10.1016/j.jeurceramsoc.2010.02.009.

[11] R.L. Walton, M.D. Vaudin, A.-K. Hofer, E.R. Kupp, R.J. Meyer, G.L. Messing, Tailoring particle alignment and grain orientation during tape casting and templated grain growth, Journal of the American Ceramic Society 102 (2019) 2405–2414. https://doi.org/10.1111/jace.16144.

[12] R. Pavlacka, R. Bermejo, Y. Chang, D.J. Green, G.L. Messing, Fracture Behavior of Layered Alumina Microstructural Composites with Highly Textured Layers, Journal of the American Ceramic Society 96 (2013) 1577–1585. https://doi.org/10.1111/jace.12292.

[13] M. Zhang, Y. Chang, R. Bermejo, G. Jiang, Y. Sun, J. Wu, B. Yang, W. Cao, Improved fracture behavior and mechanical properties of alumina textured ceramics, Materials Letters 221 (2018) 252–255. https://doi.org/10.1016/j.matlet.2018.03.123.

[14] A.-K. Hofer, R. Walton, O. Ševeček, G.L. Messing, R. Bermejo, Design of damage tolerant and crack-free layered ceramics with textured microstructure, Journal of the European Ceramic Society 40 (2020) 427–435. https://doi.org/10.1016/j.jeurceramsoc.2019.09.004.

[15] E. Suvaci, K.-S. Oh, G.L. Messing, Kinetics of template growth in alumina during the process of templated grain growth (TGG), Acta Materialia 49 (2001) 2075–2081. https://doi.org/10.1016/S1359-6454(01)00105-7.

[16] E. Suvaci, G.L. Messing, Critical Factors in the Templated Grain Growth of Textured Reaction-Bonded Alumina, Journal of the American Ceramic Society 83 (2000) 2041–2048. https://doi.org/10.1111/j.1151-2916.2000.tb01509.x.

[17] C.B. Carter, M.G. Norton, Ceramic Materials: Science and Engineering, second ed., Springer New York/ Heidelberg/ Dordrecht/ London, 2013.

[18] S.-J. L. Kang, Sintering: Densification, Grain Growth & Microstructure, Elsevier Butterworth-Heinemann, 2005.

[19] C. Wang, W. Ping, Q. Bai, H. Cui, R. Hensleigh, R. Wang, A.H. Brozena, Z. Xu, J. Dai, Y. Pei, C. Zheng, G. Pastel, J. Gao, X. Wang, H. Wang, J.-C. Zhao, B. Yang, X.(R.) Zheng, J.

Luo, Y. Mo, B. Dunn, L. Hu, A general method to synthesize and sinter bulk ceramics in seconds, Science (2020) 521–526.

[20] M. Biesuz, S. Grasso, V.M. Sglavo, What's new in ceramics sintering? A short report on the latest trends and future prospects, Current Opinion in Solid State and Materials Science 24 (2020) 100868. https://doi.org/10.1016/j.cossms.2020.100868.

[21] J. Guo, H. Guo, A.L. Baker, M.T. Lanagan, E.R. Kupp, G.L. Messing, C.A. Randall, Cold Sintering: A Paradigm Shift for Processing and Integration of Ceramics, Angew. Chem. Int. Ed Engl. 55 (2016) 11457–11461. https://doi.org/10.1002/anie.201605443.

[22] R.I. Todd, E. Zapata-Solvas, R.S. Bonilla, T. Sneddon, P.R. Wilshaw, Electrical characteristics of flash sintering: thermal runaway of Joule heating, Journal of the European Ceramic Society 35 (2015) 1865–1877. https://doi.org/10.1016/j.jeurceramsoc.2014.12.022.

[23] M. Cologna, B. Rashkova, R. Raj, Flash Sintering of Nanograin Zirconia in <5 s at 850°C, Journal of the American Ceramic Society 93 (2010) 3556–3559. https://doi.org/10.1111/j.1551-2916.2010.04089.x.

[24] Z. Shen, M. Johnsson, Z. Zhao, M. Nygren, Spark Plasma Sintering of Alumina, Journal of the American Ceramic Society (2002) 1921–1927.

[25] E.A. Olevsky, L. Froyen, Impact of Thermal Diffusion on Densification During SPS, Journal of the American Ceramic Society 92 (2009) S122-S132. https://doi.org/10.1111/j.1551-2916.2008.02705.x.

[26] A. Kocjan, M. Logar, Z. Shen, The agglomeration, coalescence and sliding of nanoparticles, leading to the rapid sintering of zirconia nanoceramics, Sci. Rep. 7 (2017) 2541. https://doi.org/10.1038/s41598-017-02760-7.

[27] A.-K. Hofer, A. Kocjan, R. Bermejo, High-strength lithography-based additive manufacturing of ceramic components with rapid sintering, Additive Manufacturing 59 (2022) 103141. https://doi.org/10.1016/j.addma.2022.103141.

[28] R.P. Behera, M.J.-H. Reavley, Z. Du, C.L. Gan, H. Le Ferrand, Ultrafast high-temperature sintering of dense and textured alumina, Journal of the European Ceramic Society 42 (2022) 7122–7133. https://doi.org/10.1016/j.jeurceramsoc.2022.08.014.

[29] M. Schwentenwein, J. Homa, Additive Manufacturing of Dense Alumina Ceramics, International Journal of Applied Ceramic Technology 12 (2015) 1–7. https://doi.org/10.1111/ijac.12319.

[30] A.D. Lantada, A. de Blas Romero, M. Schwentenwein, C. Jellinek, J. Homa, Lithography-based ceramic manufacture (LCM) of auxetic structures: present capabilities and

challenges, Smart Mater. Struct. 25 (2016) 54015. https://doi.org/10.1088/0964-1726/25/5/054015.

[31] A. de Blas Romero, M. Pfaffinger, G. Mitteramskogler, M. Schwentenwein, C. Jellinek, J. Homa, A.D. Lantada, J. Stampfl, Lithography-based additive manufacture of ceramic biodevices with design-controlled surface topographies, Int J Adv Manuf Technol 88 (2017) 1547–1555. https://doi.org/10.1007/s00170-016-8856-1.

[32] W.L. Bradbury, E.A. Olevsky, Production of SiC–C composites by free-pressureless spark plasma sintering (FPSPS), Scripta Materialia 63 (2010) 77–80. https://doi.org/10.1016/j.scriptamat.2010.03.009.

[33] EN 623-2, Advanced technical ceramics - Monolithic ceramics - General and textural properties - Part 2: Determination of density and porosity, 1994.

[34] F.K. Lotgering, Topotactical Reactions with Ferrimagnetic Oxides having Hexagonal Crystal Structures - I, Journal of Inorganic and Nuclear Chemistry (1958) 113–123.

[35] ISO/FDIS 23146, Fine ceramics (advanced ceramics, advanced technical ceramics) - Test methods for fracture toughness of monolithic ceramics - Single-edge V-notch beam (SEVNB) method, 2008.

[36] E. Suvaci, K.-S. Oh, G.L. Messing, Kinetics of template growth in alumina druing the process of templated grain growth (TGG), Acta Materialia (2001) 2075–2081.

[37] M.M. Seabaugh, E. Suvaci, B. Brahmaroutu, G.L. Messing, Modeling Anisotropic Single Crystal Growth Kinetics in Liquid Phase Sintered α-Al2O3, Interface Science (2000) 257–267.

[38] E.A. Olevsky, S. Kandukuri, L. Froyen, Consolidation enhancement in spark-plasma sintering: Impact of high heating rates, Journal of Applied Physics 102 (2007) 114913. https://doi.org/10.1063/1.2822189.

[39] M. Kermani, J. Dong, M. Biesuz, Y. Linx, H. Deng, V.M. Sglavo, M.J. Reece, C. Hu, S. Grasso, Ultrafast high-temperature sintering (UHS) of fine grained α-Al2O3, Journal of the European Ceramic Society 41 (2021) 6626–6633. https://doi.org/10.1016/j.jeurceramsoc.2021.05.056.

[40] J. Schlacher, Z. Chlup, A.-K. Hofer, R. Bermejo, High-temperature fracture behaviour of layered alumina ceramics with textured microstructure, Journal of the European Ceramic Society (2022). https://doi.org/10.1016/j.jeurceramsoc.2022.11.046.

[41] R. Danzer, T. Lube, R. Morrell, P. Supancic, Handbook of Advanced Ceramics: Materials, Applications, Processing, and Properties, 2nd ed., Elsevier, 2013.

[42] A.-K. Hofer, I. Kraleva, T. Prötsch, A. Vratanar, M. Wratschko, R. Bermejo, Effect of second phase addition of zirconia on the mechanical response of textured alumina ceramics, Journal of the European Ceramic Society (2023) 2935–2942. https://doi.org/10.1016/j.jeurceramsoc.2022.08.058.

Supplementary Information

Templated grain growth in rapid sintered 3D-printed alumina ceramics

Anna-Katharina Hofer[1], Andraž Kocjan[2], Raul Bermejo[1]

[1]Department of Materials Science, Montanuniversitaet Leoben, Franz Josef-Strasse 18, A-8700 Leoben, Austria

[2]Department for Nanostructured Materials, Jožef Stefan Institute, Jamova 39, Sl-1000 Ljubljana, Slovenia

Table S1: Information about the processing of various textured alumina ceramics found in literature

		Ref.	Dimensions templates [µm]	Templates content [vol%]	Templates alignment method	Liquid Phase	Liquid Phase content	Sintering temperature [°C]	Sintering time [min]	Heating rate [°C/min]
TA-LP-RS	A		5-16 x 0.1	2.5	Lithography Ceramic Manufacturing (LCM)	$CaO\text{-}SiO_2$	0.25 wt%	1600	2	450
	B								4	
	C								16	
	D								64	
TA-LP-CS	E								360	5
	F								720	
CS	G	Hofer et al. (2021) [10]		5					360	
	H	Schlacher et al. (2022) [39]			Tape-Casting (TC)		0.1 wt%	1550	120	
	I	Chang et al. (2013) [7]	3 x 0.35				0.25 wt%			
	J	Suvaci et al. (2001) [35]	15-25 x 2	1			1 vol%	1450	90	
	K			5						
UHTS	L	Behera et al. (2022) [28]	6.4 x 0.25	5	Magnetically-Assisted Slip Casting (MASC)	Fe_3O_4 (SPION)	0.75 vol%	1700	<1	10 000-12 000

Tape Casting: Compositions

Table A: Compositions of TC suspensions of TA + xZrO_2/3YSZ prepared for *Publication A*

		TA + 1vol% ZrO_2 / 3YSZ		TA + 2vol% ZrO_2 / 3YSZ	
		vol%		vol%	
		ZrO2	3YSZ	ZrO2	3YSZ
Solids	Al_2O3	17.81%	17.80%	17.56%	17.55%
	Templates	0.19%	0.19%	0.38%	0.38%
	ZrO_2 / 3YSZ	0.94%	0.94%	0.92%	0.92%
Sintering additives	$Ca(NO_3)_2{\cdot}4H_2O$	0.08%	0.08%	0.08%	18.85%
	$C_8H_{20}O_4Si$	0.15%	0.15%	0.15%	0.08%
Solvents/ dispersant	Fish oil	2.61%	2.61%	2.61%	2.61%
	Xylenes	33.18%	33.18%	33.21%	33.22%
	Ethyl Alcohol	36.10%	36.11%	36.13%	36.14%
Binder/ plasticizer	Polyvinyl Butyral	5.06%	5.06%	5.07%	5.07%
	Butylbenzyl Phthalate	2.26%	2.26%	2.26%	2.26%
	Dibutyl sebacate	1.62%	1.62%	1.62%	1.62%

		TA + 5vol% ZrO_2 / 3YSZ		TA + 10vol% ZrO_2 / 3YSZ	
		vol%		vol%	
		ZrO2	3YSZ	ZrO2	3YSZ
Solids	Al_2O_3	16.84%	16.80	15.66	15.60
	Templates	0.93%	0.93	1.83	1.82
	ZrO_2 / 3YSZ	0.89%	0.88	0.82	0.82
Sintering additives	$Ca(NO_3)_2{\cdot}4H_2O$	0.08%	0.08	0.08	0.08
	$C_8H_{20}O_4Si$	0.15	0.15	0.15	0.15
Solvents/ dispersant	Fish oil	2.62	2.62	2.63	2.63
	Xylenes	33.29	33.31	33.43	33.46
	Ethyl Alcohol	36.23	36.24	36.38	36.41
Binder/ plasticizer	Polyvinyl Butyral	5.08	5.08	5.10	5.11
	Butylbenzyl Phthalate	2.27	2.27	2.28	2.28
	Dibutyl sebacate	1.63	1.63	1.63	1.64

Table B: Compositions of TC suspensions for research of J.Schlacher, R. Papšik and future work

		ZMA15	ZTA50
		vol%	
Solids	Al_2O_3	14.81	7.78
	ZrO_2 / 3YSZ	2.61	7.78
Solvents/ dispersant	Fish oil	2.54	2.7
	Xylenes	34.13	35.64
	Ethyl Alcohol	37.14	38.78
Binder/ plasticizer	Polyvinyl Butyral	4.96	4.14
	Butylbenzyl Phthalate	2.21	1.85
	Dibutyl sebacate	1.59	1.33

		Cr_2AlC	Longlife
		vol%	
Solids	Cr_2AlC / Longlife	58.94	12.35
Solvents/ dispersant	Fish oil	1.89	2.41
	Xylenes	16.05	36.83
	Ethyl Alcohol	16.05	40.07
Binder/ plasticizer	Polyvinyl Butyral	3.93	4.72
	Butylbenzyl Phthalate	1.97	2.11
	Dibutyl sebacate	1.18	1.51

Stereolithographic 3D-printing: Thermal post processing – binder removal

Table C: Thermal post processing - binder removal of equiaxed and textured stereolithgraphic 3D-printed alumina (LithaLox HP500)

temperature	heating rate	dwell time
[°C]	[°C/min]	[h]
25		
75	0.20	3
90	0.20	5
110	0.20	12
120	0.20	38
130	0.10	4
170	0.10	4
220	0.10	4
250	0.10	6
325	0.10	6
430	0.20	2
30	1.00	
total duration	141.51 hours	